

OPTIMIZATION OF ETHANOL PRODUCTION FROM
CONCENTRATED SUBSTRATE

Except where reference is made to the work of others, the work described in this dissertation is my own or was done in collaboration with my advisory committee.
This dissertation does not include proprietary or classified information.

Byung-Hwan Um

Certificate of Approval:

Y.Y. Lee
Professor
Chemical Engineering

Thomas R. Hanley, Chair
Professor
Chemical Engineering

Gopal A. Krishnagopalan
Professor
Chemical Engineering

R. Eric Berson
Assistant Professor
Chemical Engineering at
University of Louisville

Joe F. Pittman
Interim Dean
Graduate School

OPTIMIZATION OF ETHANOL PRODUCTION FROM
CONCENTRATED SUBSTRATE

Byung-Hwan Um

A Dissertation

Submitted to

the Graduate Faculty of

Auburn University

in Partial Fulfillment of the

Requirements for the

Degree of

Doctor of Philosophy

Auburn, Alabama
August 4, 2007

OPTIMIZATION OF ETHANOL PRODUCTION FROM
CONCENTRATED SUBSTRATE

Byung-Hwan Um

Permission is granted to Auburn University to make copies of this dissertation at its discretion, upon request of individuals or institutions and at their expense. The author reserves all publication rights.

Signature of Author

Data of Graduation

VITA

Byung-Hwan Um was born in Masan on the southern coast of Korea on March 16, 1971, the son of Tae-Joon Um and Kyung-Ja Yoo. After completing high school at JoongAng High School in Masan, Korea in 1990, he attended Gyeongsang National University in Chinju, South Gyeongsang Province. (The Republic of Korea has nine provinces and thirty national universities). From 1992-1995, he joined his military service at Wonju, Gangwon Province. He graduated with a Bachelor of Science degree in 1998. He conducted research as a Research Assistant at Biochemical Laboratory at Gyeongsang National University. He attended the Colorado State University in Fort Collins, Colorado in the fall of 1999. He married Young-In Oh, daughter of Kil-Hwan Oh and Ook-Soon Kim on May 27, 2000 and earned a Master of Science in the summer of 2002. He then entered the University of Louisville in the spring of 2002. Following this academic performance, he transferred the Graduate School at Auburn University in the spring of 2004 to pursue the degree of Doctor of Philosophy in Chemical Engineering

DISSERTATION ABSTRACT

OPTIMIZATION OF ETHANOL PRODUCTION FROM
CONCENTRATED SUBSTRATE

Byung-Hwan Um

Doctor of Philosophy, August 4, 2007
(M.S. Chem. Eng., Colorado State University, 2002)

268 Typed Pages

Directed by Thomas R. Hanley

This research optimizes ethanol production from high concentrations of cellulosic substrates in order to produce ethanol economically from renewable resources. This study identifies and quantifies the factors that influence ethanol yield on high solids biomass slurries during saccharification followed by fermentation (SFF) processes leading to development of a computational fluid dynamics (CFD) model. This model describes slurry rheology in terms of measurable parameters and slurry/biomass characteristics as these parameters undergo transformation during the SFF process.

To obtain five percent (v/v) ethanol production needed for an economically viable industrial-scale ethanol distillation, high carbonate concentration is required. High carbonate concentration can be achieved only with high initial cellulose concentration combined with a favorable conversion yield of cellulose into soluble sugars.

Many researchers have reported repeatedly that solid concentrations above 10 percent resulted in poor ethanol yield due to inefficient mass transfer and to the different operating temperatures required for enzymatic hydrolysis and fermentation.

To develop data for a full scale design, ethanol fermentation of concentrated Solka Floc is evaluated in a three-liter bioreactor. The effects of mixing are evaluated using computational fluid dynamics (CFD) simulations of the three-liter reactor.

ACKNOWLEDGMENTS

I would like to sincerely thank all the individuals who in one way or another assisted me with the challenge that this work presented to me. Specifically, my great appreciation goes to my advisor, Dr. Thomas R. Hanley, for intellectual support, encouragement, and enthusiasm throughout my study, and for his patience in correcting both my stylistic and scientific errors. The completion of this work would not have been possible without my boss.

I would like to acknowledge with sincere gratitude to the members of my dissertation committee, Dr. Y. Y. Lee, Dr. Gopal A. Krishnagopalan, and Dr. Eric Berson. I am grateful for their helpful advices on various topics. Thanks also to Dr. Sung-Bae Kim, for the opportunity he offered me previously that helped to conduct this research.

I would like to thank my brother in law Dr. Cha-Su Ahn, my sister Hye-Sun Um, for their constant support and encouragement which have motivated me through my entire endeavor. The author wish to thank Dr. Teak-Keun Kim, Dr. Moon-Seong Kang, and Mr. Rajesh K. Dasari for their valuable discussion and the support of this project.

During my stay in USA, my thoughts were never far away from my parents, Tae-Joon Um, Kyung-Ja Yoo, and parents in law, Kil-Hwan Oh, Oak-Soon Kim in Korea.

Finally, this dissertation is dedicated to my wife, Young-In Oh. I want to thank my lovely wife for her assistance and faith in me, and thanks to my best friends, Su-Man Paeng, Sang-Hwan Lee, and Hyung-Wook Kim.

Style manual or journal used Chemical Engineering (Biochemical Technology)

Computer software used Microsoft Office XP (Professional)

TABLE OF CONTENTS

LIST OF TABLES	xi
LIST OF FIGURES	xiv
I. INTRODUCTION	1
Objectives	5
II. LITERATURE REVIEW	6
THE BIOMASS-TO-ETHANOL PROCESS OVERVIEW	6
BIOETHANOL AS FUEL	7
Ethanol and its properties.....	8
What are the benefits of bioethanol ?	9
Bioethanol production from biomass.....	10
LIGNOCELLULOSIC BIOMASS	10
Structure of biomass	11
Cellulose	11
Hemicellulose	13
Lignin.....	13
Solka Floc	14
PRETREATMENT IMPORTANCE	14
PRETREATMENT TECHNIQUES	15
ENZYMATIC HYDROLYSIS.....	17
ETHANOL FERMENTATION.....	18
ETHANOL FERMENTATION PROCESS	20
Direct Microbial Conversion (DMC).....	20
Separate Hydrolysis and Fermentation (SHF)	21
Simultaneous Saccharification and Cofermentation (SSFC).....	21
Simultaneous Saccharification and Fermentation (SSF)	22
Theoretical Ethanol Yield via Fermentation Process.....	23
BIOREACTOR DESIGN	24
Mixing in Bioreactors	25
Reactor Geometries.....	26
Turbine Agitations.....	27
Helical-Ribbon and Anchor Impellers.....	30
Conventional Radical Flow Turbine.....	32

Flow Patterns	32
Scale-Up Method For Fermentors	34
Simulation Using Computational Fluid Dynamics	37
Physical Model for Turbulence Fluid Motion	42
Approaches for Mixing Tank Simulation	45
Structured and Unstructured Mesh	47
Multiphase Simulation	47
VISCOSITY OF CELLULOSIC SLURRIES	48
Non-Newtonian Behavior	49
Measurement Techniques	51
Impeller Ribbon Viscometer Technique	54
Ruston Impeller Programmed Viscometer	55
III. HIGH SOLID ENZYMATIC HYDROLYSIS AND FERMENTATION OF SOLKA FLOC TO ETHANOL	56
ABSTRACT	56
INTRODUCTION	58
MATERIAL AND METHODS	61
Raw Material	61
Commercial Enzyme	61
Microorganism	61
Bench Scale Reactor	62
Strategy of High Solid Loading on Enzyme Hydrolysis and Fermentation	63
Enzymatic Hydrolysis	63
Cell Stock Culture	65
Preliminary Fermentation	66
2 L Fermentation	66
ANALYSIS AND ASSAY	68
Carbohydrate	68
Moisture and Ash	68
Dry Cell Weight vs Optical Density	69
Glucose and Ethanol	70
RESULTS AND DISCUSSION	71
Enzymatic Hydrolysis Below 10 % (w/v)	71
Stirring Power in 3L Fully-Baffled Tanks	75
The Effect of Bioreactor Configuration on Bioconversion	78
The Effect of Rotational Speed on Glucose Yield	85
High-Solids Saccharification by Portion Loading	88
The Effects of Temperature on High-Solid Bioconversion	92
The Effect of Substrate Concentration on Ethanol Yield	95
CONCLUSIONS	98
IV. RHEOLOGICAL PARAMETER DETERMINATION FOR ENZYMATIC SUSPENSIONS AND FERMENTATION BROTHS WITH HIGH SUBSTRATES LOADING	100

ABSTRACT	100
INTRODUCTION	102
MATERIAL AND METHODS	104
Suspension Fluids used for Measurements	104
Viscometer	104
Concentric Cylinder System	104
Measurement of Particle Size	106
Calculation of Power Law Parameters.....	106
Yield Stress	107
RESULTS AND DISCUSSION	108
Rheological Behavior of Enzymatic Hydrolysis Suspension	108
Rheological Parameter Estimation for Pseudoplastic Suspension.....	112
Determination of Particle Size Treated by Enzyme.....	126
CONCLUSION.....	131
V. FLOW PATTERN SIMULATION IN A HIGH SOLIDS CELLULOSE TO ETHANOL BIOREACTOR USING COMPUTATIONAL FLUID DYNAMICS	132
ABSTRACT	132
INTRODUCTION	134
MATERIAL AND METHODS	136
Tank Geometric Configuration of the Investigated Vessel.....	136
The k- ϵ Mathematical Models	137
Constant N_p and P per Liquid Volume.....	138
Simulation Model.....	138
Simulation Tool Package	138
Description of Supercomputer	139
RESULTS AND DISCUSSION	140
Vessel Geometry and Grid Generation	140
Convergence Criteria and Blend Time	142
Grid Refinement.....	143
Power Law Flow Behavior Index ($0.46 \leq n \leq 0.97$)	148
Turbulence a Tank with Baffled Rushton Impeller	148
Predicted Velocity Distribution	156
Axial Velocity	157
Stagnant and Slow Flow Zone	166
Shear Stress and Turbulent Viscosity in Mixing Tank	173
Turbulence Kinetic Energy and Dissipation Rate.....	174
CONCLUSION.....	183
VI. OVERALL CONCLUSIONS AND RECOMMENDATIONS	185
BIBLIOGRAPHY	191
APPENDICES	202

APPENDIX A.....	202
MEDIA FOR FERMENTATION AND BIOREACTOR PROTOCOLS	202
A-1. Agar media composities	203
A-2. Revival and growth of <i>Zymomonas mobilis</i> 39679 pZB 4L.....	205
A-3. Set up of BioFlo 3000 (New Brunswick Scientific).....	209
APPENDIX B.....	215
RHEOLOGY AND RHEOLOGICAL PARAMETER DETERMINATION	215
.....	215
APPENDIX C.....	234
SIMULATION METHODS, PROCEDURES, AND APPARATUS	234
C-1. Start Mixism and Fluent.....	235

LIST OF TABLES

Table II-1	Important physical properties of ethanol	9
Table II-2	Methods used for pretreatment of lignocellulosics.....	16
Table II-3	K-values for effective shear-rate model.....	28
Table II-4	Scale-up criteria in fermentation industries	36
Table II-5	Overview of Turbulence Models	44
Table III-1	Initial composition of untreated Solka Floc	61
Table III-2	Ethanol yield and conversion percent for <i>Zm. mobilis</i> after 48 hours.....	96
Table IV-1	Determination of rheological parameter as function of time during initial 4-hr enzymatic hydrolysis (10 percent, w/v)	116
Table IV-2	Determination of rheological parameter as function of time during initial 4-hr enzymatic hydrolysis (15 percent, w/v)	117
Table IV-3	Determination of rheological parameter as function of time during initial 4-hr enzymatic hydrolysis (20 percent, w/v)	118
Table IV-4	Determination of rheological parameter as function of time during initial SSF process.....	120
Table IV-5	Determination of rheological parameter as function of time during initial SFF process.....	121
Table IV-6	Determination of rheological parameter as function of time during initial Fermentation process	130
Table B-1	Determination of rheological parameter as function of time during initial 4-hr enzymatic hydrolysis (10 percent, w/v, 30 FPU, 50 °C).....	225

Table B-2	Determination of rheological parameter as function of time during initial 4-hr enzymatic hydrolysis (10 percent, w/v, 15 FPU, 50 °C).....	226
Table B-3	Determination of rheological parameter as function of time during initial 4-hr enzymatic hydrolysis (10 percent, w/v, 30 FPU, 30 °C).....	227
Table B-4	Determination of rheological parameter as function of time during initial 4-hr enzymatic hydrolysis (15 percent, w/v, 30 FPU, 50 °C).....	228
Table B-5	Determination of rheological parameter as function of time during initial 4-hr enzymatic hydrolysis (15 percent, w/v, 15 FPU, 50 °C).....	229
Table B-6	Determination of rheological parameter as function of time during initial 4-hr enzymatic hydrolysis (15 percent, w/v, 30 FPU, 30 °C).....	230
Table B-7	Determination of rheological parameter as function of time during initial 4-hr enzymatic hydrolysis (20 percent, w/v, 30 FPU, 50 °C).....	231
Table B-8	Determination of rheological parameter as function of time during initial 4-hr enzymatic hydrolysis (20 percent, w/v, 15 FPU, 50 °C).....	232
Table B-9	Determination of rheological parameter as function of time during initial 4-hr enzymatic hydrolysis 20 percent, w/v, 30 FPU, 30 °C)	233
Table C-1	Geometry of 3L mixing tank	242
Table C-2	Blend time and flow rate (RPM=120)	243
Table C-3	Power draw and correlation for water simulation ($\mu=0.0010$, RPM=120).244	
Table C-4	Power draw and correlation for 10 % Solka Floc fermentation broth ($\mu=0.0192$, RPM=120).....	245
Table C-5	Power draw and correlation for 15 % Solka Floc fermentation broth ($\mu=0.0775$, RPM=120).....	246
Table C-6	Power draw and correlation for 20 % Solka Floc fermentation broth ($\mu=0.1050$, RPM=120).....	247

LIST OF FIGURES

Figure II-1	Basic biomass-to-ethanol flow diagram	6
Figure II-2	A simplified model to illustrate the cross-linking of cellulose micro fibrils and hemicellulose in the lignocellulosic biomass	12
Figure II-3	The standard geometry of mixing tank; nomenclature used to describe the mixing system	26
Figure II-4	A wide variety of turbine is available to handle viscosities to about 50 pa-s	27
Figure II-5	Helical-ribbon and anchor impellers provide an alternative to turbine impeller	30
Figure II-6	Streamline pattern in a standard cylindrical system with axial high-speed impeller and radial baffles	33
Figure II-7	Streamline patterns in cylindrical system with axial high-speed impeller and draft tube	33
Figure II-8	Streaklines showing flow around a 2d bluff body	45
Figure II-9	Sliding Grid Motion	46
Figure III-1	Strategy of high solid loading on enzyme hydrolysis and fermentation	64
Figure III-2	The glucose conversion rate during the initial 6-hr enzymatic hydrolysis of 5 percent (w/v) Solka Floc	72
Figure III-3	Enzymatic hydrolysis of Solka Floc at lower percent solid concentration (III-3a) and Solka Floc at 5 percent solid for different impeller type (III-3b) as a function of time at constant cellulase activity	74
Figure III-4	Power consumption in 2 L bioreactor with 5 percent (w/v) Solka Floc suspension with various bioreactor configuration as function of RPM	76

Figure III-5	Power consumption in 2 L bioreactor with 15 percent (w/v) Solka Floc suspension with various bioreactor configuration as function of RPM.....	77
Figure III-6	The effect of baffles on enzymatic hydrolysis of Solka Floc at 5 percent (III-6a) and 10 percent solid concentration with Rushton impeller as a function of time at constant cellulose activity	80
Figure III-7	The glucose conversion as a function of time for the two bioreactor: Baffled Rushton and Baffled Marine Configuration at 5 percent (w/v) Solka Floc	81
Figure III-8	The effect of baffles on enzymatic hydrolysis of Solka Floc at 13 % (III-6a) and 15 % solid concentration with Rushton impeller as a function of time at constant cellulase activity	82
Figure III-9	The effect of RPM on enzymatic hydrolysis of Solka Floc at 10 (III-8a), 13 (III-8b) and 15 percent (III-8c) solid concentration with baffled Rushton bioreactor as a function of time at constant cellulose activity.....	84
Figure III-10	The enzymatic hydrolysis for the baffled Rushton (III-9a) and Marine (III-9b) impellers as a function of time at constant cellulose activity	87
Figure III-11	The effects of temperature on high solid enzyme hydrolysis	90
Figure III-12	The effects of temperature on cell growth curve and ethanol production	91
Figure III-13	The time course of substrate utilization and ethanol production by <i>Zymomonas mobilis</i> at 10 (III-13a), 15 (III-13b), and 20 percent (III-13c) solid concentration with Rushton impeller as a function of time at constant cellulase activity.....	94
Figure III-14	The ethanol conversion yield (CEtOH) with Rushton impeller as a function of retention time during SFF at 30 °C (III-14a) and 40 °C (III-14b) with 10, 15, and 20 percent substrate concentration constant cellulase activity. Note: same as condition of Figure III-13	97
Figure IV-1	Scheme of concentric cylinder (stirrer FL 100/6W) system of Paar Physica modular compact rhoemeter (MCR 300)	105
Figure IV-2	Viscosity and shear stress curves as a function of shear rate for different time during initial 4-hours enzymatic hydrolysis (10 percent, w/v).....	109
Figure IV-3	Viscosity and shear stress curves as a function of shear rate for different time during initial 4-hours enzymatic hydrolysis (15 percent, w/v).....	110

Figure IV-4	Viscosity and shear stress curves as a function of shear rate for different time during initial 4-hour enzymatic hydrolysis (20 percent, w/v).....	111
Figure IV-5	Viscosity and shear stress curves as a function of shear rate for different time during initial SSF process (40 °C)	113
Figure IV-6	Viscosity and shear stress curves as a function of shear rate for different time during initial SFF process (combined temperature 50 °C -30 °C).....	114
Figure IV-7	Comparison of the different rheological models used to fit the shear stress as function of shear rate data of 10 percent sold concentration of fermentation broth at t=0. Symbols represent experimental measurements and lines represent four different model predictions	122
Figure IV-8	Comparison of the different rheological models used to fit the shear stress as function of shear rate data of 15 percent sold concentration of fermentation Broth at t=0. Symbols represent experimental measurements and lines represent four different model predictions	123
Figure IV-9	Comparison of the different rheological models used to fit the shear stress as function of shear rate data of 20 percent sold concentration of fermentation broth at t=0. Symbols represent experimental measurements and lines represent four different model predictions	124
Figure IV-10	Percentage (10a) volume and (10b) cumulative volume particle size distribution for the substrate during SSF and SFF process (10 percent, w/v).....	127
Figure IV-11	Percentage (10a) volume and (10b) cumulative volume particle size distribution for the substrate during SSF and SFF process (15 percent, w/v).....	128
Figure IV-12	Percentage (10a) volume and (10b) cumulative volume particle size distribution for the substrate during SSF and SFF process (20 percent, w/v).....	129
Figure V-1	NBS 3 L bioreactor tank geometry	136
Figure V-2	Nomenclature used to describe the mixing system	140
Figure V-3	Grid edge (3 L Mixing Tank).....	144
Figure V-4	Outline (3 L Mixing Tank).....	145
Figure V-5	Grid face (3 L Mixing tank).....	146

Figure V-6	Sweep surface in mixing tank	147
Figure V-7	Velocity vectors colored by velocity magnitude (m/s, 10 percent suspension).....	149
Figure V-8	Contour of velocity magnitude-panel 2, 4, and 6 (m/s, 10 percent suspension).....	150
Figure V-9	Contour of velocity magnitude-panel 3 and 5 (m/s, 10 percent suspension).....	151
Figure V-10	Contours of axial velocity (m/s, 10 percent suspension)-panel 1	152
Figure V-11	Contour of turbulence kinetic energy (k, m ² /s ² , 10 percent suspension)-panel 1	153
Figure V-12	Contour of turbulent dissipation rate (k, m ² /s ³ , 10 percent suspension)-panel 1	154
Figure V-13	Contour of turbulent viscosity (kg/m-s, 10 percent suspension)-panel 1	155
Figure V-14	Velocity vectors colored by velocity magnitude (m/s, 15 percent suspension) - panel 1.....	159
Figure V-15	Velocity vectors colored by axial velocity (m/s, 15 percent suspension)-panel 7.....	160
Figure V-16	Contours of axial velocity (m/s, 15 percent suspension)-panel 1	161
Figure V-17	Velocity vectors colored by velocity magnitude (m/s, 15 percent suspension)- impeller and panel 1.....	162
Figure V-18	Contour of turbulence kinetic energy (k, m ² /s ² , 15 percent suspension)-panel 1	163
Figure V-19	Contour of turbulent dissipation rate (k, m ² /s ³ , 15 percent suspension)-panel 1	164
Figure V-20	Contour of turbulent viscosity (kg/m-s, 15 percent suspension)-panel 1	165
Figure V-21	Velocity vectors colored by velocity magnitude (m/s, 20 percent suspension)- panel 1.....	167

Figure V-22	Velocity vectors colored by velocity magnitude (m/s, 20 percent suspension)-bottom of panel 6	168
Figure V-23	Contours of axial velocity (m/s, 20 percent suspension)-panel 1	169
Figure V-24	Contour of turbulence kinetic energy (k, m ² /s ² , 20 percent suspension)-panel 1	170
Figure V-25	Contour of turbulent dissipation rate (k, m ² /s ³ , 20 percent suspension)-panel 1	171
Figure V-26	Contour of turbulent viscosity (kg/m-s, 20 percent suspension)-panel 1	172
Figure V-27	Average of axial velocity of 2 L suspension as tank radial at panel 1	175
Figure V-28	Average of axial velocity of 2 L suspension as tank radial at panel 2	175
Figure V-29	Average of axial velocity of 2 L suspension as tank radial at panel 4	176
Figure V-30	Average of axial velocity of 2 L suspension as tank radial at panel 6	176
Figure V-31	Average of axial velocity of 2 L suspension as tank radial at panel 7	177
Figure V-32	Average of shear stress of 2 L suspension as tank radial at panel 1	177
Figure V-33	Average of shear stress of 2 L suspension as tank radial at panel 3	178
Figure V-34	Average of shear stress of 2 L suspension as tank radial at panel 4	178
Figure V-35	Average of shear stress of 2 L suspension as tank radial at panel 5	179
Figure V-36	Average of turbulent kinetic energy (k) of 2 L suspension as tank radial at panel 1	179
Figure V-37	Average of turbulent kinetic energy (k) of 2 L suspension as tank radial at panel 3	180
Figure V-38	Average of turbulent kinetic energy (k) of 2 L suspension as tank radial at panel 5	180
Figure V-39	Average of turbulent dissipation rate (ϵ) of 2 L suspension as tank radial at panel 1	181
Figure V-40	Average of turbulent dissipation rate (ϵ) of 2 L suspension as tank radial at panel 3	181

Figure V-41	Average of turbulent dissipation rate (ϵ) of 2 L suspension as tank radial at panel 5	182
Figure VI-1	Schematic diagram of continuous saccharification and fermentation at separate temperature condition	189
Figure A-1	Preparation and representative streak plate	208
Figure B-1	Viscosity and shear stress curves as a function of shear rate for different time during initial 4-hr enzymatic hydrolysis (10 percent, w/v, 30 FPU, 50 °C)	216
Figure B-2	Viscosity and shear stress curves as a function of shear rate for different time during initial 4-hr enzymatic hydrolysis (10 percent, w/v, 15 FPU, 50 °C)	217
Figure B-3	Viscosity and shear stress curves as a function of shear rate for different time during initial 4-hr enzymatic hydrolysis (10 percent, w/v, 15 FPU, 30 °C)	218
Figure B-4	Viscosity and shear stress curves as a function of shear rate for different time during initial 4-hr enzymatic hydrolysis (15 percent, w/v, 30 FPU, 50 °C)	219
Figure B-5	Viscosity and shear stress curves as a function of shear rate for different time during initial 4-hr enzymatic hydrolysis (15 percent, w/v, 15 FPU, 50 °C)	220
Figure B-6	Viscosity and shear stress curves as a function of shear rate for different time during initial 4-hr enzymatic hydrolysis (15 percent, w/v, 30 FPU, 30 °C)	221
Figure B-7	Viscosity and shear stress curves as a function of shear rate for different time during initial 4-hr enzymatic hydrolysis (20 percent, w/v, 30 FPU, 50 °C)	222
Figure B-8	Viscosity and shear stress curves as a function of shear rate for different time during initial 4-hr enzymatic hydrolysis (20 percent, w/v, 15 FPU, 50 °C)	223
Figure B-9	Viscosity and shear stress curves as a function of shear rate for different time during initial 4-hr enzymatic hydrolysis (20 percent, w/v, 30 FPU, 30 °C)	224
Figure C-1	The graphical user interface (GUI) Components (MixSim 2.1.10).....	240

Figure C-2	Scaled residuals	241
Figure C-3	Histogram of tank cell equiangle skew	241

I. INTRODUCTION

In August 2005, President George W. Bush signed into law the Energy Policy Act (EPACT) of 2005, creating a national Renewable Fuels Standard (RFS). This watershed legislation establishes a baseline for renewable fuel use, beginning with 4 billion gallons per year in 2006 and expanding to 7.5 billion gallons by 2012. The vast majority of the renewable fuel used will be ethanol, resulting in a doubling of the domestic ethanol industry in the next six years.

The United States and other industrialized countries of the world are dependent on imported oil, and oil imports continue to increase, threatening the strategic security of these countries (USA Today, 2005). For instance, the United States imports almost 60 per cent of its current oil supply (RFA, 2003). The transportation sector in the United States is particularly dependent on oil with around 97 per cent of transportation energy being derived from petroleum. Few substitutes exist for petroleum for transportation usage (Wyman et al., 1993).

One of the most immediate and important applications of biological energy systems is in the production of ethanol from biomass. Ethanol could reduce vehicle pollution by as much as 54 per cent. Currently, 1.5 billion gallons of ethanol are added to gasoline in the United States each year to improve vehicle performance and reduce air

pollution (Montross et al., 2004). While having these advantages, alcohol fuel still cannot be used extensively due to limitations in technology, economic and regional considerations. Since ethanol can be fermented and distilled from biomass, it is considered to be a renewable energy source. Environmentally, ethanol blended with gasoline is better than pure gasoline because of its renewability and lower toxicity (RSA, 2003).

The bioconversion of lignocellulosic feed stocks to fuel-grade ethanol offers a means to alleviate and/or mitigate some of the environmental impacts of the petroleum based transportation sector, such as the generation of airborne pollutants and greenhouse gases, while concurrently reducing the amount of biomass that is land-filled. Various feedstocks, including hardwoods, softwoods, and agricultural residues have been evaluated for their potential as a feedstock for bioconversion. Numerous researchers have investigated the production of ethanol from various lignocellulosic materials (Sun and Cheng, 2002). Of the agricultural residues, corn stover is the most abundant with annual US production of 150 million tons per year (Kadam and McMillan, 2003).

The polysaccharide fraction of agricultural residues can be hydrolyzed using acids or enzymes as catalysts (Zhang et al., 1999). Cellulases catalyze the hydrolysis of cellulose, the major structural component of biomass and the most abundant organic material on earth (Scott et al., 1994). Complete hydrolysis of cellulose yields the easily fermentable sugar, allowing biomass to be a potential renewable energy source (Fein et al., 1991; RSA, 2003; Scott et al., 1994). As a result, there is strong interest in understanding the process of enzymatic cellulose degradation (Fein et al., 1991). It is well known that enzymatic hydrolysis of cellulosic biomass is severely hampered by the

crystallinity of the cellulose, the noncellulosic fraction, and the presence of end-products during hydrolysis (McMillian, 1994). The problem is compounded by the relatively small pore sizes in untreated substrates, creating mass transfer limitations on both microorganisms and hydrolytic enzymes (Grohmann et al., 1985). Therefore, effective pretreatment is an essential prerequisite to improve the rate and yields of saccharification.

With regard to the fermentation step, several strategies have been investigated to obtain high ethanol yields. One leading approach is the simultaneous saccharification and fermentation (SSF) process (Cheung and Anderson, 1997; Öhgren et al., 2006; Takagi et al., 1977). Typically, as much as 90 per cent or more of the fermentation broth is water, which must be removed. Water separation is not only costly but also produces a large aqueous stream that must then be disposed of or recycled. Integrative approaches to water reduction include increasing the biomass concentration. When concentrated slurries are processed during SSF, the high viscosity prevents efficient mixing. It has been reported repeatedly that solid concentrations above 10 per cent result in poor ethanol yields due to inefficient mass transfer (Lübbert and Jørgensen, 2001, Mohagheghi et al., 1992; Spindler et al., 1988). Numerous attempts have been made to enhance the fermentation under high solid substrate (Öhgren et al., 2006; Philippidis and Hatzis, 1997; Stenberg, 2000; Teymouri, 2005; Varga et al., 2004). This difficulty partly accounts for the lack of literature concerning fermentation of biomass suspensions more concentrated than 10 per cent (Philippidis and Hatzis, 1997).

An SSF process at high solids concentrations using both enzymes and recombinant bacteria (for xylose conversion) appears to be the simplest and most economically viable way to attain suitable ethanol concentrations in the broths for

distillation. On the whole, several process parameters must be optimized: high initial substrate concentration, enzyme-to-substrate ratio, dosage of the active components (β -glucosidase-to-cellulase ratio) in the enzymatic mixture, bacteria concentration, and reactor conditions.

The process of designing, constructing and evaluating bioreactors for the high-substrate concentration fermentation is both costly and time-consuming in industrial fields (Oldshue, 1983). The use of computational fluid dynamics (CFD) can aid in bioreactor development by providing detailed information on the hydrodynamic and chemical environments necessary for optimal hydrolysis and cell growth.

Agitation in bioreactors is an important process design factor that can influence the hydrolysis operation in several ways. Considering the heterogeneity of the hydrolysis reaction environment where a liquid enzyme acts on a solid substrate, adequate mixing is required to ensure sufficient contact between the reactants as well as to promote heat and mass transfer within the reaction vessel. Moreover, it has been shown that excessive mixing can deactivate the enzyme and microorganism reducing production (sugar/ethanol) yields, owing to the shear force generated by the mixer and the entrapment of air bubbles into the medium at the air liquid surface (Reese, 1980; Ursula, 2002). Therefore, one way of improving the problems of the overall process is to determine the optimum level of mixing and reactant amount to minimize the extent of shear-induced enzyme and microorganism deactivation and to lower the mixing energy costs.

Objectives

Thus, the overall objectives of the research were developed to answer definitely the following issues

- To design and optimize a high solid slurry fermentation using commercial enzymes and recombinant microorganisms.
- To investigate ethanol yield using high-solids, concentrated Solka-Floc slurries (> 10 per cent w/v).
- To determine a fundamental understanding of the rheology of high solids biomass slurries during enzymatic hydrolysis.
- To develop fluid dynamic models to assist in full-scale design.

II. LITERATURE REVIEW

THE BIOMASS-TO ETHANOL PROCESS OVERVIEW

Lignocellulosic biomass can be converted to ethanol by acid or enzymatic approaches. In either option, the material must first be processed in some way to reduce its size and facilitate subsequent handling. Then, acids or enzymes are used to break apart or hydrolyze the hemicellulose and cellulose chains to form their component sugars. These sugars are fermented to bioethanol by adding yeasts, bacteria, or other suitable microorganisms, and the ethanol is recovered by distillation or other separation technologies for use as fuel. A process overview may be found in Figure II-1. This figure is a basic biomass-to-ethanol flow diagram (Wayman et al., 1993)

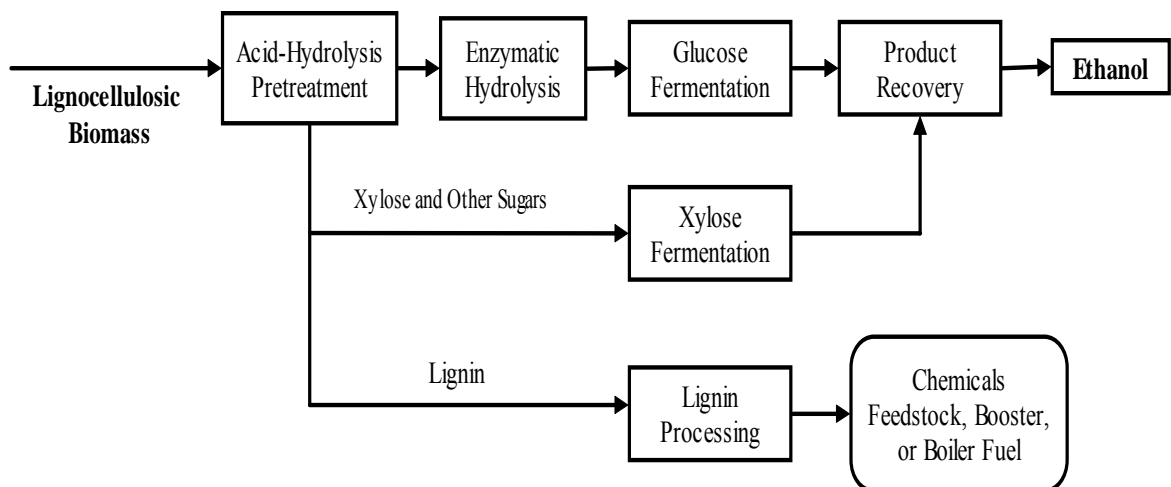


Figure II-1. Basic Biomass-to-Ethanol Flow Diagram (Wayman et al., 1993)

BIOETHANOL AS FUEL

Biofuel is a generic term for any liquid fuel produced from sources other than mineral reserves such as oil, coal and gas (EECA, 2005). In general biofuels can be used as a substitute for, or an additive to, gasoline and diesel fuel in most transport and non-transport applications. The most commonly used biofuels are biodiesel and bioethanol.

The use of ethanol as an automobile fuel in the United States dates as far back as 1908, to the Ford Model T. Henry Ford was a supporter of home-grown renewable fuels, and his Model T could be modified to run on either gasoline or pure alcohol (Carson, 2005). Ethanol was used to fuel cars well into the 1920s and 1930s as several efforts were made to sustain a U.S. ethanol program. Standard Oil marketed a 25 per cent ethanol by volume gasoline in the 1920s in the Baltimore area.

Utilizing cellulose to synthesize alternative renewable transportation fuels such as ethanol to replace gasoline is a technology that can provide a permanent solution to our energy needs (Wyman, 1994). Bioethanol is produced from the fermentation of sugar by enzymes produced from specific varieties of yeast. The five major sugars are the five-carbon xylose and arabinose and the six-carbon glucose, galactose, and mannose (Wyman, 1996). Traditional fermentation processes rely on yeasts that convert six-carbon sugars to ethanol. Glucose, the preferred form of sugar for fermentation, is contained in both carbohydrates and cellulose. Because carbohydrates are easier than cellulose to convert to glucose, the majority of ethanol currently produced in the United States is made from corn, which supplies large quantities of carbohydrates. Also, the

organisms and enzymes for carbohydrate conversion and glucose fermentation on a commercial scale are readily available.

Ethanol and Its Properties

Ethanol or ethyl alcohol, $\text{CH}_3\text{CH}_2\text{OH}$, has been described as one of the most exotic synthetic oxygen-containing organic chemicals because of its unique combination of properties as a solvent, a germicide, a beverage, an antifreeze, a fuel, a depressant, and especially because of its versatility as a chemical intermediate for other organic chemicals (U.S. Department of Energy, 2005).

Ethanol under ordinary condition is a volatile, flammable, clear, colorless liquid. Its odor is pleasant, familiar, and characteristic, as is its taste when it is suitably diluted with water. The physical and chemical properties of ethanol are primarily dependent upon the hydroxyl group. This group imparts polarity to the molecule and also gives rise to intermolecular hydrogen bonding. In the liquid state, hydrogen bonds are formed by the attraction of the hydroxyl hydrogen of one molecule and the hydroxyl oxygen of a second molecule. The effect of this bonding is to make liquid alcohol behave as though it were largely dimerized. This behavior is analogous to that of water, which is more strongly bonded and appears to exist in liquid clusters of more than two molecules.

The chemistry of ethanol is largely that of the hydroxyl group, namely, reactions of dehydration, dehydrogenation, oxidation, and esterification. The hydrogen atom of the hydroxyl group can be replaced by an active metal, such as sodium,

potassium, and calcium, to form a metal ethoxide (ethylate) with the evolution of hydrogen gas. Table II-1 lists the physical properties of ethanol.

Table II-1. Important physical properties of ethanol.

Property	Value
Normal Boiling Point (°C)	78.32
Critical Temperature (°C)	243.1
Density (g/mL)	0.789
Energy Density (MJ/kg)	25.0
Auto-Ignition Temperature (°C)	793.0
Flammable Limits in Air	
Lower, (vol %)	4.3
Upper, (vol %)	19.0
* Heat of combustion at 25°C, J/g	29676.69

What are the benefits of Bioethanol?

Bioethanol has a number of advantages over conventional fuels. It comes from a renewable resource (i. e., crops) and not from a finite resource. These crops typically can grow well in the United States (U.S. Department of Energy, 2001).

Another benefit over fossil fuels is the greenhouse gas emissions. The road transport network accounts for 22 per cent of all greenhouse gas emissions. Through the use of bioethanol, some of these emissions will be reduced as the growing fuel crops absorb carbon dioxide (Tyson et al., 1993). Also, blending bioethanol with gasoline will help extend the life of the oil supplies in the United States and ensure greater fuel security, avoiding heavy reliance on oil producing nations. By encouraging bioethanol use, the rural economy would also receive a boost from growing the necessary crops.

Bioethanol is also biodegradable and far less toxic than fossil fuels. In addition, using bioethanol in older engines can help reduce the amount of carbon monoxide produced by

the vehicle, thus improving air quality. Another advantage of bioethanol is the ease with which it can be integrated into the existing road transport fuel system. In quantities up to 5 per cent, bioethanol can be blended with conventional fuel without the need of engine modifications. Bioethanol is produced using familiar methods, such as fermentation, and it can be distributed using the existing gasoline and transportation systems.

Bioethanol Production from Biomass

Ethanol can be produced from biomass by the hydrolysis and sugar fermentation processes. Biomass wastes contain a complex mixture of carbohydrate polymers from the plant cell walls known as cellulose, hemicellulose and lignin (Um, 2002). In order to produce sugars from the biomass, the biomass is pre-treated with acids or enzymes in order to reduce the size of the feedstock and to open up the plant structure. The cellulose and the hemicellulose portions are broken down (hydrolyzed) by enzymes or dilute acids into sucrose that is then fermented into ethanol (Wyman, 1996). The lignin which is also present in the biomass is normally used as a fuel for the ethanol production plants boilers. There are three principle methods of extracting sugars from biomass: concentrated acid hydrolysis, dilute acid hydrolysis and enzymatic hydrolysis.

LIGNOCELLULOSIC BIOMASS

The structural materials that plants produce to form the cell walls, leaves, stems, stalks, and woody portions of biomass are composed mainly of cellulose, hemicellulose,

and lignin (Fan et al., 1987). Together, they are called lignocellulose, a composite material of rigid cellulose fibers embedded in a cross-linked matrix of lignin and hemicellulose that bind the fibers. Lignocellulose plant structures also contain a variety of plant-specific chemicals in the matrix, called extractives (resins, phenolics, and other chemicals), and minerals (calcium, magnesium, potassium, and others) that will leave ash when biomass is burned (WBDI, 2004).

Lignocellulosic materials are underutilized by the agricultural processing industry. Indeed, lignocellulose, in the form of oat hulls, corn stover, wheat straw, and similar materials, are usually considered as wastes (Wyman 1996). However, it has long been recognized that cellulose can be converted to sugars followed by fermentation to alcohol or organic acids. If agricultural wastes such as corn stover could be economically converted to industrial chemicals, it would represent an important new source of income for farmers or profit centers for agricultural businesses.

The biomass feedstocks typically contain from 55 to 75 per cent (by dry weight) carbohydrates, typically polymers of five- and six-carbon sugar unit (Wyman, 2003). Most of all these carbohydrates can be converted to maximize ethanol production.

Structure of Biomass

Cellulose

Cellulose, a higher molecular weight linear polymer, is composed of D-glucose building blocks, joined by β -1,4-glucosidic bonds (Tengborg et al., 1998). In native cellulose, each cellulose molecule is a long unbranched chain of D-glucose subunits with

a molecular weight ranging from 50,000 to over 1 million (James and David, 1986). These molecules, along with hemicellulose and lignin, are aggregated into long bundles called microfibrils. Hydrogen bonding binds the cellulose molecules. As a result, these fibers are composed of a crystalline or highly-ordered region that protects the microfibrils from hydrolytic degradation and a less ordered, amorphous region (Fan et al., 1983). The amorphous component is digested more easily by enzymatic attack than the crystalline component. This results in a difference in reactivity and adsorption that may result from variation in crystal structure, accessibility to the enzyme, and the degree of polymerization (Gould, 1984; Shiang, 1985)

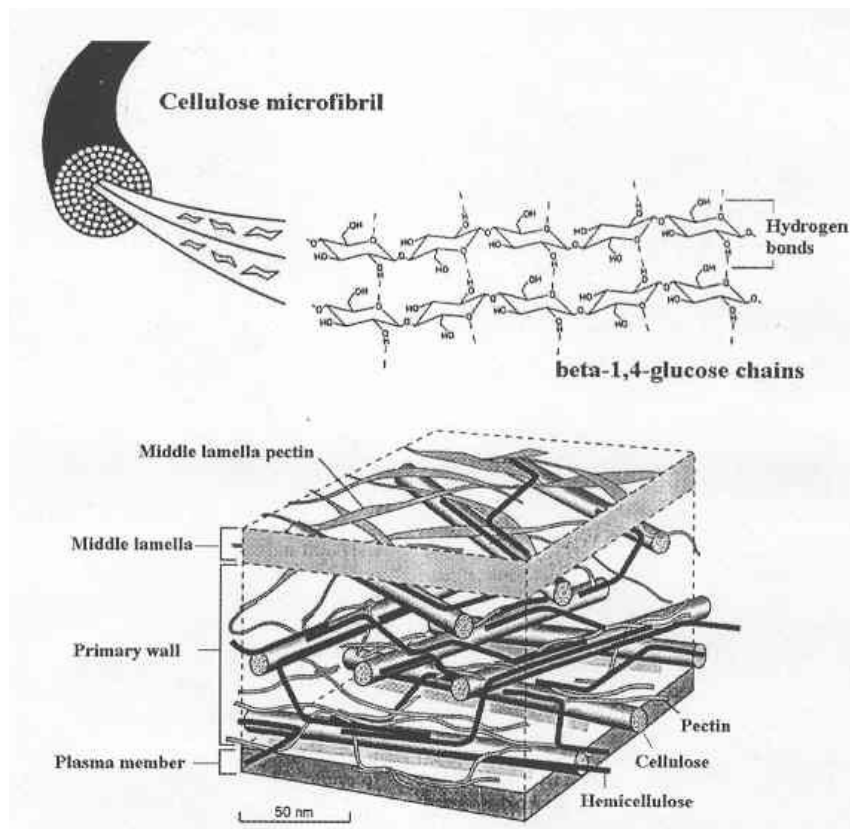


Figure II-2. A simplified model to illustrate the cross-linking of cellulose microfibrils and hemicellulose in the lignocellulosic biomass. Source: Hopkins, W.G., Introduction to Plant Physiology, 2nd edition. John Wiley & Sons, Inc., New York.

The cellulose fibrils are clustered in microfibrils, which are often depicted in cross section as in Figure II-2. Here the solid lines denote the planes of the glucose building blocks, and the broken lines represent orientation of another important group of polysaccharides called hemicellulose.

Hemicellulose

Hemicellulose is a shorter chain, amorphous polysaccharide of cellulans and polyuronides (Wyman, 1996). Cellulans are heteropolymers made up of hexosans (mannan, galactan, and glucan) and pentosans (xylan and arabinan). Polyuronides are similar to cellulans, but contain appreciable quantities of hexuronic acids as well as some methoxyl, acetyl, and free carboxylic groups. Xylan and glucomannan are dominant carbohydrate components of hemicellulose (Chum et al., 1985).

Lignin

Lignin is composed of polymerized phenylpropanoic acids in a complex three-dimensional structure. Ether and carbon-carbon bonds hold individual monomers together (Chang et al., 1981; James and David, 1986). Lignin is formed by a free radical polymerization mechanism and has a random structure. Lignin and hemicellulose are believed to form an effective sheath around cellulose fibers, which adds structural strength to the biomass matrix. Covalent bonds may exist between hemicellulose and lignin, but this is uncertain. The amount of lignin in herbaceous species and agricultural residues is approximately 10 to 20 per cent (Ooshima et al., 1990; Schell et al., 1998).

Solka Floc

Highly purity samples of cellulose and its derivatives have been produced from various kinds of naturally occurring celluloses. The transformation of the naturally-occurring cellulose into pure cellulose or cello-oligomers involves complicated processes such as the removal of hemicellulose and lignin, acetylation of hydroxyl groups, acidic cleavage of the cellulose backbone, and fractionation by chromatography (Kobayashi et al., 1999).

Solka Floc, a purified cellulose, is made from wood pulp through a cellulose transformation process. The KS1016 and the BW300 grades of Solka Floc have an average particle (fiber) length of 290 μm and 22 μm , respectively. The BW300 grade has a degree of crystallinity of 62 to 65 per cent whereas the KSI016 grade has a greater proportion of crystalline cellulose at 75 to 77 per cent (Murray, 1993).

PRETREATMENT IMPORTANCE

The susceptibility of cellulose as a substrate for enzymatic conversion processes is determined by its accessibility to extracellular enzymes or other reactants secreted by cellulosic microorganisms (McMillan, 1994). The structure of lignocellulosics in the cell wall resembles that of a concrete pillar with cellulose fibers being the metal rods and lignin the natural cement. Biodegradation of untreated native lignocellulosics is slow, giving a very low extent of degradation (Chang et al., 1981; Kaar et al., 1998). To increase the susceptibility of cellulosic material, structural modification by means of various pretreatment strategies is indispensable. The resistance of biomass to enzymatic attack can be contributed to three major factors (James and David, 1986):

- Cellulose in lignocellulosic biomass has highly resistance crystalline structure.
- Lignin surrounding cellulose forms a physical barrier.
- Sites available for enzymatic attack are limited.

Cellulose in lignocellulosics is composed of crystalline and amorphous components. The amorphous component is digested more easily by enzymatic attack than the crystalline component. The presence of lignin forms a physical barrier for enzymatic attack, and hence, pretreatment causing disruption of the lignin linkage, increases the accessibility of cellulose and eventually its hydrolysis rate.

Thus, pretreatment is as essential prerequisite to enhance the susceptibility of lignocellulosic residues to enzyme action. An ideal pretreatment would accomplish reduction in crystallinity, concomitant with a reduction in lignin content and increase in surface area. Of various pretreatment methods, chemical pretreatments have been used extensively to remove lignin and for structural modification of lignocellulosics.

Although various forms of chemical pretreatment of cellulosic materials have been proposed, their effectiveness varies, depending on the substrate. Hence optimal pretreatment must be established for each substrate.

PRETREATMENT TECHNIQUES

Depending on the material, most pretreatment techniques require preparation of the starting substrate, normally involving a mechanical size reduction step with the substrates sized appropriately for handling (Chum, 1985; Um, 2002). With this definition, pretreatment can be broadly classified into three methods: physical, chemical, or biological, Depending on the principal mode of action on the substrate

(Chang et al., 1981). The various pretreatment methods that can enhance the cellulose digestibility are summarized in Table II-2 (James and David, 1986). Some processes are combinations of two or more pretreatment techniques applied in parallel or in series. Although various forms of pretreatment of cellulosic material have been proposed, their effectiveness varies with the substrate characteristics. Thus, an optimal method of pretreatment must be established for each substrate.

Table II-2. Methods used for Pretreatment of Lignocellulosics.

Physical	Chemical	Biological
Ball-milling	Alkali	Fungi
Two-roll milling	Sodium hydroxide	
Hammer milling	Ammonia	
Colloid milling	Ammonium sulfite	
Vibro energy milling	Acid	
High pressure steaming	Sulfuric acid	
Extrusion	Hydrochloric acid	
Pyrolysis	Phosphoric acid	
High energy radiation	Gas	
	Chlorine dioxide	
	Nitrogen dioxide	
	Sulfur dioxide	
	Oxidizing agents	
	Hydrogen peroxide	
	Ozone	
	Cellulose solvents	
	Cadoxen	
	CMCS	
	Solvent extraction of lignin	
	Ethanol-water extraction	
	Benzene-ethanol extraction	
	Ethylene glycol extraction	
	Butanol-water extraction	
	Swelling agents	

(James and David, 1986).

ENZYMATIC HYDROLYSIS

Enzymatic hydrolysis of cellulose is carried out by cellulase enzymes that are highly specific (Béguin and Aubert, 1994). The products of the hydrolysis are usually reducing sugars, including glucose. Utility cost of enzymatic hydrolysis is low compared to acid or alkaline hydrolysis, is usually conducted at mild conditions (pH 4.8 and temperature 45 to 50°C) and does not have a corrosion problem (Duff and Murray, 1996).

Cellulases are usually a mixture of several enzymes. Three major types of cellulolytic activity produced by fungi are (Gould, 1984):

- Endoglucanase (1, 4- β -D-glucan 4-glucanohydrolase)
- Cellobiohydrolase (1, 4- β -D-glucan cellobiohydrolase)
- β -Glucosidase (β -D-glucoside glucohydrolase)

These enzymes have been purified or partially purified from fungi and their properties studied. In spite of differences reported in substrate specificity, the general view can be summarized as follows: (Shiang 1985; Um 2002):

Endoglucanase randomly hydrolyzes β -1, 4-glycosidic linkages. It does not attack cellobiose but hydrolyzes cellodextrins, acid-swollen cellulose and substituted celluloses, such as CMC (carboxymethyl cellulose) and HEC (hydroxyethyl cellulose). It is also claimed that some endoglucanases act on crystalline cellulose. The specificity of this enzyme cannot be high since it readily attacks highly substituted celluloses.

Cellobiohydrolase acts on cellulose, splitting-off cellobiose units from the non-reducing end of the chain. This enzyme does not attack substituted celluloses, reflecting higher substrate specificity than that of endoglucanase. Cellobiohydrolase hydrolyzes

cellodextrins but not cellobiose. β -Glucosidase hydrolyzes cellobiose and cello-oligosaccharides to glucose. The enzyme does not attack cellulose or higher cellodextrins.

In addition to these groups of cellulase enzymes, a number of ancillary enzymes, such as glucuronidase, acetyesterase, xylanase, β -xylosidase, galactomannanase and glucomannanase, attack hemicellulose (Duff and Murray, 1996). During the enzymatic hydrolysis, cellulose is degraded by the cellulases to reducing sugars that can be fermented by yeasts or bacteria to ethanol.

Cellulase activity is inhibited by cellobiose and, to a lesser extent, by glucose. Several methods have been developed to reduce the inhibition, including the use of high concentrations of enzymes, the supplementation of β -glucosidase during hydrolysis, and the removal of sugars during hydrolysis by ultrafiltration or simultaneous saccharification and fermentation (SSF). The SSF process has been extensively studied to reduce the inhibition by end products of hydrolysis (Takagi et al., 1977; Blotkamp et al., 1978; Szczodark and Targonski, 1989; Saxena et al., 1992; Philippidis et al., 1993; Zheng et al., 1998; Varga, 2004). In the process, reducing sugars produced in cellulose hydrolysis or saccharifications are simultaneously fermented to ethanol, greatly reducing the end product inhibition to the hydrolysis.

ETHANOL FERMENTATION

Fermentation, one of the oldest chemical processes known to man, is used to make a variety of products, including foods, flavorings, beverages, pharmaceuticals, and chemicals (Fan et al., 1987). At present, however, many of the simpler products, such as

ethanol, are synthesized from petroleum feedstocks at lower costs. The future of the fermentation industry therefore depends on its ability to utilize the high efficiency and specificity of enzyme catalysis to synthesize complex products and on its ability to overcome variations in quality and availability of raw materials (NREL, 2001).

Ethanol is made from a variety of agricultural products such as grain, molasses, fruit, whey and sulfite waste liquor. Generally, most of the agricultural products mentioned above command higher prices as foods, and others, like potatoes, are uneconomical because of their low ethanol yield and high transportation cost. The energy crisis of the early seventies may have generated renewed interest in ethanol fermentation, but ethanol's use still depends on the availability and cost of the carbohydrate relative to the availability and cost of ethylene (Capital Press, 2005). Sugar and grain prices, like oil prices, have risen dramatically since 1973.

Fermentation processes from any material that contains sugar can produce ethanol. The many and varied raw materials used in the manufacture of ethanol via fermentation are conveniently classified under three types of agricultural raw materials: sugar, starches, and cellulose materials (Wyman, 1994). Sugars (from sugar cane, sugar beets, molasses, and fruits) can be converted to ethanol directly. Starches (from grains, potatoes, root crops) must first be hydrolyzed to fermentable sugars by the action of enzymes from malt or molds. Cellulose from wood, agricultural residues and waste sulfite liquor from pulp and paper mills must likewise be converted to sugars, generally by the action of mineral acids. Once simple sugars are formed, enzymes from yeast can readily ferment them to ethanol.

BIOETHANOL FERMENTATION PROCESS

The hydrolysis of cellulose yields glucose and xylose. Once these sugars are available, the fermentation of carbon source is no longer a difficult task, as this technology is well-developed. Essentially four types of processes that can convert cellulose to ethanol: direct microbial conversion (DMC), separate hydrolysis and fermentation (SHF), simultaneous saccharification and cofermentation (SSCF), and simultaneous saccharification and fermentation (SSF). Extensive research has shown that among the various cellulose bioconversion schemes, SSF seems to be the most promising approach to biochemically convert cellulose to ethanol in an effective way (Takagi et al., 1977; Wright et al., 1988; Varga, et al., 2004).

Direct Microbial Conversion (DMC)

DMC uses one microorganism such as *Fusarium sp.*, *Neurospora crassa* or *Clostridium sp.* for both cofermentation and enzyme production. To date this process has not been successful due to its complexity. The current DMC strains are typically characterized by slow growth rates. A low ethanol yield and productivity can be achieved in DMC with low ethanol selectivity; therefore the strains used produce other fermentation products (e. g., acetic acid) at nearly equivalent levels as ethanol (Christakopoulos et al., 1990; Padukone, 1996; Himmel et al., 1997). However, South et al. (1993) have reported a promising conversion of substrate (pretreated hardwood flour) to ethanol (77per cent) in the DMC system with *Clostridium thermocellum* using a well-mixed stirred-tank reactor (CSTR). Stevenson et al. (1999) have made genetic

engineering attempts to develop a microorganism starting from *Clostridium thermocellum* for DMC.

Separate Hydrolysis and Fermentation (SHF)

SHF is a conventional two-step process where cellulose is enzymatically hydrolyzed by cellulase to form glucose in the first step and glucose is fermented to ethanol in the second step by using *Saccharomyces* or *Zymomonas* (Bisaria and Ghose, 1981; Johnson et al., 1982; Hogsett et al., 1992; Philipidis, 1996, Lawford et al., 1999). The main advantage of SHF is the ability to carry out each step at its optimum temperature, 45 to 50 °C and 30 °C, respectively. The major disadvantage results from the fact that enzymatic hydrolysis severely inhibits cellulase activity during hydrolysis. Hence, lower cellulose concentration and higher enzyme loading must be used to obtain reasonable ethanol yields

Simultaneous Saccharification and Cofermentation (SSCF)

The fermentation of hexoses and pentoses is carried out simultaneously with a cofermenting microorganism such as *Zymomonas mobilis* (Himmel et al., 1997; Lawford et al., 1999; Glazer and Nikaido, 1995; Takagi et al., 1978). When the lignocellulosic substrate has a high content of pentoses, e. g. xylose, a separate pentose fermentation step is required to convert the substrate to ethanol economically, as the currently used fermentative microorganism in SSF does not convert pentoses.

The SSCF process option offers the possibility of substantial capital and operational savings by reducing the number of required reactors and saving the cost of

steam separation. Based on preliminary economic analysis, the cofermentation indicates a potential 18 per cent reduction in the ethanol cost compared to the basic design (Padukone, 1996).

Simultaneous Saccharification and Fermentation (SSF)

SSF is the most promising process for ethanol production from lignocellulosic materials with multiple researchers focusing on the process (Lawford et al., 1999; Klinke et al., 2001; Öhgren et al., 2005; Philippidis and Hatzis, 1997; Stenberg, 2000; Teymouri, 2005 ;Varga et al., 2004;). In SSF, the enzymatic hydrolysis and fermentation steps are performed simultaneously with only low levels of cellulobiose and glucose observed in the reactor. Cellulase inhibition is reduced thus increasing sugar production rates, concentrations, and yields and decreasing enzyme loading requirements. The drawbacks associated with this process include the different operating conditions required for enzymatic hydrolysis and fermentation and the problem of yeast and bacteria recycling. Krishnan et al. (1997) have reported a fed-batch SSF process for ethanol production from pretreated corn fiber that achieves higher ethanol productivity at reduced enzyme loadings compared to the batch SSF process. Padukone et al. (1996) have demonstrated that, in the late stage of SSF with near starvation of the yeast, the addition of glucose shifted the metabolic pathway to ethanol production from succinic and acetic pathways. Varga et al. (2004) have conducted SSF process with high initial pretreated corn stover at flask scale.

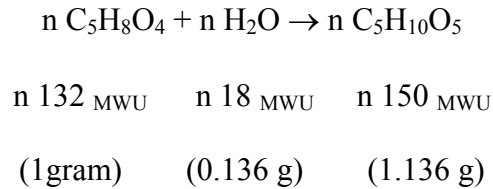
Theoretical Ethanol Yield via Fermentation Process

The amount of product formed per unit of substrate consumed by the organism is a useful way to refer to yields. Yields are expressed on either molar or weight basis.

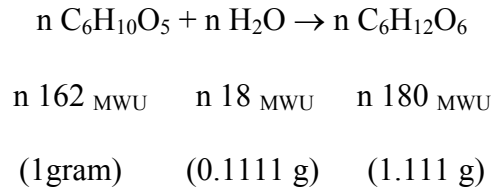
For process cost accounting purpose, weight is more meaningful.

In this case the primary stoichiometric equations for the ethanol production are as follows (Hettenhaus, J. R. 1998):

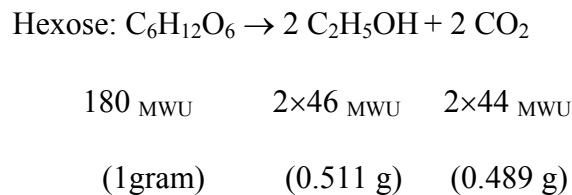
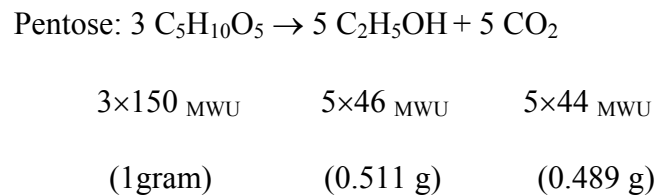
Pentosan to Pentose (13.6 weight per cent gain)



Hexosan to Hexose (11.1 per cent weight gain)



Pentose and Hexose to Ethanol (48.9 per cent weight loss)



A reduction in yield below theoretical values always occurs since the microorganism requires a portion of the substrate for cell growth and maintenance. The fermentation process takes around three days to complete and is carried out at a temperature of between 25 and 30°C.

BIOREACTOR DESIGN

For high-solids fermentations an effective bioreactor should achieve good enzyme, substrate, microorganism distribution and uniform temperature control with low mixing power input. Production-scale bioreactors can be developed by modeling laboratory reactor performance and by scaling up a process design that minimizes ethanol cost and maximizes SSF's productivity. Batch experimental studies have helped identify enzymatic hydrolysis as the limiting step in the SSF and the need to enhance substrate accessibility by improving the effectiveness of biomass pretreatment.

SSF studies have provided information on crucial operating parameters, performance variables, and scale-up considerations, such as dilution rate and ethanol yield and predictability, as the process moves toward commercialization. Cellulose conversion factors of major importance, such as the effect of substrate and enzyme loading on ethanol predictability, the most efficient mode of operation, the effect of feedstock composition, and the desired pretreatment effectiveness can be systematically evaluated to improve the overall biomass-to-ethanol technology.

CFD provides for the numerical modeling of the flow field imposed by the impeller and sparging system (including shear rates) and a prediction of the mixing of chemical species with the vessel. The development of cell culture and fermentation

processes using CFD significantly reduces the amount of experimentation required, provides more data than physical trials, and allows for the evaluation of new equipment prior to purchase.

Mixing in Bioreactors

Mixing effects in chemical reactors are usually separated into two components: macromixing and micromixing. In many cases for simple homogeneous reactions micromixing has a limited effect on conversion. However, this effect usually cannot be neglected in the design of heterogeneous reactors or in homogeneous reactors where complex or autocatalytic reactions take place. The importance of mixing was summarized by Cooke et al. (1988) as follows:

- Poor mixing leads to undesirable nutrient concentration gradients and can lead to nutrient starvation in stagnation regions of the vessel. For aerobic yeast production oxygen starvation leads to ethanol production which adversely affects productivity.
- Good mixing is important for heat transfer. Fermentation equipment needs to be designed to provide adequate fluid velocities adjacent to heat transfer surface.
- When mixing constants approach those of the time constant for mass transfer, the commonly-used well mixed liquid phase assumption for the determination and scale-up of mass transfer is no longer appropriate. Obviously, if the mixing is not considerably faster than the mass transfer, then the chance of undesirable oxygen and other nutrient gradients are enhanced. These effects require quantification for scale-up.

Reactor Geometries

Figure II-3 illustrates the nomenclature used to describe the mixing system (Oldshue, 1983).

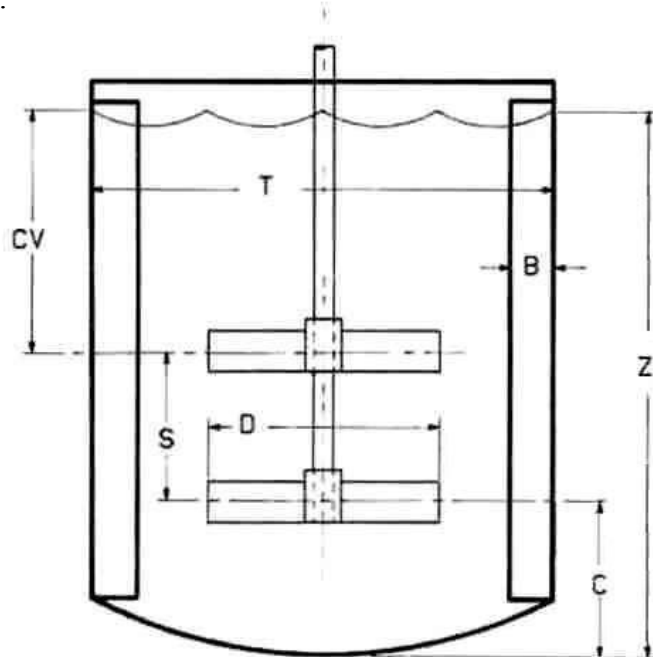


Figure II-3. The standard geometry of mixing tank; nomenclature used to describe the mixing system (Oldshue, 1983).

Impeller off-bottom distance C is measured from the lower impeller's horizontal centerline to the lowest point on the tank bottom. Flat bottoms, shallow cones, and standard ASME dishes ($\text{depth} = \frac{1}{6} T$) are treated in the same manner. Coverage CV is measured from the static liquid surface to the horizontal centerline of the upper or lower (single) impeller. Spacing between impellers S is measured from one impeller horizontal centerline to the next. Liquid depth Z is measured from the static liquid surface to the lowest point on the tank bottom.

Turbine Agitators

A wide variety of turbine-style impellers are available. Figure II-4 lists the most common ones: the pitched-blade turbine, high efficiency impeller, disc turbine, and simple straight-blade turbine. Well designed turbine impeller systems can be used up to viscosities of about 50 Pa-s, depending on the scale, application, and process requirements (Bakker, 1995).

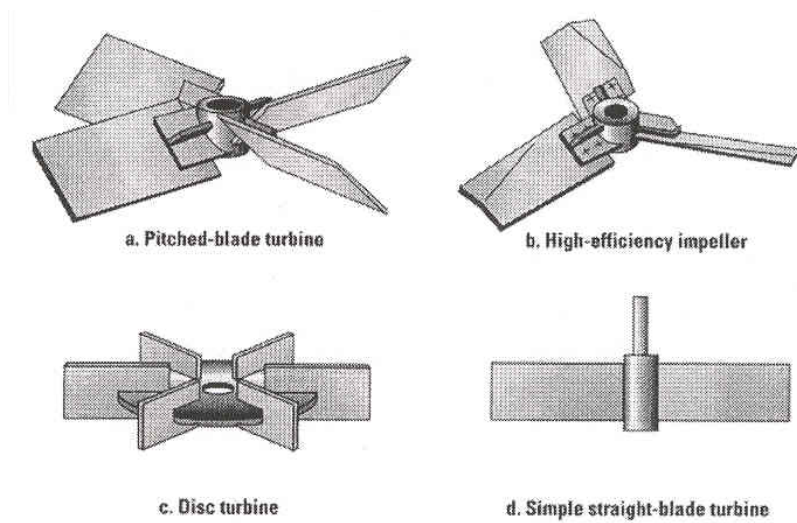


Figure II-4. A wide variety of turbine is available to handle viscosities to about 50 Pa-s.

Each impeller has its own characteristics and its own area of application. Straight-blade impellers and disc turbines tend to be used to create zones with high shear rates, such as in dispersion. High-efficiency and pitched-blade turbines tend to be used at Reynolds numbers larger than about 100 where a good overall circulation flow is important. The impeller Reynolds number is defined as:

$$N_{Re} = \frac{\rho ND^2}{\mu_{eff}} \quad (1)$$

For Newtonian fluids, the effective viscosity μ_{eff} is simply the dynamic viscosity. For non-Newtonian fluids, the viscosity will vary with shear rate throughout the volume of the tank. To calculate the average viscosity experienced by the impeller, an effective shear rate S_{eff} is calculated by Metzner and Otto (1957):

$$S_{eff} = KN \quad (2)$$

Here, N is the impeller rotational speed in reciprocal seconds and K is an impeller constant. Table II-3 lists K-values for several different impeller types. Substituting the effective shear rate in the viscosity equation for the particular fluid then gives the effective viscosity that can be used to calculate the impeller Reynolds number.

Table II-3. K-Values for Effective Shear-Rate Model

Impeller Type	K
High Efficiency	10
Pitched Blade	11
Straight Blade	11
Disc Turbine	11.5
Anchor (D/T=0.98)	24.7
Helical Ribbon (D/T=0.96, P/D=1)	29.4

The values for the anchor and helical ribbon impellers are for the specified standard geometries only.

Several other methods of calculating the effective shear rate have been reported in the literature. Most of these are more complicated than the method used here, while not always more accurate.

Two other dimensionless numbers that are often used to characterize the impeller are the power number and the pumping number. The power number N_p is implicitly defined by the following equation:

$$P = N_p \rho N^3 D^5 \quad (3)$$

When the power number of an impeller is known, the power can be calculated using this equation, given liquid density, impeller speed, and diameter.

The pumping number N_q is implicitly defined by:

$$Q_l = N_q N D^3 \quad (4)$$

When the pumping number of an impeller is known, the pumping rate of the impeller Q_l can be calculated for a given diameter and speed. Both the impeller power number and pumping number depend on a variety of factors, such as the ratio of impeller to tank diameter D/T , the impeller off-bottom clearance ratio C/T , and the impeller Reynolds number.

For Reynolds number above 10,000, both N_p and N_q show little variation with Reynolds number. In this regime, the flow is considered to be fully turbulent. When the Reynolds number decreases, the pumping number decreases, while the power number increases. This regime is usually called the transitional regime.

At very low Reynolds numbers ($N_{Re} < 10$), the power number is inversely proportional to the Reynolds number. In this Reynolds number regime, the flow is considered laminar. The exact Reynolds numbers at which the transitions occur are a function of impeller type, size and number (Grenville et al, 1995). The correlation for the Reynolds number at the boundary between the turbulent and transitional regime is as follows

$$N_{Re} = \frac{6,370}{N_p^{1/3}} \quad (5)$$

Helical-Ribbon and Anchor Impellers

An alternative to selecting a turbine impeller system is the use of a helical-ribbon impeller or an anchor impeller (Figure II-5). These impellers sweep the whole wall surface of the tank and physically agitate most of the fluid batch. As a result, they can be used at much lower Reynolds numbers ($N_{RE} \leq 400$) than the open-style turbines.

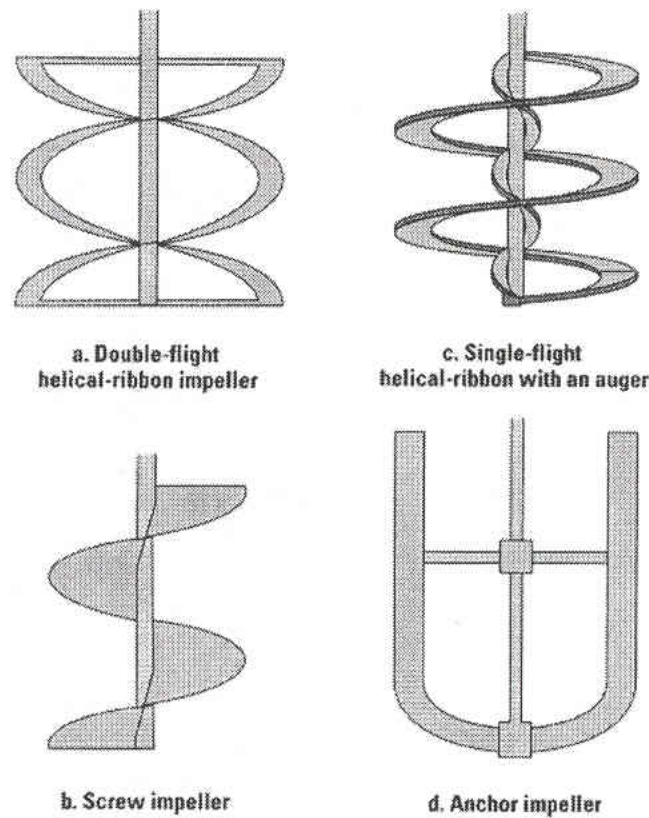


Figure II-5. Helical-Ribbon and Anchor Impellers Provide an Alternative to Turbine Impeller.

Helical ribbons are primarily used when very viscous materials are to be mixed starting at viscosities of about 20 Pa-s and higher, depending on the scale. Helical ribbons have been successfully used for viscosities up to 25,000 Pa-s (Bakker, 1995).

These impellers often have a diameter that is close to the inside diameter of the tank and therefore, are sometimes called close clearance agitators. They guarantee liquid motion all the way to the wall of the tank, even for viscous materials.

Helical impellers can also be manufactured in a different configuration, with the helical impeller blade wrapped closely around the shaft (Figure II-5 b). Such impellers are also called helical screw impellers and are sometimes used in combination with draft tube.

When these screw impellers are combined with a close-clearance helical ribbon as shown in Figure II-5 c, the screw is sometimes called an auger. The power draw from an impeller is proportional to the diameter to the 5th power, as in equation (3). Since the diameter of the auger is much smaller than the diameter of the outside helical ribbon, the power draw of an auger is often less than 1 per cent of that of a helical ribbon. When correctly designed, an auger can be used to improve the mixing near the shaft without significantly increasing the power draw and torque requirement of the agitator. If the auger is incorrectly designed and the pumping capacity of the auger does not match the flow created by the helical ribbon impeller, the auger may actually block the liquid flow near the shaft and hamper the mixing process.

When it is important to have high velocities at the tank wall, for example, in heat-transfer applications, it is recommended to make the clearance between the helix and the tank wall as small as possible. Further, the helix can be equipped with scrapers that physically remove the fluid from the tank wall.

Conventional Radial Flow Turbine

The flat-blade or Rushton turbine (Figure II-4c) is the historic standard for gas-liquid applications and is widely employed throughout the process industries. Given its simple construction, it can be easily 'tuned' to an application by adding or subtracting blades, or by adjusting the radial position of the blades to change turbine diameter. While the impeller features high pumping capacity, its radial discharge is not efficient for solids suspension. Similarly, it is capable of dissipating a large amount of energy, although this is done at the expense of high shear input. The nature of the Rushton turbine blade shape and the vortex that forms behind it leads to a marked decrease in power draw as gas is introduced. Two-speed motors can be used to optimize the drive system for both gassed and ungassed operation.

Given the variety of gas handling impellers available, there are typically better-suited options that can be employed to achieve desired process results. Applications requiring high shear or high-energy dissipation rates remain the primary use for flat-blade turbines.

Flow Patterns

When an impeller is used in a tank which has a high ratio of its height to diameter, a draft tube can ensure good top-to-bottom mixing (Oldshue, 1983). This circular duct which is used to direct fluid flow to and from the impeller is most commonly used with axial-flow devices, which are inserted into the tube.

The distribution of flow in an open-impeller system is shown in Figure II-6 and Figure II-7. When the ratio of liquid depth to the tank diameter is greater than 1.0,

uniform solids suspension is not readily obtained for fast settling solids. A strong flow pattern produced by down-pumping draft tube circulators sweeps the solids away from the draft tube and reduces the tendency for solids deposition.

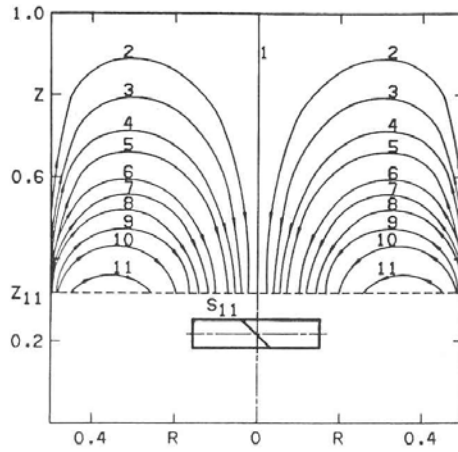


Figure II-6. Streamline Pattern in a Standard Cylindrical System with Axial high-speed Impeller and Radial Baffles (Oldshue, 1983, from Fort et al.).

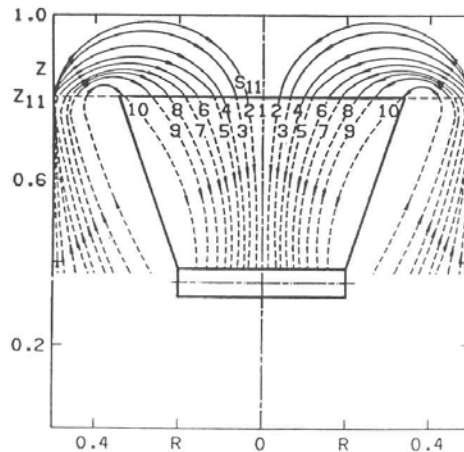


Figure II-7. Streamline Patterns in Cylindrical System with Axial High-Speed Impeller and Draft Tube (Solid lines are calculated streamlines; dashed lines are anticipated course of streamlines) (Oldshue, 1983, from Fort et al.).

Examination of flow and power numbers for both open tank and draft tube using the same impeller indicates that a specified primary circulation rate can be achieved more efficiently with the draft tube unit (Oldshue, 1983). Since the draft tube serves to improve (i.e., make more uniform) the inlet fluid velocity profile, it markedly reduces the variation in load experienced by the impeller. Thus, the fluid forces acting on an impeller in a draft tube are markedly reduced. Based on limited testing, the force is observed to be less than 20 per cent of that observed in similar open tank service.

Scale Up Method for Fermentors

Agitation and aeration directly influence transport phenomena in the fermentor; therefore, the study of scale-up is based on the agitation and aeration of the fermentor (Maxon and Johnson, 1953). To solve the scale-up problems, the principal environmental parameters affected by aeration and agitation (oxygen concentration, shear, bulk mixing) are identified and studied. The process variables (airflow rate and agitation speed) are calculated for the large-scale fermentor to give the same environmental parameters as in the small-scale fermentor.

Ju and Chase (1992) suggest that the following environmental parameters should be kept constant during scale-up:

- reactor geometry
- volumetric oxygen transfer coefficient
- maximum shear rate
- power input per unit volume of liquid
- volumetric gas flow rate per unit volume of liquid

- superficial gas velocity
- mixing time
- impeller Reynolds number
- momentum factor

The standard geometry is assumed to be the optimum geometry for reactors.

The standard geometry is shown in Figure II-3 (Oldshue, 1983). All scale up studies of fermentors are developed experimentally using geometrically similar reactors of different sizes. Instead of using geometrically similar reactors, the constant mixing time is used in a viscous non-Newtonian system. This criterion is unnecessary for normal fermentations and requires more power. Impeller Reynolds Number and momentum factor criteria are not considered in calculating the effect of aeration on the process.

The most important problem in aerobic fermentations is oxygen transfer. To maintain the oxygen transfer rate as vessel size increases, scale-up of aerobic fermentations is typically done with a constant volumetric oxygen transfer coefficient (Karow et al, 1953; Andrew, 1982). The criterion to keep power input per unit volume of liquid and maximum shear constant is important when growing shear-sensitive microorganisms. The volumetric gas flow rate per unit volume of liquid (Q) criterion and the superficial gas velocity (V_s) criterion are contradictory to each other when applied to geometrically similar fermentors. If the Q is maintained constant, the superficial gas velocity will increase directly with the scale ration. The choice between the volumetric gas flow rate per unit volume of liquid criterion and the superficial gas velocity criterion has to be carefully considered for the process.

Scale up rules generally used in the fermentation industries are constant power input per unit volume of liquid (P/V), constant $k_L a$, constant impeller tip speed (v_{tip}), and constant dissolved oxygen concentration (Mavituna, 1996). Frequency of use of the various rules is given in Table II-4. For scale up of aerobic fermentation, the oxygen transfer rate is the important factor (Hubbard, 1987) and can be calculated as follows:

For the plant-scale fermentor:

- choose the required volume
- calculate the dimensions based on geometry similarity
- establish the scale-up strategy to be used $(k_L a)_{plant} = (k_L a)_{lab}$
- calculate air flow rate (V_{air}) and agitation rate (N) with either method 1 or 2
- estimate power consumption

Method 1:

- determine V_{air} using Q
- calculate N from power and $k_L a$ correlation

Method 2:

- determine N using πND constant (v_{tip} constant)
- calculate V_{air} from power and $k_L a$ correlation

Table II-4. Scale-up criteria in fermentation industries.

Scale-Up Criterion Used	Percentage of Industries
Constant P/V	30
Constant $k_L a$	30
Constant v_{tip}	20
Constant pO_2	20

F. Mavituna, Strategies for bioreactor scale-up, In: *Computer and Information Science Application in Bioprocess Engineering* (A. R. Moreira and K.K. Wallace), Kluwer Academic Publishers, Dordrecht, Netherlands, 1996, pp. 129.

The accuracy of this procedure depends on the relationship between $k_L a$ and power consumption. This procedure is used widely in scale-up aerobic fermentation. However, poor mixing and hidden auxotroph are two factors still uncertain on scale-up (Humphrey, 1998). Success in scale-up of fermentation requires the preliminary calculation of environmental parameters and then trial and error testing to achieve the same results as in the laboratory scale.

Simulation Using Computational Fluid Dynamics

Computational fluid dynamics has evolved over the forty years of its existence from the specialty of a small, closely knitted band of enthusiasts into a vast and many-sided enterprise. The business of CFD applications alone now employs several tens of thousands of people and has a turnover of some billions of dollars a year. Moreover, the material resource committed to CFD research and developments are still increasing rapidly, as existing areas of application continue to expand and new areas are constantly being opened up.

The automatic digital computer, invented by Atanasoff in the late 1930's, was used from nearly the beginning to solve problems in fluid dynamics (Anderson et al., 1984). The development of the high-speed digital computer has had a great impact on the way in which CFD principles from the science of fluid mechanics are applied to problems of design in modern engineering practices.

The application of computational fluid dynamics can be found in (FLUENT INC., 2001)

- Process and process equipment applications
- Power generation and oil/gas and environmental applications
- Aerospace and turbo machinery application
- Automobile applications
- Heat exchanger applications
- Electronics/HVAC/appliances
- Materials processing applications
- Architectural design and fire research

In this approach, the equations (usually in partial differential form) that govern a process of interest are solved numerically.

The basic equations describing the laminar flow of continuous fluid are (FLUENT INC., 2001):

conservation of mass:
$$\frac{\partial \rho}{\partial t} + \frac{\partial}{\partial x_i}(\rho u_i) = S_m$$

conservation of momentum:
$$\frac{\partial}{\partial x_i}(\rho u_i) + \frac{\partial}{\partial x_j}(\rho u_i u_j) = -\frac{\partial p}{\partial x_i} + \frac{\partial \tau_{ij}}{\partial x_j} + \rho g_i + F_i$$

where the stress τ_{ij} is given by:
$$\tau_{ij} = \left[\mu \left(\frac{\partial u_i}{\partial x_j} + \frac{\partial u_j}{\partial x_i} \right) \right] - \frac{2}{3} \mu \frac{\partial u_i}{\partial x_i} \delta_{ij}$$

conservation energy:

$$\frac{\partial}{\partial t}(\rho h) + \frac{\partial}{\partial x_i}(\rho u_i h) = \frac{\partial p}{\partial x_i} \left(k \frac{\partial T}{\partial x_i} \right) - \frac{\partial}{\partial x_i} \sum h_j J_j + \frac{\partial p}{\partial t} + u_i \frac{\partial p}{\partial x_i} + \tau_{ij} \frac{\partial u_i}{\partial x_j} + S_h$$

h is defined as $h = \sum_i m_i h_i$ and $h_i = \int_{T_{ref}}^T C_{pi} dT$

conservation of chemical species:
$$\frac{\partial}{\partial t}(\rho m_i) + \frac{\partial}{\partial x_i}(\rho u_i m_i) = \frac{\partial}{\partial x_i}(J_{i',i'}) + S_{i'}$$

where
$$J_{i',i'} = -\rho D_{i',m} \frac{\partial m_{i'}}{\partial x_i}$$

The equations are reduced to their finite difference algebraic equations by integration over the computational cells into which the domain is divided. After integration of the fluid motion governing equations, the resulting algebraic equations can be written in the following common form:

$$\phi_p \sum_i (A_i - S_p) = \sum_i (A_i \phi_i) + S_c$$

Where the summation is over the neighboring finite difference cells $i=N, S, E, W, F, B$ (which stand for North, South, East, West, Front, and Back). The A 's are coefficients which contain contributions from the convective and diffusive fluxes, and S_c and S_p are the components of the linearized source term, $S_\phi = S_c + S_p \phi_p$. A power law differencing scheme is used for interpolation between grid points and to calculate the derivatives of the flow variables. The set of simultaneously algebraic equations is solved by a semi-implicit iterative scheme which starts from arbitrary initial conditions and converges to the correct solution after performing a number of iterations.

Each iteration consists of the steps which are outlined below (FLUENT INC., 2001).

- The u, v and w momentum equations are each solved in turn using current values for pressure, in order to update the velocity field.
- Since the velocities obtained in the above step may not satisfy the mass continuity equation locally, a “Poisson-type” equation is derived from the continuity

equation and linearized, momentum equations. This “pressure correction” equation is then solved to obtain the necessary corrections to the pressure and velocity fields such that continuity is achieved.

- The k and ε equations are solved using the updated velocity field (for turbulent flow only)
- Any auxiliary equation (e.g. enthalpy, species conservation, or any additional turbulence quantities) are solved using the previously updated values of the other variables
- The fluid properties are updated
- A check for convergence of the equation set is made

These steps are continued until the error has decreased to a required value.

The accuracy of a computational solution to a partial differential equation can be affected by two types of source errors (Souvaliotis et al., 1995)

- Truncation error
- Round-off error

The limiting behavior of the truncation error can be characterized by employing a Taylor series expansion for $u(x_0 + \Delta x, y_0)$ about (x_0, y_0)

$$u(x_0 + \Delta x, y_0) = u(x_0, y_0) + \left(\frac{\partial u}{\partial x}\right)_0 \Delta x + \left(\frac{\partial^2 u}{\partial x^2}\right)_0 \frac{(\Delta x)^2}{2!} + \dots$$

In terms of the finite difference representation for $\frac{\partial u}{\partial x}$

$$\frac{\partial u}{\partial x} = \frac{u_{i+1,j} - u_{i,j}}{\Delta x} + \text{truncation error}$$

The round-off errors are generated by rounding floating point numbers to a finite number of digits in the arithmetic operations in obtaining machine solutions to finite difference equations because of the large number of dependent, repetitive operations which are usually involved. Anderson et al. (1984) state that, in some type of calculations, the magnitude of the round-off error is proportional to the number of grid points in the problem domain. In these cases refining the grid may decrease the truncation error but increase the round-off error.

Anderson et al. (1984) propose that, in order for the computational solution to be acceptable, the finite difference representation of the partial differential equation needs to meet the conditions of consistency, stability, and convergence.

Consistency deals with the extent to which the finite difference equations approximate the partial differential equations. A finite difference representation of a partial differential equation is consistent if it can be shown that the difference between the partial differential equation and its difference representation vanishes as the mesh is refined.

A stable computational scheme is one for which errors from any source (round-off, truncation, mistakes) are not permitted to grow in the sequence of numerical procedure as the calculation proceeds from one marching step to the next. Anderson et al. (1984) observed that concern over stability occupies much more attention than concern over consistency.

Convergence here means that the solution to the finite difference equation approaches the true solution to the partial differential equation having the same initial and boundary conditions as the mesh is refined. Lax's equivalence theorem shows that,

given a properly posed initial value problem and a finite difference approximation that satisfies the consistency condition, stability is the necessary and sufficient condition for convergence.

Physical Model for Turbulence Fluid Motion

From the classical point of view, turbulence fluid motion is an irregular condition of flow in which the various quantities (velocity, pressure, concentration, temperature, etc.) show a random variation with time and space coordinates, but in such a way that statistically distinct averages can be discerned (Hinze, 1989). It can also be defined as an eddying motion with a wide spectrum of eddy size and a corresponding spectrum of fluctuation frequencies. The motion is always rotational. The forms of the largest eddies (low-frequency fluctuations) are usually determined by the boundary conditions, while the forms of the smallest eddies (highest-frequency fluctuations) are determined by the viscous forces (Rodi, 1980).

Basically, the physical turbulence models provide the solution the closure problem in solving Navier-Stokes equations. While there are ten unknown variables (mean pressure, three velocity components, and six Reynolds stress components), there are only four equations (mass balance equation and three velocity component momentum balance equations). This disparity in number between unknowns and equations make a direct solution of any turbulent flow problem impossible in this formulation. The fundamental problem of turbulence modeling is to relate the six Reynolds stress components to the mean flow quantities and their gradients in some physically plausible manner.

The time-averaged turbulence models (Table II-5) employ transport equations for quantities characterizing the turbulence. So far, standard k- ϵ model, RNG k- ϵ model, and RSM model have been implemented in the commercial CFD codes. These turbulent models are different in terms of the number of transport equations used for turbulence quantities.

It is worthwhile to note that the standard k- ϵ model is usually employed with the five coefficients as recommended by Launder and Spalding (1972). The five coefficients are empirical, obtained based on simple experimental flow situation. Rodi (1980) reported that solutions have been found to be sensitive to the five coefficients in the standard k- ϵ turbulence model. Although the standard k- ϵ model with these five coefficients has successfully simulated a number of real, fluid flow problems in two and three dimensions, it is necessary to alter drastically the magnitude of the five coefficients, so as to calibrate the model for a particular flow situation.

The RNG k- ϵ model is touted by CFD code vendors as accurate, economic in computer time and capable of prediction near wall transport phenomena without limitations associated with the wall function approach. Streaklines showing flow around a 2D bluff body are shown in Figure II-9. The RSM model may give better simulation results, but this model may confront with the convergence problem and is very demanding in terms of computational effort.

The RNG k- ϵ model is touted by CFD code vendors as accurate, economic in computer time and capable of prediction near wall transport phenomena without limitations associated with the wall function approach. The RSM model may give better

Table II-5. Overview of Turbulence Models (FLUENT INC., 2001)

Turbulence Model	Description, Advantage, and Disadvantages
k- ϵ	The most widely used model. Its main advantages are short computation time, stable calculations, and reasonable results for many flows. Not recommended for highly swirling flows, round jets, and in areas with strong flow separation.
RNG k- ϵ	A modified version of the k- ϵ model, with improved results for swirling flows and flow separation. Not suited for round jets. Not as stable as the standard k- ϵ model.
k- ϵ Realizable	Another modified version of the k- ϵ model. Solves the flow in round jets correctly, and provides much improved results for swirling flows and flows involving separation when compared to the standard k- ϵ model. More stable than the k- ϵ RNG model.
RSM	The full Reynolds stress model provides good predictions for all types of flows, including swirl, separation, and round and planar jets. Longer calculation times than the k- ϵ .
LES	Large Eddy Simulation provides excellent results for all flow systems. LES solves the Navier-Stokes equations for large scale motions of the flow and models only the small scale motions. The main disadvantage is that the required computational resources are considerably larger (often 10 to 100 times) than with the RSM and k- ϵ styles models, mainly because all calculations are conducted in a time dependent fashion since steady state flow is not assumed, and a finer grid is needed to allow for accurate modeling of the turbulence at the subgrid small scale level.

simulation results, but this model may confront with the convergence problem and is demanding in terms of computational effort.

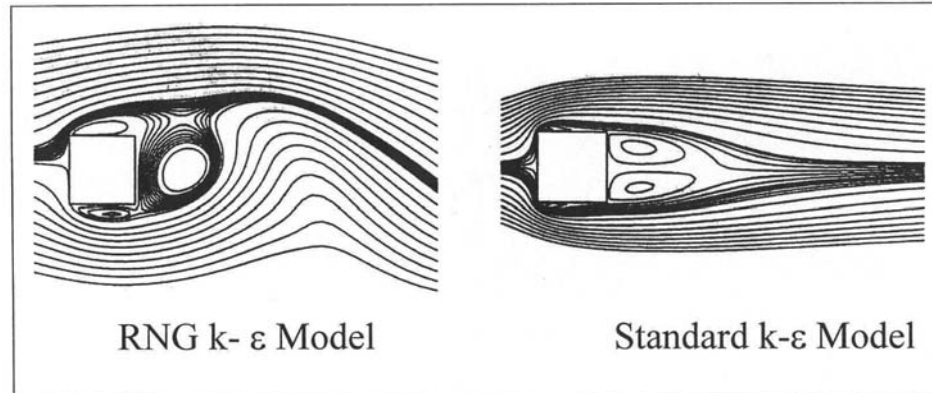


Figure II-8. Streaklines Showing Flow around a 2D Bluff Body (FLUENT, 2001).

Approaches for Mixing Tank Simulation

The CFD code users demand the approach for mixing tank simulation should have the following capabilities:

- Independence from experimental data
- Capabilities to handle all impellers with complicated geometry
- Capability to model a non-symmetrically located impeller
- Capability to model a tank with complicated geometry
- Capability to model with the three types turbulence models
- Capability to model with a multiphase model
- Convergence in a stable and robust manner

However, none of the CFD code vendors has provided the module to meet the above requirement from the users. Consideration effort has been contributed to develop the source code to predict the fluid flow in a mixing tank with powerful capabilities.

The LDA data approach has been used by a number of investigators. This approach can handle the complicated geometry tank and non-centrally located impellers. The limitations with LDA data approach is that LDA data are expensive to obtain, and the simulation result is sensitive to the small error in specifying the boundary conditions for the impeller region.

The rotating reference frame approach saves significant computational efforts over full time-dependent simulations, but this approach poses a problem with convergence because of the high degree of coupling between the momentum equations.

The sliding mesh approach, illustrated in Figure II-9, is touted by FLUENT to be able to handle the impeller-baffle interaction without the need to simplify the problem. The limitation with this approach is that RSM turbulence model and multiphase model cannot be included.

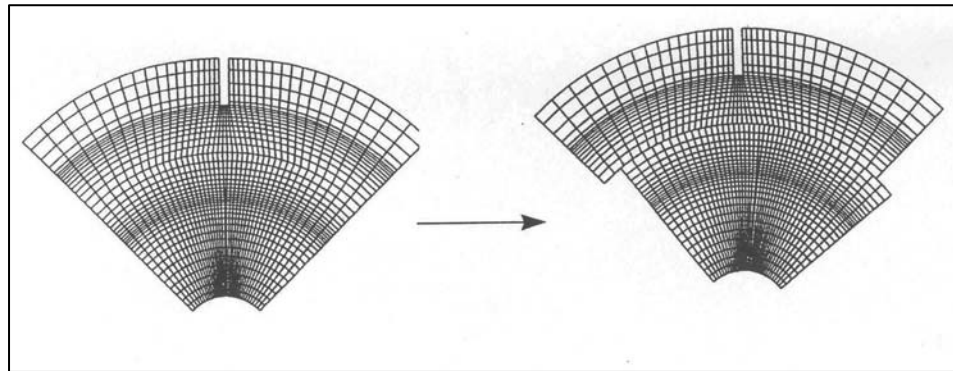


Figure II-9. Sliding Grid Motion (FLUENT, 2001).

The rotating reference frame approach based on the unstructured mesh is quite promising. This approach utilizes the powerful capabilities of unstructured mesh to handle the complicated geometry. It could take a few years for this approach to be released as a commercial CFD code.

Structured and Unstructured Mesh

Traditionally, CFD analysis of a design was based on the structure mesh. The current move towards concurrent engineering requires that the analysis occur concurrently with the development of the design. Integration of CFD analysis into this process requires that the CFD analysis cycle time be significantly reduced. Currently, one of the most time-consuming parts of performing a CFD analysis is the creation of the geometry and an appropriate grid. One way to significantly reduce this is to provide automatic unstructured mesh implementation. Also, unstructured mesh can be employed to handle the complicated geometry, and the local mesh can be refined without having to carry a fine mesh throughout the whole domain.

The drawback with the unstructured is that unstructured mesh module is not compatible with the utility module used by structured mesh. This difference could require considerable effort to develop the new utility code in the CFD vendor's side and the training and learning period in the user's side.

Multiphase Simulation

Basically, the multiphase model is based on a number of assumptions to obtain the necessary additional equations to close the partial differential equations. The coefficients used in the assumption equations are obtained from empirical information. The limitation is obvious. The application must possess similar physical phenomena.

The Eulerian multiphase model employed the concept of volume fractions, which is quite pseudo one phase model. The coupling between each phase is achieved through the pressure and interphase drag coefficients.

The Larangian multiphase model attempts to track a large number of dispersed particles through the calculated continuous phase. The scarcity of the information about mechanism of dispersed phase breakup and coalescence is one of the limitations for multiphase models.

VISCOSITY OF CELLULOSIC SLURRIES

Rheology is defined as the science of deformation and flow properties of materials. Rheological measurements provide critical information for product and process performance and quality control and help reduce the cost and time needed for development.

High solids saccharification and fermentation are difficult due to the challenging rheological characteristics of high-solid biomass slurries that can cause non-uniform heat and mass transfer. In addition, dynamic changes in rheology and biomass properties occur as the cellulose structure is broken down during enzymatic hydrolysis.

Pimenova and Hanley (2003) estimated the viscosities of pretreated corn stover slurries (average fiber length = 120 μm) using a helical ribbon impeller viscometer. Because the high-solids slurries were non-Newtonian, the viscosities varied with shear rate in a power law relation, with order of magnitude increases starting at approximately 50 centipoise (Newtonian) at a level of 5 per cent solids (w/w, dry basis) and reaching more than 10^6 centipoise (highly non-Newtonian) at a level of 30 per cent solids. The viscosities of distiller's grain slurries were measured for solids concentrations of 21, 23, and 25 per cent using a helical impeller viscometer over a range of rotational speeds. The reported value of c (Newtonian impeller constant) was 151 and k (non-Newtonian

shear rate constant) was 10.30. The comparison was made to power law, Herschel-Bulkley, and Casson viscosity models by regression analysis of experimental data with regression coefficients exceeding 0.99 in all cases (Houchin and Hanley, 2004).

Non-Newtonian Behavior

Newtonian fluids can be described by Newton's law of viscosity (Bird et al., 2001):

$$\tau_{yx} = -\mu \frac{\partial V_x}{\partial y} = -\mu \dot{\gamma} \quad (6)$$

Newton's equation for viscosity can be modified to characterize non-Newtonian behavior. Some of the more widely used empirical models include the Bingham, Casson and power law models. The two-parameter models (Bingham, power law, and Casson) have three advantages. These methods can accurately fit data for a shear rate range, can usually describe the rheology of filamentous suspensions, and are widely used in correlations of transport properties of non-Newtonian systems with moderate success (Allen et al., 1990). The Herschel–Bulkley model, proposed in 1926, describes the rheological characteristics of filamentous suspensions.

The four model equations are frequently used to describing filamentous suspensions:

Power law	$\tau = K \dot{\gamma}^n$	(7)
-----------	---------------------------	-----

Bingham	$\tau - \tau_y^B = \eta_p \dot{\gamma}$	(8)
---------	---	-----

Casson (1959)	$\tau^{0.5} = (\tau_y^C)^{0.5} + \eta^C (\dot{\gamma})^{0.5}$	(9)
---------------	---	-----

Herschel-Bulkley (1926)
$$\tau = \tau_y^{HB} + K^{HB} \dot{\gamma}^{n_{HB}} \quad (10)$$

For some thick suspensions and pastes no flow occurs until critical stress, the yield stress is reached. The fluid flows in such a way that part of the stream are in plug flow. The simplest model of a fluid with a yield value is the Bingham model. From Equation 8 it follows that, if the shear stress is significantly larger than the yield stress, Newton's law applies (Bird et al., 2001).

The Casson and Bingham plastic models are similar because they both have a yield stress. Each, however, gives different values of the fluid parameters depending on the data range used in the mathematical analysis. The most reliable value of yield stress, when determined from a mathematical intercept, is found using data taken at low shear rates. For example, the Casson model has produced results for penicillin broths (Roels, 1974) and for interpreting chocolate flow behavior (Steffe, 1996).

The simplest empiricism for $\eta(\dot{\gamma})$ is the two-parameter power law expression. This simple relationship states that the plot of the log (shear stress) versus log (shear rate) is linear. If the slope of this curve, n , is one, the fluid is Newtonian. If n is less than one, the fluid is pseudoplastic; if greater than one, the fluid is dilatant.

Roels et al. (1974) found that the power law model could not adequately describe the behavior of a penicillin broth over a large range of shear rates. Another study of penicillin broth, completed by Bongenaar et al. (1973), indicates the power law model can be successfully used to describe the rheological behavior over narrow shear rate ranges.

The Herschel-Bulkley model also was used to fit the rheological data. If the fluid does not have yield stress, the model reduces to the power law model. The three parameters in this model were highly interdependent with each other (Allen et al., 1990). Therefore, having wide variability, these parameters did not correlate well with biomass concentration. Also, as shown by Reuss et al. (1982), there is no significant difference between the Casson, power law and Herschel-Bulkley models over a limited range of shear rates.

Measurement Techniques

Rheological measurements of filamentous suspensions using conventional methods (cone and plate, concentric cylinder, and rotating bob viscometers) can be difficult due to phase separation and other non-homogeneities (Dronawat et al., 1996).

The impeller method is often employed to measure the rheology of suspensions. Previous workers assumed that the effective shear rate of such a device is related to the impeller speed by a fluid-independent constant, but there is evidence that this is not true for all impellers (Allen et al., 1990; Dronawat et al., 1996). It has been suggested by Allen that a properly designed helical ribbon impeller might be more appropriate for this technique.

The complex flow field created by the impeller does not allow the direct calculation of shear rate (Charles, 1978; Allen et al., 1990). The “average” shear rate in the measuring vessel, $\dot{\gamma}_{avg}$, is assumed to be proportional to the impeller speed, N , and independent of the rheology of the fluid in the vessel.

$$\dot{\gamma}_{avg} = kN \quad (11)$$

Then it is assumed that the dimensionless power number (p_{No}) is inversely proportional to the impeller Reynolds number (Re_i) for Newtonian fluids in laminar flow regime where the impeller Reynolds number is less than 10:

$$p_{No} = c / Re_i = \frac{2\pi M}{\rho N^2 D_i^5} \quad \text{for } Re < 10 \quad (12)$$

$$Re_i = \frac{\rho N D_i^2}{\mu} \quad (13)$$

where k and c are empirically determined constants. Replacing the viscosity, μ in the impeller Reynolds number with the apparent viscosity of the non-Newtonian fluid, η_a , at the average shear rate, solving Equation 12 for the apparent viscosity

$$\eta_a = \frac{2\pi M}{c N D_i^3} \quad (14)$$

substituting for η_a and $\dot{\gamma}_{avg}$

$$\tau = \eta_a \dot{\gamma}_{avg} = \frac{2\pi k M}{c D_i^3} \quad (15)$$

The lack of general applicability of the “average shear rate” concept and the inaccuracies arising from its application also can be explained by considering the analogy between the impeller and the rotating cylinder viscometers. In rotating cylinder viscometers, the shear rate can be significantly affected by the test fluid’s rheological properties. For example, for a power law fluid with flow behavior index, n , and with Couette flow between the cup wall (radius R_o) and bob (radius R_{in}) the ratio of the actual

shear rate $\dot{\gamma}_{act}$ to the shear rate determined for a Newtonian fluid ($n=1$), $\dot{\gamma}_{Newt}$, at a given rotational speed, is

$$\frac{\dot{\gamma}_{act}}{\dot{\gamma}_{Newt}} = \frac{[1 - (R_{in} / R_0)^2]}{n[1 - (R_{in} / R_0)^{2/n}]} \quad (16)$$

For an impeller viscometer there also can be a much higher average shear rate in the vessel and, hence, a higher shear rate than that determined on the basis of using a shear rate relationship, which is independent of rheological properties.

Ulbrecht and Carreau(1985) determined an analogy between the Coette flow in a rotating cylinder viscometer and an impeller rotating in the laminar flow regime. They reported the empirical expression for k :

$$\frac{\dot{\gamma}_{avg}}{N} = [cD_t^3 / \pi^2 D_t^2 H_l] \left\{ \frac{n[(D_t / d_e)^{2/n} - 1]}{4\pi} \right\}^{n/(n-1)} \quad (17)$$

where D_t is the tank diameter; H_l is the height of liquid in the tank; n is the flow behavior index of a power law fluid, and d_e is the equivalent diameter of the impeller determined with the help of the relationship obtained for Newtonian liquids:

$$c = \frac{P_{No}}{Re_i} = 4\pi^3 D_t^2 H_l / D_t^3 [(D_t / d_e)^2 - 1] \quad (18)$$

The dependence of k on the fluid rheology is evident from comparison of Equations 12 and 17.

Brito-de La Fuente et al. (1992) in their study of a helical ribbon impeller also suggest the shear rate constant is dependent on the consistency index number, n . These researchers also employed Equation 6 in their investigation. Comparison of the shear

rate constants calculated using the two methods for a consistency index number range of 0.1 to 0.7 produce k that are functions of n .

Impeller Ribbon Viscometer Technique

Newtonian and Non-Newtonian calibration fluids are used to calculate the constants necessary to relate torque and rotational speed measurements to shear rates and stresses. The Newtonian fluids are utilized to calculate c , using Equation 6. The parameter c is then used to transform torque and impeller speed-readings to shear rate and shear stress data.

Torque and impeller speed measurements are taken for non-Newtonian fluids calculation of the shear rate constant, k , which allows to determination of the shear stress, shear rate, and apparent viscosity.

In summary, for the impeller ribbon viscometer technique, the power number of an impeller is inversely proportional to the impeller Reynolds number (Equation 12). As the impeller rotational speed increases, the flow gradually changes from laminar to turbulent, passing through a transition region. Parameter c can be obtained from the calibration fluids. If the same value for c is assumed to apply to a non-Newtonian fluid, then this equation can be used to calculate the apparent viscosity of that fluid. The shear stress can be expressed in Equation 15. Once the parameter c and the shear rate constant are known, the shear rate and shear stress of the non-Newtonian fluid can be calculated (Metz et al., 1979). The range of the impeller method is determined by the minimum and maximum torques that can be measured (Metz et al., 1979).

Ruston Impeller Programmed Viscometer

The MCR rheometer has many advantages over the previous techniques. It can be programmed to operate between controlled shear stress (SS) and controlled shear rate (SR), an option usually available only in high-end research rheometers. The device is based on a rotating or oscillating parallel-plate geometry in combination with a low friction electronically commutated motor system. The instrument is also well suited for investigations into the mixing and stirring behavior of emulsions and dispersions. Sophisticated RheoPlus software is available for operating the instrument from a computer. It can be connected either via the RS232 interface or via a LAN–Ethernet interface directly to the network. Numerous analysis models and automation routines include a special quality control module.

The rheometers perform a wide range of steady and dynamic tests in both SS and SR mode. From generating simple flow curves to the dynamic analysis of complex fluids, melts, and co-polymers, all Physica rheometers offer simple programming and test setup. Part of the flexibility of the software lies in its ability to mix or chain different test types together to help simulate process and end-use conditions. SS and SR standard tests, a combination of rotation and oscillation as well as demanding measurements such as multiwave tests, time/temperature shifts and the superimposition of oscillation/rotation can be carried out.

III. HIGH SOLIDS ENZYMATIC HYDROLYSIS AND FERMENTATION OF SOLKA FLOC TO ETHANOL

ABSTRACT

To lower the cost of ethanol distillation of fermentation broths, a high initial glucose concentration is desired. However, an increase of substrate concentration typically reduces the ethanol yield due to insufficient mass and heat transfer. In addition, different operating temperatures are required to optimize enzymatic hydrolysis (50°C) and fermentation (30°C). To overcome the incompatible temperatures, Saccharification Followed by Fermentation (SFF) was employed at relatively high solids concentrations (10 to 20 per cent) using portion loading method.

Before a full scale system can be designed, fermentation studies are required on a bench scale. Small scale experiments can be used to predict how a large scale process will behave. The reactor configuration affects the reaction productivity with data from bench scale enzymatic hydrolysis and fermentation used to design larger production reactors.

In this study glucose and ethanol were produced from Solka Floc, first digested by enzyme at 50°C for 48 hours, followed by fermentation. In this process, commercial enzymes were used in combination with a recombinant strain of *Zymomonas mobilis*

(39679:pZB4L). The effects of the substrate concentration (10 to 20 per cent w/v) and reactor configuration were investigated. In the first step, the enzyme reaction was achieved with 30 FPU/g cellulose at 50°C for 96 hours. The fermentation was then performed at 40°C for 96 hours. Enzymatic digestibility was 50.7, 38.4, and 29.4 percent at after 96 hours with a baffled Rushton impeller at 10, 15, and 20 per cent initial solids (w/v), respectively, which was significantly higher than that obtained with a baffled marine impeller. The highest ethanol yield, 83.6, 73.4, and 21.8 per cent of the theoretical based on the glucose, was obtained at 10, 15, and 20 per cent substrate concentration, respectively. This yield corresponds to 80.5 percent of the theoretical based on the cell biomass and soluble glucose present after 48 hours of SFF. Compared with traditional SSF process for high solid substrate at 40°C, SFF gave a higher ethanol yield.

INTRODUCTION

Demand for petroleum products continue to rise. In 2004, global oil consumption jumped 3.5 per cent, or 2.8 million barrels per day (USA TODAY, 2005). The U.S. Energy Information Administration projects demand rising from the current 84 million barrels per day to 103 million barrels by 2015 (BP, 2005). If China and India - where cars and factories are proliferating - consume oil at just one-half of current U. S. per-capita levels, global demand would jump 96 per cent, according to Dr. Amos Nur (Stanford University).

Thus, with the increase of oil consumption, the production of bioethanol is looking ever more promising. In order to have a significant impact on our current oil consumption, ethanol must be both inexpensive and plentiful (Zhang et al., 1999). Lignocellulosic biomass such as agricultural residues, wood, and crops are abundant renewable materials for the production of sugars as a carbon source for subsequent fermentation. Of the agricultural residues, corn stover yields have increased proportionately. About 250 million dry tons of stover is produced each year. For delivery within a 50 mile radius, \$30 to \$35/dry ton delivered is a good number (Hetternhaus et al., 2002). The major cost is baling. A sizable resource for biochemical production of fuels and chemicals thus remains undeveloped.

The polysaccharide fraction of agricultural residues can be hydrolyzed using acids or enzymes as catalysts (Zhang et al., 1999; Um, 2002). Cellulases catalyze the hydrolysis of cellulose, the major structural component of biomass, the most abundant organic material on earth (Scott, 1994). Complete hydrolysis of cellulose yields

the easily fermentable sugar, glucose, allowing biomass to be a potential renewable energy source (Fein et al., 1991, Kim et al., 2001). As a result, there is strong interest in understanding the process of enzymatic cellulose degradation at high initial solid concentration (Fein et al., 1991).

Typically, as much as 90 per cent or more of the broth is water that must be removed during SSF. This separation is costly and also produces a large aqueous stream that must then be disposed of or recycled. A high initial cellulose concentration combined with a favorable conversion yield of cellulose into soluble sugars reduces the cost of water removal. When concentrated slurries are processed, the medium mixing/enzyme homogenization becomes difficult and often results in low bioconversion yields (Lübbert et al., 2001). This difficulty partly accounts for the lack of literature concerning fermentation of biomass suspensions at concentrations greater than 10 per cent (Philippidis et al., 1997). For high-solids saccharification and fermentation, the reaction rate and bioreactor configuration are of critical importance to the economic feasibility of a larger scale industrial process, since this unit operation requires the longest residence time relative to the other major biomass conversion reactions of enzyme hydrolysis and fermentation. These longer residence times during saccharification translate into higher operating and capital costs per unit of product output.

However, this approach appears to be the simplest and most economically viable way to attain suitable ethanol concentrations in the broths for distillation. On the whole, several process parameters must be optimized: substrate concentration, enzyme-to-substrate ratio, dosage of the active components (β -glucosidase-to-glucanase ratio) in the enzymatic mixture, bacteria concentration, and reactor conditions. Lastly, one of the

most important factors affecting the overall economics is the compatible temperature between enzymatic hydrolysis and fermentation process at high slurries during the saccharification followed by fermentation (SFF) process.

In the present study, enzymatic hydrolysis and fermentation of concentrated Solka Floc were evaluated at conditions optimal for the highest glucose and ethanol yields using SFF process in a three-liter bioreactor. The influence of dry matter concentration and bioreactor configuration on the yield of glucose and ethanol was also investigated.

MATERIALS AND METHODS

Raw Material

Solka Floc (Fiber Sale & Development Corporation, Urbana, Ohio), a delignified spruce pulp, was used as raw material for this research. The composition of this material, analyzed according to NREL Standard Procedure, is shown in Table III-1.

Table III-1. Initial composition of untreated Solka Floc

Ingredient	Cellulose (%)	Ash (%)	Moisture (%)	The rest (%)
Solka Floc	88	0.5	5.2	-

Commercial Enzyme

Commercially produced Spezyme CP and Novozyme 188 were used for enzymatic hydrolysis. The cellulose enzyme Spezyme CP, secreted by *Trichoderma longibrachiatum*, formerly *Trichoderma reesei*, was from Genencor International, Inc. (Palo Alto, CA). The enzyme had an activity of 82 GCU/g as provided by the manufacturer and 55 IFPU/mL as determined by NREL standard procedure 006 (Adney and Baker, 1992). Novozym 188 purchased from Sigma (Cat. No. G-0395) were used for cellulose hydrolysis with a volume ratio of 4 IFPU Celluclast / CBU Novozyme to alleviate end-product inhibition by cellobiose.

Microorganism

The organism used for this experimentation was *Zymomonas mobilis* 39679 (pZB2L4). This organism is a proprietary organism obtained from the National

Renewable Energy Laboratories of Golden (CO).

Bench-Scale Bioreactor

The two-liter fermentation tests were conducted in a 3.3-liter bench top, BioFlo[®] 3000 bioreactor (New Brunswick Scientific Co. Inc., Edison, New Jersey). BioFlo[®] 3000 is a versatile bioreactor that provides a fully equipped fermentation system, adaptable for cell culture, in one compact package. The fermentor is equipped with four baffles and two 6-flat-blade Rushton impellers. The stainless steel head plate, bottom dish, and penetrations are polished to a mirror finish to minimize contamination. The bioreactor can be employed for batch or continuous culture with built-in controllers for pH, dissolved oxygen (DO), foam/level, agitation, and temperature. It also includes pumps for acid, base, antifoam, and nutrient addition.

The pH is measured by a glass electrode (Ingold) and controlled by a Proportional /Integral/Derivative (PID) controller. The pH controller operates two peristaltic pumps to maintain the pH value. Sterile air was supplied to the broth through the ring sparger and was controlled by the needle valve of the flowmeter. A DO electrode (Ingold) was used to measure the dissolved oxygen concentration. A PID controller controlled the agitation speed with an optical encoder coupled to the motor shaft. The medium temperature was measured with a platinum resistance temperature director (RTD) and controlled by a PID controller. Foam was controlled during the fermentation by the antifoam probe (conductivity probe), which was located in the headplate and adjustable in height from the medium surface. The BioFlo[®] 3000 unit cannot be sterilized in place,

but must be disassembled and sterilized in an autoclave.

Strategy of High Solid Loading on Enzyme Hydrolysis and Fermentation

To maximize the glucose and ethanol concentrations, substrate concentrations were employed from 10 to 20 per cent on a dry basis, corresponding to cellulose concentrations of 8 to 17 percent. In several studies for traditional batch enzyme reaction and fermentation of high substrate concentration (> 10 percent), there is no visible liquid phase due to complete absorption of liquid by the biomass. In this state no sugar and ethanol products could be seen for tests between 10 and 20 percent. To overcome this problem the Solka Floc was added to the reactions in three portions during both enzyme reaction and fermentation up to the 20 percent final substrate concentration. The portions were added to the reaction in the initial four hours of the reactions. And then the inoculum prepared as 10 per cent by volume of the total working volume (two liters) was transferred into the reactor after enzymatic hydrolysis for 48 hours. The enzyme loading was 30 FPU per gram of cellulose, supplemented by β -glucosidase to prevent product inhibition by cellobiose. The SFF experiments were operated for 96 hours, initially at 50°C and finally at 30°C. Figure III-1 illustrates the strategy for high solids loading.

The substrate and nutrient media were autoclaved (120°C for 20 minutes), but the enzyme solutions were not sterile. The Solka Floc slurry, diluted to different dry weights of solid material (10, 13, 15, and 20 per cent), was used as substrate.

Enzymatic Hydrolysis

The enzymatic digestibility of Solka Floc was tested in duplicate according to

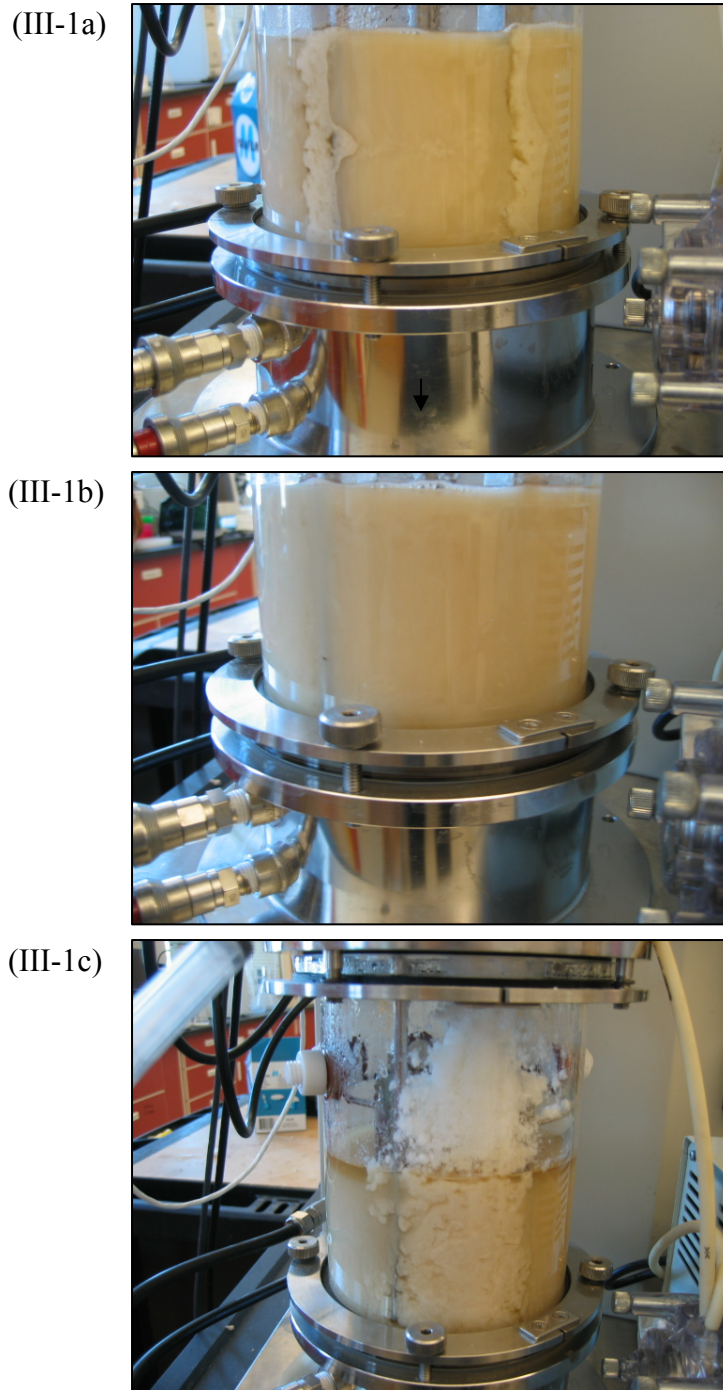


Figure III-1. Strategy of high solid loading on enzyme hydrolysis and fermentation.

- III-1a:** 5 percent (w/v) suspension (t=0)
- III-1b:** 5 percent (w/v) suspension (t=0 to 4 hr)
- III-1c:** Reload 5 percent (w/v) suspension (t=4 hr)

the NREL Chemical Analysis and Testing Standard Procedure (CAT) No. 009 (NREL,1996). The substrate concentration ranged from was 100 to 150 grams of cellulose per liter. Cellulase enzyme (Spezyme CP, Lot 301-05021-011) was kindly provided by Genencor International.

Excess amounts of β -glucosidase Novozyme 188, 250 CBU/g of activity were added to completely convert cellobiose to glucose, i. e., 30 CBU/g cellulose. Cellulase was added at 15 to 30 FPU/g cellulose. Citrate buffer (0.05 M, pH 4.8, in reaction mixture) and 8 mL *Tetracycline* (10mg/mL in 70 percent ethanol) were used to keep constant pH and prevent microbial contamination, respectively. The total glucose content after 96 hours of hydrolysis was used to calculate the enzymatic digestibility. All of the hydrolysis was conducted in 3.3-liter bench top, BioFlo[®] 3000 bioreactor. Using the same method, 250 mL Erlenmeyer flask scale was used as control.

Cell Stock Culture

A recombinant bacterium, *Zymomonas mobilis* ATCC 39679, carrying the plasmid pZB4L (designated as *Zm* 39679:pZB4L), was provided by means of a material transfer agreement to Dr. Thomas R Hanley by M. Zhang from the National Renewable Energy Laboratory (NREL, Golden, CO) was used in these studies. Stock culture was maintained on a Difco Rich-Media (RM) agar medium at 4°C and was subcultured every week to maintain viability. Difco RMGTc medium was used to prepare preculture and fermentation media. The RMGTc consisted of yeast extract (DIFCO Laboratories Inc, Detroit, MI) 10 g/L; KH₂PO₄, 2 g/L; Tetracycline 20 mg/L; glucose 20 g/L. The stock solutions of the mineral salts and tetracycline were prepared to 10 times the desired

concentration (g/L). Yeast extract was mixed with the mineral salt solutions and autoclaved separately from the carbohydrate solutions to prevent caramelization of the media. Tetracycline solutions were sterilized by syringe filtration (Gelman 0.2 μm pore size) and any concentrated glucose was added aseptically after autoclaving. Initial pH was not adjusted, although measurement confirmed that the initial pH was consistently in the range of 5.0 to 5.8. Cells were stored in stock cultures preserved by mixing 1 mL culture and 0.5 mL of 60 percent sterile glycerol in a 2 mL cryovial at $-70\text{ }^{\circ}\text{C}$.

Preliminary Fermentation

Preliminary experiments using recombinant *Zymomonas mobilis* were conducted in 500 mL Erlenmeyer flasks to provide the growth pattern of the yeast. The RM broth solution (200 mL) was sterilized at $121\text{ }^{\circ}\text{C}$ for 20 minutes in an autoclave (SR-24B, Consolidated Stills and Sterilizers, Boston, MA). Three loops of the stock culture were transferred to 200 mL of sterilized RM broth solution and the inoculum was incubated at $30\text{ }^{\circ}\text{C}$ on a platform shaker (Innova 2000, New Brunswick Scientific Co Inc) agitated at 120 rpm for 24 hours. During the shake flask-fermentation, 2 mL-samples were taken with Eppendorf pipette (series 2000, Brinkmann Instruments) every hour. The optical density (OD) of the sample was measured at 600 nm with a Spectronic 1001 instrument (Milton Roy, NY). The fermentation was continued until the stationary phase of the microorganism was reached.

Two-Liter Fermentation

The RM broth was prepared for the two-liter fermentation (21 g of RM broth in

1000 mL of deionized water). The pH probe was calibrated before the sterilization. The pH measuring system was calibrated using two buffer solutions of known pH (4 and 7). The pH measuring switch and the mode switch were set to pH and ZERO, respectively. The pH probe was immersed into a pH 7 buffer solution and the display was adjusted to read pH 7 with INC/DEC switch. The complete fermentor assembly with medium was sterilized at 121°C for 20 minutes in an autoclave. After sterilization, about 200 mL of sterilized water was added to the fermentor through the inoculum port to make up the volume to 2.0 liters. When the medium cooled down to 30°C, the dissolved oxygen (DO) probe and the selector switch was set to DO and the mode switch was set to ZERO. The display was adjusted to read zero with INC/DEC switch. The DO probe cable was connected to the DO probe and the mode switch was set to SPAN. Nitrogen at 1.0 liter per minute was introduced into the vessel and the agitation speed was set to 500 rpm. When the DO value stabilized after 30 minutes, the DO values were adjusted to 100 percent saturation with the INC/DEC switch.

About 200 mL of starter culture was prepared for inoculation. The cap of the inoculum port was wiped with ethanol-soaked paper towel and screwed back in place. The fermentation was conducted at 30°C at pH 5. The temperature of the fermentor was controlled by cooling /hot water in the jacket of the fermentor. The pH of the broth was adjusted with automatic periodic addition of 1.0 M NaOH. Nitrogen gas was supplied to the fermentation medium through the sparger ring under the six-blade impeller. The gas rate was set at 100 milliliters per minute using a rotameter. This flow rate was equivalent to 0.1 volume of air per volume of medium per minute (0.1 VVM).

ANALYSIS AND ASSAY

Carbohydrates

NREL standard procedure No. 002 was used to determine the quantity of cellulose in the solid Solka Floc. A 0.3 g sample of the biomass was treated at 30°C with 72 per cent sulfuric acid for two hours and then autoclaved at 121 °C after diluting the acid to four per cent with deionized water. Both reagent grade glucose and xylose were autoclaved together in order to calibrate the amount of sugar decomposed during the reaction. The hydrolyzate was centrifuged at 15,000 rpm. After centrifuging, the hydrolyzate was tested on YSI for glucose. The YSI model 2700 glucose analyzer (YSI, Yellow Spring, Ohio) was used as the standard laboratory analyzer that employs the glucose oxidase method to quantify glucose concentration.

Moisture and Ash

National Renewable Energy Laboratory (NREL) Standard Procedure No. 001 and 006 were followed. A 1.5 g sample of the biomass was weighed in an aluminum pan and dried in a convection oven at 105 ± 3 °C for over four hours. The oven-dried sample was cooled in a desiccator and weighed to obtain the weight difference caused by moisture. The initial materials used in every experiment contained 5.2 percent moisture.

After determination of total solids and moisture in biomass, a 1.0 g sample of the biomass was weighed in an ignitable ceramic crucible and brought to constant weight by igniting at 575 ± 25 °C. The crucible was removed from the furnace, cooled to room temperature in a desiccator, and weighed to the nearest 0.1 mg. The initial materials used in every experiment contained 0.5 percent ash.

Dry Cell Weight vs. Optical Density

Dry cell weight (DCW) is necessary for the determination of several key parameters in these fermentation studies. These values were found by determining a linear correlation between the total cell mass and the absorbance of visible light at 600 nm (OD_{600}) across a 1 cm light path. Yellow colored growth media has minimal absorption at 600 nm, so using that wavelength gives you a minimal contribution from the media blank.

Samples of *Zymomonas* 39679 pZB4L were collected in the late exponential phase. A portion of these samples was saved for OD analysis. The remainder was centrifuged (Sorvall RC-5B, Du Pont instruments) for 10 minutes at 15,000 rpm. The resulting supernatant was removed, and the biomass pellet was resuspended in DI water and centrifuged again. This washing procedure ensured the removal of all noncellular material that could be potentially reactive with the biomass during drying. The washing procedure was repeated twice, and the biomass pellet and deionized water was added to previously dried and tared aluminum dishes. These samples were dried in a desiccator at 40°C for 12 hours and allowed to equilibrate to room temperature in a dry box for 3 hours before the mass was measured. The total cell mass was then determined and divided by the original sample volume to give the cell concentration.

The samples that were set aside for DCW measurement were diluted to various concentrations and the DO_{600} was taken with the spectrophotometer (Spectronic 20 GENESYS Spectrophotometer) zeroed on curvette blank containing deionized water as reference. Any OD_{600} measurement larger than 0.6 was considered out of the linear range of the calibration with more dilution required.

Glucose and Ethanol

Aliquots were taken from the sample port every hour for 24 hours. A 10 mL plastic syringe attached to the sampling port facilitated the sampling procedure. A four-drum (15 mL) vial was tightened to the sampling port, the sample valve was opened and the syringe slowly released. When the desired volume of sample was obtained (5 mL), the sample valve was closed. The cell mass concentration for 2 mL samples was measured in the Spectronic 20 GENESYS Spectrophotometer using the calibration curve previously determined. About 1.5 mL of the sample was centrifuged (15000 rpm for 10 minutes) and the supernatant was used for glucose and ethanol analysis. The dissolved oxygen saturation values (DO) were recorded immediately after taking the sample. The ethanol yield and digestibility was calculated for the glucose and ethanol following the procedure of NREL Chemical Analysis and Testing Standard Procedures No. 008 and 009.

RESULTS AND DISCUSSION

Concentrated solid saccharification following fermentation can be roughly defined as beginning at the insoluble solids level where free liquid is no longer present in the slurry such that the separation of a liquid and solid phase from the suspension is not spontaneous. The presence of free water in high-solids slurries depends strongly on both the insoluble solids level and the cellulose content of the solids, which influences lignocellulosic-water interactions and cellulose swelling. Alternatively, this concentrated suspension definition can be regarded as the solids region where the slurry viscosity is highly non-Newtonian (Pimenova *et al.*, 2003). For Solka Floc substrates, this region begins at approximately 10 per cent to 20 per cent (w/v) insoluble solids. Performing the saccharification following fermentation at high insoluble solids introduces a new set of process-related problems associated with slurry mixing, method of substrate loading, and effectiveness of tank configuration.

Enzymatic Hydrolysis Below 10 Percent (w/v)

Figure III-2 shows cellulose conversion to ethanol for the two-liter batch hydrolysis in the initial six-hour enzyme reaction with other enzyme parameters (T and enzyme loading) held constant. The experiments at five per cent initial insoluble solids by weight and 30 FPU/g cellulose with 30 CBU/g cellulose addition of Novozym to reduce cellobiose inhibition. This plot shows that the conversion rates exhibit linear behavior at the beginning of the reaction, thus cellulosic material was sufficiently liquidized in four hours.

Many researchers have shown that the initial rate of hydrolysis is much higher

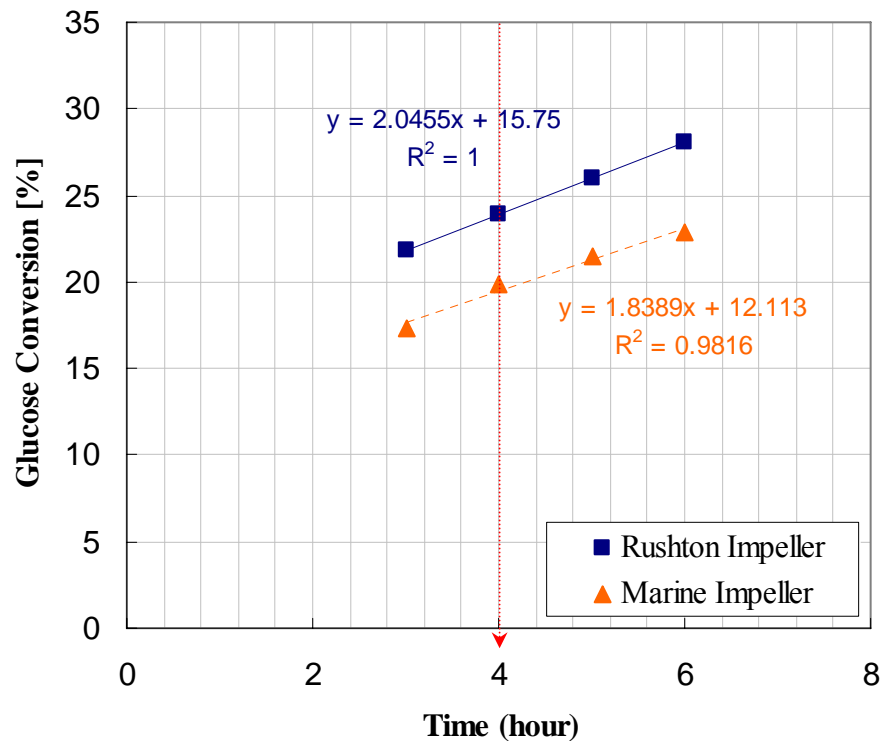


Figure III-2. The glucose conversion rate during the initial 6-hour enzymatic hydrolysis of 5 per cent (w/v) Solka Floc

Note:

1. Enzymatic hydrolysis condition: six hours, 30 FPU/g cellulose, pH 4.8 to 5.0, 50°C, 120 rpm.
2. All data points given are the average yields for the duplicate determinations.

than the subsequent rate (Zhang and Lynd, 2004), while proposed reasons include selective initial hydrolysis of amorphous cellulose (Davis *et al.*, 2002; Mansfield *et al.*, 1999), decreases in specific enzyme adsorption or subsequent inability of bound cellulases to reach new catalytic sites (Lynd *et al.*, 2002; Eriksson *et al.*, 2002), and steric preferences (Väljamäe *et al.*, 1998; Ooshima *et al.*, 1990; Converse *et al.*, 1990). The specific rate at which the majority of the cellulose is utilized remains approximately constant until a critical value is reached at approximately 80 per cent cellulose conversion.

However, in order to overcome of poor mass and heat transfer the Solka Floc was added to the reaction in three portions in four hours during enzymatic hydrolysis up to 20 per cent final substrate concentration.

The enzymatic digestibilities as function of time for each lower solid concentration are shown in Figure III-3a. The digestibility was 79, 68, and 63 per cent at 1, 3, 5 per cent solids concentration, respectively. The conversion yields were, in general, higher at the lower substrate concentration (~ 5 percent, w/v) because of lower mass transfer limitations within the reaction medium. Figure III-3b shows percent of glucose conversion during enzymatic hydrolysis as a function of impeller type. On average, the baffled Rushton bioreactor gave 63 per cent conversion of cellulose at the 5 per cent solid concentration, which generated 5 per cent more glucose than baffled marine bioreactor.

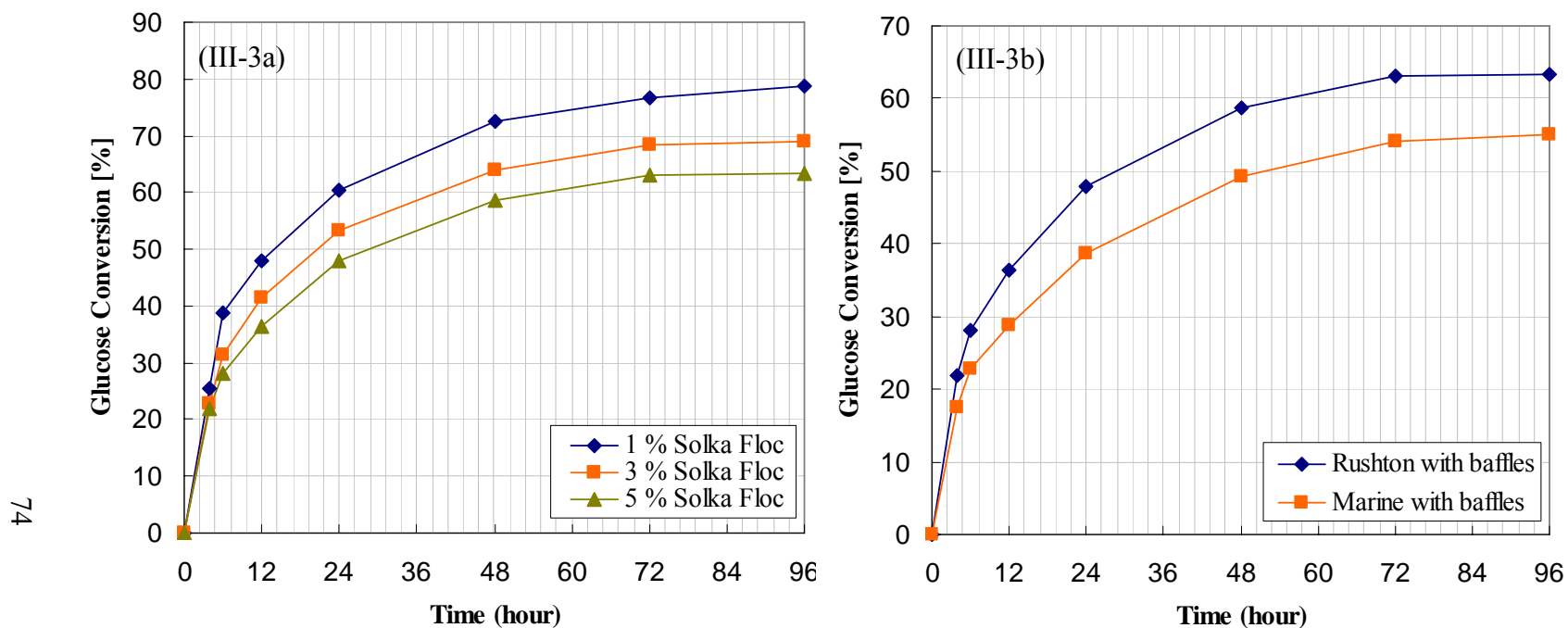


Figure III-3. Enzymatic hydrolysis of Solka Floc at lower percent solid concentration (III-3a) and Solka Floc at 5 per cent(w/v) solid for different impeller type (III-3b) as a function of time at constant cellulase activity.

Note:

1. Enzymatic hydrolysis condition: 96 hours, 30 FPU/g cellulose, pH 4.8~5.0, 50°C, 120 rpm.
2. All data points given are the average yields for the duplicate determinations.

Stirring Power in Three-Liter Fully-Baffled Tanks

The generally accepted measurements of stirring power in fully-baffled tanks containing non-Newtonian fluids with various impellers were made by Rushton, Costich, and Everett (1950). Pitched-blade turbine stirring power measurements in Newtonian fluids were made by Bates, Fondy and Corpstein (1963). Metzner and Otto (1957) measured power consumption for shear-thinning, non-Newtonian fluids with little viscoelastic response (mainly carboxymethyl cellulose (CMC) and Carbopol in vessels stirred by disk turbines. They correlated their data using a Reynolds number corrected for the shear thinning viscosity computed at a shear rate based on a constant $KMO (=13)$ times rotation rate N . Their data showed a mild power reduction from the Newtonian data in the transition regime from laminar to turbulent agitation.

Figure III-4 show the power consumption for the baffled three-liter bioreactor at 5 per cent Solka Floc suspension with a working volume of two liters. Figure III-4a shows that the measurements were made with a 0.046 m diameter Rushton impeller, with and without wall baffles. The power consumption increases with increasing rotational speed, and power consumption was same up to 400 rpm with and without wall baffles. A significant difference of power consumption was seen beginning at 600 rpm. Figure III-4b shows results obtained with Rushton and marine impellers, respectively. At the 5 per cent solid suspension, power consumption is significantly lower for marine impeller than for Rushton impeller. Figure III-5 is analogous to Figure III-4 and shows the power consumption at a relatively high solid concentration (15 percent, w/v) and otherwise unchanged operating conditions. This diagram reflects difference in power consumption between impellers in this type of baffled mixing tank. Specifically, power

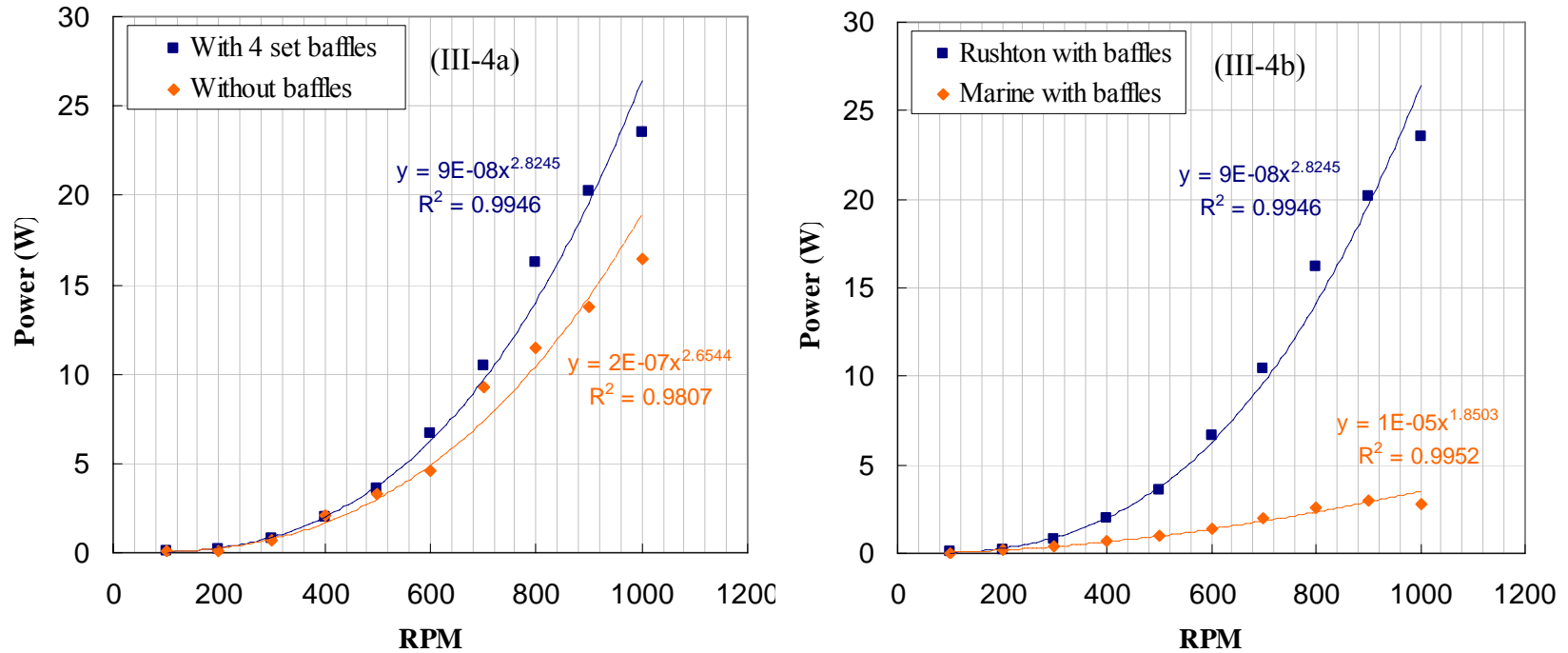


Figure III-4. Power consumption in the two-liter bioreactor with 5 per cent (w/v) Solka Floc Suspension with various bioreactors configurations as function of RPM.

Note:

1. Enzymatic hydrolysis condition: 30 FPU/g cellulose, pH 4.8~5.0, 50°C.
2. Figure III-4a: Rushton impeller with or without baffles, Figure III-4b: baffled with Rushton or Marine impeller.
3. All data points given are the average yields for the duplicate determinations.

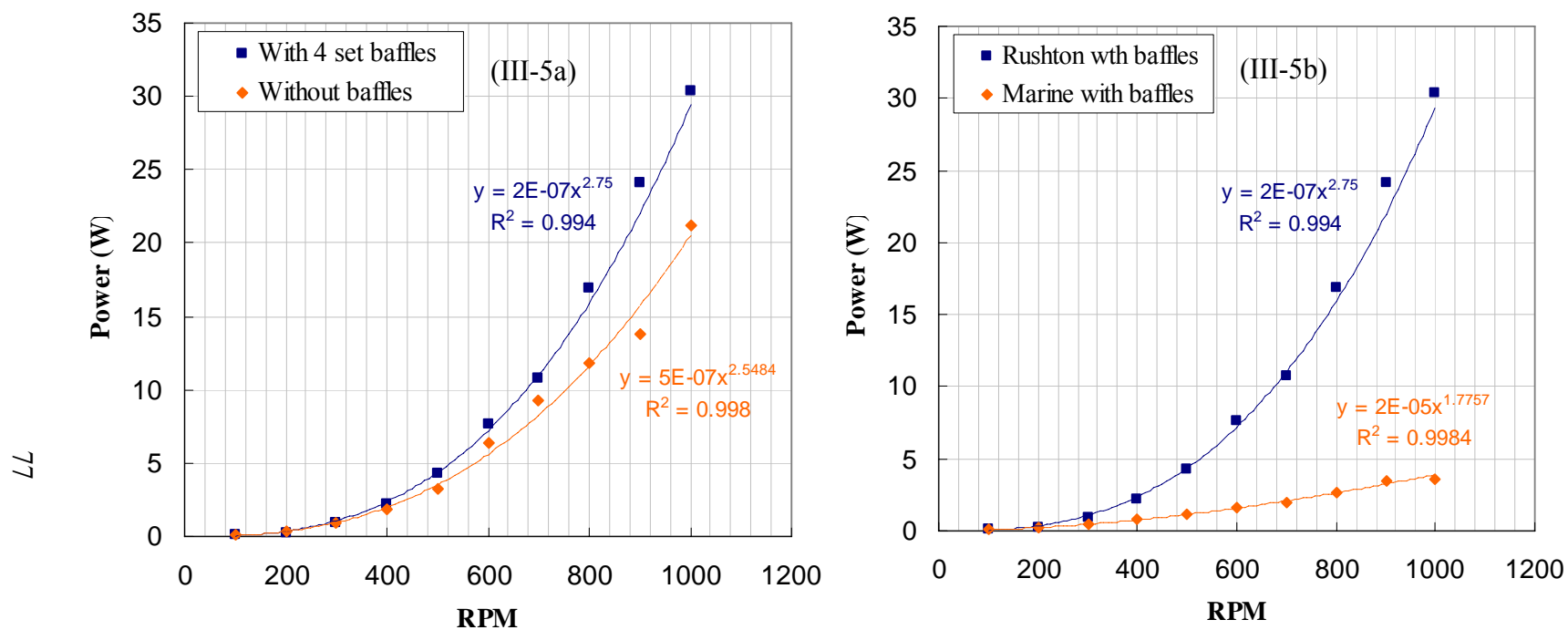


Figure III-5. Power consumption in two-liter bioreactor with 15 per cent (w/v) Solka Floc Suspension with various bioreactors configurations as function of RPM.

Note:

1. Enzymatic hydrolysis condition: 30 FPU/g cellulose, pH 4.8~5.0, 50°C.
2. Figure III-5a: Rushton impeller with or without baffles, Figure III-5b: baffled with Rushton or Marine impeller.
3. All data points given are the average yields for the duplicate determinations.

consumption result in the same trend as seen with Figure III-3. At an agitation speed of 900 rpm for Rushton bioreactor, power consumption is much higher than that of 5 per cent solid concentration. This result implies that fluid flow and power consumption increases with increasing viscosity. The 1000 rpm agitation speed required power inputs of 30 and 3.6 W for the baffled Rushton turbine and the baffled marine configuration, respectively. Figure III-5a shows the power consumption for the Rushton impeller with and without baffles, with the power required for the baffled configuration larger by 10 W at 15 per cent solids concentration.

These findings demonstrate the similarity of hydrodynamic effects caused by viscosity and baffles; both adding a resistance to flow. The effect is the same - more mechanical power must be introduced to the system to maintain fluid motion.

The Effect of Bioreactor Configuration on Bioconversion

The bioreactor was tested with a 4.6 cm diameter Rushton and 1.0 cm diameter marine impeller for glucose conversion, with or without wall baffles to give four bioreactor configurations: Rushton, baffled Rushton, marine, and baffled marine. The Rushton impeller had six blades; each blade was 1.0 cm (height) by 1.5 cm (width) by 0.05 cm (thickness). The marine impeller had three inclined curved blades of standard configurations. Each of four wall baffles was 17.5 cm (height) by 1.5 cm (width) by 0.05 (thickness). The substrate used for the hydrolysis studies was shown to be primarily composed of cellulose, since glucose constituted the majority of the sugars in the substrates (88 percent). Figure III-6 illustrates the effect of baffles on glucose conversion for a Rushton turbine and 5 and 10 per cent solids. Baffles become more

important for glucose conversion as the solids concentration increases. Figure III-7 shows the enzymatic digestibility (g released glucose/g initial cellulose) studies suggested by the NREL standard procedure for various reactor configurations at 5 per cent solids concentration. All of the portion methods are performed starting with 5 per cent solids concentration. The baffled Rushton bioreactor produced 10 per cent more glucose than the baffled Marine bioreactor (Figure III-3).

Mixing efficiency in a bioreactor for glucose and ethanol production is affected by various numbers of parameters such as baffles, impeller speed, impeller type, clearance, tank geometry, solubility of substance, and eccentricity of the impeller (Oldshue, 1983). A vortex is generated owing to centrifugal force acting on the rotating suspension. If the vortex reaches the impeller severe air entrainment occurs. The depth and the shape of the vortex depend on impeller and vessel dimensions, the rotational speed and the presence of baffles.

Figure III-8 show results of cellulose digestibility with and without baffles at relatively high solids concentration (13 and 15 per cent, w/v). As expected, baffled configurations gave higher glucose conversion than unbaffled configuration at 13 and 15 per cent solids concentration. In baffled tanks, a better concentration distribution throughout the tank and therefore improvement in the mixing efficiency is achieved to yield high glucose conversion at high solid substrates. In the unbaffled vessel with the impeller rotating in the center, centrifugal force acting on the fluid raises the fluid level at the wall and lowers the level at the shaft.

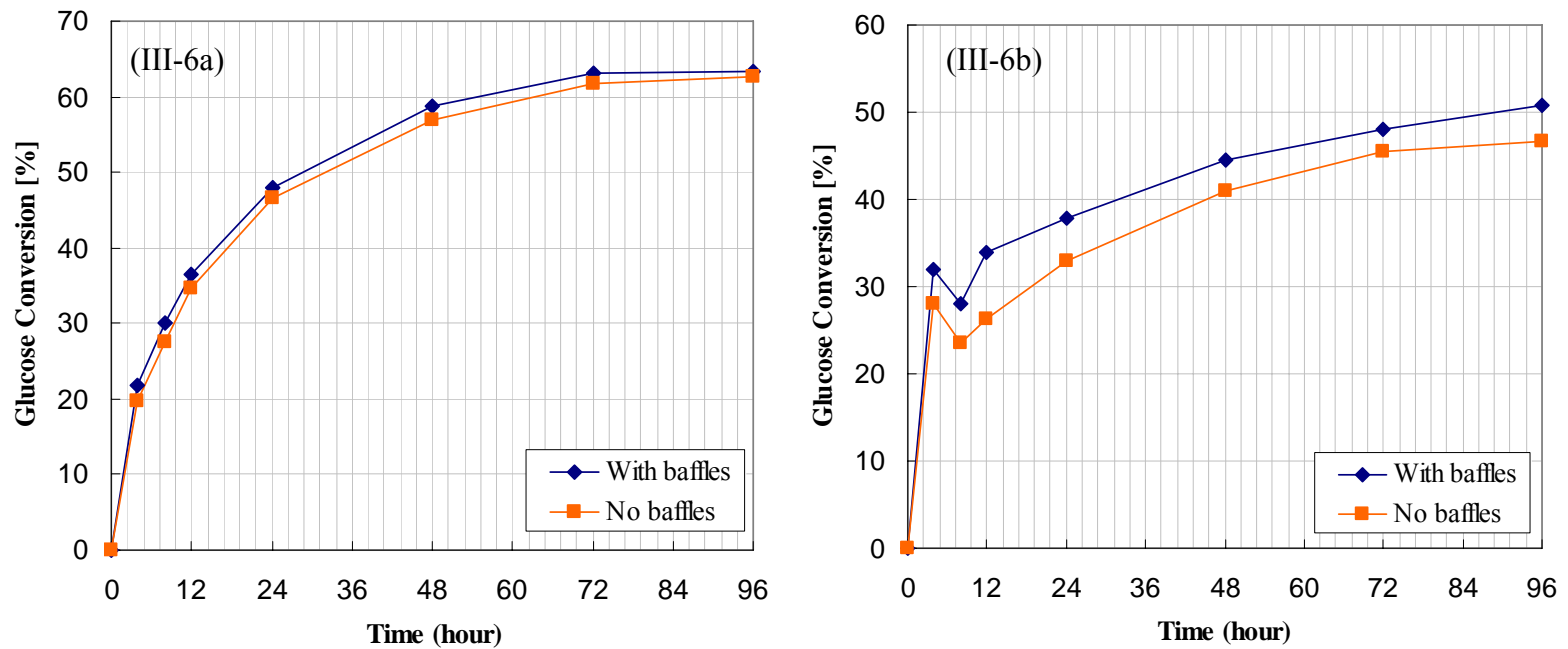


Figure III-6. The effect of baffles on glucose conversion of Solka Floc at 5 (III-6a) and 10 per cent (III-6b) solids concentration with a Rushton impeller as a function of time at constant cellulase activity.

Note:

1. Enzymatic hydrolysis condition: 96 hours, 30 FPU/g cellulose, pH 4.5 to 5.0, 50°C, 120 rpm.
2. Substrates were added to the reactions in one portion during fermentation up to 10 % final substrate concentration (III-6b)
3. All data points given are the average yields for the duplicate determinations.

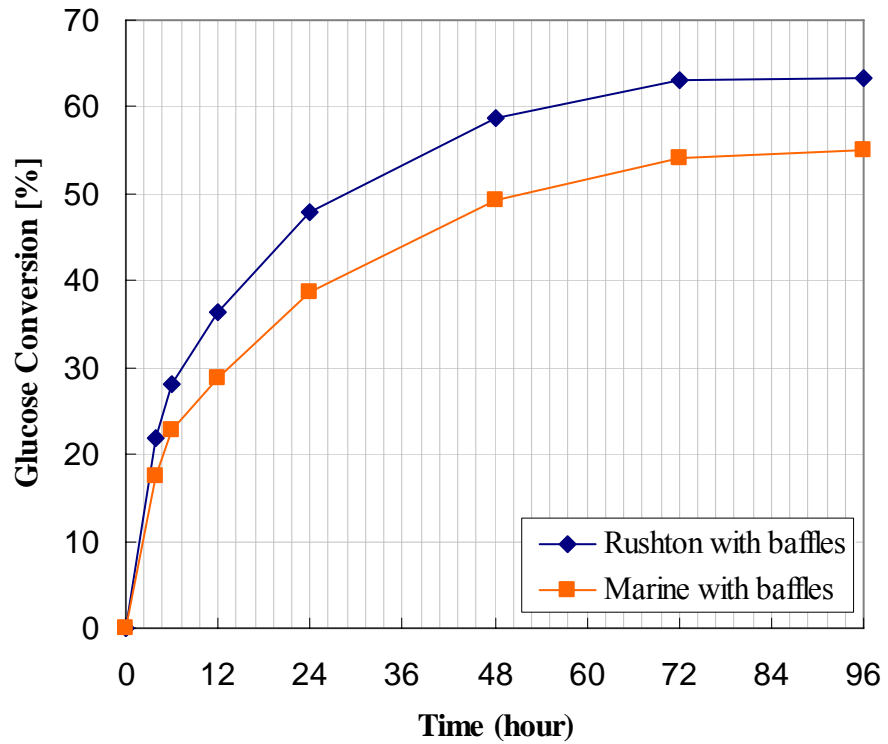


Figure III-7. The glucose conversion as a function of time for the two bioreactors: baffled Rushton and baffled Marine configuration at 5 per cent (w/v) Solka Floc.

Note:

1. Enzymatic hydrolysis condition: 96 hours, 30 FPU/g cellulose, pH 4.8 to 5.0, 50°C, 120 rpm.
2. All data points given are the average yields for the duplicate determinations.

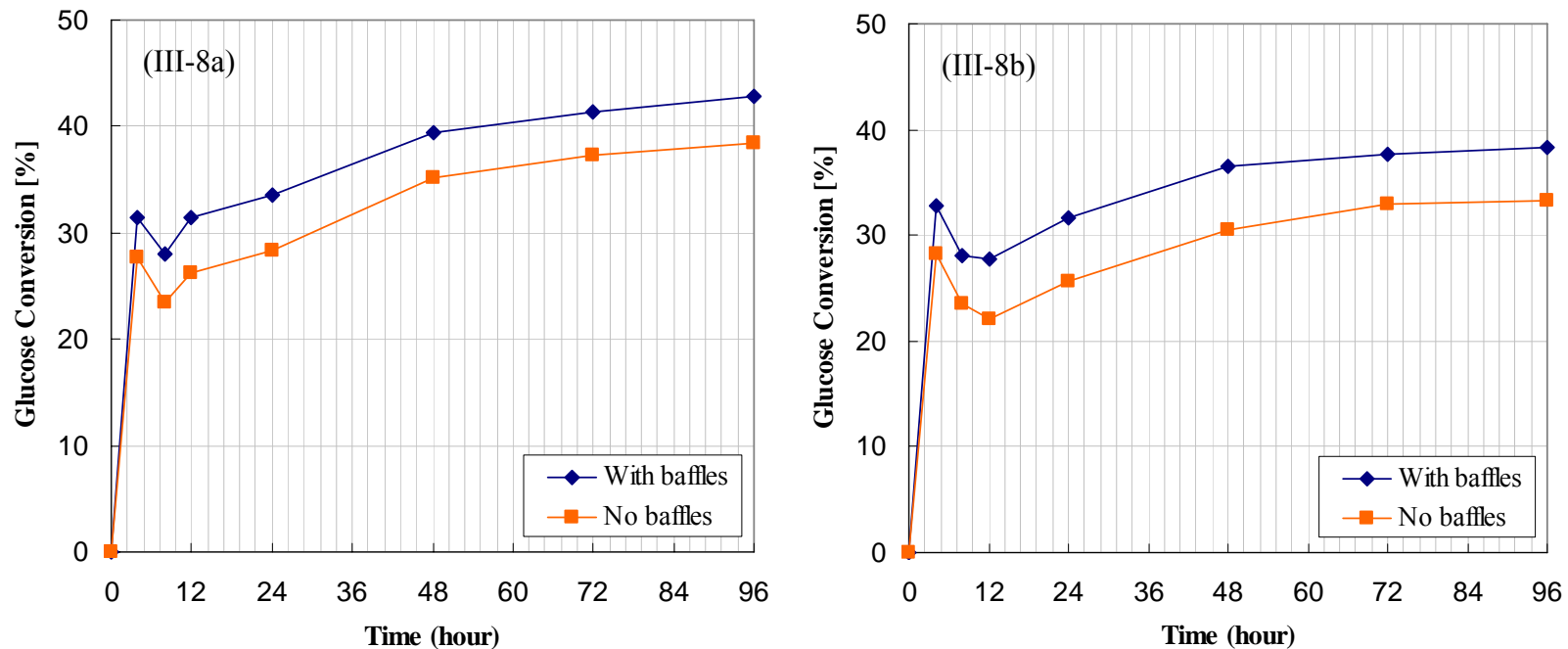
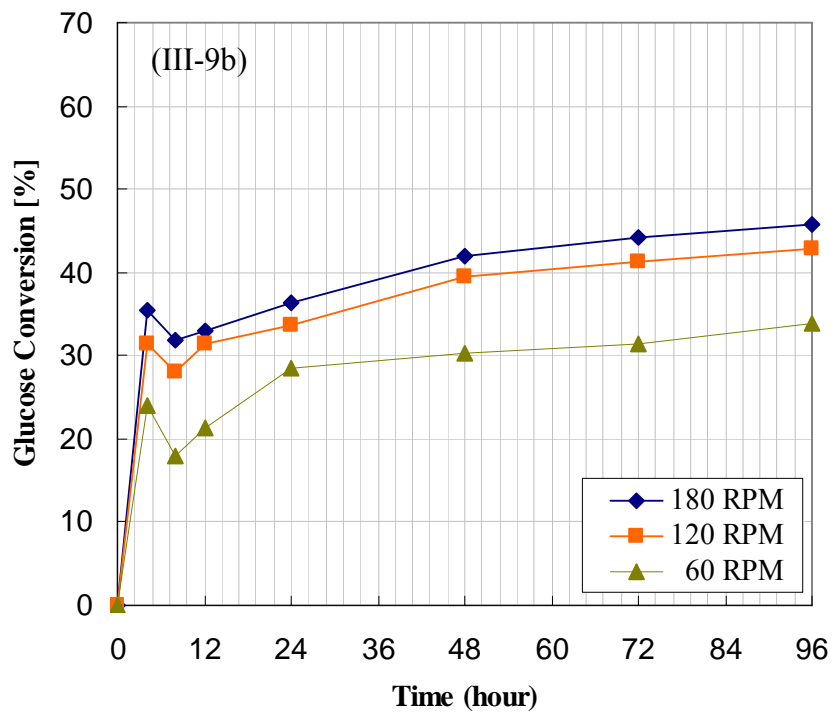
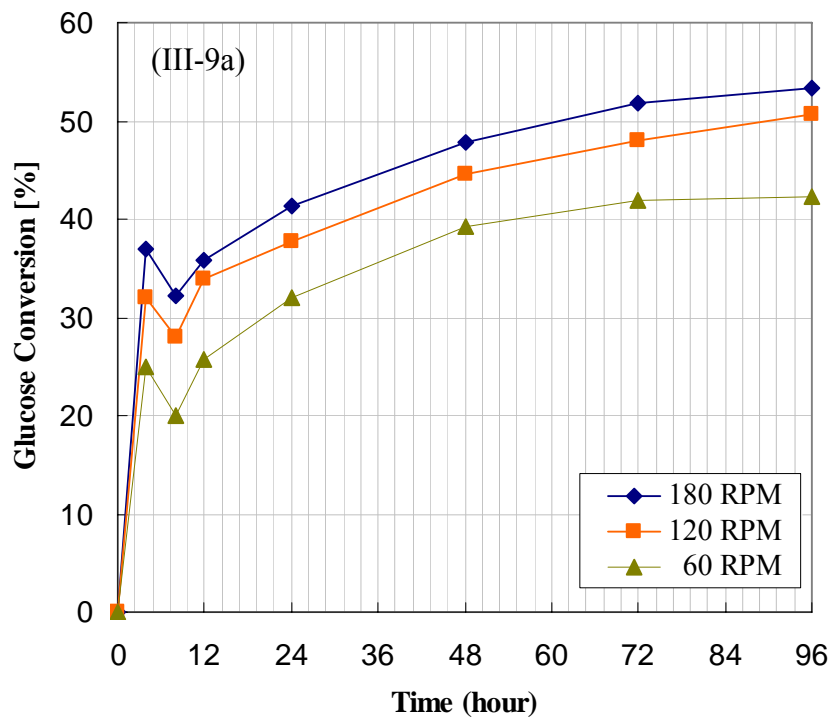


Figure III-8. The effect of baffles on glucose conversion of Solka Floc at 13 (III-8a) and 15 per cent (III-8b) solids concentration with baffled Rushton bioreactor as a function of time at constant cellulase activity.

Note:

1. Enzymatic hydrolysis condition: 96 hours, 30 FPU/g cellulose, pH 4.8 to 5.0, 50°C, 120 rpm.
2. Substrates were added to the reactions in two portions during enzymatic hydrolysis up to 13 % and 15 % final substrate concentration.
3. All data points given are the average yields for the duplicate determinations.



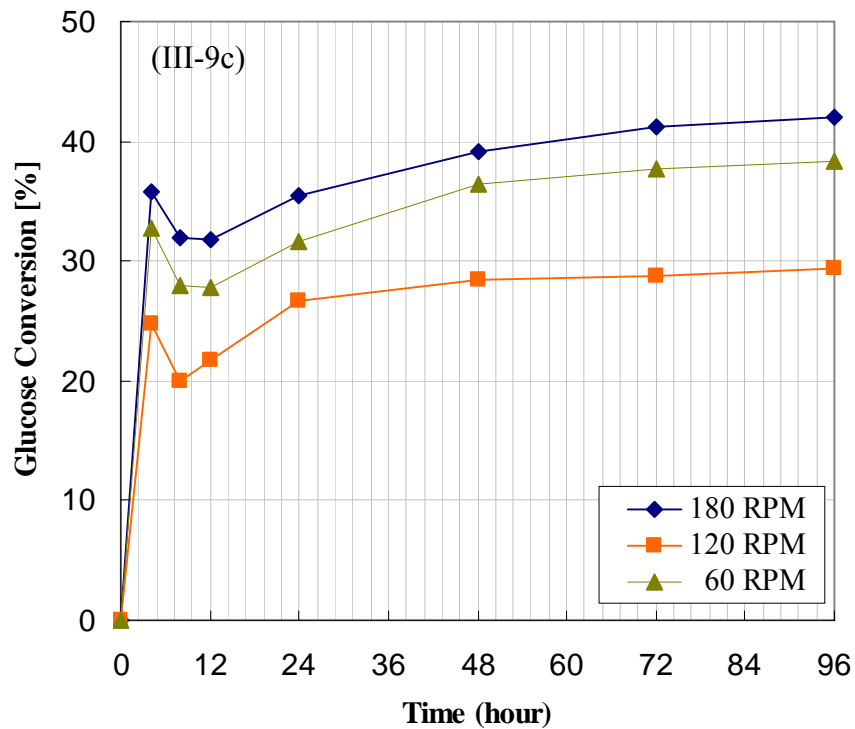


Figure III-9. The effect of RPM on enzymatic hydrolysis of Solka Floc at 10 (III-9a), 13 (III-9b) and 15 per cent (III-9c) solid concentration with baffled Rushton bioreactor as a function of time at constant cellulase activity.

Note:

1. Enzymatic hydrolysis condition: 96 hours, 30 FPU/g cellulose, pH 4.8 to 5.0, 50°C.
2. Substrates were added to the reactions in portions during enzymatic hydrolysis up to 10, 13, and 15 percent final substrate concentration.
3. All data points given are the average yields for the duplicate determinations.

The Effect of Rotational Speed on Glucose Yield

One important parameter in the current bioreactor design is the rotational speed of the impeller. Filamentous fungal fermentations in a stirred tank bioreactor usually experience the high apparent viscosity and the non-Newtonian broth behavior that can lead to the use of high agitation speed to provide adequate mixing and oxygen transfer in order to improve the cell and ethanol production rate. However, mycelial damage at high power input and rigorous agitation can limit the acceptable range of agitation speed. This damage is probably results from the higher shear rates present at the impeller tip. Therefore, the high rate of cell damage could lower growth and product formation (Amanullah et al., 2002; Li et al., 2000; Tamerler and Keshavarz, 1999).

Similarly, for enzyme suspensions in the stirred tank bioreactor, the rotational speed of the fibrous matrix influenced glucose conversion by cellulase. Due to the high shear rate around impeller, the higher rotational speed than 200 rpm could damage the enzyme and/or the *Zymomonas mobilis*. Therefore, the effect of rotational speed was determined at the levels of 60, 120, and 180 rpm at solid concentrations of 10, 13, and 15 per cent respectively. Figure III-9 shows the glucose conversion of the enzymatic hydrolysis at different rotational speeds at various solid concentrations. It was found that the rotational speed tested in this study did not greatly affect glucose yield between 120 rpm and 180 rpm; however, the increase in glucose productivity was observed at high rotational speeds (Figure III-9a, b, and c). It was also found that low rotational speeds (60 rpm) tested in this study did not appear to be sufficient to produce contact between the substrate and the enzyme. Consequently, conversion yields were 5 to 10 percent lower than those obtained under 120 and 180 rpm. There was no significant

difference in conversion for various rotational speeds at relative low solid concentration. This result was probably due to the substantial decrease in the viscosity of the reaction mixture and better interaction between the enzymes and the remaining substrates. In addition, Figure III-9 shows profiles for rotational speeds. Tests revealed no significant effect of mixing speed in the range 120 to 180 rpm on the glucose conversion after 96 hours. Low power inputs for mixing are therefore possible. Thus, in this project, a rotational speed setting of 120 rpm was selected for ethanol fermentation and CFD simulation. This result suggests that a threshold value of the rotational speed (mass transfer related) has to be achieved for efficient glucose conversion.

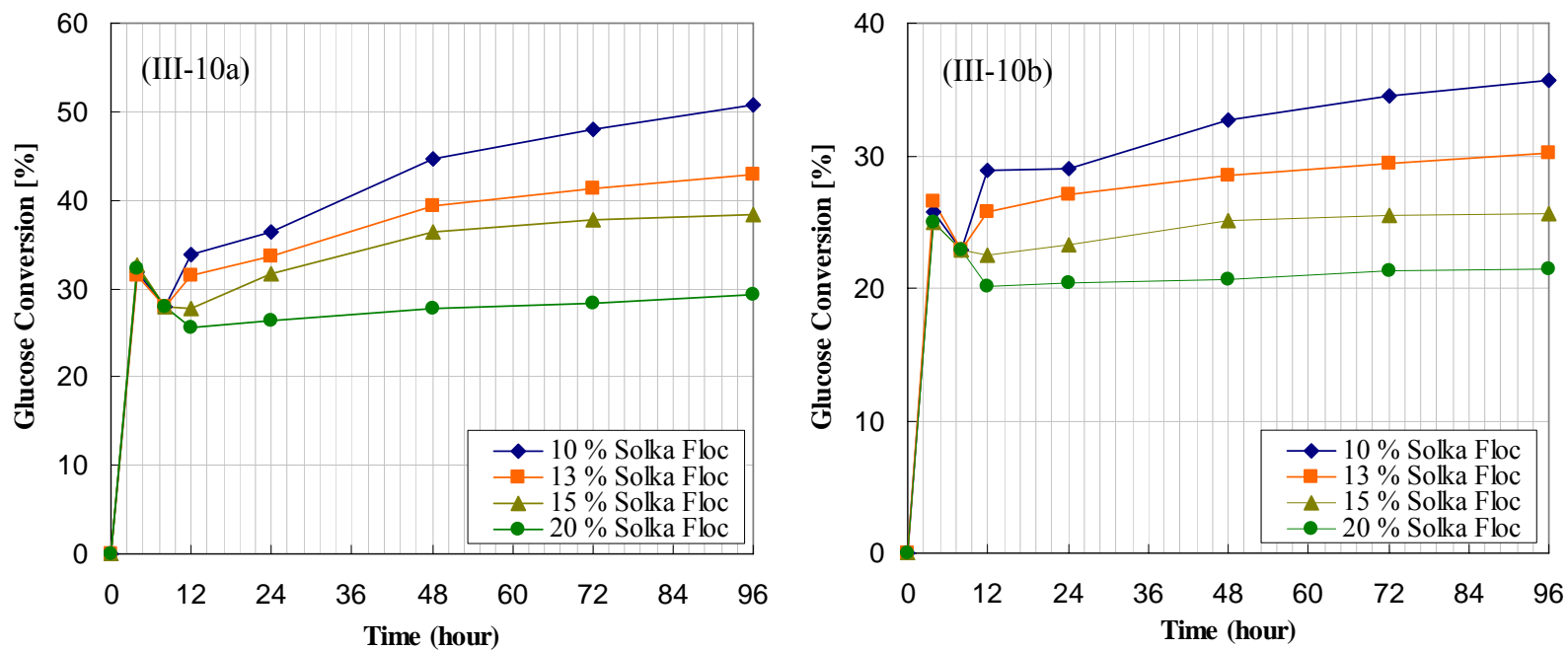


Figure III-10. The enzymatic hydrolysis for the baffled Rushton turbine (III-10a) and the marine propeller (III-10b) as a function of time at constant cellulase activity.

Note:

1. Enzymatic hydrolysis condition: 96 hours, 30 FPU/g cellulose, pH 4.8 to 5.0, 120 rpm.
2. Substrates were added to the reactions in portions during enzymatic hydrolysis up to 20 percent final substrate concentration.
3. All data points given are the average yields for the duplicate determinations.

High-Solids Saccharification by Portion Loading

To improve process economics of the lignocellulosic biomass to ethanol process, a bioreactor system for enzymatic saccharification at high solids concentrations was developed. The saccharification was performed in a three-liter bioreactor (New Brunswick Scientific Co. Inc., Edison, New Jersey) with a baffled Rushton turbine and a baffled marine propeller. As discussed in the material and method section, substrates were added to the reactions in portions during enzymatic hydrolysis up to 20 percent (w/v) final substrate concentration.

During batch system saccharification in bench scale fermentor, the solids concentration is one of the most important variables affecting the rate and extent of conversion. Figure III-10 shows the effects of Solka Floc solids loading on rates and extent of glucose conversion for increasing solids levels with two different reactor configurations at the constant enzyme loading. From the data shown in Figure III-10a for the 30 FPU/g cellulose loading, it is apparent that increasing the solids loading up to 20 percent (w/v) significantly decreases the rate of hydrolysis and the conversion of glucose. The most likely reasons for this decrease in rate and conversion are a combination of cellobiose and glucose inhibition of the enzyme system from the correspondingly higher sugar levels reached using higher solids and mass transfer limitations. Specifically, in case of mass transfer, a relatively weak axial flow was found near the center bottom of the tank and below the baffle from CFD simulation.

Figure III-10a shows that for all cases presented, glucose concentrations in the liquid phase greater than 41 g/L are achievable, and, for the case of 20 per cent solids, over 50 g/L of glucose is attained after 48 hours. However, higher solids loadings

require significantly longer residence times to achieve these high liquid phase sugar levels. As in previous work (Um, 2002), the effect of glucose on β -glucosidase activity is the most important inhibition concern, and this can become the ultimate rate limiting step when glucose accumulates to very high levels. At 20 per cent solids concentration, the glucose digestibility is lower than at 10 per cent solids concentration, indicating that mixing limitations for this level of solids has become a significant factor in addition to glucose inhibition. On average, the baffled Rushton bioreactor had higher glucose conversion than baffled marine configuration by as much as 15 per cent (Figure III-10b).

Most importantly, this work also demonstrates that cellulose conversions greater than 20 percent can be achieved at initial insoluble solids levels as high as 20 percent by portion loading method. No continuous liquid phase exists at a concentration of 20 per cent in the bioreactor without portion method. Shear stress is 10 times higher than that of 20 per cent loaded by portion method (Appendix Table B-7). This result indicates that flowability depends on the presence of a continuous liquid phase.

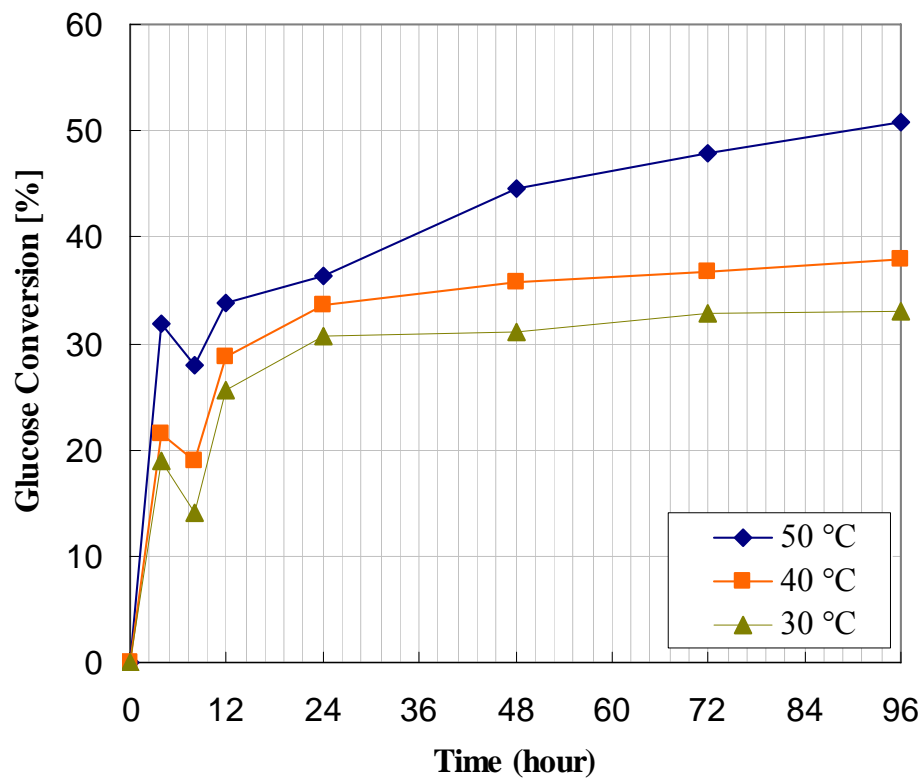


Figure III-11. The effects of temperature on high solid enzyme hydrolysis.

Note:

1. Enzymatic hydrolysis condition: 96 hours, 30 FPU/g cellulose, pH 4.8 to 5.0, 120 rpm.
2. Substrates were added to the reactions in portions during enzymatic hydrolysis up to 10 per cent final substrate concentration.

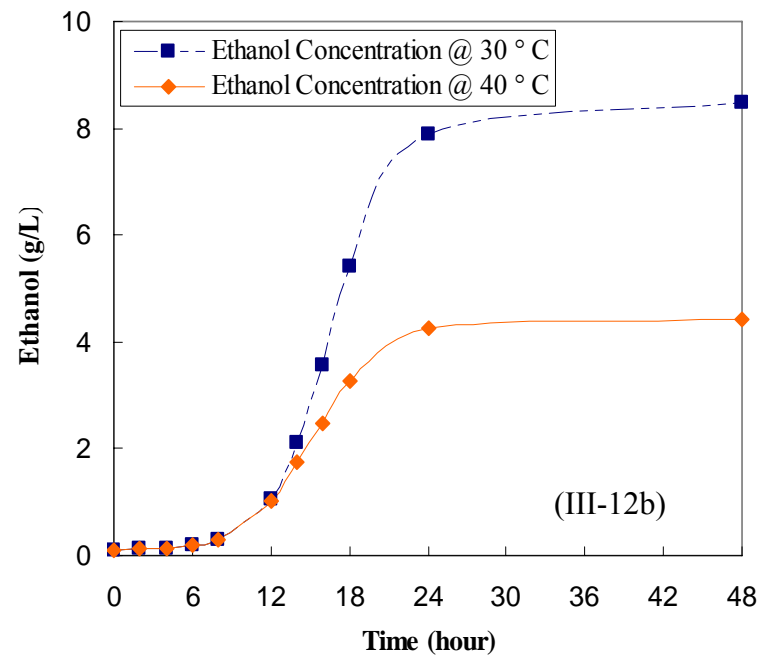
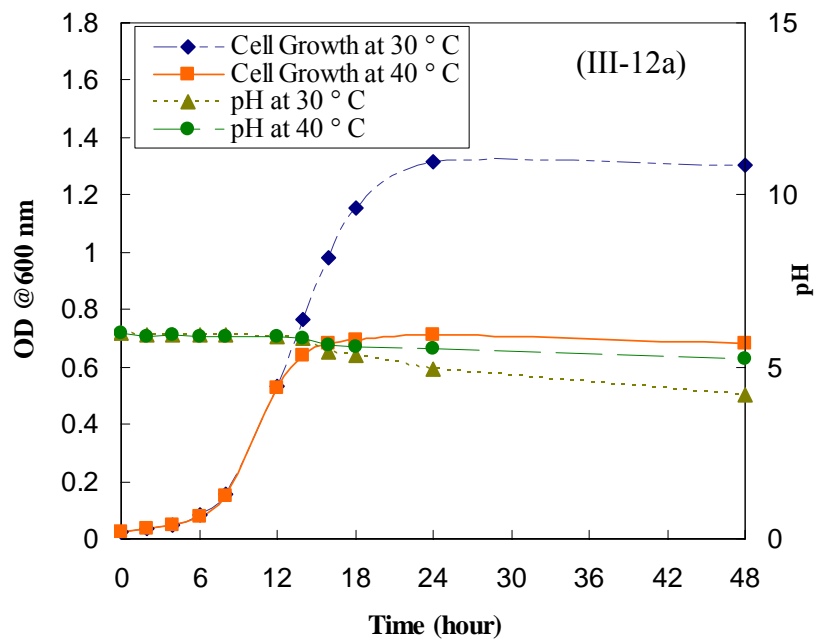


Figure III-12. The effects of temperature on cell growth curve and ethanol production.

Note:

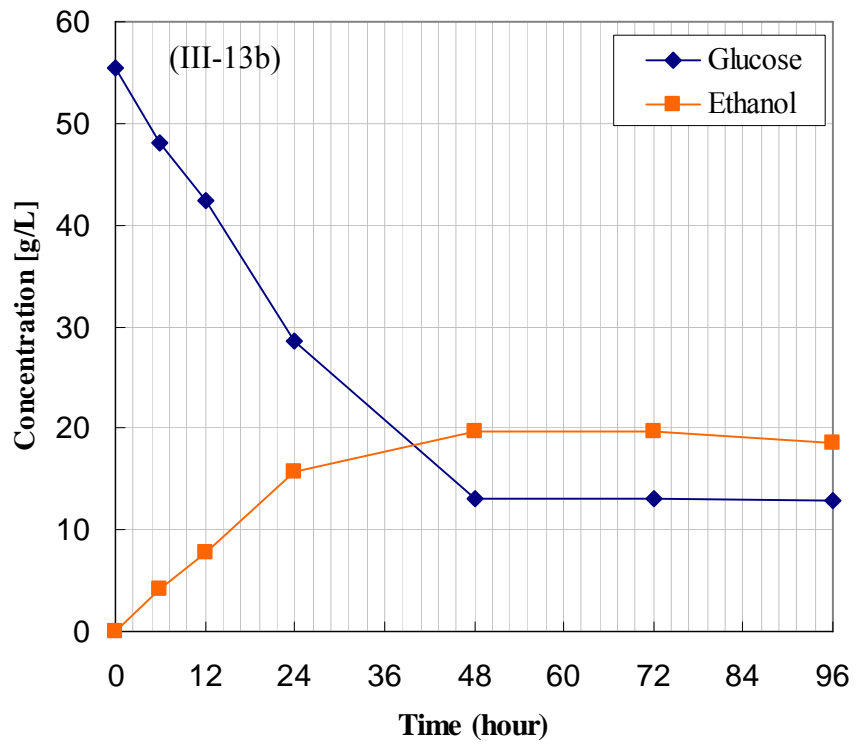
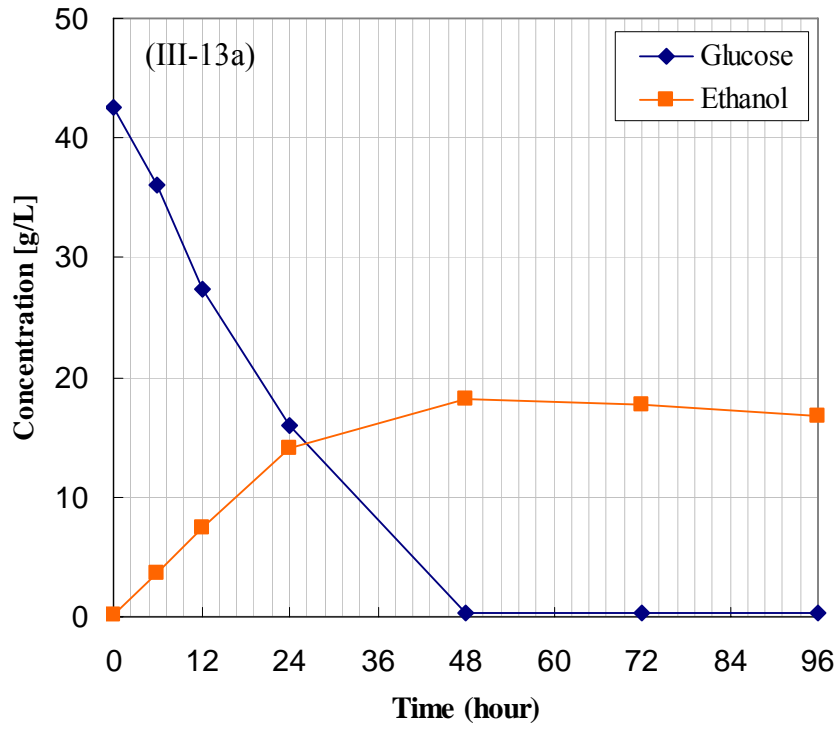
1. Yeast extract = 0.1 g/L, KH_2PO_4 = 0.02 g/L, DI water = 9 mL, 20 per cent glucose stock solution = 1 mL, and *Zm. mobilis* = 5~10 colonies: RM liquid for growing bacterial in 10 mL solution.
2. All data points given are the average yields for the duplicate determinations.

The Effects of Temperature on High-Solid Bioconversion

Operating temperature is another significant parameter that strongly affects enzyme stability as well as bacterial activation on enzymatic hydrolysis and fermentation. For SFF process, it is necessary to compromise with a temperature that is tolerable for microbial fermentation but still provides a reasonable hydrolysis rate. Figure III-11 shows the effect of temperature on enzyme reaction with a baffled Rushton turbine for 10 per cent (w/v) initial insoluble solids. By comparing the conversion profiles for the 50°C, 40°C and 30°C experiments, it is clear that long-term exposure to a temperature of 30°C and 40°C does not result in activation of enzymes as has been previously suspected. For a baffled Rushton bioreactor, operation at 30°C (the temperature that *Zm. mobilis* SSF is typically performed) decreases the conversion of glucose by nearly 20 per cent relative to conversion at 50°C.

To investigate the effect of temperature on cell growth mode, cell density and ethanol concentration were examined in stationary cultures for 48 hours at 30°C and 40°C. Figure III-12 shows the optical density of the cells, the pH curve, and ethanol concentration. From the figures, it is clear that the temperature for bacterial fermentation is a major factor affecting the rate of cell growth as might be supposed. The maximum ethanol concentration for the specific cell growth rates is comparable to those from Figure III-12 - approximately 8 g/L and 4 g/L for the temperature of 30°C and 40°C respectively. Figure III-12a demonstrates that the value of pH decreased with increasing the rate of cell growth curve.

An important consideration for the cell growth results is that at 40°C, the microorganism failed to ferment glucose to ethanol. The ethanol concentration was



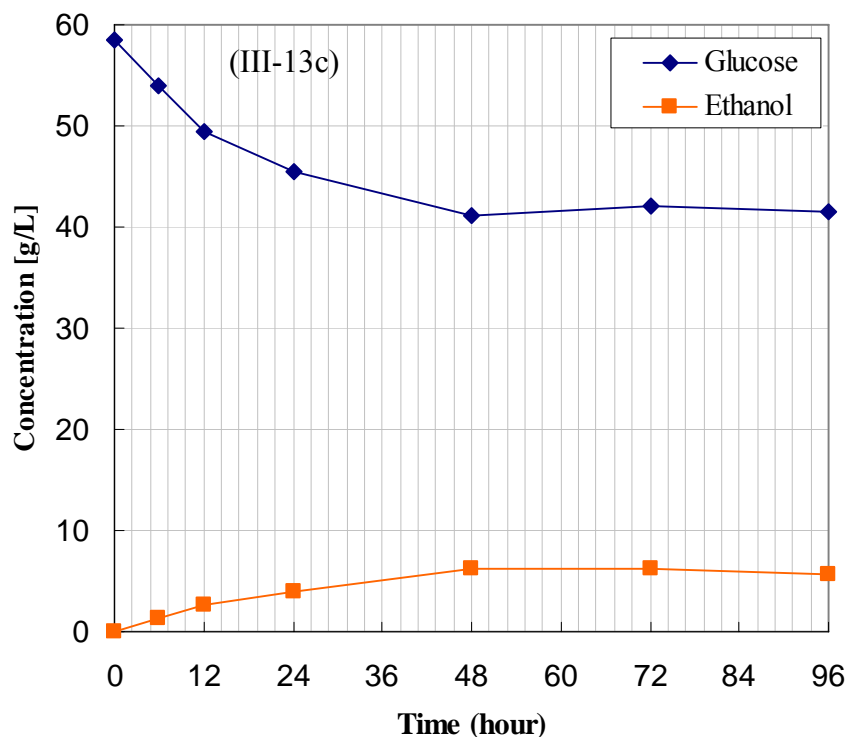


Figure III-13. The time course of substrate utilization and ethanol production by *Zymomonas mobilis* at 10 % (III-13a), 15 % (III-13b), and 20 % (III-13c) solid concentration with a Rushton impeller as a function of time at constant cellulase activity.

Note:

1. Enzymatic hydrolysis condition: 48 hours, 30 FPU/g cellulose, pH 4. to 5.0, 50°C.
2. Cell transfer after 48 hours, Initial OD₆₀₀ 0.52.
3. Fermentation condition: 96 hours, *Zymomonas mobilis* (39679:pZB4L), pH 5.0, 30°C.
4. Substrates were added to the reactions in portions during enzymatic hydrolysis up to 20 % final substrate concentration.
5. All data points given are the average yields for the duplicate determinations.

decreased by nearly 50 per cent relative to 30°C after 2 days.

The Effect of Substrate Concentration on Ethanol Yield

In several studies it was found that for conventional fermentation of lignocellulosic biomass, the content of solids is initiated to about 10 per cent, resulting in a maximum ethanol concentration of 4 per cent (v/v). However, if higher solids levels could be fermented, it might be possible to achieve higher ethanol concentration reducing downstream cost (Varga, et al., 2004; Mohagheghi et al., 1992; Spindler et al., 1988). SFF baffled Rushton bioreactors were operated in the three-liter fermentor after enzymatic hydrolysis (after 48 hours) using a maximum 20 per cent DM, corresponding to cellulose concentration 17 percent. As previous mentioned, to avoid poor mass and heat transfer, the substrate was added to the reaction in three portions during enzymatic prehydrolysis up to 20 per cent final substrate concentration. The portion was added to the hydrolysis in four-hour intervals (Figure III-2). The rate of enzymatic hydrolysis after four hours was dramatically high, thus the initial five percent substrate was sufficiently liquidized to allow the loading of another 5 per cent substrate (Figure III-1).

The effect of substrate concentration on the ethanol yields at 96 hours SFF using Solka Floc is shown in Table III-2 and Figure III-14. Figure III-13 shows that the time course of substrate utilization and ethanol production by *Zymomonas mobilis* at 10 (III-13a), 15 (III-13b), and 20 percent (III-13c) solid concentration with Rushton impeller as a function of time at constant cellulase activity. Increasing the DM content to 20 percent, the ethanol yield was dramatically reduced at a substrate concentration of 20 per cent DM compared to 10 and 15 per cent solid concentration, which is probably due to insufficient

Table III-2. Ethanol yield and conversion (%) for *Zm. mobilis* after 48hours

	10 %	15 %	20 %
Initial glucose after enzyme reaction (g/L)	42.6	55.5	58.4
Final ethanol concentration at 48 hours (g/L)	18.2	19.7	6.3
Conversion of the consumed glucose to ethanol (%)	83.6	73.4	21.8
Theoretical ethanol yield (%)	80.5	68.6	19.1
Total Fermentation time with portion method (hours)	106	110	114

mass transfer caused by different viscosity and flow patterns for those concentrations.

At relatively high substrate concentrations the enzymes could not liquefy the cellulose fibrous material, and a low enzyme reaction rate resulted in low ethanol yields of nearly 21 percent. The maximum ethanol yield of 83 percent was achieved at 10 per cent solid concentration after 48 hours. However, the ethanol yields were also favorable at 73 percent, using 15 percent solid concentration.

Figure III-14 further shows that at a 30 FPU/g cellulose enzyme loading at 40°C which was chosen to overcome incompatible temperature during SSF, the process provides no significant improvement in either rate or extent of conversion over high solids Solka Floc. An important consideration for the SSF results is that at 40°C the microorganism failed to ferment glucose to ethanol at reasonable pH (~5.0) after 4 days. The ethanol yields were below 10 per cent relative to all of substrate concentration.

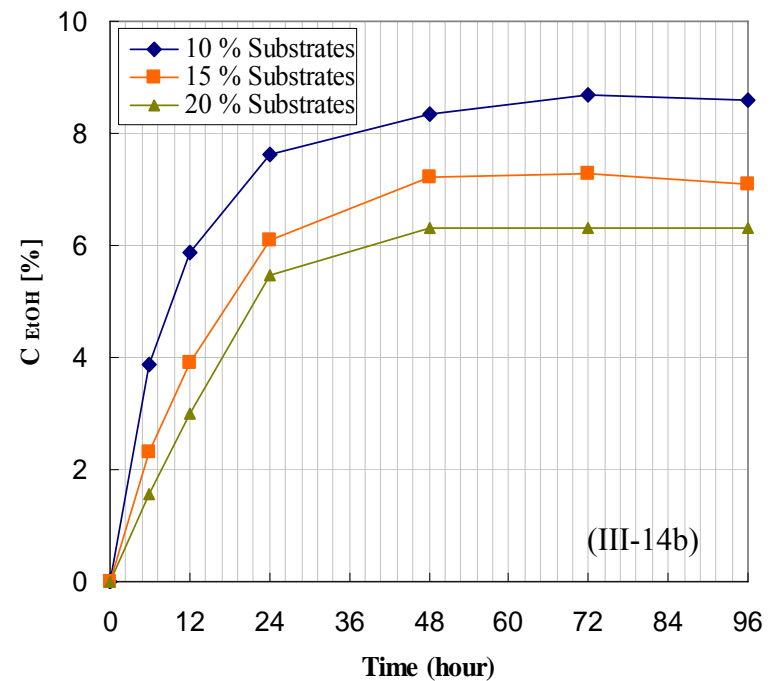
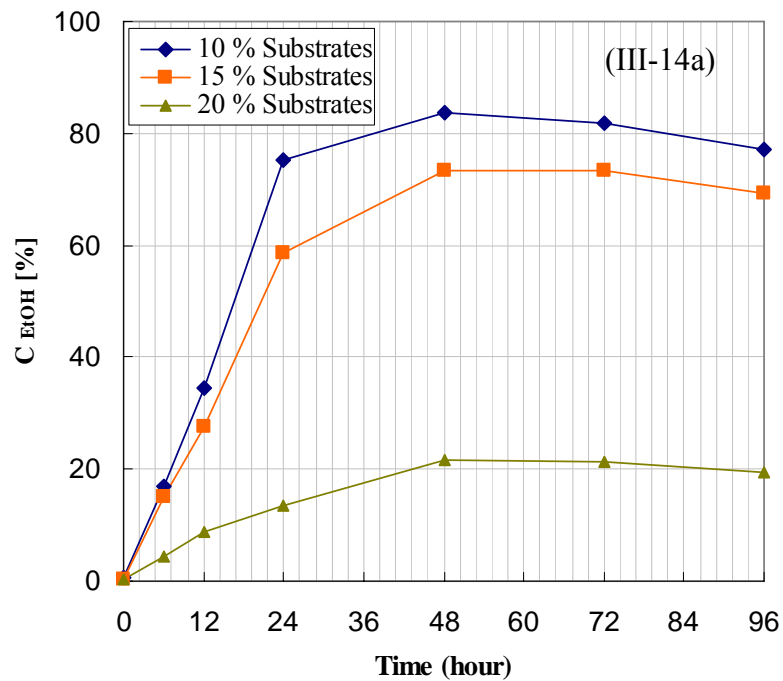


Figure III-14. The ethanol conversion yield (C_{EtOH}) with Rushton impeller as a function of retention time during SFF at 30°C (III-14a) and 40°C (III-14b) with 10, 15, and 20 percent substrate concentration and constant cellulase activity. Note: same as condition of Figure III-13.

CONCLUSIONS

This project demonstrated a number of important novel conclusions related to high solids saccharification following fermentation systems. First, critical to the design and optimization of agitated bioreactor processes is understanding and assessing the effect of reactor configuration on glucose and ethanol production. In this investigation, high-solids enzymatic saccharification was performed under a two liter working volume in various bioreactor configurations. At 120 rpm, reactors with Rushton impellers achieved much higher concentrations of glucose when compared to marine impellers. The result of enzymatic hydrolysis indicated that wall baffles significantly increased digestibility in the Rushton bioreactor but not in the marine bioreactor. Therefore, the baffled Rushton bioreactor should be used for high-solid bioconversion process.

Second, it was demonstrated that sugar inhibition of enzymatic saccharification rates is not as compelling a concern as had previously been suspected, and that remarkably high concentrations of glucose are achievable in high solids enzymatic reactions. Besides sugar inhibition, other parameters including bioreactor configuration and temperature were identified as important for high-solids enzymatic saccharification. This remarkable improvement in rate, in addition to the high product concentrations, has the potential to greatly improve the economics of enzymatic saccharification.

Most importantly, this project also demonstrated that glucose concentration and ethanol conversion was greater than 50 g/L and 20 per cent at 20 per cent solid concentration respectively, which is likely due to adopting an optimal substrate loading strategy.

The portion loading method provides a feasible method for fermenting cellulosic material while avoiding mass transfer limitation at higher solids loading. In traditional batch fermentation, there is visually no continuous liquid phase at concentrations of 20 per cent in the bioreactor, which is likely due to complete absorption of liquid by the biomass before reacting between microorganism and substrates.

An additional observation from this work is that it is important to keep this fermentation anaerobic, even though increased cellulosic biomass concentration is desirable in SFF process. Small amounts of acetate and glycerine are produced. If oxygen is introduced to the reaction, the production of acetate and glycerine increases, thus decreasing the purity of the desired ethanol product.

IV. RHEOLOGICAL PARAMETER DETERMINATION FOR ENZYMATIC SUSPENSIONS AND FEMENTATION BROTHS WITH HIGH SUBSTRATE LOADING

ABSTRACT

Traditionally, as much as 80 percent or more of an ethanol fermentation broth is water that must be removed. This mixture is not only costly to separate, but also produces a large aqueous stream that must then be disposed of or recycled. Integrative approaches to water reduction include increasing the biomass concentration during fermentation.

In this paper experimental results are presented for the rheological behavior of high-solids enzymatic cellulose hydrolysis and ethanol fermentation for biomass conversion using Solka Floc as the model feedstock. The experimental determination of the viscosity, shear stress, and shear rate relationships of the 10 to 20 per cent slurry concentrations with constant enzyme concentrations are performed with a variable speed rotational viscometer (2.0 to 200 RPM) at 40°C and combined temperature (50°C, 30°C) for the initial four hours. The viscosities of enzymatic suspension observed were in range of 0.0418 to 0.0144, 0.233 to 0.0348 and 0.292 to 0.0447 Pascal-seconds for shear rates up to 100 reciprocal seconds at 10, 15, and 20 per cent initial solids (w/v), respectively.

The average particle size during the enzymatic treatment and fermentation process of Solka Floc at 40 °C and combined temperature (50 to 30°C) was approximately 57.8 to 70.0 µm, and 44.0 to 57.5 µm for the SSF and SFF process at 10, 15, and 20 per cent initial solids (w/v), respectively.

A recombinant strain of *Zymomonas mobilis* (39679:pZB4L) was used in saccharification following the fermentation (SFF) process varying the initial concentration of Solka Floc. The viscosities of fermentation broth observed were in range of 0.024 to 0.028, 0.401 to 0.058, and 0.840 to 0.087 paschal-seconds for shear rates up to 100 reciprocal seconds at 10, 15, and 20 per cent initial solids (w/v), respectively.

The fluid behavior of the suspensions and broth slurries in *Zymomonas mobilis* ethanol fermentation was modeled using the power-law, the Herschel-Bulkley, the Casson, and the Bingham model. The results showed that broth slurries were pseudoplastic with a yield stress. The model slope increased and the model intercept decreased with increasing fermentation time at shear rates normal for the fermentor. The broth slurries exhibited Newtonian behavior at high and low shear rates during initial SFF process.

INTRODUCTION

Production of fuel ethanol from lignocellulosic biomass has the potential to reduce world dependence on petroleum while decreasing net emissions of carbon dioxide, the principal greenhouse gas. There continues to be times, however, when ethanol cannot compete economically with gasoline or petroleum derivatives of fossil fuels. The opportunity therefore exists for process improvements in the conversion of biomass to fuel alcohol that will result in more favorable production economics. High solid loading fermentation is one such process improvement aimed at increasing both the rate of fermentation and the final ethanol concentration and thereby reducing processing costs (Ingledeu, 1993). Positive economic advantages associated with a high-solids saccharification process over a conventional low solids process include: lower capital costs due to the reduced volume; lower operating costs due to less energy required for heating and cooling; lower downstream processing costs due to higher product concentrations; reduced disposal and treatment costs due to lower water usage (Mohagheghi *et al.*, 1992).

Understanding rheology of concentrated biomass slurries is important for designing equipment and predicting process performance. Specifically, shear rate of the flow in a mixing tank is an important parameter controlling many important industrial processes. Fundamentally, shear rate affects processes involving mixing of Newtonian and non-Newtonian fluids, generating/dispersing liquid/liquid droplets, and producing fine gas bubbles for gas-to-liquid mass transfer.

Stirred tanks are usually used for the thermo-chemical fermentation. To simulate flow of Solka Floc slurries in stirred tanks, the rheological properties of these

suspensions must be known. This high-solids slurry definition can be regarded as the solids region where the slurry viscosity is highly non-Newtonian at approximately 12 to 15 per cent insoluble solids (Pimenova and Hanley, 2003). The corn stover slurries in stirred tank reactors typically range from 10 to 40 percent solids (Ranatunga et al., 2000).

The overarching goal of this work is to investigate high-solids saccharification following fermentation for biomass conversion using Solka Floc as the model feedstock. The immediate objectives are to understand the high-solids SFF process, which is expected to reduce both the risk and cost of enzyme and microorganism based process technology. This subtask has two distinct but related efforts:

- to understand the rheology and mixing characteristics of high-solid fermentation broths and
- to understand the performance of enzymatic cellulosic saccharification at high solids loadings.

The primary objective of this study is to investigate the rheological behavior of high-solids Solka Floc slurries and the particle size distribution during ethanol fermentation, and to fit an appropriate model on the experiment data. Additionally, the present findings can be applied to bioreactor design using computational fluid dynamics.

MATERIALS AND METHODS

Suspension Fluids used for Measurements

The fermentation fluids and enzyme hydrolysis suspensions used in this research were obtained from the cultivation of *Zymomonas mobilis* and Spezyme CP (Novozyme 188) respectively. The composition of the culture medium, enzyme suspension, and their reaction conditions were the same as outlined in a previous section chapter III.

Viscometer

The viscosity of the suspension at different biomass concentration was measured by Modular Compact Rheometer Physica MCR 300 (Paar-Physica). Controlled shear-stress measurements were done using concentric cylinder system with FL 100/6W impeller at two different temperatures of 30, 40, and 50°C respectively. The sample with desirable concentration was prepared and homogenized prior to measurements. Then an appropriate volume was placed into the viscometer and was left for few minutes to allow the temperature to stabilize. Then, rheological measurements were done three times for each value of biomass concentration using always a fresh sample.

Concentric Cylinder System

The system consists of a stationary outer cylinder with the radius $R_a=15$ mm and a rotational inner cylinder with $R_i=10$ mm. The cylinders are separated by the gap $R_a-R_i=5$ mm into which the sample is introduced (Figure IV-1). The length of the inner cylinder is $L_c=16$ mm. By the rotation of the inner cylinder with the torque M , the sample in the gap is sheared and the angular velocity ω is measured. Using M , ω , and

the geometry of the system, the shear stress τ and the shear rate $\dot{\gamma}$ can be determined

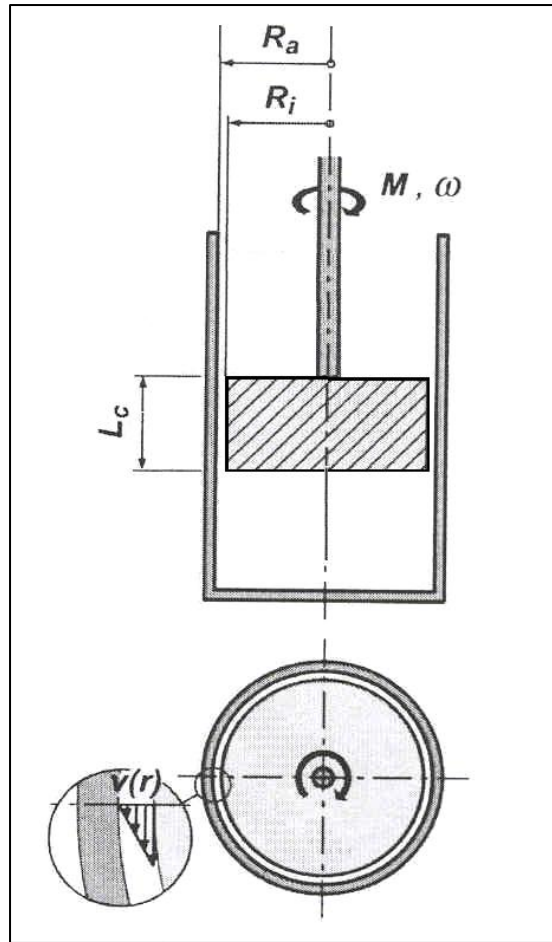


Figure IV-1. Scheme of concentric cylinder (Stirrer FL 100/6W) system of Paar Physica modular compact rheometer (MCR 300).

Model equations:

$$\tau = \frac{M}{2 \cdot \pi \cdot L_c \cdot R_i^2} \quad \dot{\gamma} = \frac{2 \cdot R_a^2}{(R_a^2 - R_i^2)} \cdot \omega$$

Measurement of Particle Size

All particle size analyses performed on the Mastersizer S (Malvern Instruments Ltd., Malvern, U. K) using the magnetically stirred cell or the small volume sample dispersion unit which must have a liquid phase to carry the material to be tested. The Malvern Mastersizer-S is based on the principle of laser ensemble light scattering. It is categorized as a non-imaging optical system, as sizing is accomplished without forming an image of the particle on a detector. For analysis, each sample was diluted approximately 500-fold in tap water, and the mean value between the low and high particle sizes for a given channel were used (range: 0.01 to 1000 μm) before being analyzed 10 times. These results were then averaged to produce the particle size distribution.

Calculation of Power Law Parameters

The power law parameters were calculated from concentric cylinder system with FL 100/6W impeller data for the non-Newtonian calibration fluids for comparison purposes. The parameters were calculated from impeller data of the Solka Floc suspensions for comparison to published data. A linear regression analysis was performed on the log of viscosity and log of shear rate data for the non-Newtonian fluids and the Solka Floc slurries. The consistency index constant, K , was calculated from the intercept of the regression analysis and the index number, n , was calculated from the slope.

Yield Stress

Yield stress is defined as the shear stress that has to be applied before the material starts to flow. Nguyen et al. (1992) indicated that the yield stress can be measured by either direct or indirect methods. Indirect methods consist of either using rheological models to fit the shear stress-shear rate experimental data or extrapolating the shear stress-shear rate data to a zero shear rate. Indirect determination of the yield stress involves extrapolation of the experimental shear stress-shear rate data to obtain the yield value as the shear stress limit at zero rate of shear. The extrapolation is performed numerically on the available data, or the latter can be fitted to a suitable rheological model representing the fluid and the yield stress parameter in the model is determined.

The direct method involves shearing a fluid in a rotational viscometer at a low and constant shear rate and measuring the shear stress as a function of time. The stress versus time (or shear strain) response typically consists of an initially linear portion indicating elastic solid behavior, followed by a nonlinear region, a stress overshoot, and a stress decay region (Nguyen et al., 1992). A more convenient extrapolation technique is to approximate the experimental data with one of the viscoelastic flow models. The Bingham model postulates a linear relationship between τ and $\dot{\gamma}$. However, this model can lead to unnecessary overprediction of the yield stress. Extrapolation by means of the nonlinear Casson model is straightforward from a linear plot of $\tau^{1/2}$ versus $\dot{\gamma}^{1/2}$. The application of the Herschel-Bulkley model is more tedious and less certain although systematic procedures for determination of the yield value and the other model parameters are available.

RESULTS AND DISCUSSION

High solids saccharification and fermentation are difficult due to the challenging rheological characteristics of high-solid biomass slurries that can cause non-uniform heat and mass transfer. In addition, dynamic changes in rheology and biomass properties occur as the cellulose structure is broken down during enzymatic hydrolysis. To overcome the poor transfer, both enzymatic hydrolysis and saccharification followed by fermentation (SFF) process was employed at relative high solid concentration (10 to 20 per cent) using a portion loading method. The substrates were added to the reactor in three portions (starting concentration, 5 per cent, w/v) during both reactions up to 20 per cent final DM concentration at every four hours.

Rheological Behavior of Enzymatic Hydrolysis Suspension

Figures IV-2, IV-3 and IV-4 show the dependence of apparent viscosity of enzyme hydrolysis suspension on biomass concentration. The graphs clearly demonstrate a dramatic decrease of viscosity for the reloading point (i. e. initial 4 hours) with increasing shear rate. The experimental determination of the viscosity-shear rate and shear stress-shear rate relationships of the various formulation suspensions with different concentrations was performed with a variable speed rotational viscometer (2 to 200 RPM).

The viscosities observed were in range of 0.0418 to 0.0144, 0.233 to 0.0348 and 0.292 to 0.0447 paschal-seconds for shear rates up to 100 reciprocal seconds and substrate concentrations of 10, 15, and 20 per cent initial solids (w/v) measured at 50°C. The fermentation viscosity and shear stress curves are depicted in Figures IV-5 and IV-6.

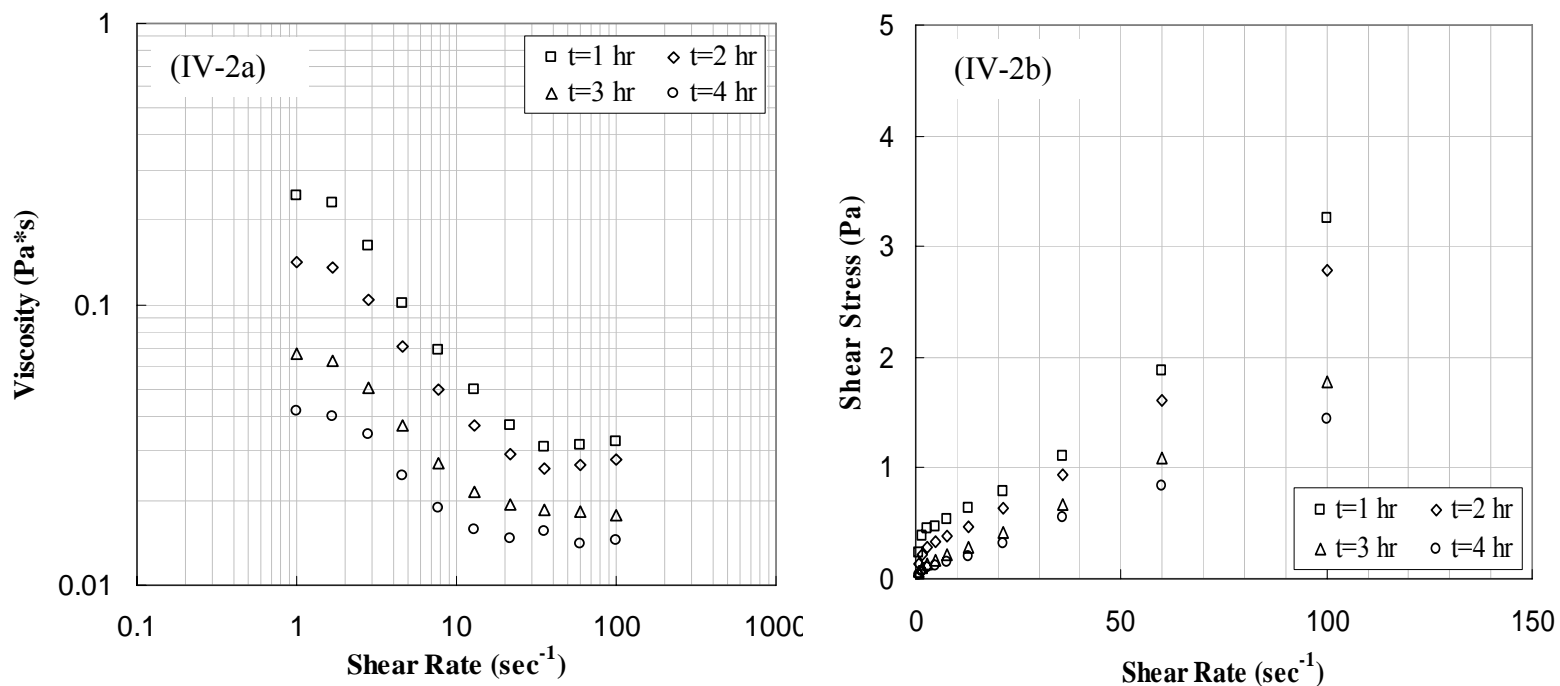


Figure IV-2. Viscosity and shear stress curves as a function of shear rate for different time during initial 4-hours enzymatic hydrolysis.

Note:

1. Hydrolysis condition: 30 FPU/g of glucan, pH 4.8 to 5.0, 50°C, 120 rpm.
2. Substrates were added to the reactions in one portion during fermentation up to 10 percent final substrate concentration.

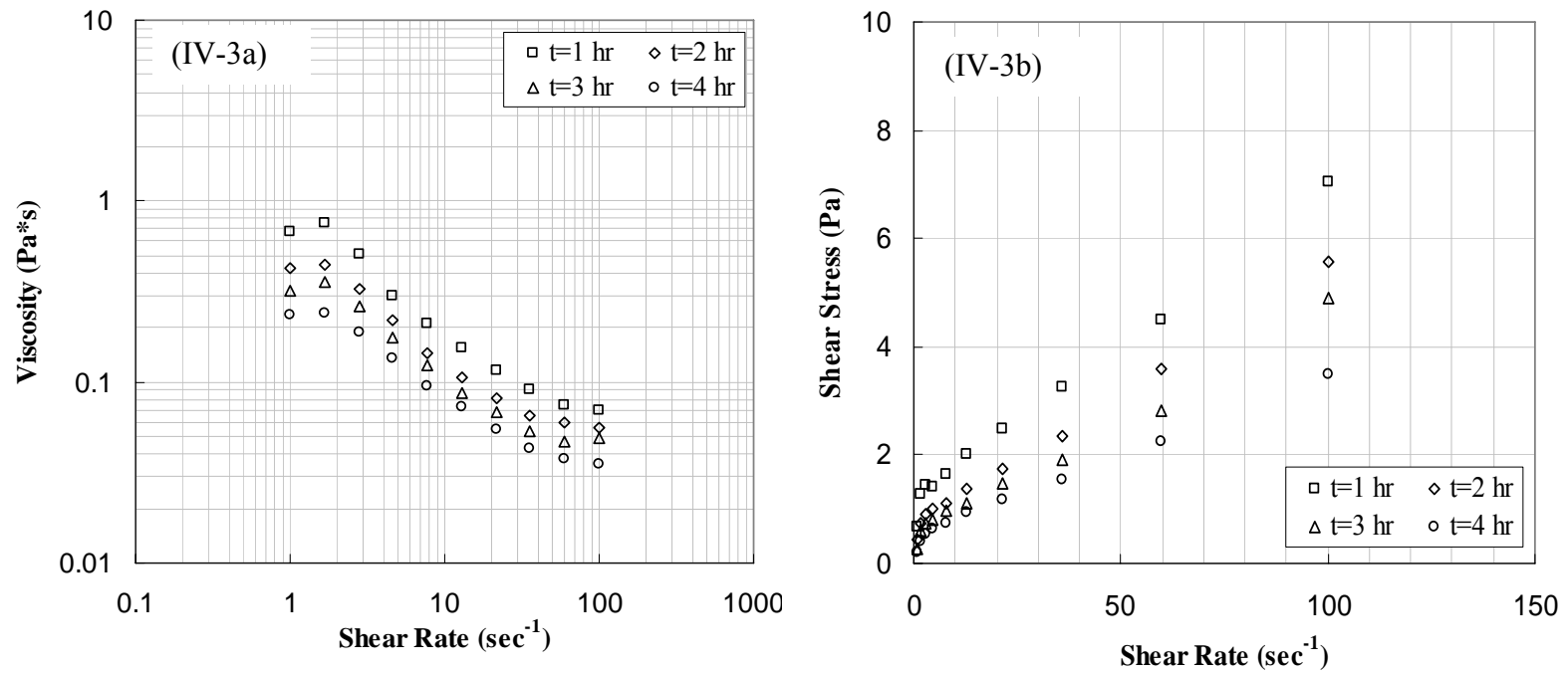


Figure IV-3. Viscosity and shear stress curves as a function of shear rate for different time during initial four-hour enzymatic hydrolysis.

Note;

1. Hydrolysis condition: 30 FPU/g of glucan, pH 4.8 to 5.0, 50°C, 120 rpm.
2. Substrates were added to the reactions in two portions during fermentation up to 15 percent final substrate concentration.

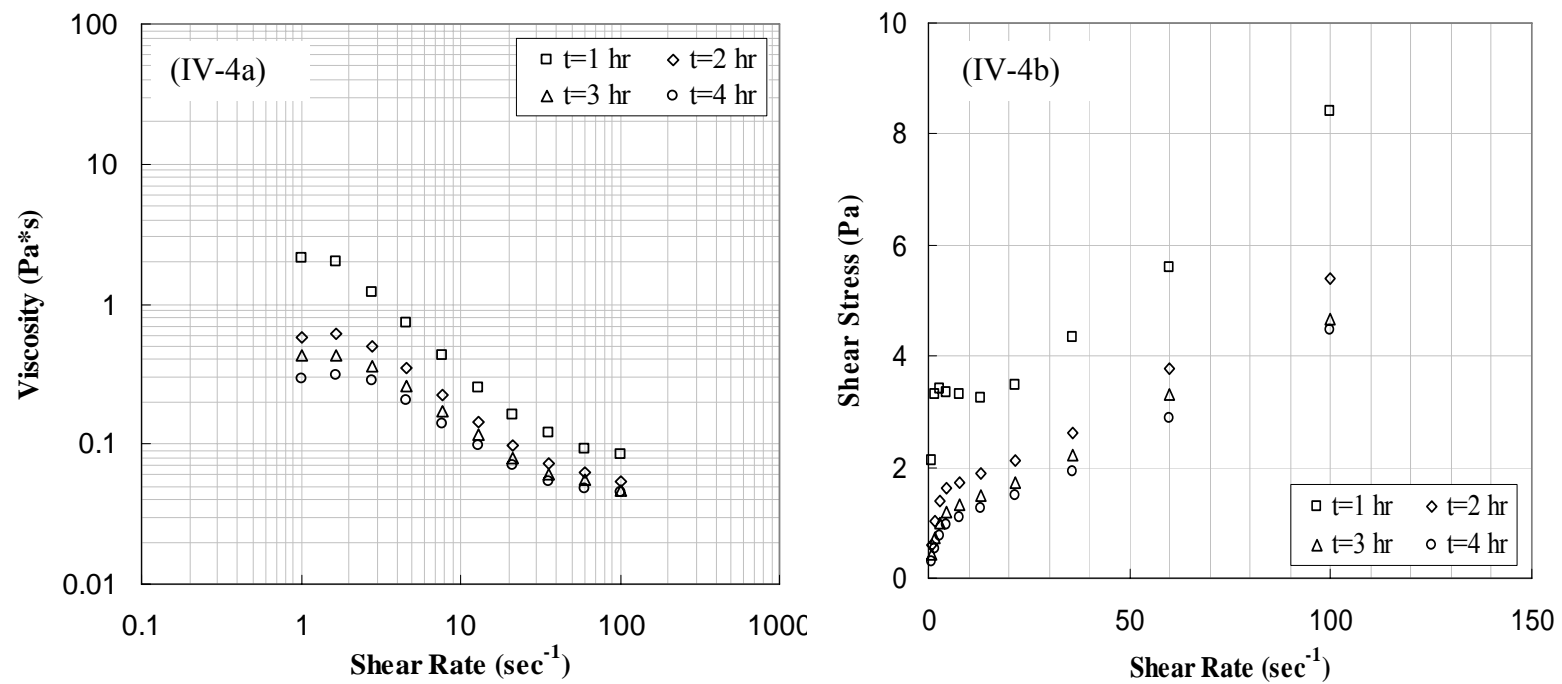


Figure IV-4. Viscosity and shear stress curves as a function of shear rate for different time during initial four-hour enzymatic hydrolysis.

Note;

1. Hydrolysis condition: 30 FPU/g of glucan, pH 4.8 to 5.0, 50°C, 120 rpm.
2. Substrates were added to the reactions in three portions during fermentation up to 20 percent final substrate concentration.

In this fermentation experimental results are presented for the rheological behavior and ethanol yield of high-solids ethanol fermentation for biomass conversion using Solka Floc as the model feedstock. A recombinant strain of *Zymomonas mobilis* 39679:pZB4L was used in SSF and SFF processes as a function of varying initial concentration of Solka Floc and constant enzyme dosage. Compared with the traditional SSF process for high solid substrate at 40°C, the rheological behavior in the SFF process significantly decreased in the beginning of ethanol fermentation. The viscosities observed were in range of 1.220 to 0.098, 3.36 to 0.133, and 5.18 to 0.192 Pa-s for shear rates up to 100s⁻¹ (Figure VI-5a). On the other hand, the initial viscosities were in range 0.024 to 0.028, 0.423 to 0.067, and 0.840 to 0.087 Pa-s for shear rates up to 100s⁻¹ in combined temperature (50°C and 30°C) at 10, 15, and 20 percent initial solids (w/v), respectively (Figure IV-6a). One can see that the rheological behavior of suspensions of fermentation broth significantly changes with its concentration and reaction condition. At all concentration, both enzymatic suspension and fermentation broths exhibit a pseudoplastic behavior with two Newtonian regions. However, at relatively high solid concentration loaded by the portion method, constant viscosity was observed, indicating only the Newtonian behavior of slurries at low and high shear rate during initial enzymatic hydrolysis and SFF process (Figure IV-4, IV-6).

Rheological Parameter Estimation for Pseudoplastic Suspension

Several researchers reported viscoelastic behavior of yeast suspensions. Labuza

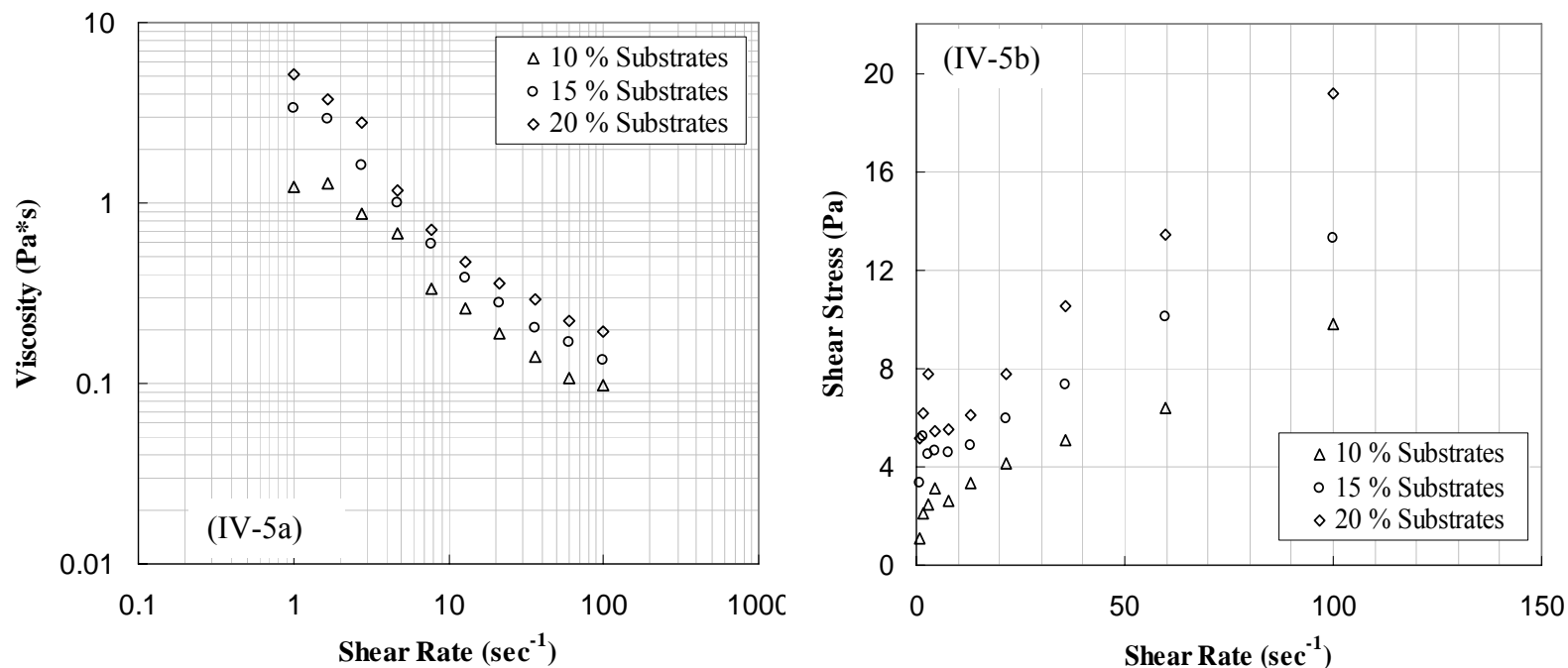


Figure IV-5. Viscosity and shear stress curves as a function of shear rate for different time during initial SSF process.

Note;

1. SSF condition: 30 FPU/g of glucan, pH 4.8 to 5.0, 40°C, 120 rpm, *Zymomonas mobilis*, strain 39679:pZB4L.
2. Substrates were added to the reactions in three portions during fermentation up to 20 percent final substrate concentration.
3. The substrate and nutrient media were autoclaved (120°C and 20 min).

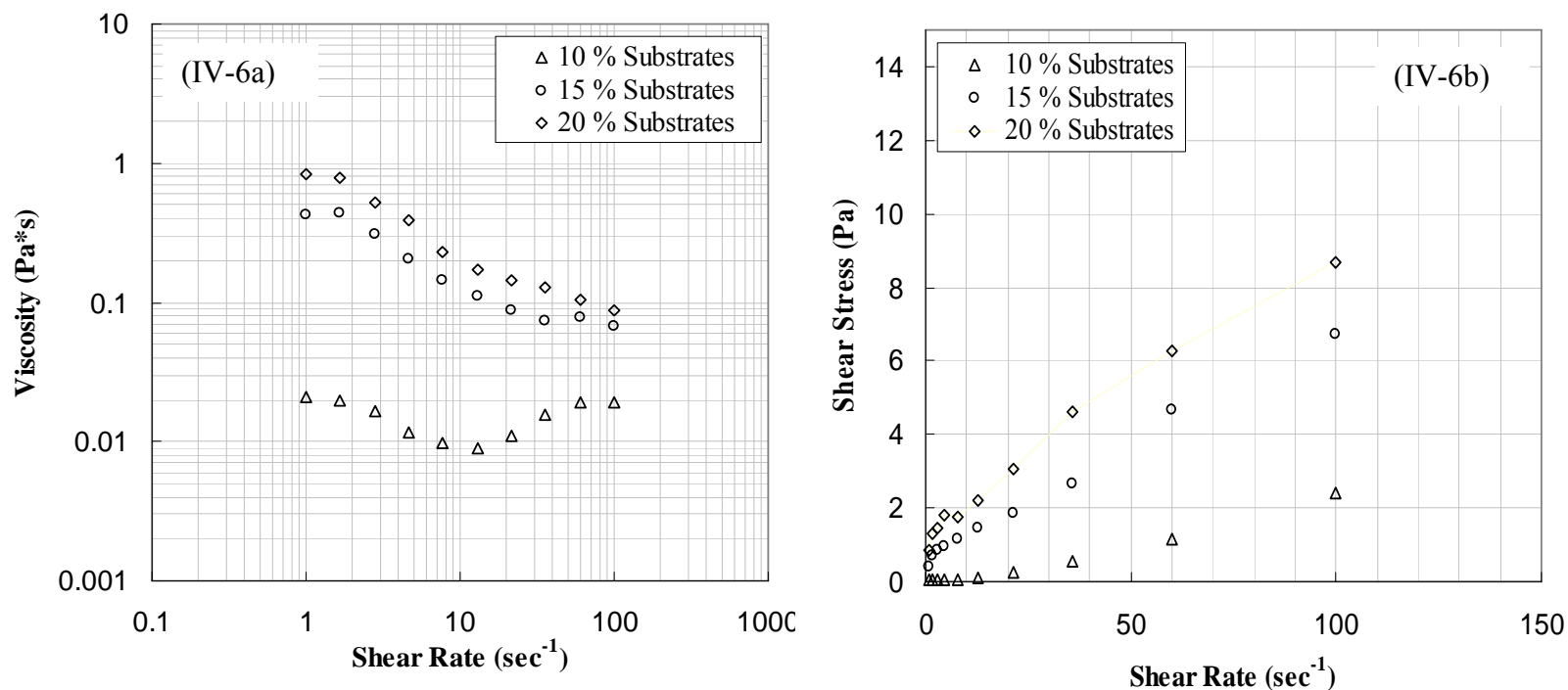


Figure IV-6. Viscosity and shear stress curves as a function of shear rate for different time during initial SFF process.

Note;

1. SFF condition: 30 FPU/g of glucan, pH 4.8 to 5.0, 120 rpm, *Zymomonas mobilis*, strain 39679:pZB4L.
2. Combined temperature: 50°C and 30°C.
3. Substrates were added to the reactions in three portions during fermentation up to 20 percent final substrate concentration.
4. The substrate and nutrient media were autoclaved (120 °C and 20 min).

et al. (1970) reported shear-thinning behavior of baker's yeast (*S. cerevisiae*) in the range of 1 to 100 s⁻¹ at yeast concentrations above 10.5 per cent (w/w). The power-law model was successfully applied. More recently, Mancini and Moresi (2000) measured rheology of baker's yeast using different rheometers in the concentration range of 25 to 200 g/dm³. While a Haake rotational viscometer confirmed Labuza's results on the pseudoplastic character of yeast suspension, dynamic stress rheometry revealed definitive Newtonian behavior. This discrepancy was attributed to the lower sensibility of Haake viscometer in the range of viscosity tested (1.5 to 12 mPa-s). Speers et al. (1993) used a controlled shear-rate rheometer with a cone-and-plate system to measure viscosity of suspensions of flocculating and nonflocculating strains of *S. cerevisiae* and *S. uvarum*. They used the Bingham model for description of viscoelastic flow behavior of cell suspension.

The normal procedure for the estimation of the model parameters for pseudoplastic fluids with a yield stress using rheological models employs non linear regression of the viscometric data from concentric cylinder geometry with a numerical package, minimizing the sum of error squares. Nonlinear fit to various data with a statistics package (RHEOLPLUS) has sometimes given the best fit with negative yield values, which is meaningless. So, the first point at low shear stress was not considered in the regression analysis.

Figure IV-2b, IV-3b, and IV-6b show shear stress curves as a function of shear rate for different times during initial enzymatic hydrolysis. The yield stress values are

Table IV-1. Determination of rheological parameter as function of time during initial 4-hour enzymatic hydrolysis.

Reaction Time	Herschel-Bulkley Model $\tau = \tau_y + K \dot{\gamma}^n$				Bingham Model $\tau = \tau_y + K \dot{\gamma}$			Casson Model $\tau^{0.5} = (\tau_y)^{0.5} + n(\dot{\gamma})^{0.5}$			Power Law $\tau = K \dot{\gamma}^n$		
	τ_y (pa)	K	n	R ²	τ_y (pa)	n	R ²	τ_y (pa)	n	R ²	K	n	R ²
t= 1 hr	0.391	0.012	1.175	0.996	0.360	0.022	0.994	0.226	0.100	0.982	0.269	0.404	0.948
t= 2 hr	0.213	0.019	1.024	0.995	0.209	0.021	0.995	0.335	0.107	0.990	0.155	0.507	0.972
t= 3 hr	0.099	0.009	1.176	0.994	0.081	0.171	0.992	0.031	0.108	0.987	0.063	0.669	0.973
t= 4 hr	0.065	0.005	1.294	0.995	0.044	0.014	0.988	0.013	0.105	0.983	0.037	0.766	0.972

Note;

1. Hydrolysis condition: 30 FPU/g of glucan, pH 4.8 to 5.0, 50°C, 120 rpm.
2. Substrates were added to the reactions in two portions during fermentation up to 10 % final substrate concentration.

Nomenclature;

- τ : shear stress, Pa
 τ_y : yield shear stress, Pa
n: flow behavior index
K: consistency index constant, Pasⁿ
R²: squared multiple correlation coefficient

Table IV-2. Determination of rheological parameter as function of time during initial 4-hour enzymatic hydrolysis.

Reaction Time	Herschel-Bulkley Model $\tau = \tau_y + K \dot{\gamma}^n$				Bingham Model $\tau = \tau_y + K \dot{\gamma}$			Casson Model $\tau^{0.5} = (\tau_y)^{0.5} + n(\dot{\gamma})^{0.5}$			Power Law $\tau = K \dot{\gamma}^n$		
	τ_y (pa)	K	n	R ²	τ_y (pa)	n	R ²	τ_y (pa)	n	R ²	K	n	R ²
t= 1 hr	1.191	0.060	0.987	0.998	0.763	0.071	0.931	0.759	0.1611	0.991	0.835	0.403	0.958
t= 2 hr	0.713	0.055	0.968	0.997	0.731	0.048	0.997	0.424	0.156	0.993	0.489	0.466	0.967
t= 3 hr	0.577	0.044	0.975	0.996	0.589	0.040	0.996	0.338	0.144	0.992	0.399	0.476	0.969
t= 4 hr	0.354	0.057	0.887	0.991	0.400	0.036	0.990	0.213	0.143	0.990	0.292	0.532	0.975

Note;

1. Hydrolysis condition: 30 FPU/g of glucan, pH 4.8 to 5.0, 50°C, 120 rpm.
2. Substrates were added to the reactions in three portions during fermentation up to 15 % final substrate concentration.

Nomenclature;

- τ : shear stress, Pa
- τ_y : yield shear stress, Pa
- n: flow behavior index
- K: consistency index constant, Pasⁿ
- R²: squared multiple correlation coefficient

Table IV-3. Determination of rheological parameter as function of time during initial 4-hour enzymatic hydrolysis.

Reaction Time	Herschel-Bulkley Model $\tau = \tau_y + K \dot{\gamma}^n$				Bingham Model $\tau = \tau_y + K \dot{\gamma}$			Casson Model $\tau^{0.5} = (\tau_y)^{0.5} + n(\dot{\gamma})^{0.5}$			Power Law $\tau = K \dot{\gamma}^n$		
	τ_y (pa)	K	n	R ²	τ_y (pa)	n	R ²	τ_y (pa)	n	R ²	K	n	R ²
t= 1 hr	2.707	0.036	1.083	0.972	2.658	0.052	0.926	1.488	0.115	0.930	2.363	0.205	0.859
t= 2 hr	0.960	0.140	0.730	0.981	1.173	0.044	0.976	0.815	0.133	0.983	0.854	0.353	0.966
t= 3 hr	0.600	0.154	0.693	0.987	0.827	0.041	0.979	0.535	0.138	0.989	0.589	0.408	0.978
t= 4 hr	0.372	0.158	0.677	0.986	0.573	0.041	0.978	0.358	0.144	0.988	0.424	0.464	0.981

Note;

1. Hydrolysis condition: 30 FPU/g of glucan, pH 4.8 to 5.0, 50°C, 120 rpm.
2. Substrates were added to the reactions in four portions during fermentation up to 20 % final substrate concentration.

Nomenclature;

- τ : shear stress, Pa
- τ_y : yield shear stress, Pa
- n: flow behavior index
- K: consistency index constant, Pasⁿ
- R²: squared multiple correlation coefficient

shown in Tables IV-1, IV-2, and IV-3. Shear stress-shear rate data of enzymatic hydrolysis suspension and fermentation broth were tested for various rheological models (Herschel-Bulkley, Bingham, Casson and power law models).

Three models (Herschel-Bulkley, Casson, and Bingham) were used to fit the experimental data and to determine the yield stress of the slurries. Table VI-5 and VI-6 lists the results obtained for the different parameters used to fit the experimental data of fermentation suspensions at the various concentrations. The Herschel-Bulkley model fits the data satisfactorily over the whole experimental range at 10 to 20 per cent solids concentration. On the other hand, Bingham and Casson equations are in excellent agreement with result of enzymatic suspension and fermentation broth from fermentor at 10 per cent and 20 per cent respectively (Table IV-1, Table IV-3, and Table IV-5).

Figure IV-7 through IV-9 use curve fitting with an empirical rheological model as an indirect method of determining the yield stress on a fluid. Four different models were used to fit the behavior of fermentation broth at various concentrations: the power law model, the Bingham model, the Casson model and the Herschel-Bulkley model. The results of the power law model (n and K_{pl}) were compared to those power law parameters obtained with the impeller method. The Herschel-Bulkley, Bingham and the Casson models were used to compare their yield stress results to those calculated with the direct methods, the stress growth and impeller methods. Tables IV-4 and IV-5 show the parameters obtained when the experimental shear stress-shear rate data for the fermentation suspensions were fitted with all models.

Table IV-4. Determination of rheological parameter as function of time during initial SSF process.

% (w/v) Substrates	Herschel-Bulkley Model $\tau = \tau_y + K \gamma^n$				Bingham Model $\tau = \tau_y + K \gamma$			Casson Model $\tau^{0.5} = (\tau_y)^{0.5} + n(\gamma)^{0.5}$			Power Law $\tau = K \gamma^n$		
	τ_y (pa)	K	n	R ²	τ_y (pa)	n	R ²	τ_y (pa)	n	R ²	K	n	R ²
10 %	0.787	0.906	0.474	0.982	1.931	0.092	0.973	1.378	0.198	0.994	1.622	0.357	0.970
15 %	3.269	0.052	1.134	0.989	3.139	0.093	0.989	2.407	0.173	0.961	2.700	0.264	0.879
20 %	5.516	0.044	1.257	0.980	5.175	0.132	0.948	4.107	0.197	0.941	4.597	0.235	0.848

Note;

1. SSF condition: 30 FPU/g of glucan, pH 4.8 to 5.0, 40°C, 120 rpm, *Zymomonas mobilis*, strain 39679:pZB4L.
2. Substrates were added to the reactions in four portions during fermentation up to 20 % final substrate concentration.
3. The substrate and nutrient media were autoclaved (120°C and 20 min).

Nomenclature;

- τ : shear stress, Pa
- τ_y : yield shear stress, Pa
- n: flow behavior index
- K: consistency index constant, Pasⁿ
- R²: squared multiple correlation coefficient

Table IV-5. Determination of rheological parameter as function of time during initial SFF process.

% (w/v) Substrates	Herschel-Bulkley Model $\tau = \tau_y + K \dot{\gamma}^n$				Bingham Model $\tau = \tau_y + K \dot{\gamma}$			Casson Model $\tau^{0.5} = (\tau_y)^{0.5} + n(\dot{\gamma})^{0.5}$			Power Law $\tau = K \dot{\gamma}^n$		
	τ_y (pa)	K	n	R ²	τ_y (pa)	n	R ²	τ_y (pa)	n	R ²	K	n	R ²
10 %	0.029	0.002	1.554	0.998	0.014	0.011	0.980	0.001	0.105	0.970	0.016	0.973	0.968
15 %	0.306	0.177	0.756	0.985	0.467	0.068	0.978	0.256	0.201	0.988	0.425	0.549	0.979
20 %	0.735	0.259	0.740	0.996	1.016	0.089	0.981	0.625	0.216	0.996	0.866	0.461	0.970

Note;

1. SFF condition: 30 FPU/g of glucan, pH 4.8 to 5.0, 120 rpm, *Zymomonas mobilis*, strain 39679:pZB4L.
2. Combined temperature: 50°C and 30°C.
3. Substrates were added to the reactions in four portions during fermentation up to 20 % final substrate concentration.
4. The substrate and nutrient media were autoclaved (120°C and 20 min).

Nomenclature;

- τ : shear stress, Pa
- τ_y : yield shear stress, Pa
- n: flow behavior index
- K: consistency index constant, Pasⁿ
- R²: squared multiple correlation coefficient

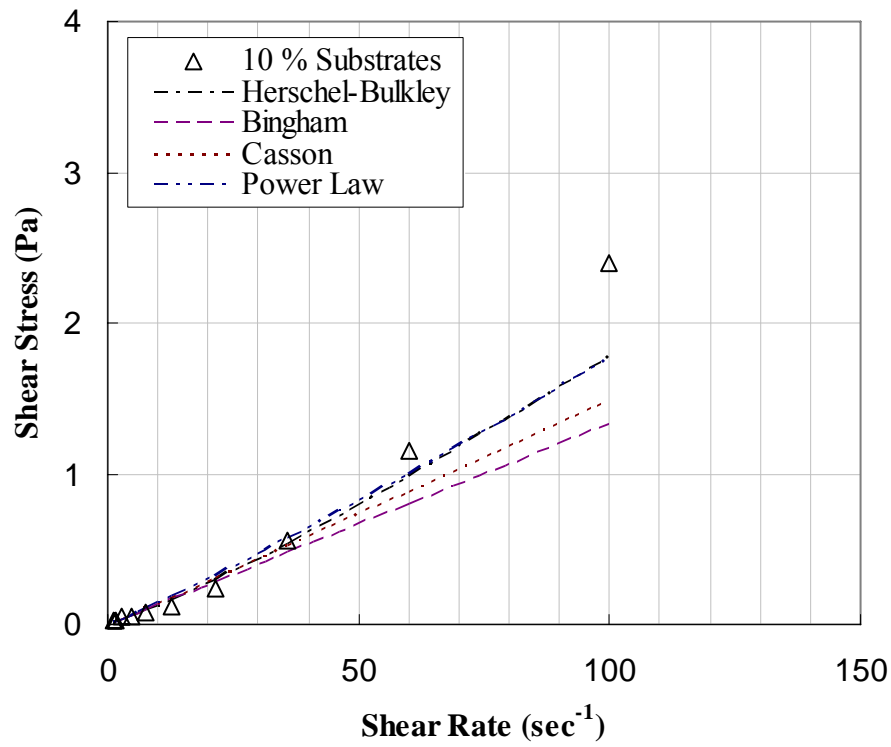


Figure IV-7. Comparison of the different rheological models used to fit the shear stress as function of shear rate data of 10 per cent solid concentration of fermentation Broth at $t=0$. Symbols represent experimental measurements and lines represent four different model predictions

Note;

1. SFF condition: 30 FPU/g of glucan, pH 4.8 to 5.0, 120 rpm, *Zymomonas mobilis*, strain 39679:pZB4L.
2. Combined temperature: 50°C and 30°C.
3. Substrates were added to the reactions in one portions during fermentation up to 10 % final substrate concentration.
4. The substrate and nutrient media were autoclaved (120°C and 20 min).

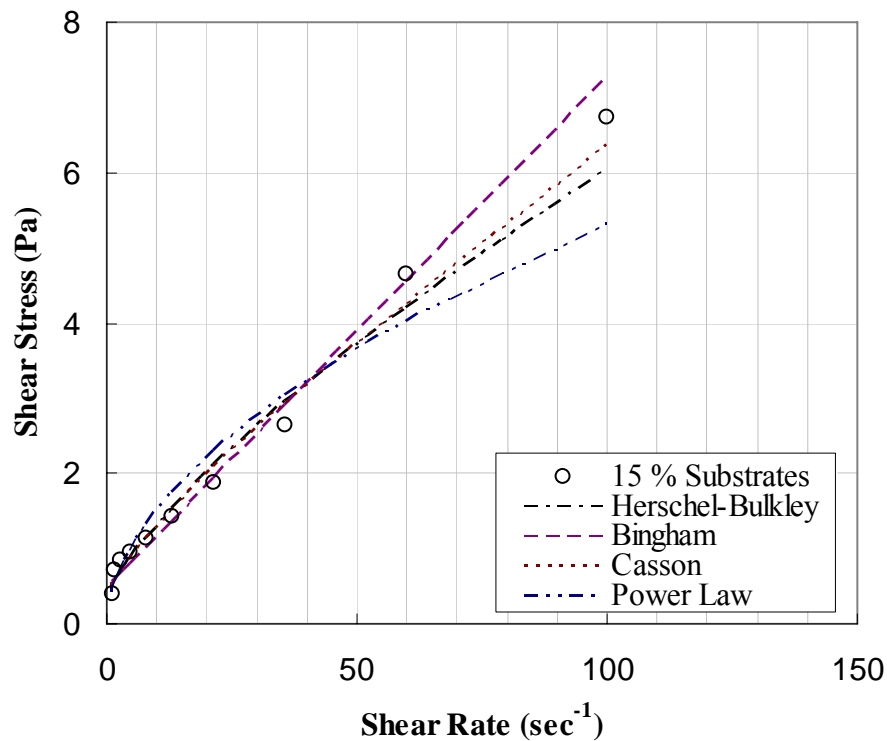


Figure IV-8. Comparison of the different rheological models used to fit the shear stress as function of shear rate data of 15 % sold concentration of fermentation Broth at t=0. Symbols represent experimental measurements and lines represent four different model predictions

Note;

1. SFF condition: 30 FPU/g of glucan, pH 4.8 to 5.0, 120 rpm, *Zymomonas mobilis*, strain 39679:pZB4L.
2. Combined temperature: 50°C and 30°C.
3. Substrates were added to the reactions in two portions during fermentation up to 15 % final substrate concentration.
4. The substrate and nutrient media were autoclaved (120 °C and 20 min).

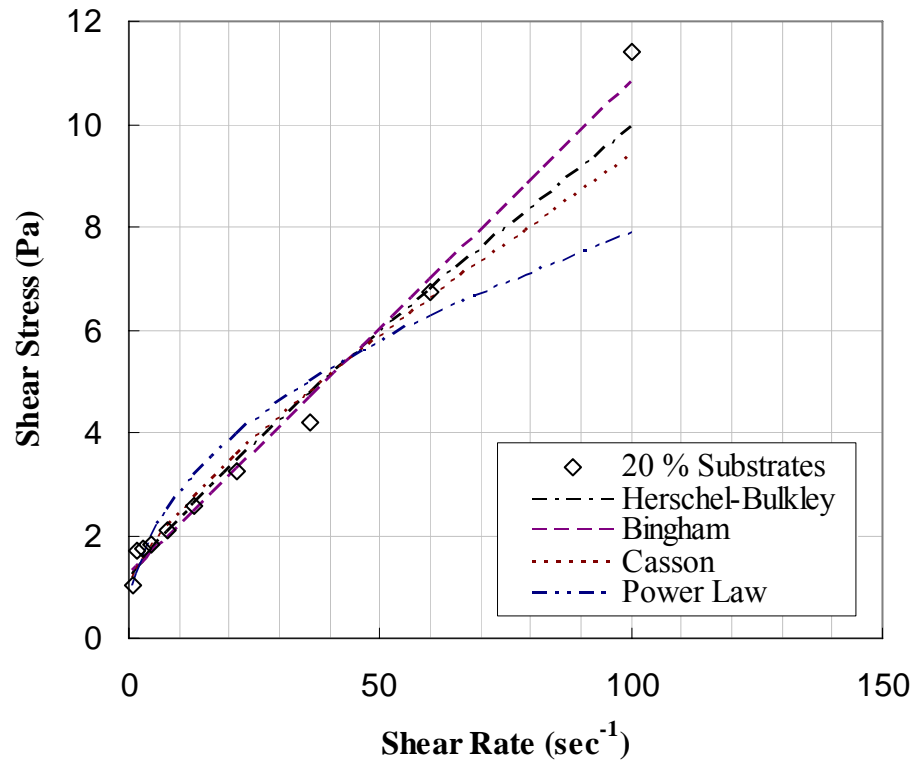


Figure IV-9. Comparison of the different rheological models used to fit the shear stress as function of shear rate data of 20 % sold concentration of fermentation Broth at t=0. Symbols represent experimental measurements and lines represent four different model predictions

Note;

1. SFF condition: 30 FPU/g of glucan, pH 4.8 to 5.0, 120 rpm, *Zymomonas mobilis*, strain 39679:pZB4L.
2. Combined temperature: 50°C and 30°C.
3. Substrates were added to the reactions in three portions during fermentation up to 20 % final substrate concentration.
4. The substrate and nutrient media were autoclaved (120°C and 20 min).

The correlation coefficients (R^2) between the shear rate and shear stress are 0.994 - 0.995 for the Herschel-Bulkley model, 0.988-0.994 for the Bingham, 0.982-0.990 for the Casson model and 0.948-0.972 for the power law model for enzymatic hydrolysis at 10 per cent solid concentration (Table IV-1). The rheological parameters for Solka Floc suspension were employed to determine if there was any relationship between the shear rate constant, k , and the power law index flow, n . The relationship between the shear rate constant and the index flow for fermentation broth at concentrations ranging from 10 to 20 percent is shown on Table IV-4 and IV-5. The yield stress, consistency coefficient and flow behavior index obtained by the FL 100/6W impeller technique decreased significantly as function of time and concentration during enzyme reaction (Table IV-1 and IV-3) and fermentation (Table IV-4 and IV-5).

Determination of Particle Size Treated by Enzyme

The particle size of the solid in the suspension was determined by Mastersizer S (Malvern Instruments Ltd., Malvern, U. K). The digested suspensions were produced in bench scale reactors at a concentration of 10 to 20 per cent (w/v) and temperature from 30 to 50°C for 4 and 48 hours followed by particle size measurements at 3000 rpm. Laser diffraction proved capable of providing rapid, reproducible results of the particle size distribution of each sample. Ten consecutive measurements were made of each sample, and the results averaged to produce the overall size distribution.

The particle size distribution of each slurry is illustrated in Figures IV-7, Figure IV-8 and IV-9, which show the percentage of particles, by volume, between 0.6 and 1000 μm . No particles $< 0.6 \mu\text{m}$ were detected in any of the samples. The digested suspension showed one main peak in the size range 35.6 to 48.3 μm (Figure IV-7a, Figure IV-8a, and Figure IV-8a). As the level of solid concentration increased, there was a shift in the particle size distribution towards larger particles with the peak at 35.6 to 48.3 μm becoming less pronounced with a decrease in the number of smaller sized particles. This is likely due to the differences in biodegradability for the different reaction conditions.

The average particle sizes during the enzymatic treatment and fermentation process of Solka Flocc at 40 °C and combined temperature (50 to 30°C) are given in Table IV-6. The solids particle size distribution ranged from 57.8 to 70.0 μm for the SSF process and from 44.0 to 57.5 μm for the SFF process at 10, 15, and 20 per cent initial solids (w/v), respectively.

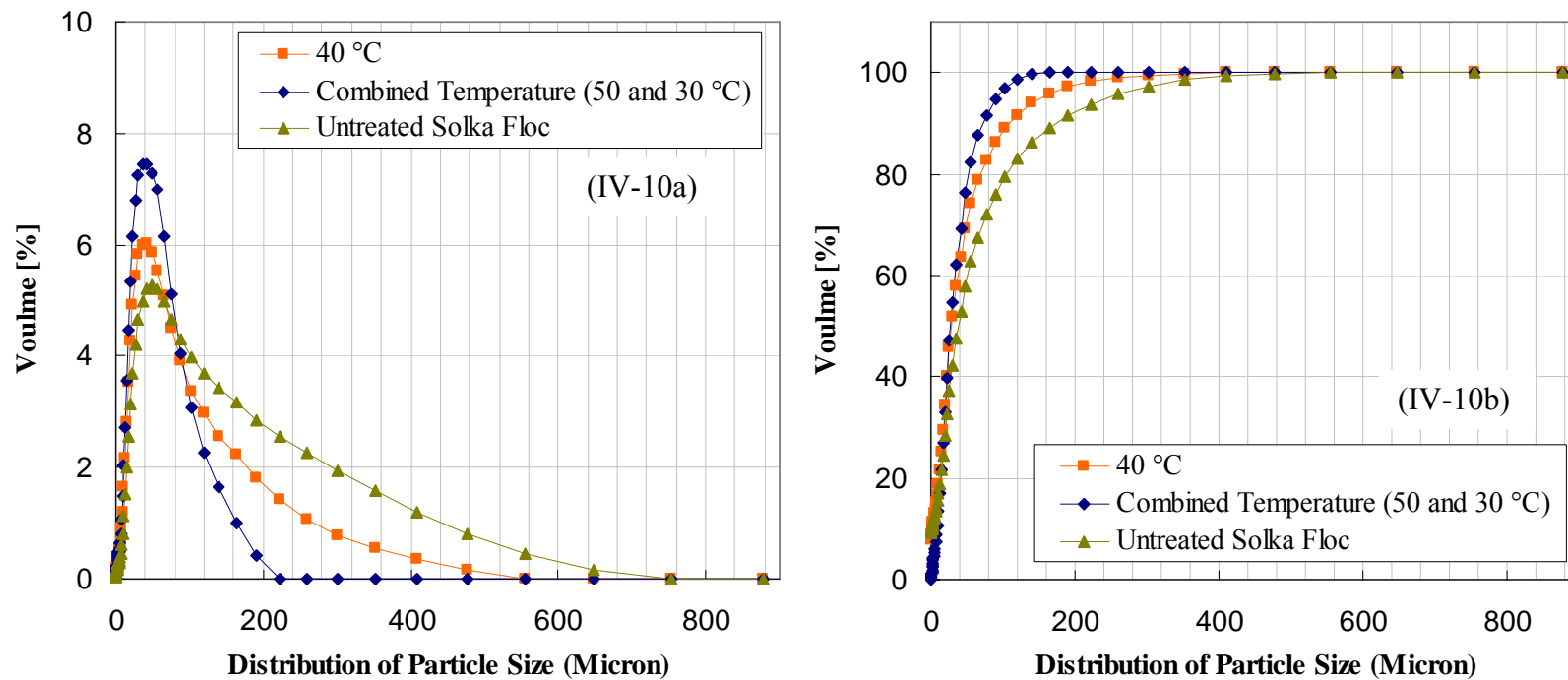


Figure IV-10. Percentage volume (10a) and cumulative volume particle size distribution (10b) for the substrate during SSF and SFF process.

Note;

1. SSF condition: 30 FPU/g of glucan, pH 4.8 to 5.0, 120 rpm, *Zymomonas mobilis*, strain 39679:pZB4L.
2. Substrates were added to the reactions in one portion during fermentation up to 10 percent final substrate concentration.
3. The substrate and nutrient media were autoclaved (120°C and 20 min).

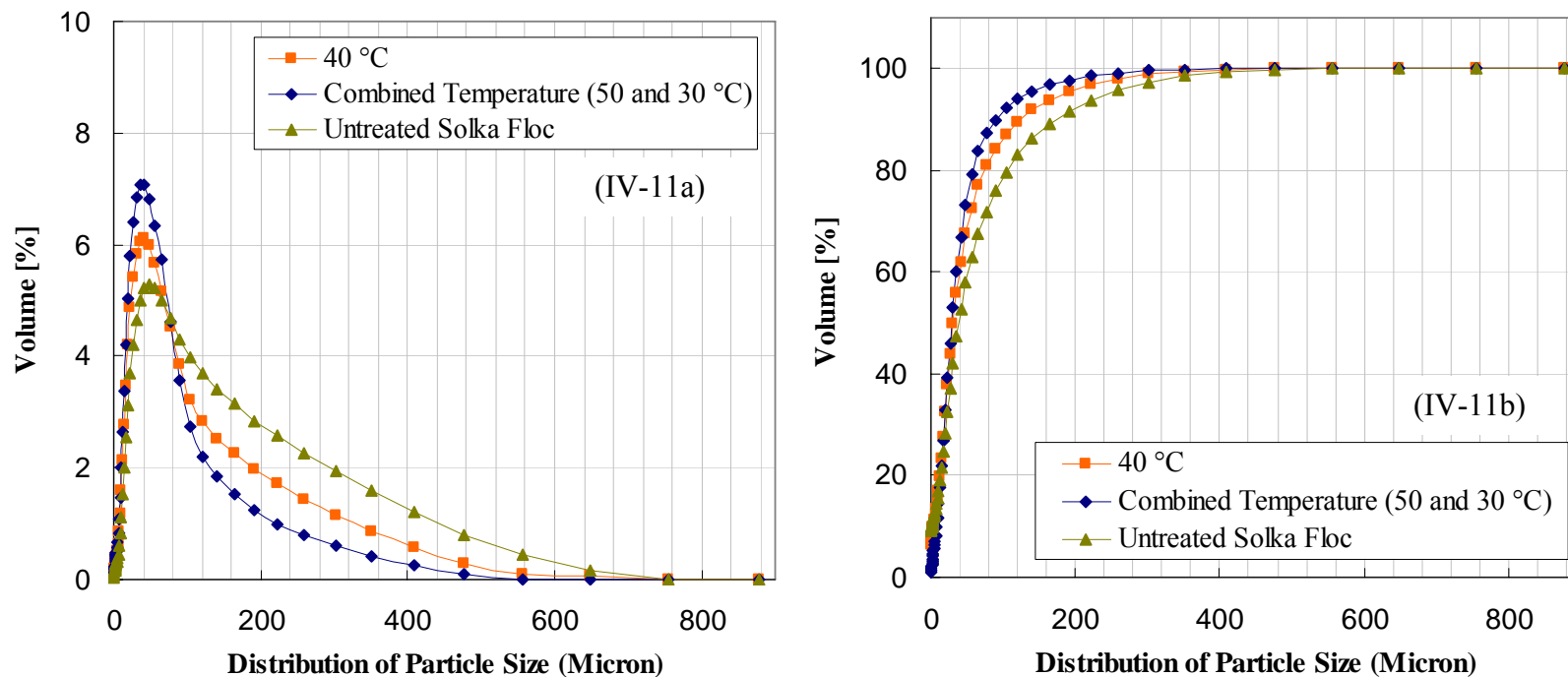


Figure IV-11. Percentage volume (11a) and cumulative volume particle size distribution (11b) for the substrate during SSF and SFF process.

Note;

1. SSF condition: 30 FPU/g of glucan, pH 4.8 to 5.0, 120 rpm, *Zymomonas mobilis*, strain 39679:pZB4L.
2. Substrates were added to the reactions in two portions during fermentation up to 15 percent final substrate concentration.
3. The substrate and nutrient media were autoclaved (120°C and 20 min).

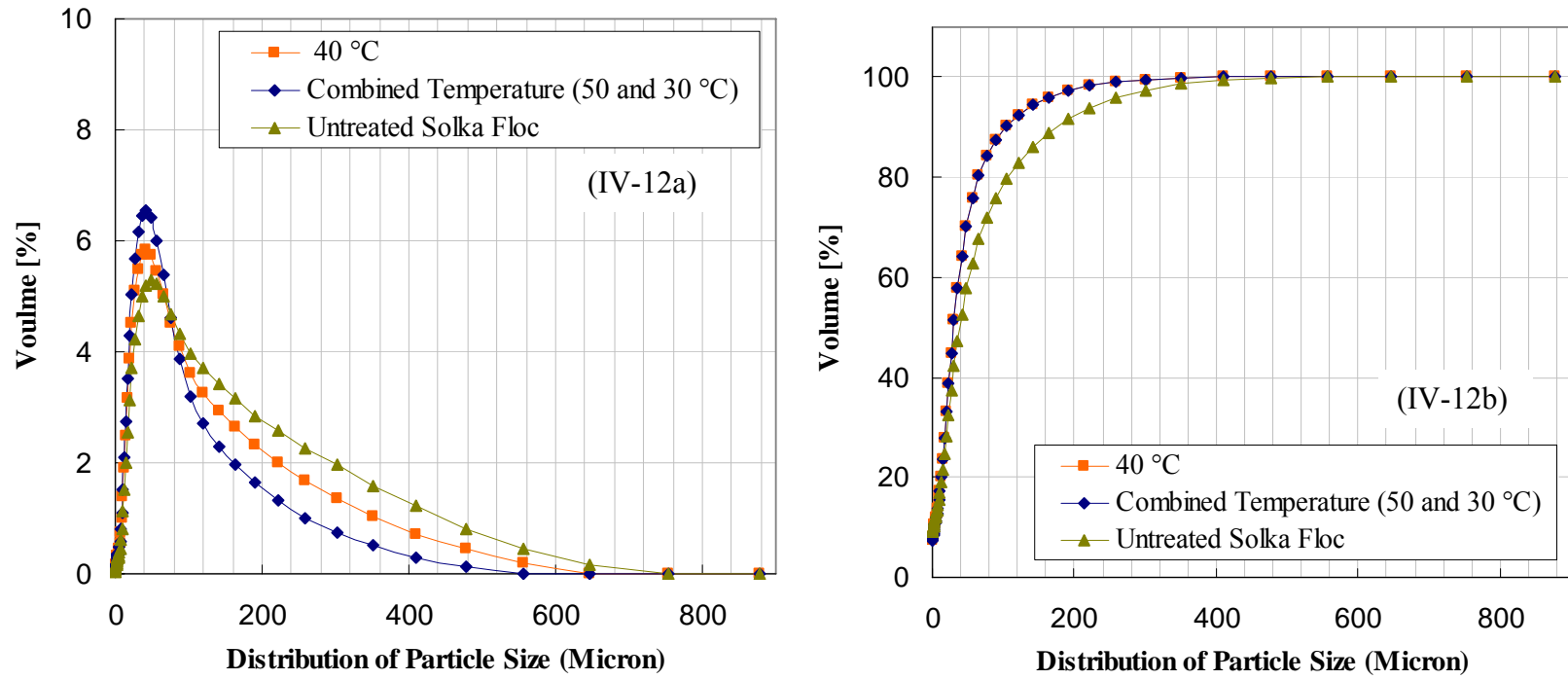


Figure IV-12. Percentage volume (12a) and) cumulative volume particle size distribution (12b) for the substrate during SSF and SFF process.

Note;

1. SSF condition: 30 FPU/g of glucan, pH 4.8 to 5.0, 120 rpm, *Zymomonas mobilis*, strain 39679:pZB4L.
2. Substrates were added to the reactions in three portions during fermentation up to 20 percent final substrate concentration.
3. The substrate and nutrient media were autoclaved (120°C and 20 min).

Table IV-6. Determination of rheological parameter as function of time during initial fermentation process.

% (w/v) Substrates	Average Particle Size		Range of Viscosity		Viscosity at 120 rpm	
	SSF	SFF	SSF	SFF	SSF	SFF
10 %	57.8 μm	44.0 μm	1.120-0.098 Pa·s	0.024-0.028 Pa·s	0.106 Pa·s	0.019 Pa·s
15 %	64.2 μm	53.0 μm	3.360-0.133 Pa·s	0.401-0.058 Pa·s	0.168 Pa·s	0.078 Pa·s
20 %	70.0 μm	57.5 μm	5.180-0.192 Pa·s	0.840-0.087 Pa·s	0.223 Pa·s	0.105 Pa·s

Note;

1. SSF condition: 30 FPU/g of glucan, pH 4.8 to 5.0, 40°C, 120 rpm, *Zymomonas mobilis*, strain 39679:pZB4L.
2. SFF condition: 30 FPU/g of glucan, pH 4.8 to 5.0, 50-30°C, 120 rpm, *Zymomonas mobilis*, strain 39679:pZB4L.
3. Range of viscosity is for shear rate up to 100 s⁻¹.
4. Substrates were added to the reactions in four portions during fermentation up to 20 percent final substrate concentration.
5. The substrate and nutrient media were autoclaved (120°C and 20 min).
6. Average particle size of untreated Solka Floc is 91.0 μm .

CONCLUSIONS

The rheological analysis of high solid substrates in the bioreactor during the enzymatic hydrolysis and ethanol fermentation showed a dramatic decrease in viscosity as function of time and solids concentration. Initial reaction time and biomass concentration were found to affect the bioreactor hydrodynamics. Adoption of high solid substrates loading by portion method in the three-liter bioreactor showed significant reduction of viscosity and a dramatic acceleration of net liquid flow appeared with increasing biomass quantity. Rheological analysis revealed a direct dependence of temperature and concentration of biomass in bioreactor on apparent viscosity of fermentation broths. An increase in the level of solid concentration, with the samples less digested, led to a shift in the size distribution, with a decrease in the number of smaller sized particles.

For a high solid bioreactor used for ethanol production, the bioreactor should operate below the critical biomass concentration to ensure operation in desirable flow regime. The SFF process can be operated with relative higher solids loading up to a maximum solids loading (20 percent w/v); however, high solids loading results in a negative effect on transport phenomena, mixing and solid distribution in the bioreactor. All of the information on hydrodynamics in the three-liter bioreactor can be used a priori or during the bioprocess to optimize operational parameters in order to avoid any occurrence of undesirable bioreactor operation to maximize the process productivity.

V. FLOW PATTERN SIMULATION IN A HIGH SOLID CELLULOSE-TO-ETHANOL BIOREACTOR USING COMPUTATIONAL FLUID DYNAMICS

ABSTRACT

The agitation system plays an important role in bioethanol production from the Simultaneous Saccharification Fermentation (SSF) and Saccharification Followed by Fermentation (SFF) processes. To understand and improve mixing and mass transfer in the viscous non-Newtonian systems, flow behavior of fermentation broth was simulated in a bench scale bioreactor (BioFlo 3000). The predictive capabilities of CFD techniques as applied to solid-liquid stirred vessels for a high solids system are investigated.

Based on the angular momentum balance, the required torque in mixing tanks was calculated after the converged solution was obtained as percent of solid suspension. The simulated power number in the turbulent regime was 5.0 for Rushton turbine impeller. The Reynolds number was 248.6, 64.5, and 50.3 at 10, 15, and 20 per cent initial solids (w/v), respectively.

The simulation of the mixed bioreactor was conducted with a baffled Rushton turbine impeller operating in laminar regime. The standard k- ϵ turbulent model was

employed in the mixing tank simulation with a Rushton turbine impeller. Fluid flow turbulent kinetic energy and turbulent dissipation rates in the three liter reactor have been simulated as a function of solid concentration. The result visually and analytically showed that slow or stagnant flow regions exist that could result in poor nutrient, gas, and heat transfer between top impellers and bottom of the tank.

INTRODUCTION

Computational fluid dynamics (CFD) is the science of predicting fluid flow, heat transfer, mass transfer, chemical reactions, and related phenomena by solving the mathematical equations which govern these processes using a numerical process (Kuipers and van Swaaij, 1997; Van den Akker, 1997; Sundaresan, 2000; Ranade, 2002). The result of CFD analyses is relevant engineering data used in conceptual studies of new designs, detailed product development, troubleshooting and redesign. This research addresses the simulation of various high solid suspensions in stirred tanks to determine apparatus performance in bioreactors.

A number of modeling techniques have been proposed and implemented in commercial codes, and the choice of techniques is not always straightforward for the normal user. Moreover, the consistency of the simulation predictions with the actual flow field and energy distribution has been demonstrated only in a few cases. Therefore, there is still a need for further analysis and development of the modeling techniques and of comparison of the simulation results with experimental data.

The economic of ethanol production are such that the cost of the power required to agitate the vessel is critical to the overall profitability of the enterprise. In the mixing process, prediction of the power or torque draw by the impeller, the flow pattern, and flow regime involved at different suspension concentration is the important information in design and operation to reach the desired process result.

In the present work computational analyses were performed for baffled tanks agitated with two Rushton impellers. The suspension of Solka Floc of different diameters

and various concentrations up to 20 per cent (w/v) were studied. Here, the Multiple Reference Frame and standard k- ϵ model for viscose flows available in commercial CFD codes have been tested, coupled with fully predictive solution of the transport of suspension in the process vessel.

The purpose of this research was to simulate the flow of a three-liter fermentor before designing a full scale high-solids fermentation. This simulation provides a starting point for identifying slow, stagnant, or recirculation zones where nutrient and gas starvation of cells could potentially occur. The commercially available programs Mixsim 2.1.10 TM and Fluent 6.2.20 TM were used to discretize the equation of continuity and motion of the relative high solid suspensions in stirred tanks. Fulfillment of these objectives will assist in better understanding of the ethanol production in the chemical mixing process and could allow fermentor design engineer to predict the degree of flow for the full scale fermentor.

MATERIALS AND METHODS

Tank Geometric Configuration of the Investigated Vessel

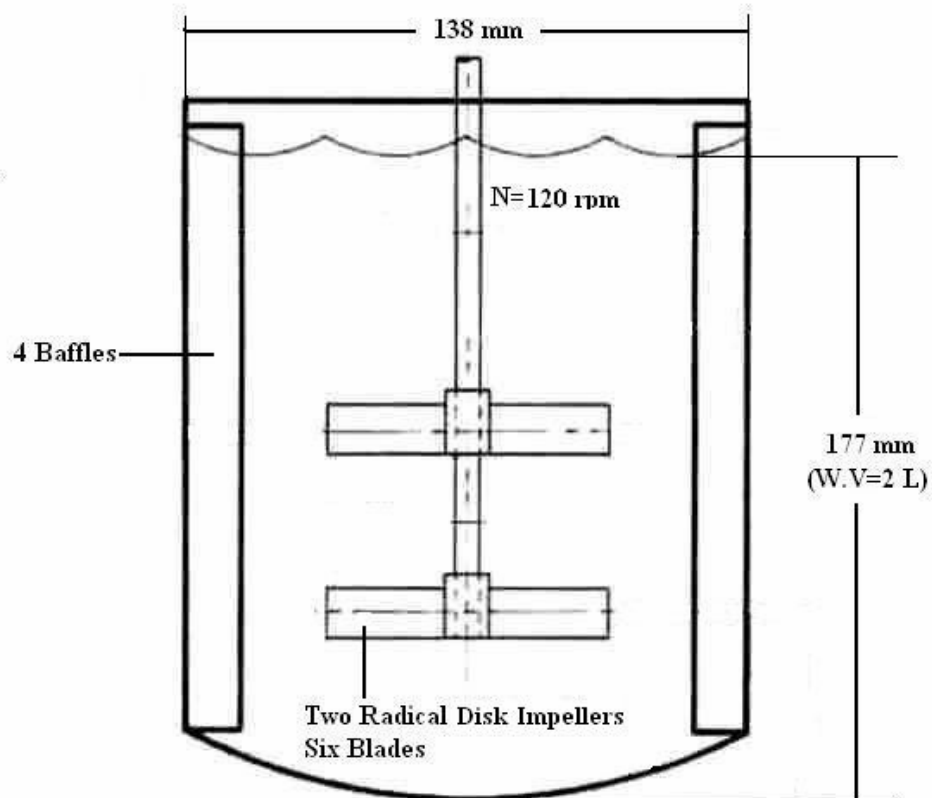


Figure V-1. NBS 3 L Bioreactor Tank Geometry: Diameter=138mm, Liquid Height=177mm, Bottom shape=ellipse, Working volume=2 L, Media= High Concentrated Solka Floc, Baffle= 4, Rotational speed: 120 rpm, Impeller Number= 2, Impeller Type= Radial disk, Number of blades= 6.

The k-ε Mathematical Models

The basic two transport equations that need to be solved for this model are for the kinetic energy turbulence, k , and the rate of dissipation of turbulence, ε (FLUENT, 2001):

$$\frac{\partial(\rho k)}{\partial t} + \frac{\partial}{\partial x_i}(\rho U_i k) = \frac{\partial}{\partial x_i} \left(\mu + \frac{\mu_t}{\sigma_k} \right) \frac{\partial k}{\partial x_i} + G_k - \rho \varepsilon \quad (\text{V-1})$$

$$\frac{\partial(\rho \varepsilon)}{\partial t} + \frac{\partial}{\partial x_i}(\rho U_i \varepsilon) = \frac{\partial}{\partial x_i} \left(\mu + \frac{\mu_t}{\sigma_\varepsilon} \right) \frac{\partial \varepsilon}{\partial x_i} + C_1 \frac{\varepsilon}{k} G_k + C_2 \rho \frac{\varepsilon^2}{k} \quad (\text{V-2})$$

The quantities C_1 , C_2 , σ_k , and σ_ε are empirical constants. The quantity G_k appearing in both equations is a generation term for turbulence. It contains products of velocity gradients, and also depends on the turbulent viscosity:

$$G_k = \mu_t \left(\frac{\partial U_i}{\partial x_j} + \frac{\partial U_j}{\partial x_i} \right) \frac{\partial U_j}{\partial x_i} \quad (\text{V-3})$$

Other source terms can be added to equation (V-1) and (V-2) to include other physical effects such as swirl, buoyancy or compressibility, for example. The turbulent viscosity is derived from both k and ε , and involves a constant taken from experimental data, C_μ , which has a value 0.09:

$$\mu_t = \rho C_\mu \frac{k^2}{\varepsilon} \quad (\text{V-4})$$

To summarize, the solution process for the k-ε model, transport equations are solved for the turbulent kinetic energy and dissipation rate.

Constant N_p and P per Liquid Volume

$$P = a \left(\frac{H_b}{0.2D} \right) \left(\frac{N_b}{6} \right)^b \quad (\text{V-5})$$

$$N_{\text{Re}} = \frac{D^2 N \rho}{\mu} \quad (\text{V-6})$$

$$N_p = \frac{P}{N^3 D^5 \rho} \quad (\text{V-7})$$

N_{Re} : Reynolds number

a, b : constant value (radical disk impeller, $a=5, b=0.8$)

N_p =power number, ratio of applied force to mass times acceleration

P =power input (W)

ρ =density of liquid (Kg/m^3)

N =impeller speed (rpm)

N_b =impeller blade number

H_b =disk height (m)

D =impeller outer diameter (m)

Simulation Model

- Type: 3D cylindrical
- Analysis model: Multiple Reference Frame (MRF)
- Turbulent model: Standard k- ϵ model

Simulation Tool Package

The simulations were performed using software package:

- Mixsim V. 2.1.10 - FLUENT V. 6.2.20

on a super computer at the University of Louisville.

Description of Supercomputer

Adelie is a Linux-based computational cluster with two master login nodes, 17 dual-processor, dual core Opteron compute nodes and six dual-Opteron compute nodes. The system has approximately 100 GB of RAM and 5.1 terabytes of external disk storage in a RAID 5 array managed by dual NAS heads with active failover and dual fiber channel NAS controllers for high availability. Each node also has additional local drive space. Backups are to an attached tape drive. The OS is SUSE Linux.

RESULTS AND DISCUSSION

Vessel Geometry and Grid Generation

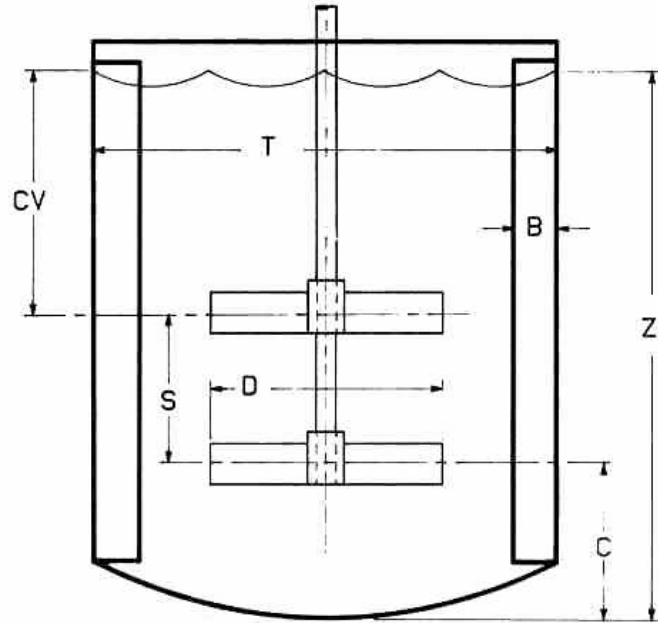


Figure V-2. Nomenclature used to describe the mixing system

The configuration of the physical model for simulating a mixing tank with Rushton impeller consists of a ellipsoidal cylindrical tank with four equally spaced wall mounted baffles extending from the vessel bottom to the free surface, stirred by a centrally-located six-blade Rushton turbine impeller. The tank diameter measured 0.138 meters, and baffle width was 0.008 meter. The impeller diameter was 0.046 m ($D/T=3$) for all impellers. The distance between the impellers was 0.061 m. The impeller center was positioned at a distance $C=T/3$ off the tank bottom. The liquid level was equal to the tank diameter, $Z/T=1.3$.

The suspension was fermentation broth with various viscosities. The impeller was mounted on a 0.0025 meter diameter shaft rotating at 120 rpm corresponding to a range of Reynolds number of 50 to 300—in both the down- and up-pumping modes.

The commercial mesh generator Mixsim 2.1.10 was used to create a structured, non-uniform multi-block grid, as shown in Figure V-3, with inner and outer zones by an interface in order to enable the use of multiple reference frame techniques. The wide nature of the impeller blades relative to the diameter of the hub results in the overlapping of blades close to the hub. Consequently, simulation of only part of the vessel in order to decrease computational expense was not possible and therefore it was necessary to model the entire vessel geometry.

Convergence Criteria and Blend Time

Simulations were typically considered converged when the scaled residuals (continuity, X, Y, Z-velocity, k, and ϵ), normalized relative to the maximum circulating flow, fell below 6E-04 by iteration 5,000. Further checks for convergence were made by verifying that global quantities, such as the power number, and the circulation number, were constant.

The model predictions are compared with the results of the experimental blend time correlation. MixSim can compute the blend time for a single impeller in a tank, as well as the effective blend time for a tank with multiple impellers.

The blend time to achieve 99 per cent uniformity in a tank with a multiple impellers is computed from (FLUENT, 2006).

$$t_{99} = \frac{4.605}{k_{m,eff}}$$

where a sum over all impellers ($i = 1$ to n) is performed to compute $k_{m,eff}$:

$$k_{m,eff} = \sum_{i=1}^n k_{m,i} = \sum a_i N_i \left(\frac{D_i}{T} \right)^{b_i} \left(\frac{T}{Z} \right)^{0.5}$$

All of the graphs show that for a uniformity above 99 % at $t=13.37s$. And, all calculations were steady state.

Grid Refinement

The geometry was defined in the Cartesian (x, y, z) coordinate system. After the grid is generated, the skewness of 97.41 percent cells was below 0.6. It is very important to assess the quality of the grid, because properties such as skewness can greatly affect the accuracy and robustness of the CFD solution. In general, high-quality meshes contain elements that possess average Q values of 0.4. Even a single cell with skewness > 0.98 may destroy convergence in the whole computation. The detailed histogram of skewness of this simulation was in Appendix C.

The computational grid was defined by 570,000 unstructured, nonuniformly-distributed, 182,000 nodes, and tetrahedral cells. When refining the mesh, care was taken to put most additional mesh points in the regions of high gradient around the blades and discharge region.

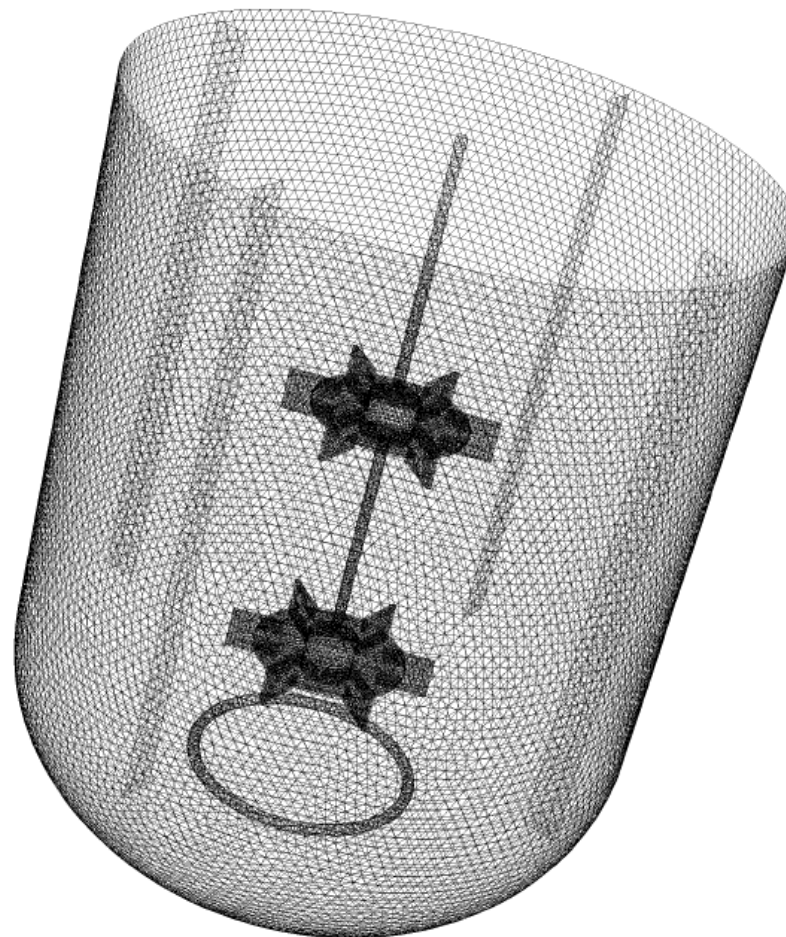
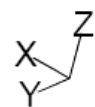


Figure V-3

Grid Edge (3 L Mixing Tank)

Jan 31, 2007
MixSim 2.1 (2.1.10)

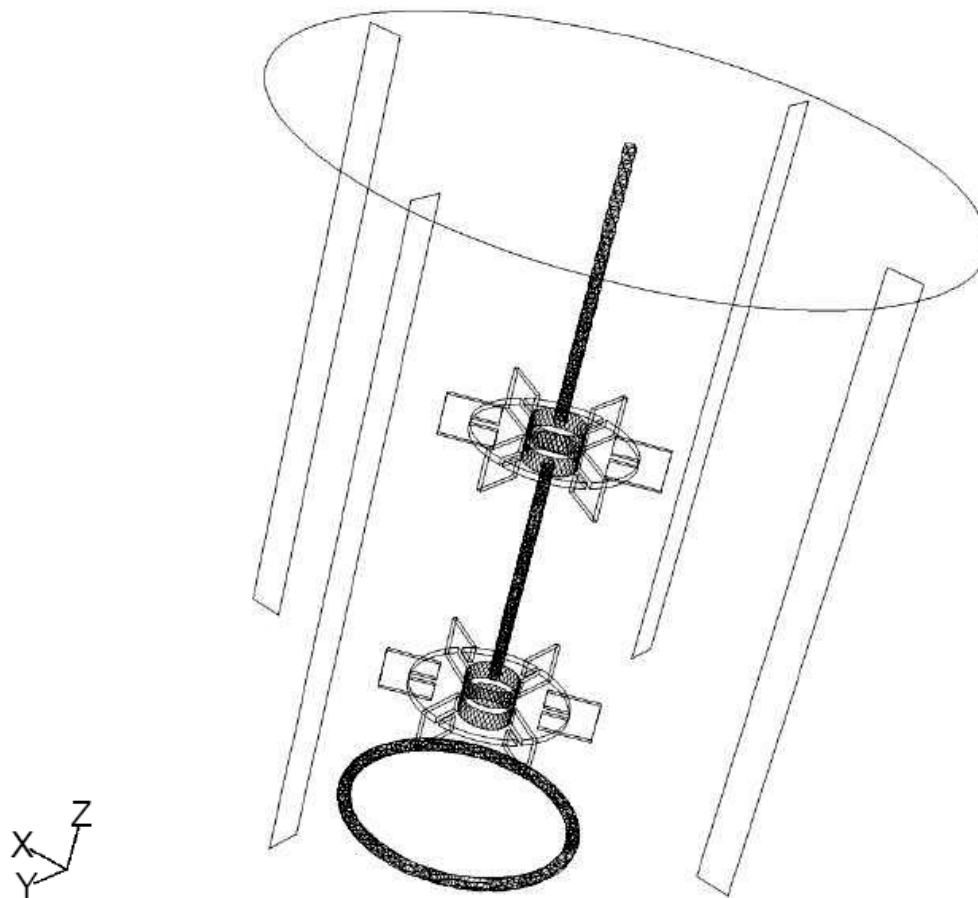


Figure V-4

Outline (3L Mixing Tank)

Jan 31, 2007
MixSim 2.1 (2.1.10)

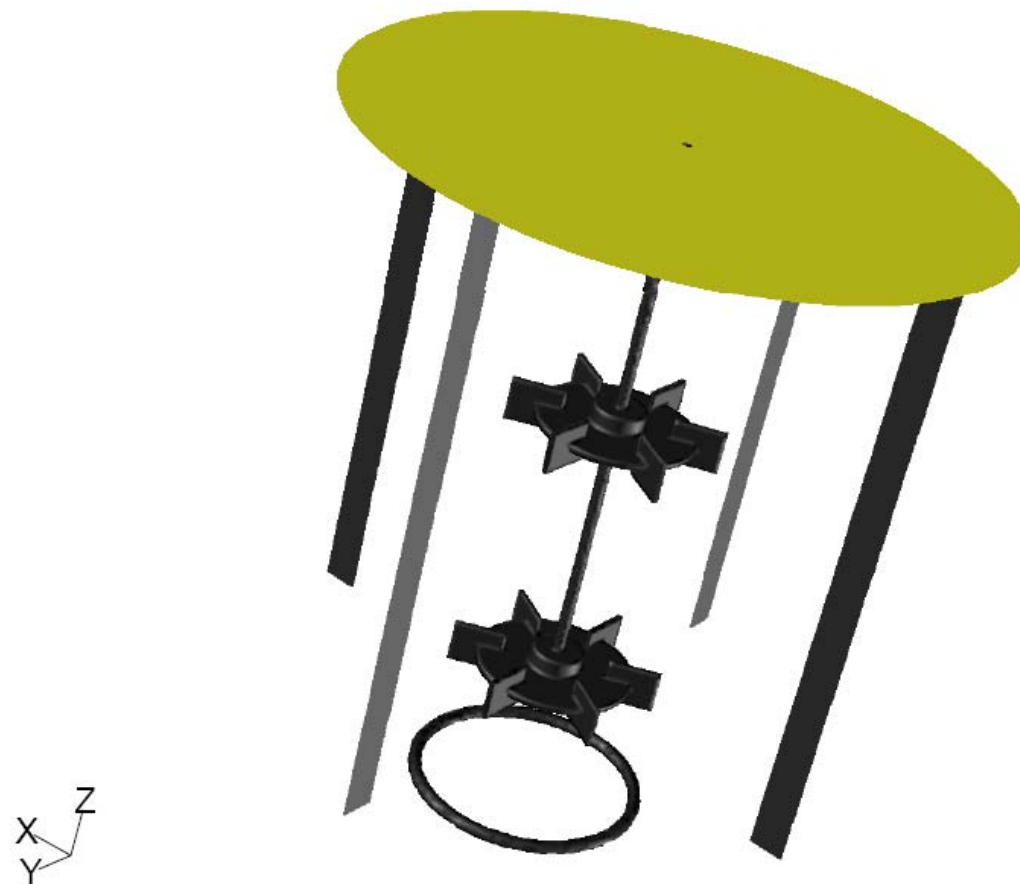


Figure V-5

Grid Face (3L Mixing Tank)

Jan 31, 2007
MixSim 2.1 (2.1.10)

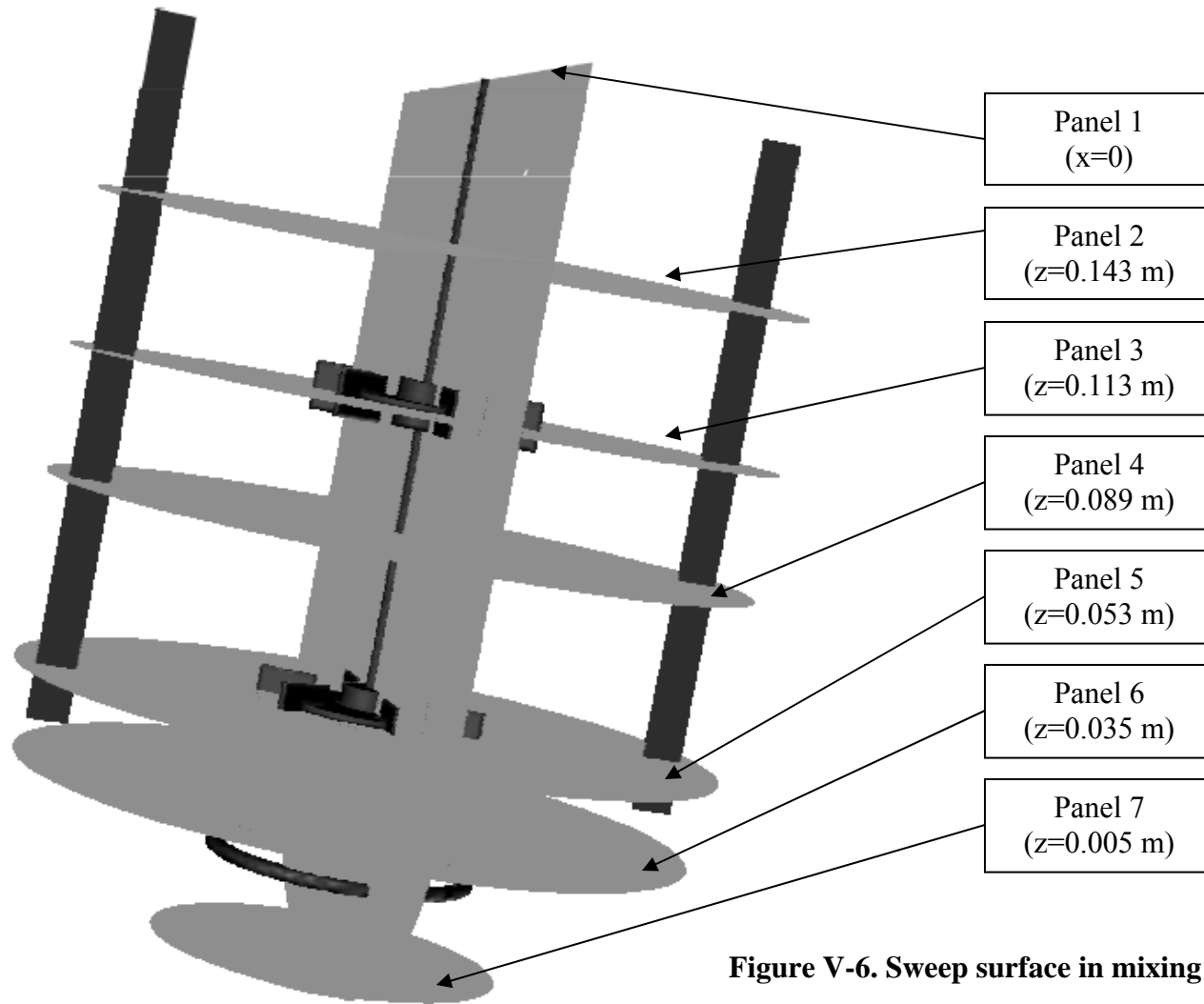


Figure V-6. Sweep surface in mixing tank

Power Law Flow Behavior Index ($0.46 \leq n \leq 0.97$)

The viscous fermentation broth used in this projects exhibited pseudoplastic rheology that is modeled quite well over a wide range of shear rates by the power law model. Consequently the power law was used to model fluid rheology in this study, with 0.0192, 0.0775, and 0.105 paschal-second at 10, 15, 20 per cent concentration respectively. The upper and lower limits for n in this study were obtained from experiments that n values for viscous fermentation broth (*Zm. mobilis* cultures) are in the range 0.46 to 0.97 during the portion batch fermentation.

Turbulence in a Tank with Baffled Rushton Impeller

The blade predicted tip velocity V_{tip} at the rotational speed of 120 RPM was 0.29 m/s (Figure V-17), and an impeller Reynolds number based on tip speed and impeller diameter was 248.6, 64.5, and 50.3 at 10, 15, and 20 per cent solid concentration respectively. The resulting simulation was in the laminar flow regime ($Re = \rho.N.D^2/\mu$), ranging from $Re = 50$ to $Re = 300$). As the impeller Reynolds number decreased, a transition to radial flow occurs. At impeller Reynolds numbers less than 100, strictly radial flow is observed.

The standard $k-\epsilon$ turbulent model was employed to treat the strong swirling flow induced by Rushton impeller. Figure V-7, V-14 and V-21 shows the predicted flow pattern for panel 1 in the mixing tank with Rushton turbine impeller respectively. The maximum and minimum velocity magnitudes were slightly different. This slight difference may be caused by different viscosity and solid concentration.

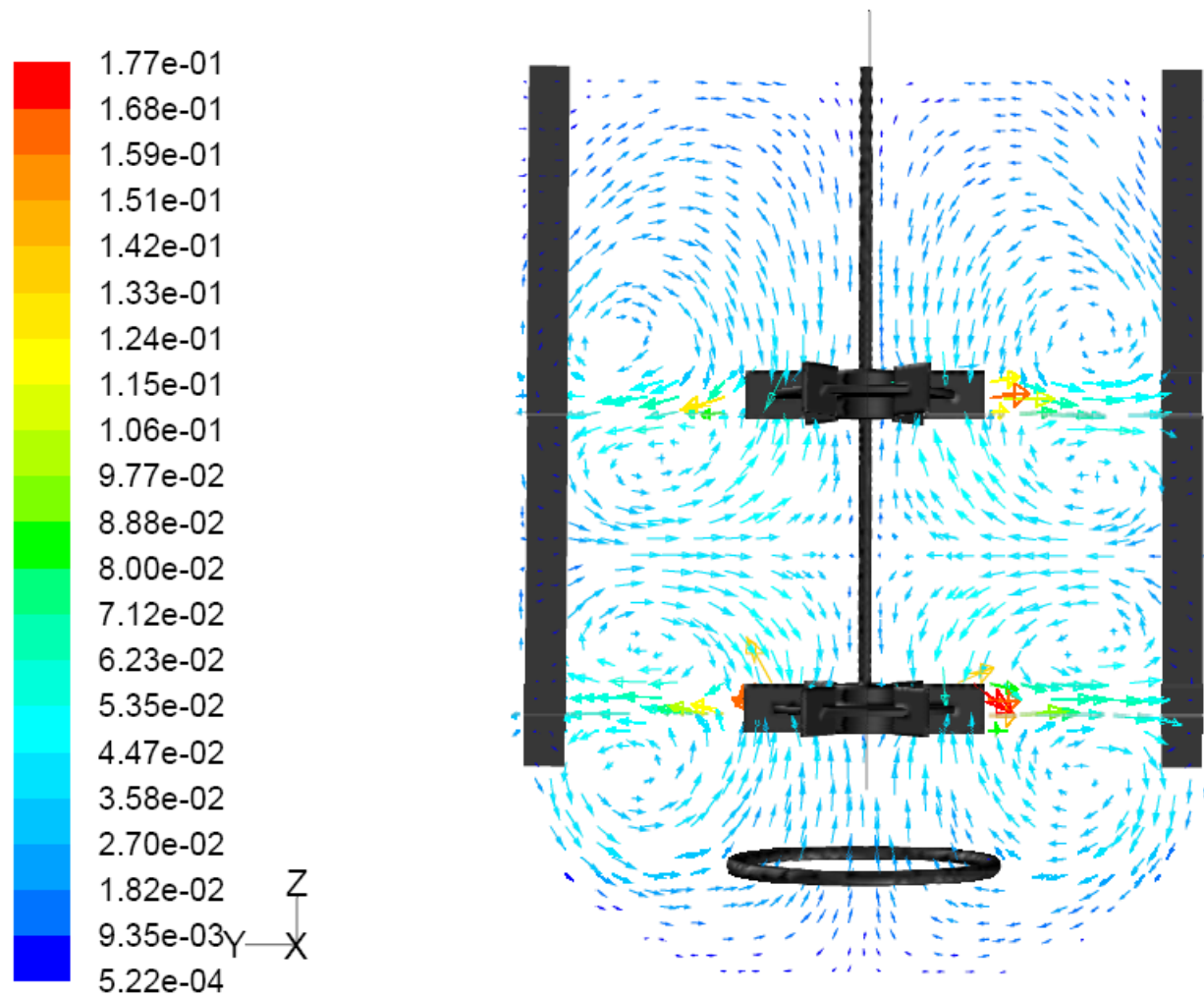


Figure V-7

10 % (w/v) Fermentation Broth
Velocity Vectors Colored By Velocity Magnitude (m/s)
Lmax=1.77E-01 Lmin=5.22E-04

Feb 07, 2007
MixSim 2.1 (2.1.10)

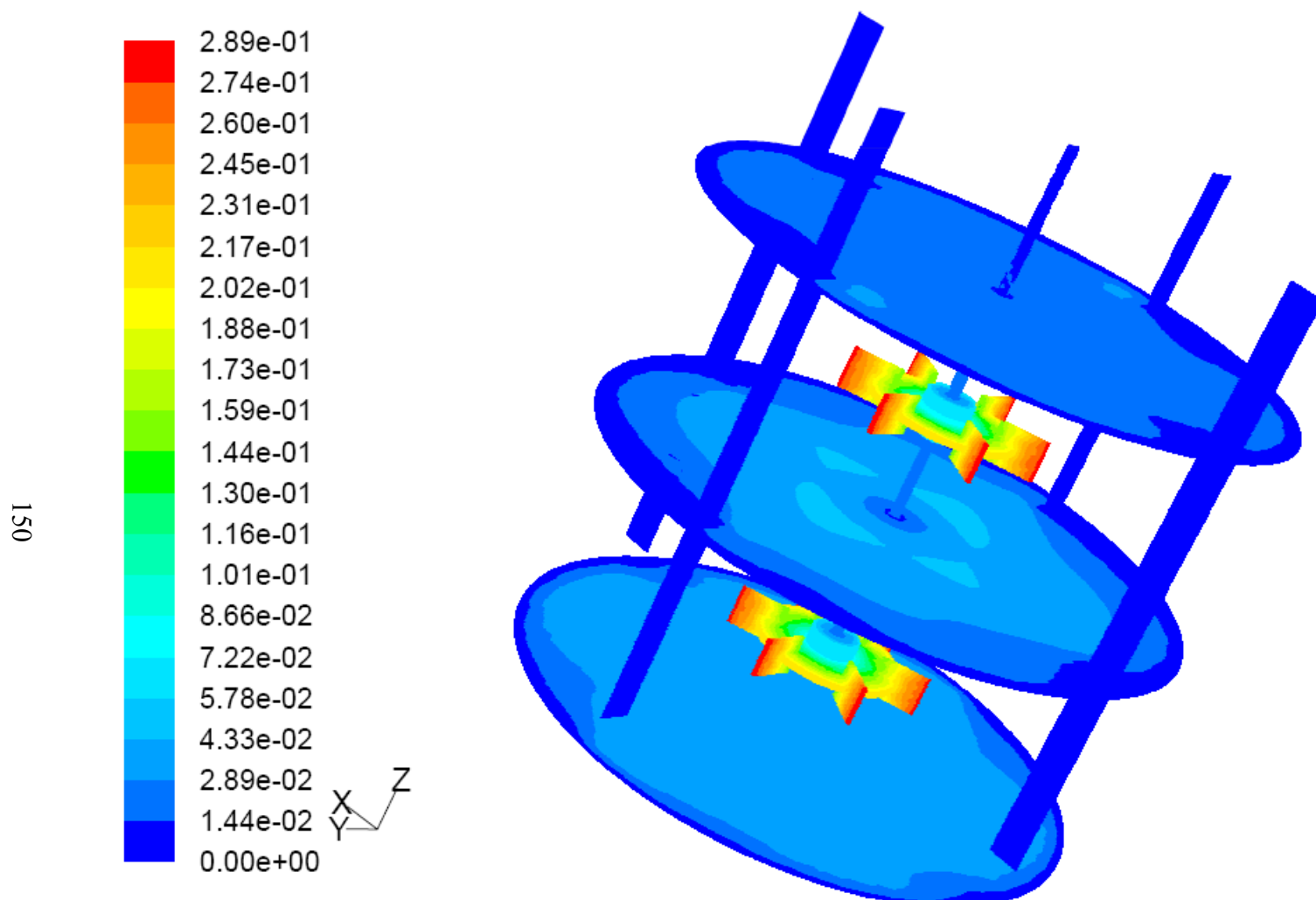


Figure V-8

10 % (w/v) Fermentation Broth
 Contours of Velocity Magnitude (m/s)
 Lmax=2.89E-01 Lmin=0.00+00

Feb 07, 2007
 MixSim 2.1 (2.1.10)

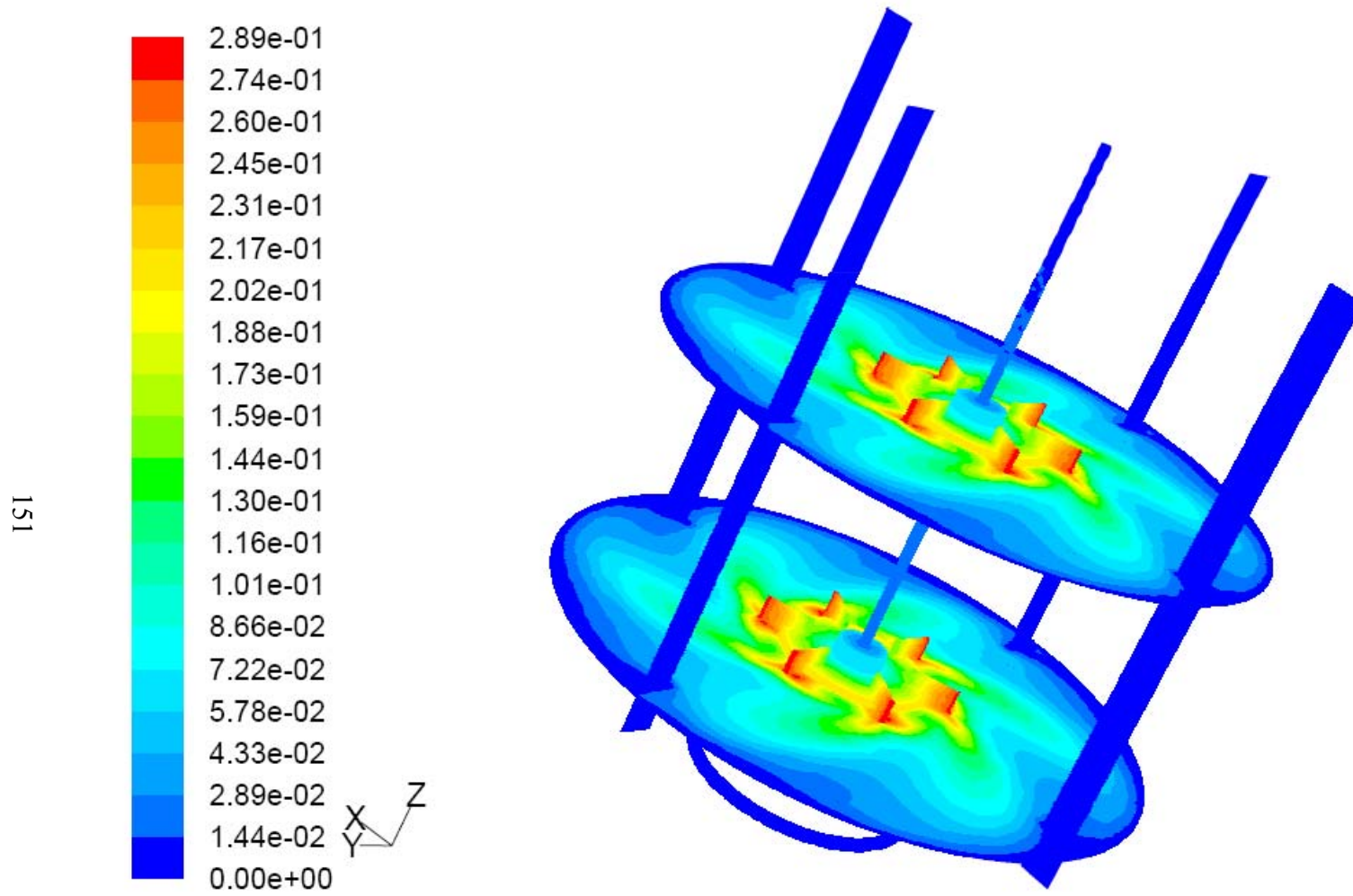


Figure V-9

10 % (w/v) Fermentation Broth
 Contours of Velocity Magnitude (m/s)
 Lmax=2.89E-01 Lmin=0.00+00

Feb 07, 2007
 MixSim 2.1 (2.1.10)

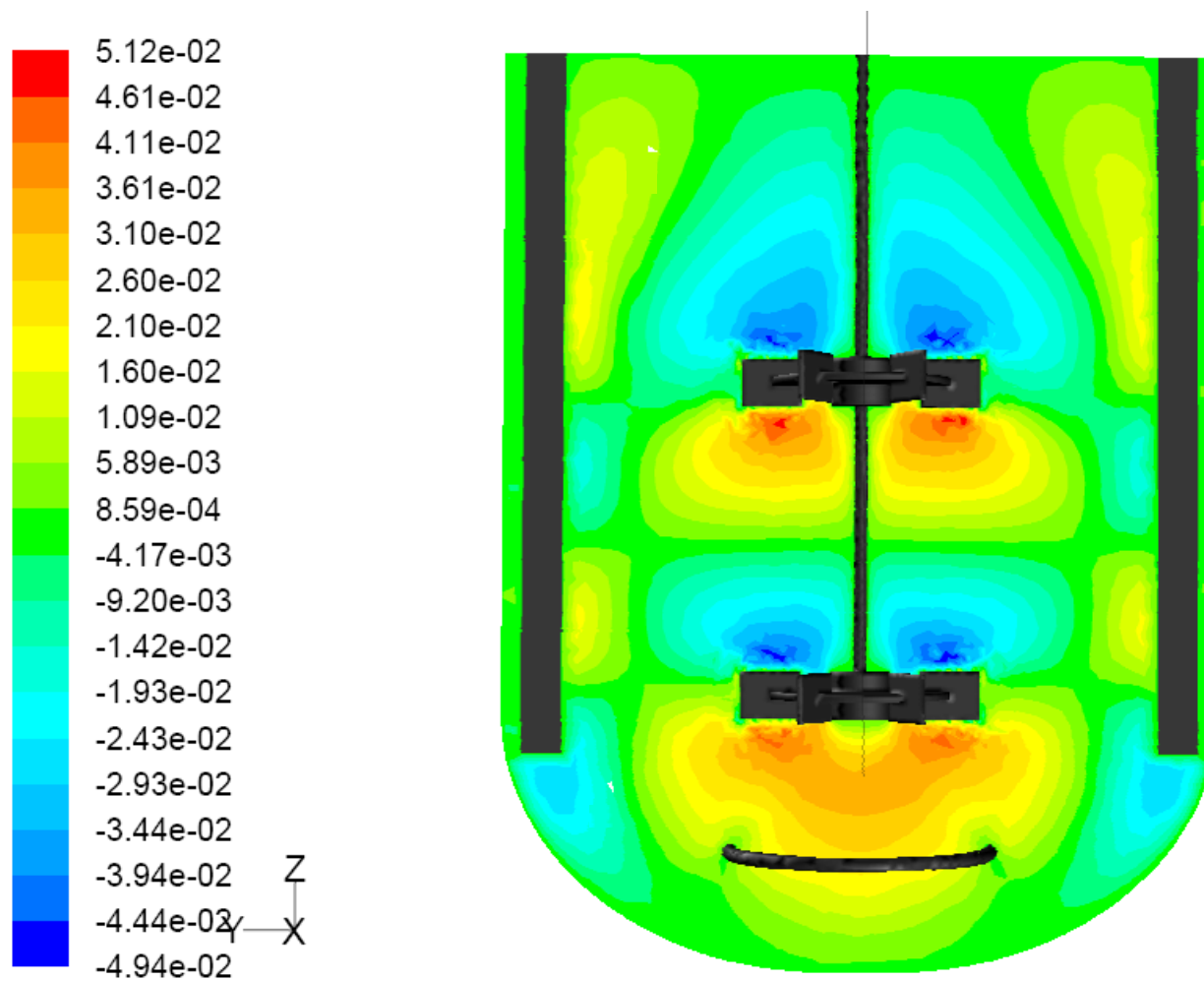


Figure V-10

10 % (w/v) Fermentation Broth
Contours of Axial Velocity (m/s)
Lmax=5.12E-02 Lmin=-4.94E-02

Feb 07, 2007
MixSim 2.1 (2.1.10)

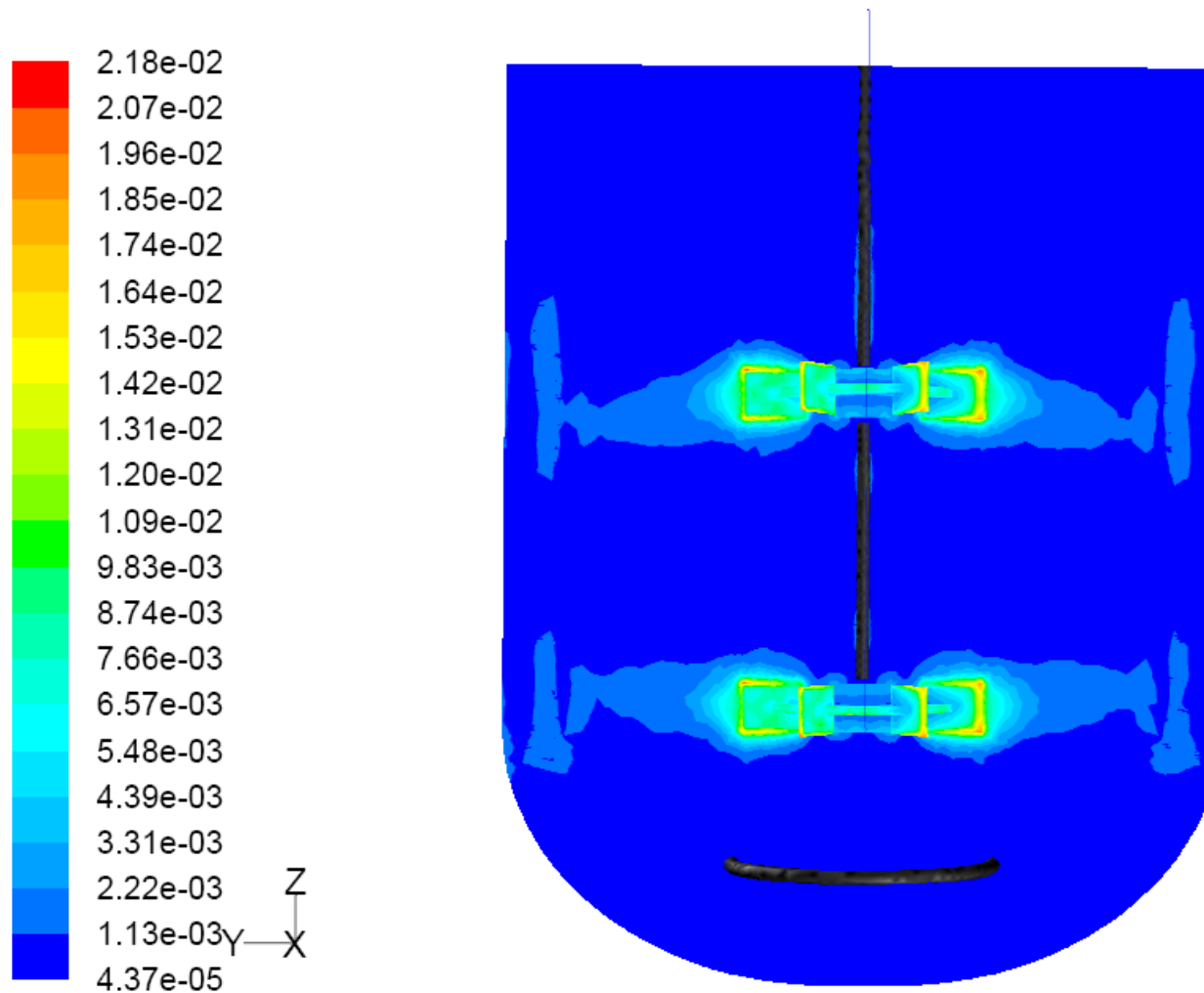


Figure V-11

10 % (w/v) Fermentation Broth
Contours of Turbulence Kinetic Energy (k) (m²/s²)
Lmax=2.18E-02 Lmin=4.37E-05

Feb 07, 2007
MixSim 2.1 (2.1.10)

154

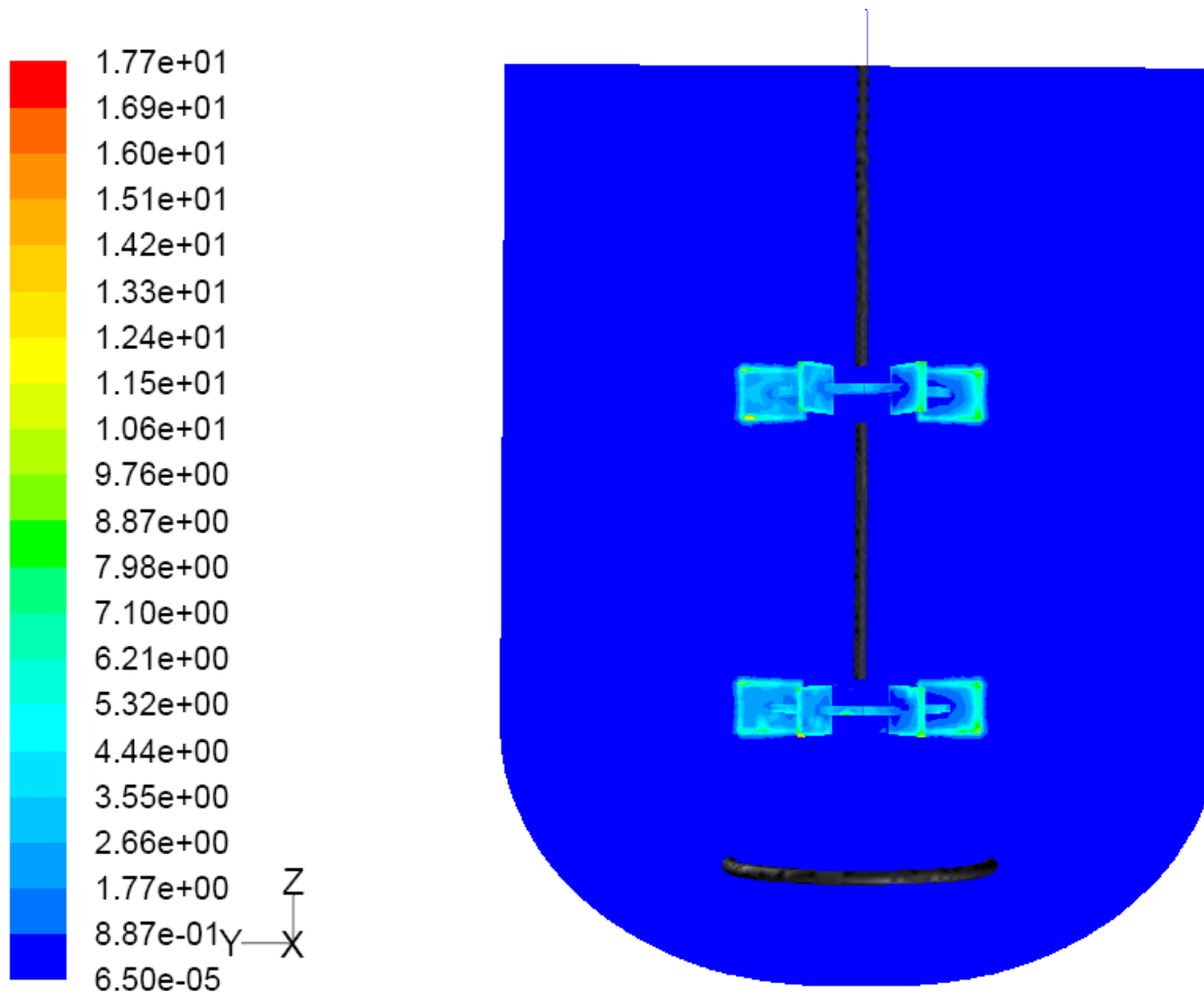


Figure V-12

10 % (w/v) Fermentation Broth
Contours of Turbulent Dissipation Rate (Epsilon) (m²/s³)
Lmax=1.77E+01 Lmin=6.50E-05

Feb 07, 2007
MixSim 2.1 (2.1.10)

155

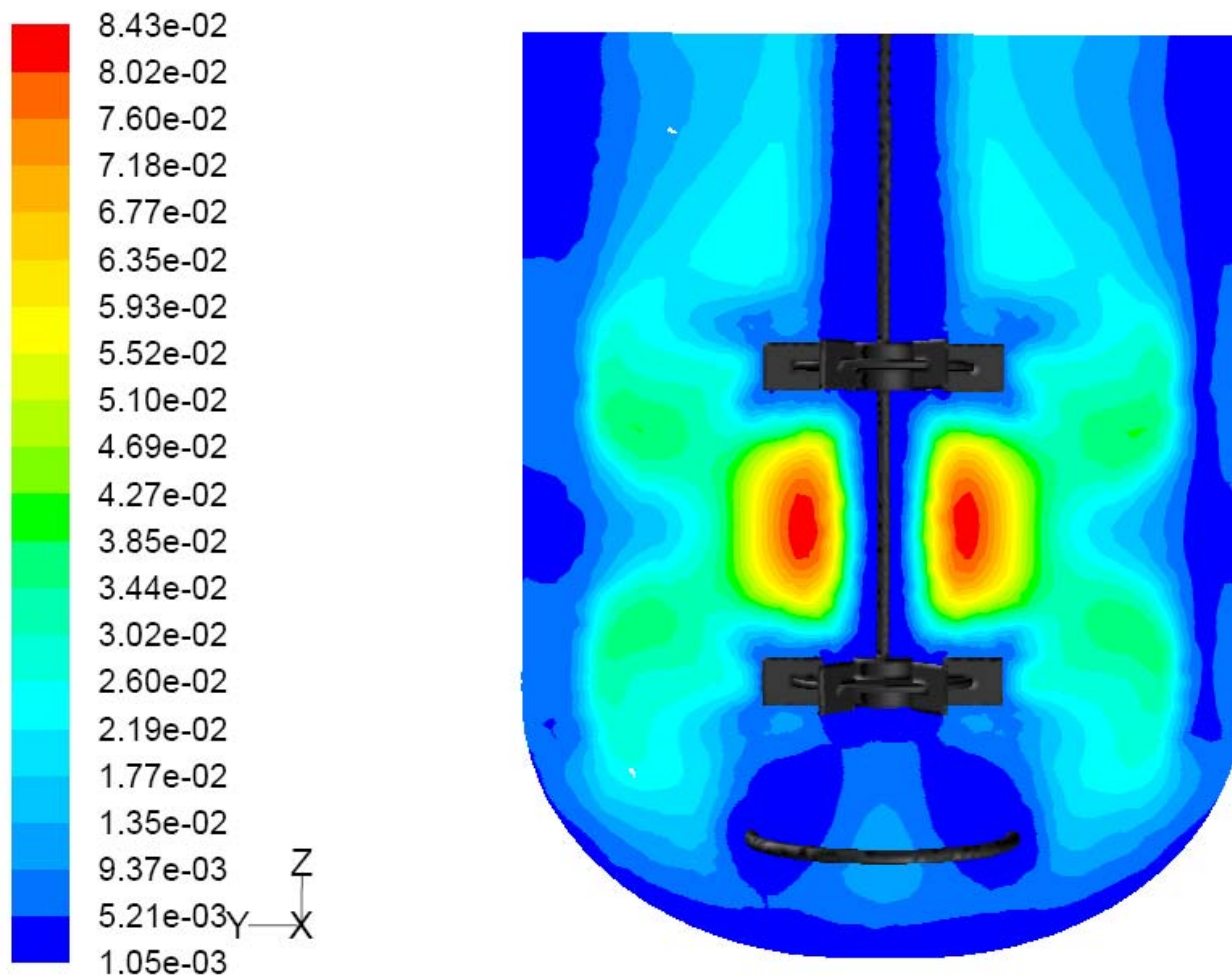


Figure V-13

10 % (w/v) Fermentation Broth
Contours of Turbulent Viscosity (kg/m-s)
Lmax=8.43E-02 Lmin=1.05E-03

Feb 14, 2007
MixSim 2.1 (2.1.10)

Predicted Velocity Distribution

Figures V-7, V-14, and V-21 show the three types of steady-state flow patterns observed with the MFR models at the vertical baffle plane (tank-cut-plane 90° , panel 1) at 10, 15, and 20 per cent solids concentration, respectively. The simulation conditions used to generate each of the flow fields are listed below each figure. The magnitude of the velocity at any point in the flow field is indicated by the length and color of the arrow at that point.

A general pattern can be described as follows: a strong flow is found right at the two impellers pushing the fluid downward at an angle of about 45° for all of the concentrated suspensions. An upward flow can be found below the two impeller, along the tank wall between the two impellers, and right off of the tip of the impellers that in turns causes some circulation. Other circulation areas can be seen around the bottom of the tank. Some of the upward flow caused by the lower impeller is drawn back to the lower impeller, while some follows the center path upward to the upper impeller. Some of the flow pumped down by the upper impellers is drawn even further down by the lower impeller, with some other circulating back to the top. Little flow occurs in the region the fermentor wall. This primary circulation pattern is completed as the liquid re-enters the impeller region at the top impeller. As a result of this flow pattern, there is virtually no movement of fluid between gas-liquid interface and the top impeller.

The three plots generally show similar flow patterns with a strong primary circulation loop in the lower half of the tank and a smaller secondary loop below the impeller. Here in the discharge jet, there are not great differences the predicted

solution between 10 per cent and 20 per cent around the impellers. This explains the portion loading of substrates could reduce viscosity for the high solid fermentation compared to traditional high substrate loading.

Axial Velocity

The contour of the axial velocity profile between tank bottom and fermentor wall is highly dependent on the value of the flow behavior index (n). As expected, higher values of n ($n= 0.97$) produce a more parabolic profile, whereas low n values ($n=0.46$) produce a more blunt profile. For most of the conditions tested for this study, the circumferential averaging axial velocity are plotted for the different solid concentration as function of tank radial position on the bottom panel of the mixing tank in Figure V-27 though V-31. The average velocities computed in the study varied from 0 to 0.003 m/s on the panel 7 (Figure V-31). Compared to water data, the suspension velocities were smaller..

Figures V-10 through V-16 and V-23 are contour plots derived from the quadratic model, showing the effects of impeller speed (120 rpm) on average velocity (m/s) in this region for three different concentration suspensions. From the contour plots, it is evident that the maximum values of V_{tip} ($0.051V_{tip}$ for 10 percent, $0.046V_{tip}$ for 15 percent, $0.045V_{tip}$ for 20 percent) are found below the agitator. The maximum V_{tip} increases as n increases.

On the other hand, a relatively weak upward flow was found near the center bottom of the tank and below the baffle, creating the circulation region. Specifically, the

reverse swirling suspension has been measured in a small region in the top of the upper impeller and in the corner of baffles with a minimal velocity ($-0.049 V_{tip}$, $-0.048 V_{tip}$, and $-0.049 V_{tip}$). These results imply that near the center bottom of the tank, the fluid axial velocities of the fluid were not uniform, perhaps resulting in the solid suspension staying on the bottom of tank. These phenomena were more significant as solid concentration increased.

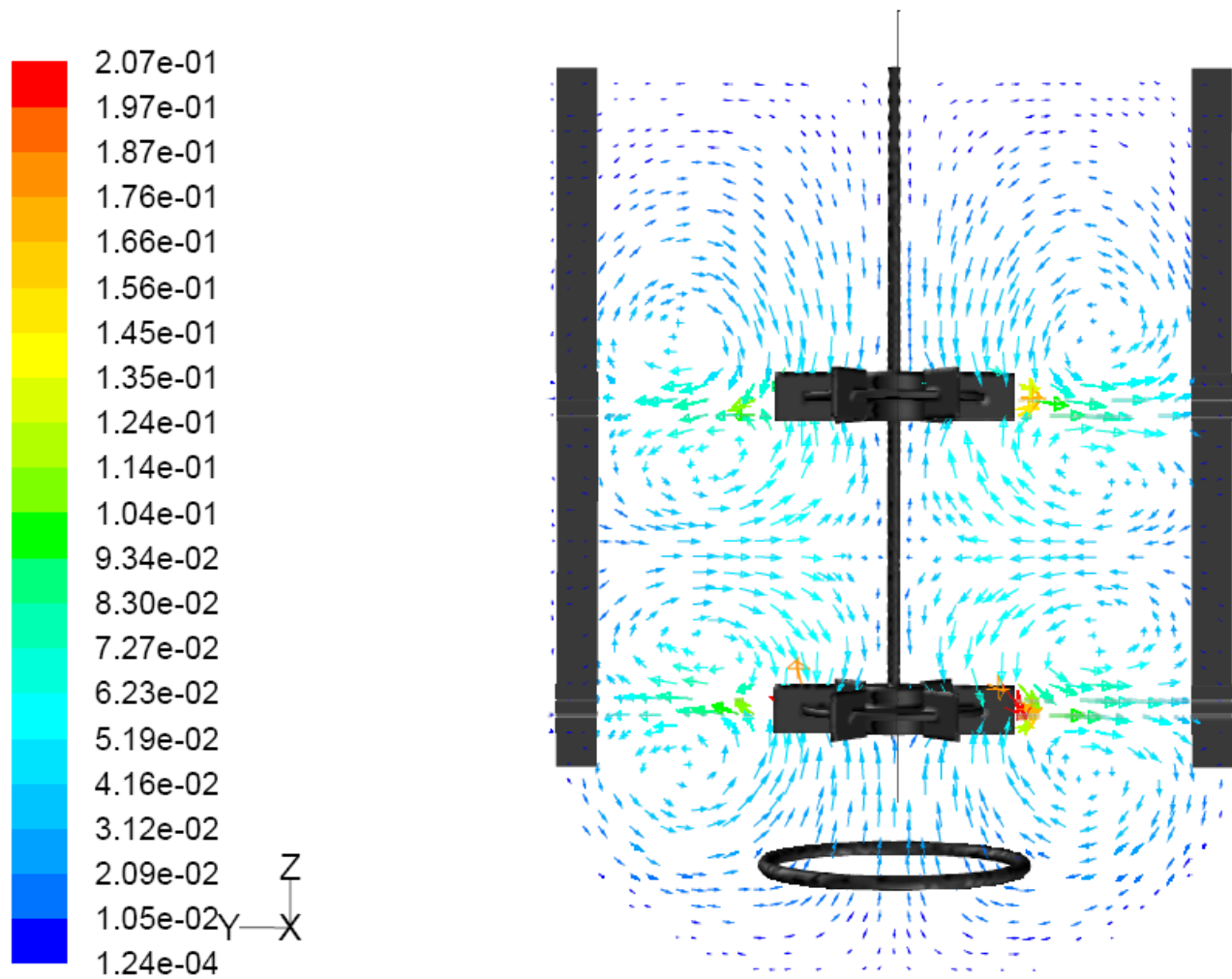


Figure V-14

15 % (w/v) Fermentation Broth
Velocity Vectors Colored By Velocity Magnitude (m/s)
Lmax=2.07E-01 Lmin=1.24E-04

Feb 07, 2007
MixSim 2.1 (2.1.10)

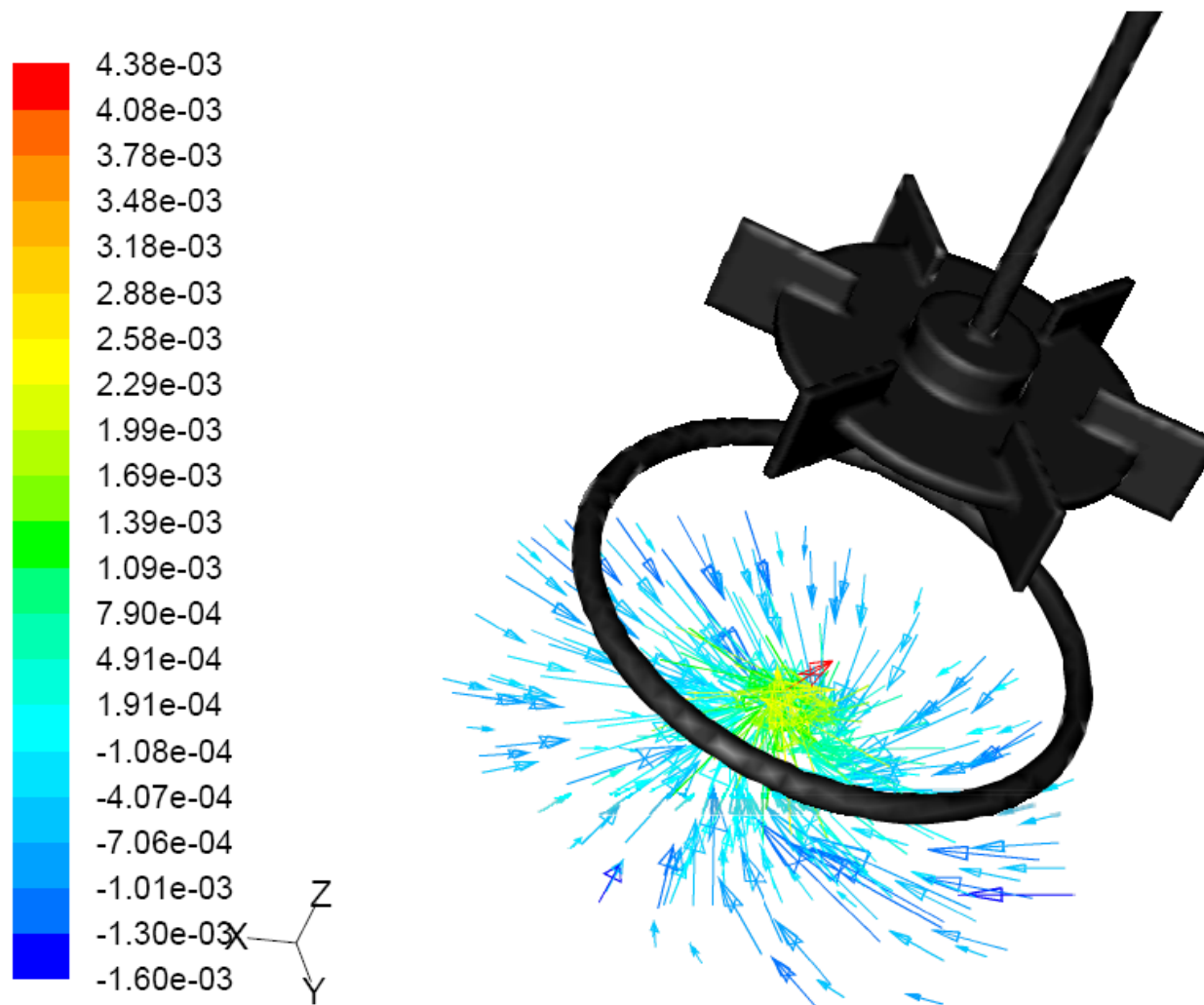


Figure V-15

15 % (w/v) Fermentation Broth
Velocity Vectors Colored By Axial Velocity (m/s)
Lmax=4.63E-02 Lmin=-1.60E-03

Feb 07, 2007
MixSim 2.1 (2.1.10)

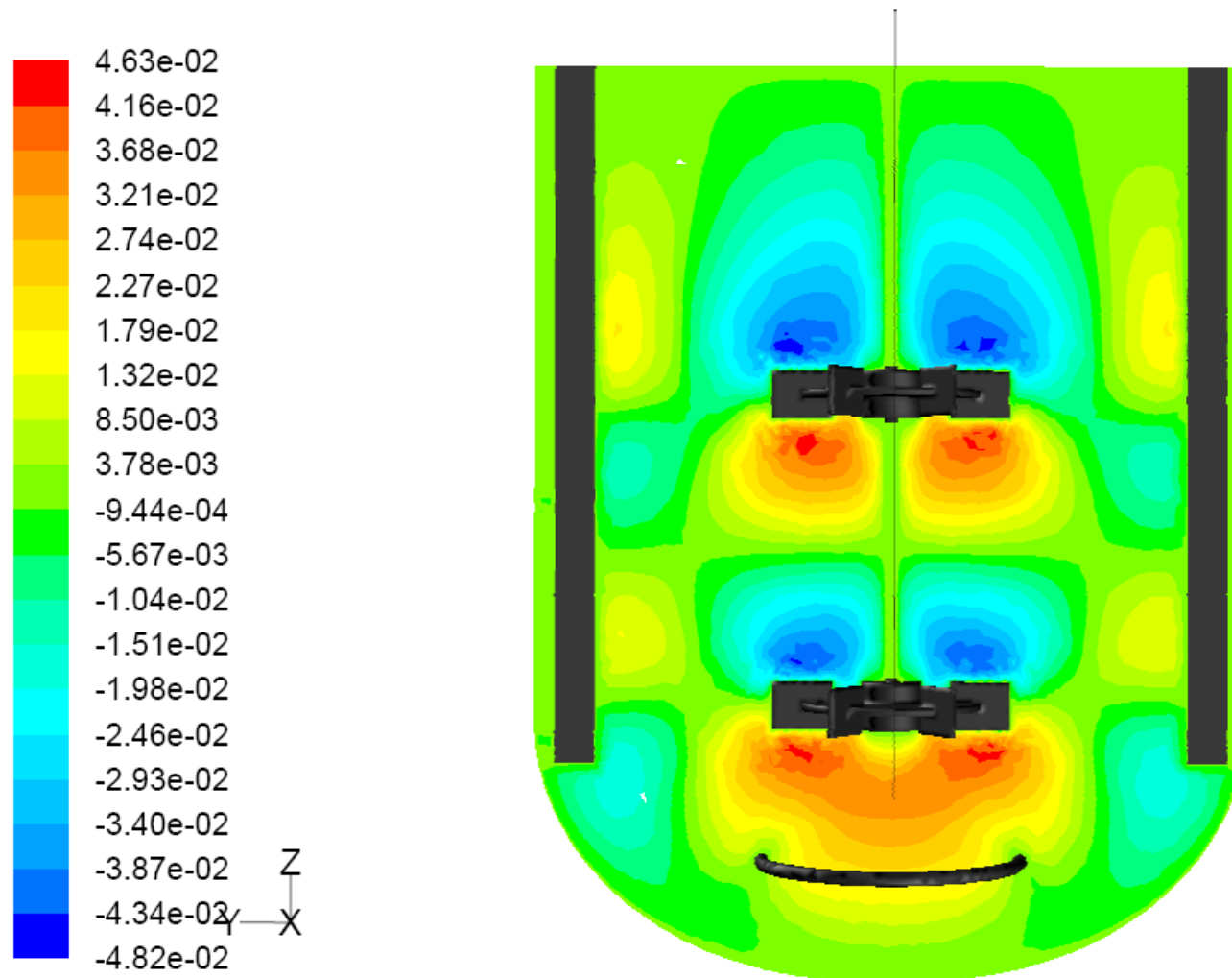


Figure V-16

15 % (w/v) Fermentation Broth
 Contours of Axial Velocity (m/s)
 Lmax=4.63E-02 Lmin=-4.82E-02

Feb 07, 2007
 MixSim 2.1 (2.1.10)

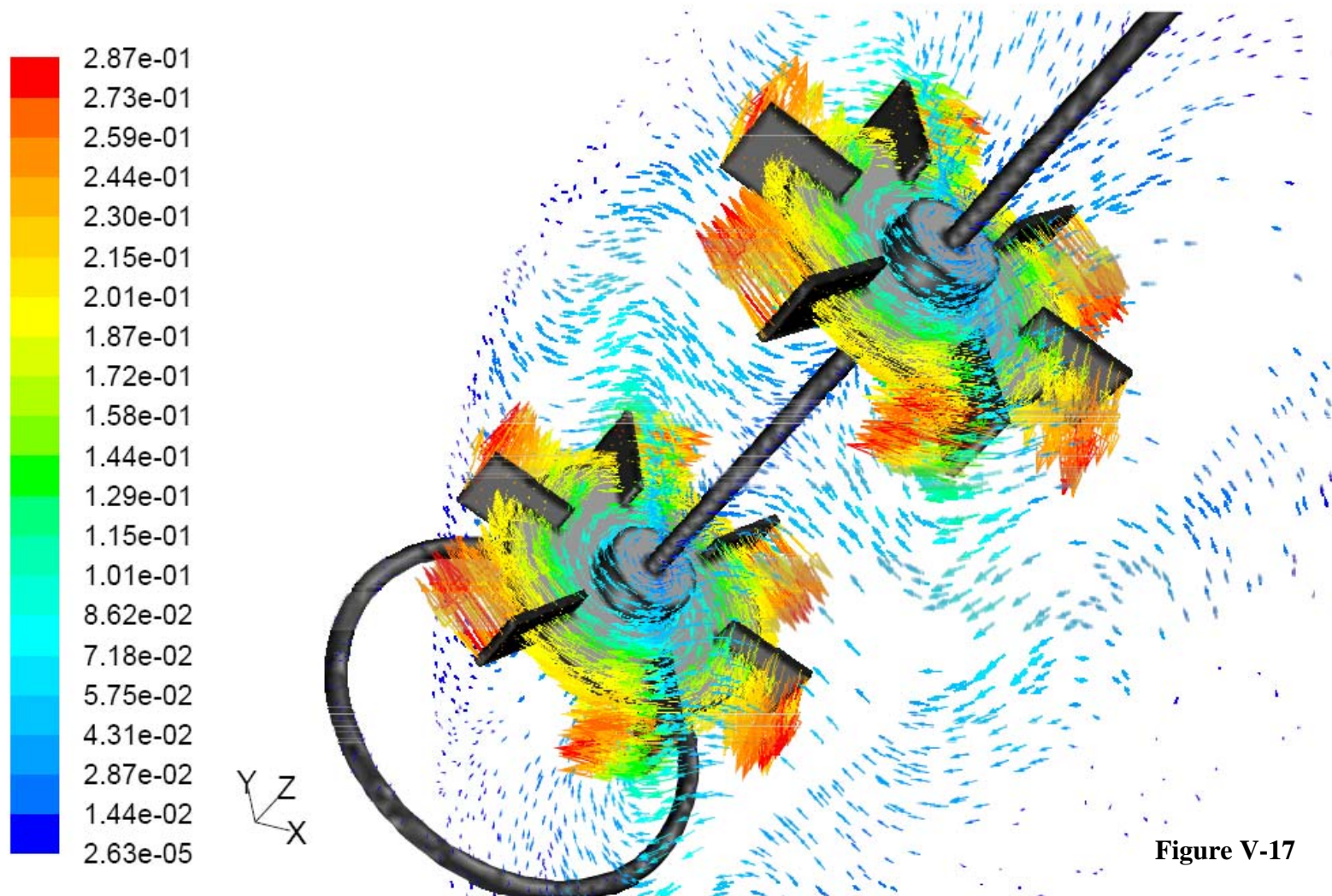


Figure V-17

15 % Fermentation Broth
Velocity Vectors Colored By Velocity Magnitude (m/s)
Lmax=2.87E-01 Lmin=2.63E-05

Feb 08, 2007
MixSim 2.1 (2.1.10)

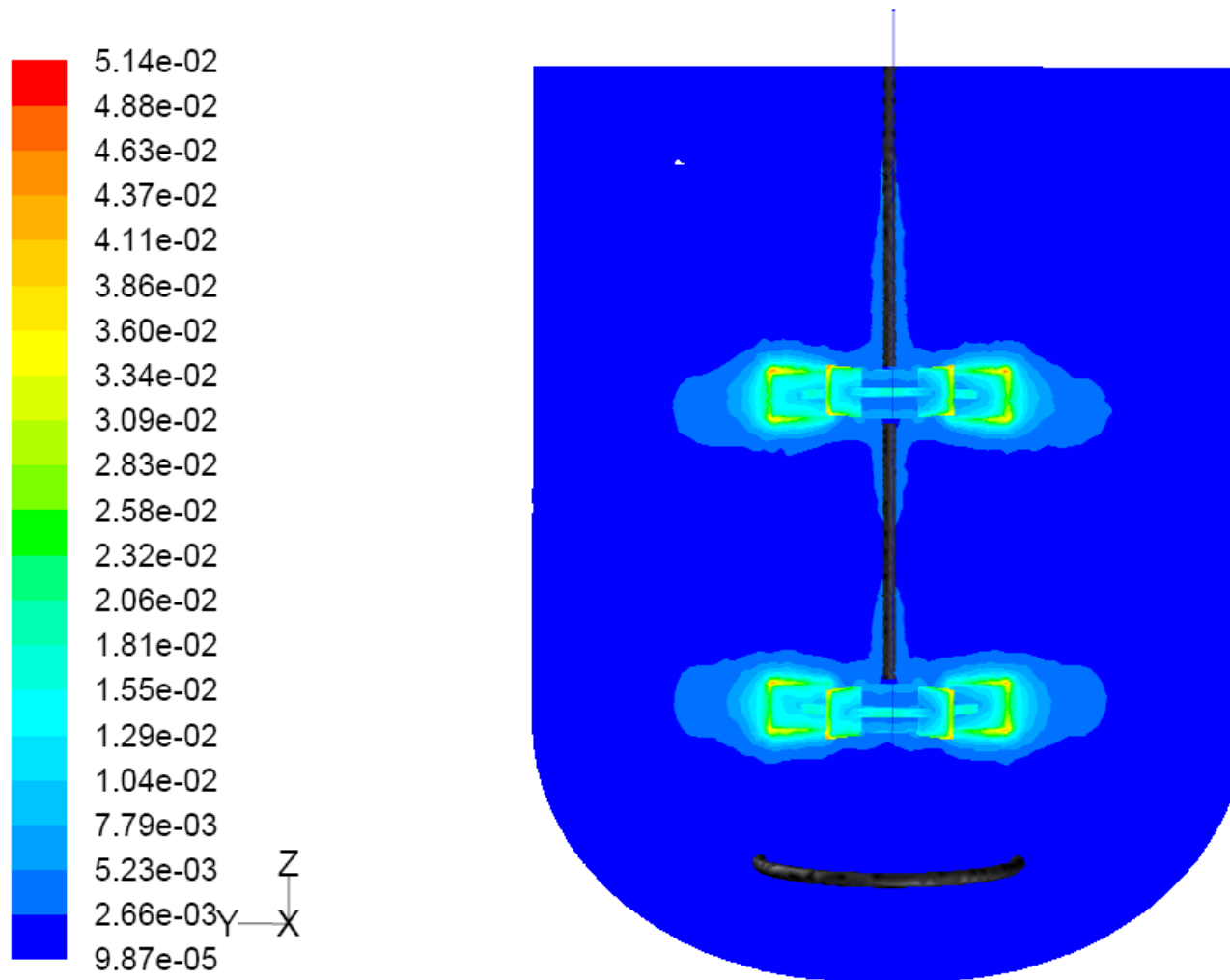


Figure V-18

15 % (w/v) Fermentation Broth
Contours of Turbulence Kinetic Energy (k) (m²/s²)
Lmax=5.14E-02 Lmin=9.87E-05

Feb 07, 2007
MixSim 2.1 (2.1.10)

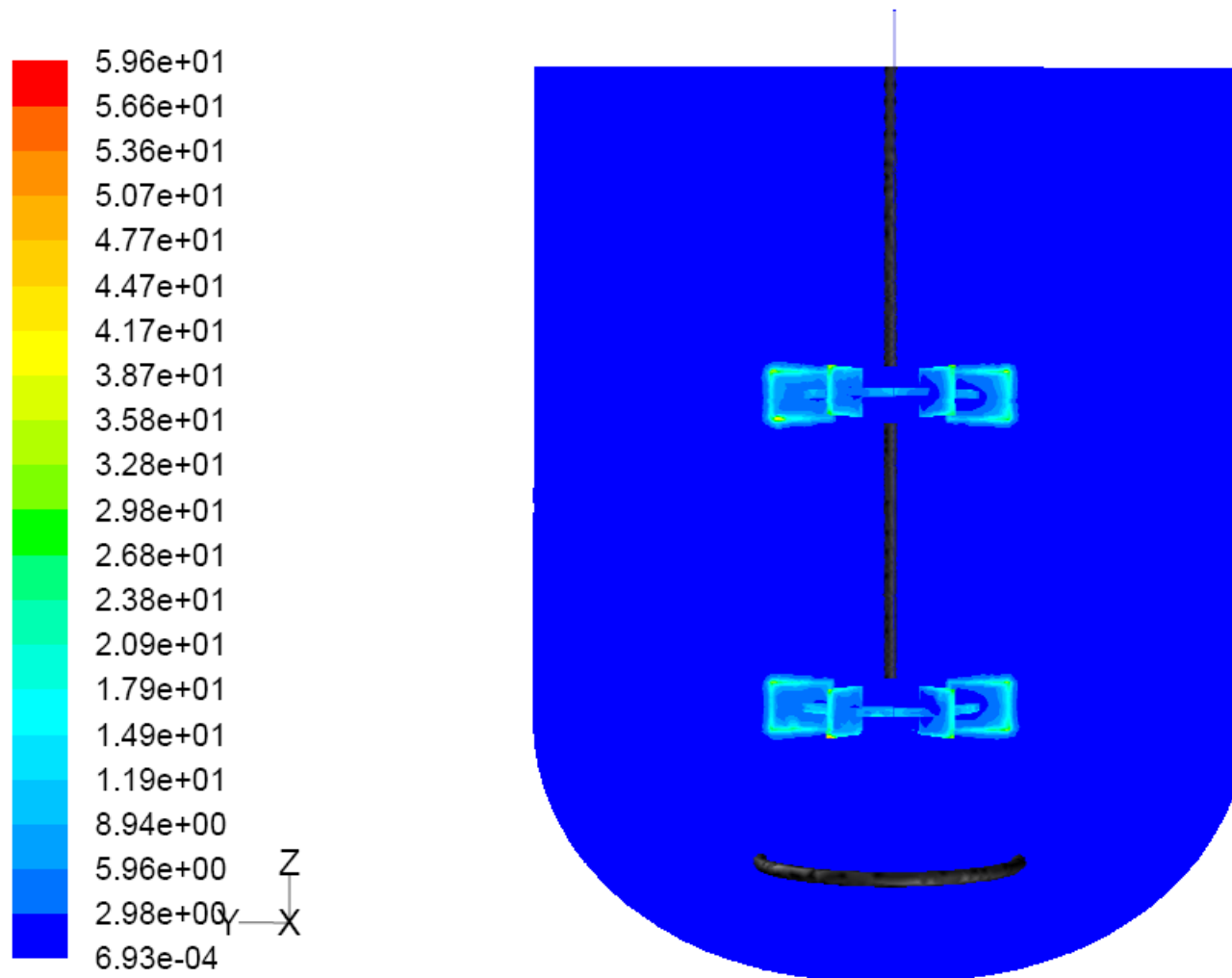


Figure V-19

15 % (w/v) Fermentation Broth
Contours of Turbulent Dissipation Rate (Epsilon) (m²/s³)
Lmax=5.96E+01 Lmin=6.93E-04

Feb 07, 2007
MixSim 2.1 (2.1.10)

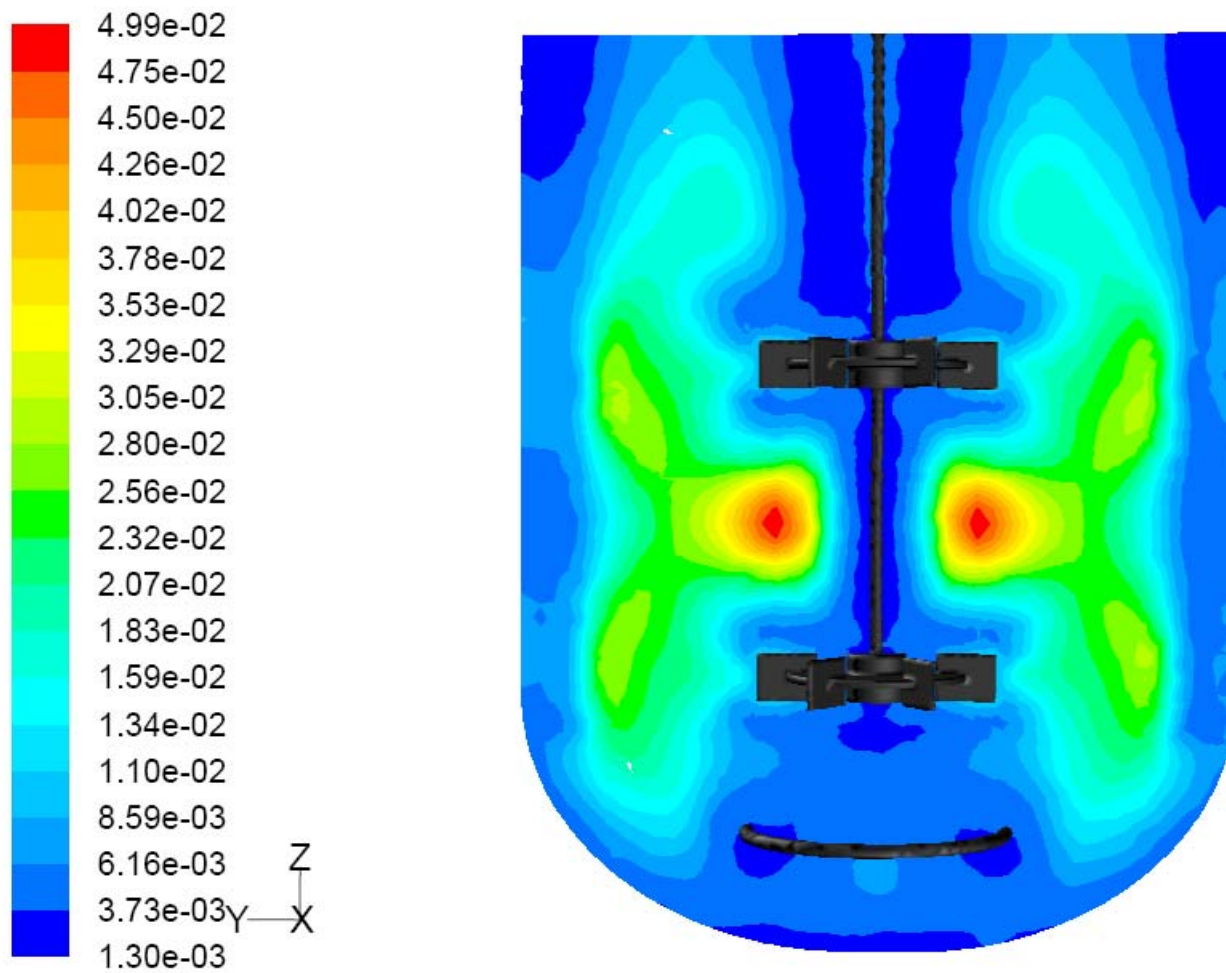


Figure V-20

15 % (w/v) Fermentation Broth
Contours of Turbulent Viscosity (kg/m-s)
 $L_{max}=4.99 \times 10^{-2}$ $L_{min}=1.30 \times 10^{-3}$

Feb 14, 2007
MixSim 2.1 (2.1.10)

Stagnant and Slow Flow Zones

From the contour plots, conditions promoting essentially stagnant flow can be identified when the average velocity is on or below the 0 m/s contour color. Of course, if anaerobic fermentation broth between the corner of baffles and the outer wall was completely stagnant, the cells would quickly become starved of nitrogen, nutrient, and stop synthesizing product. The model indicates that, with $n = 0.96, 0.55,$ and $0.46,$ flow up the under baffle region can be stagnant at the impeller speed 120 rpm and the distance between tank bottom and the baffles is 0.05 m.

In summary, it seems that, in addition to there being a potential for nitrogen nutrition starvation in the upper portion of the baffle-wall region when flow through this region is slow, there is also a potential for stagnant flow and nitrogen and nutrition starvation in the region between the top impeller and the gas-liquid interface when flow through the fermentor wall region is slow. In real fermentations, there is some surface aeration near the gas-liquid interface. As expected, the simulations with higher values of n exhibited larger low flow space.

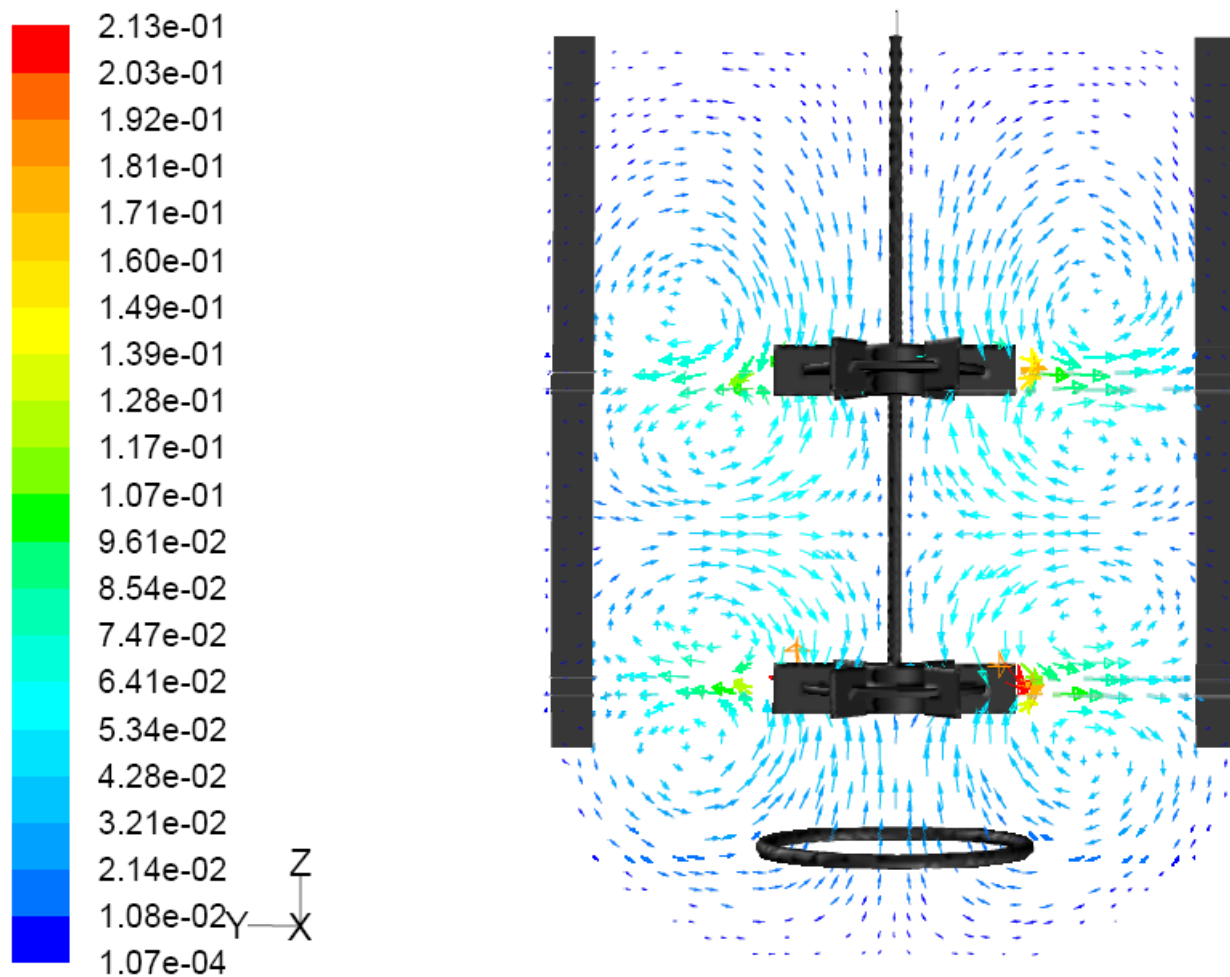


Figure V-21

20 % (w/v) Fermentation Broth
 Velocity Vectors Colored By Velocity Magnitude (m/s)
 Lmax=2.13E-01 Lmin=1.07E-04

Feb 07, 2007
 MixSim 2.1 (2.1.10)

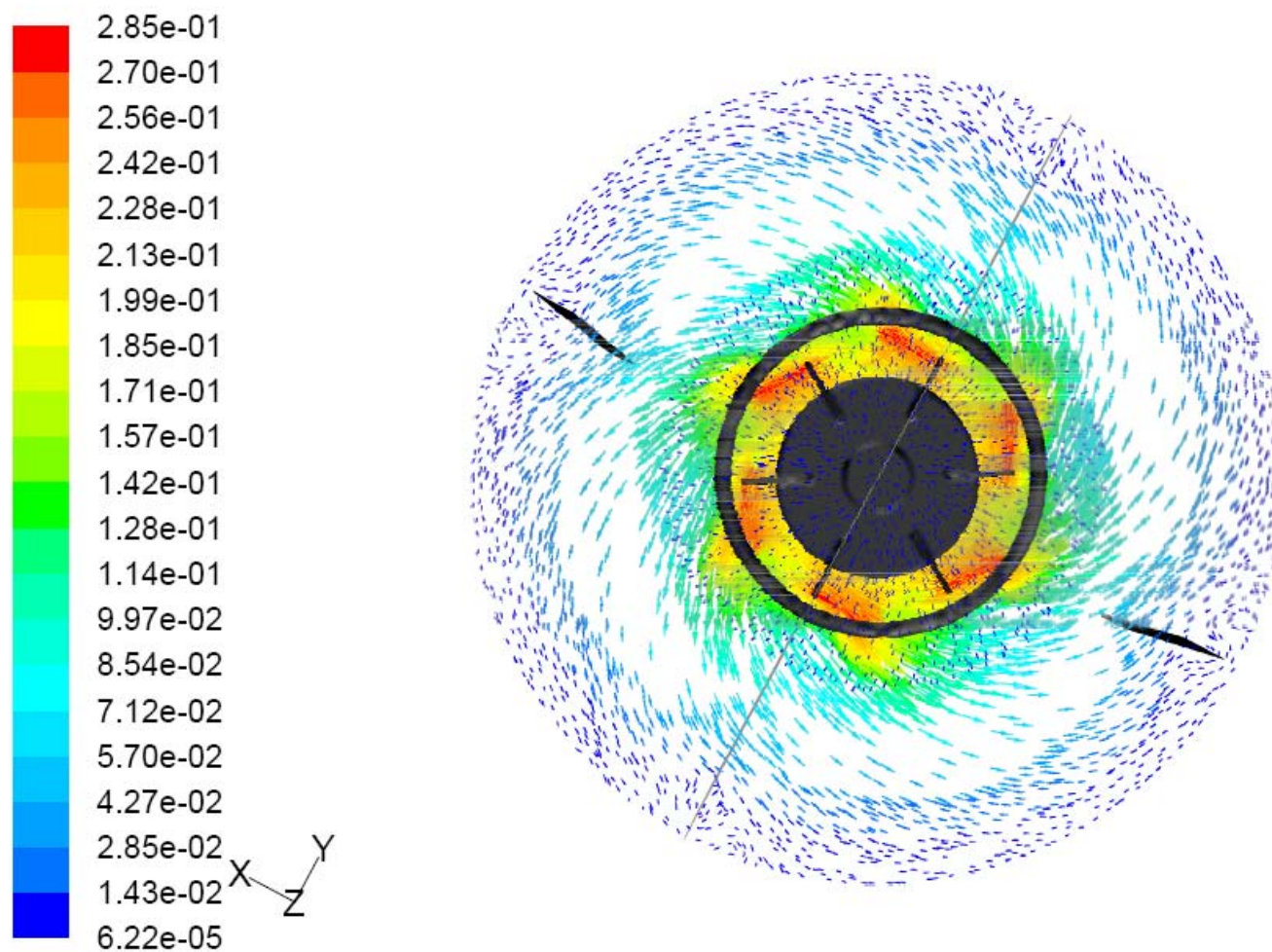


Figure V-22

20 % (w/v) Fermentation Broth
Velocity Vectors Colored By Velocity Magnitude (m/s)
Lmax=2.85E-01 Lmin=6.22E-05

Feb 07, 2007
MixSim 2.1 (2.1.10)

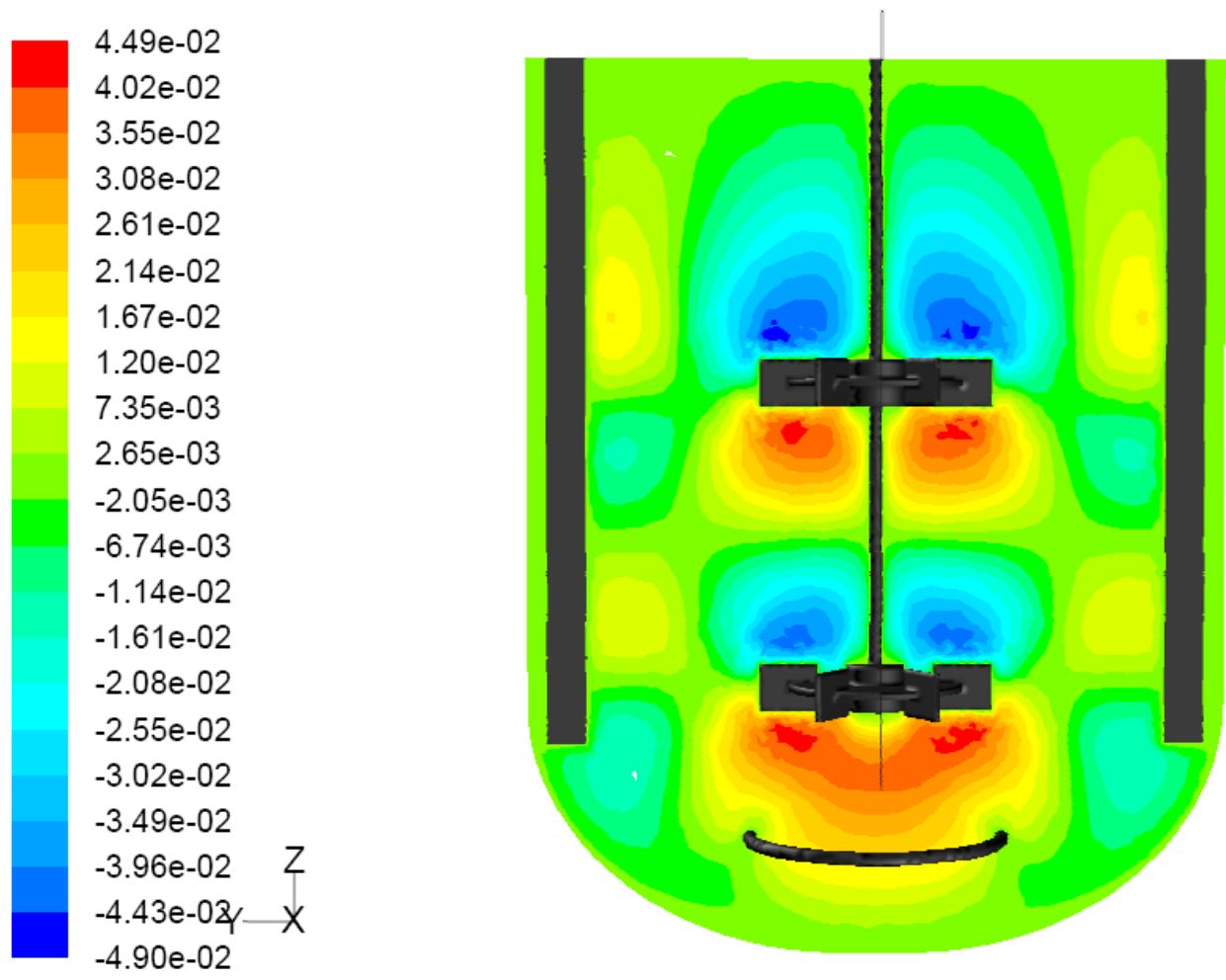


Figure V-23

20 % (w/v) Fermentation Broth
 Contours of Axial Velocity (m/s)
 Lmax=4.49E-02 Lmin=-4.90E-02

Feb 13, 2007
 MixSim 2.1 (2.1.10)

170

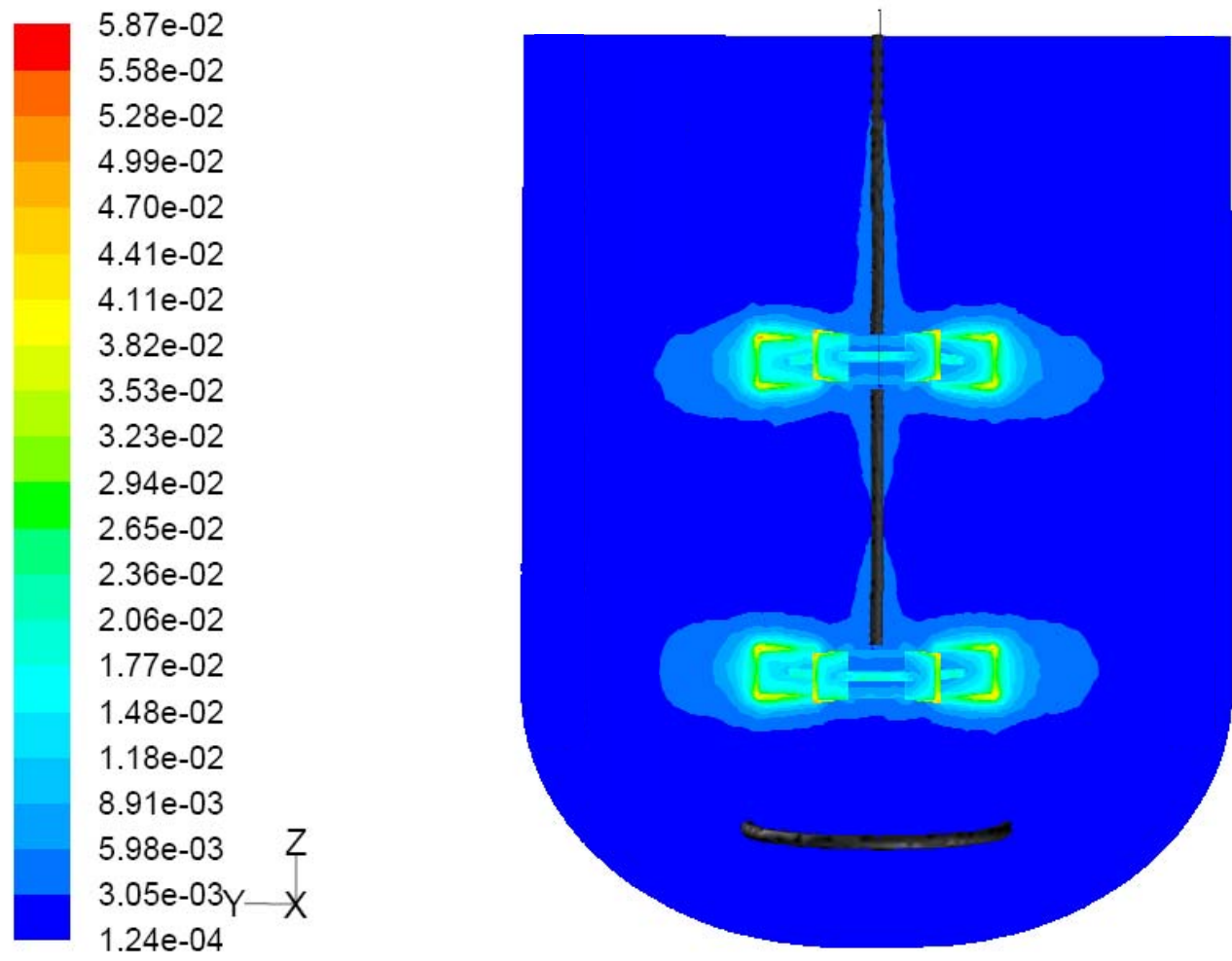


Figure V-24

20 % (w/v) Fermentation Broth
Contours of Turbulence Kinetic Energy (k) (m2/s2)
Lmax=5.78E-02 Lmin=1.24E-04

Feb 07, 2007
MixSim 2.1 (2.1.10)

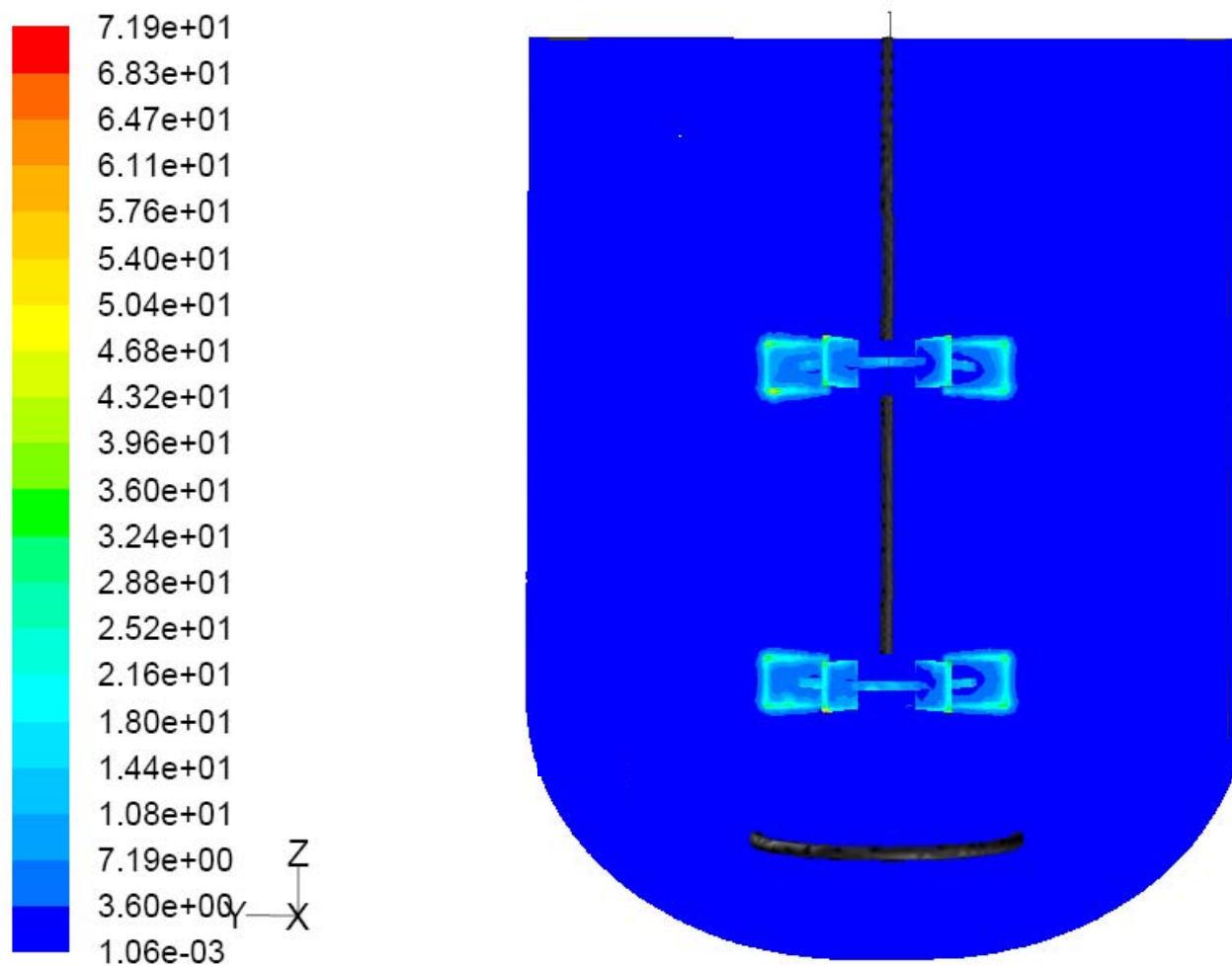


Figure V-25

20 % (w/v) Fermentation Broth
 Contours of Turbulent Dissipation Rate (Epsilon) (m²/s³)
 Lmax=7.19E+01 Lmin=1.06E-03

Feb 07, 2007
 MixSim 2.1 (2.1.10)

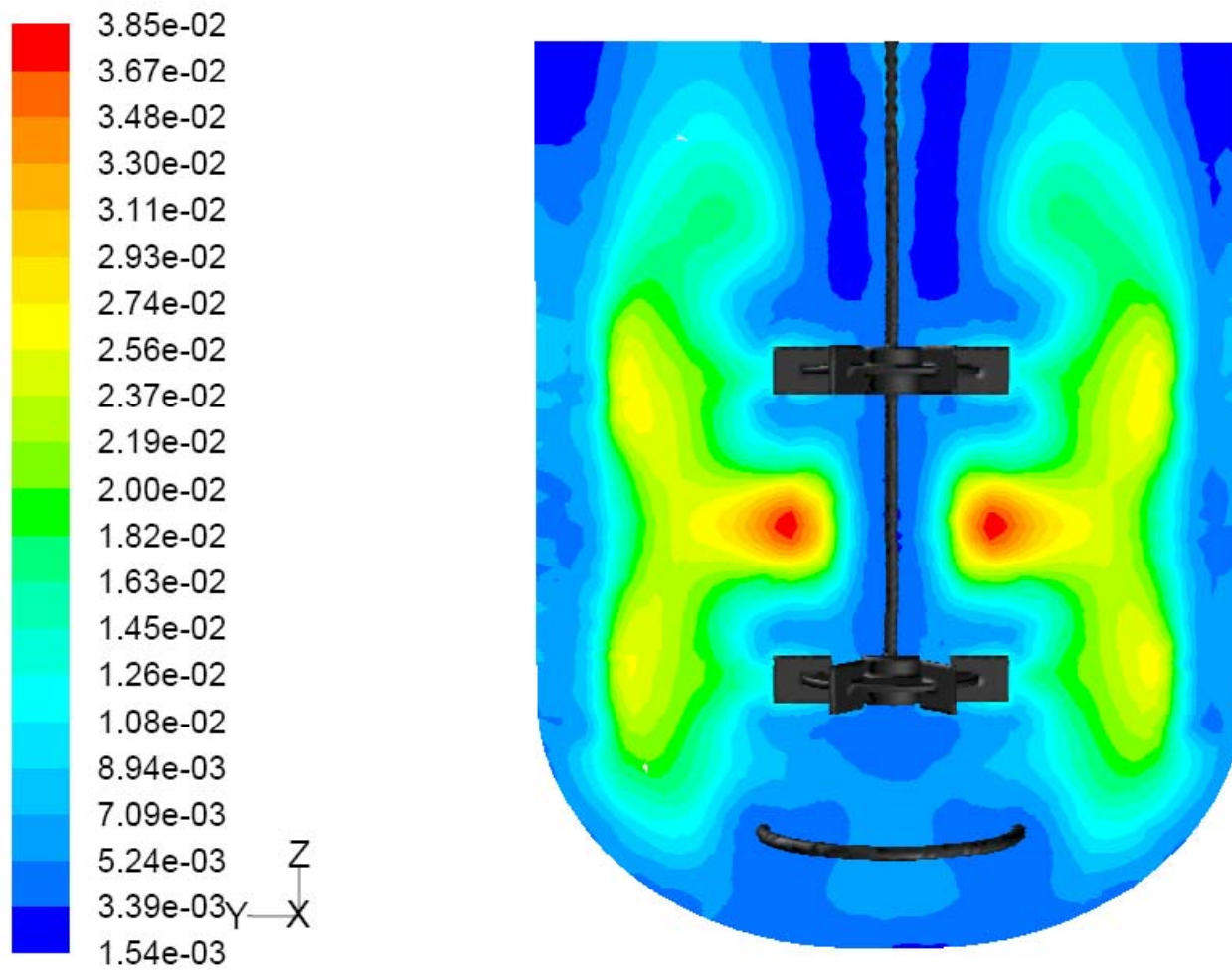


Figure V-26

20 % (w/v) Fermentation Broth
Contours of Turbulent Viscosity (kg/m-s)
Lmax=2.89E-01 Lmin=0.00E+00

Feb 13, 2007
MixSim 2.1 (2.1.10)

Shear Stress and Turbulent Viscosity in Mixing Tank

An understanding of the velocity flow fields is a prerequisite to understanding mixing and key physical parameters such as shear stress, flow fluctuations, and vorticity fields. The circumferential averaging shear stresses are plotted for the different solid concentration as function of tank radial position on three different panels by z direction of the mixing tanking in Figures V-32 through V-35. The fluid suspension near the blade wall is accelerated by an imbalance of shear forces. The average maximum values determined by circumferential averaging model on the middle of tank were ($0.008 \tau_{avg}$ for 10 per cent, $0.025 \tau_{avg}$ for 15 per cent, and $0.035 \tau_{avg}$ for 20 per cent) near the impellers.

Figures V-13, 20, and 26 show the contour of the distribution of the turbulent viscosity, modeled by three different flow behavior indexes. The maximum viscosity were found in the midpoint ($z=0.09\text{m}$) of the tank -0.084 paschal-seconds for 10 per cent, 0.050 paschal-seconds for 15 per cent, 0.039 paschal-seconds for 20 per cent. With higher values of n , the fluid viscosity was less affected by shear and the fluid encountered a resistance that significantly impeded flow in the wall region.

Results for average shear stress and contour distributions of viscosity over the range of tank radial position in the mixing tank illustrated that the fluid viscosity was significantly reduced in the high shear stress regions. Consequently, the fluid encountered little resistance as it moved rapidly through this region.

Turbulence Kinetic Energy and Dissipation Rate

The distribution of turbulent kinetic energy and dissipation rates as shown in Figures V-11, V-18 and V-24 and Figures V-12, V-19 and V-25 are characteristic of the reactor geometry. Specifically, these turbulent dissipation rates have been used to obtain the local shear rates for calculating the fermentation broth viscosity. The turbulent k and ε predicted by the various viscosity suspension with the maximum values ($k=0.022V_{tip}^2$ for 10 per cent, $k=0.051V_{tip}^2$ for fifteen per cent $k=0.059V_{tip}^2$ for 20 per cent) and found in the discharge region and a surrounding zone of relatively high turbulent kinetic energy.

The circumferential averaging k and ε are plotted for the different solid concentration as function of tank radial on panels by $x=0$ of the mixing tank in Figures V-39 through V-41. As expected, relatively high dissipation rates were found near the impellers. The values of k are close to zero with low dissipation rates elsewhere.

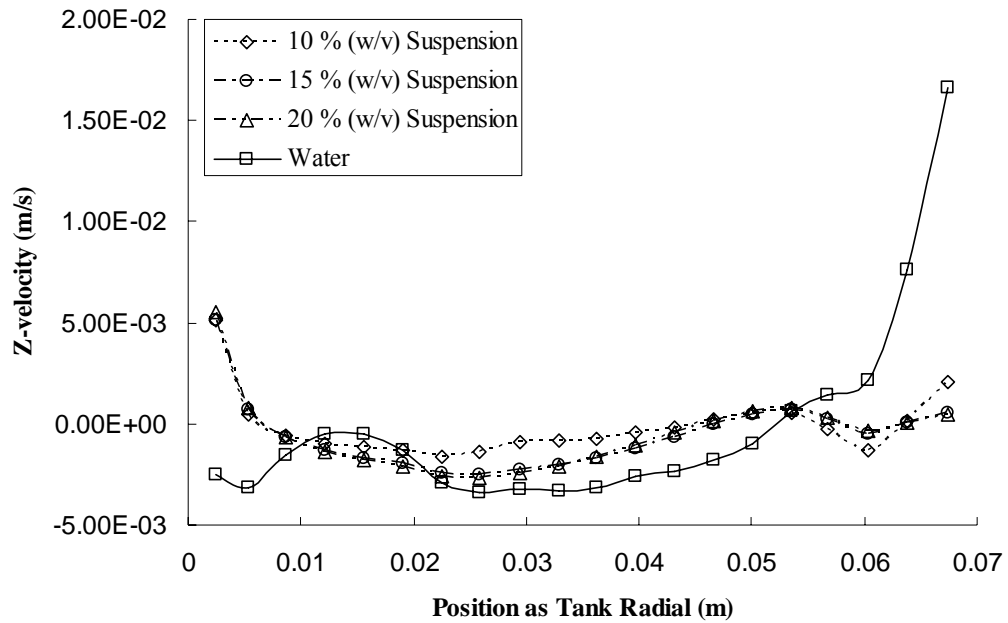


Figure V-27. Average of axial velocity of 2 L suspension as tank radial at panel 1.

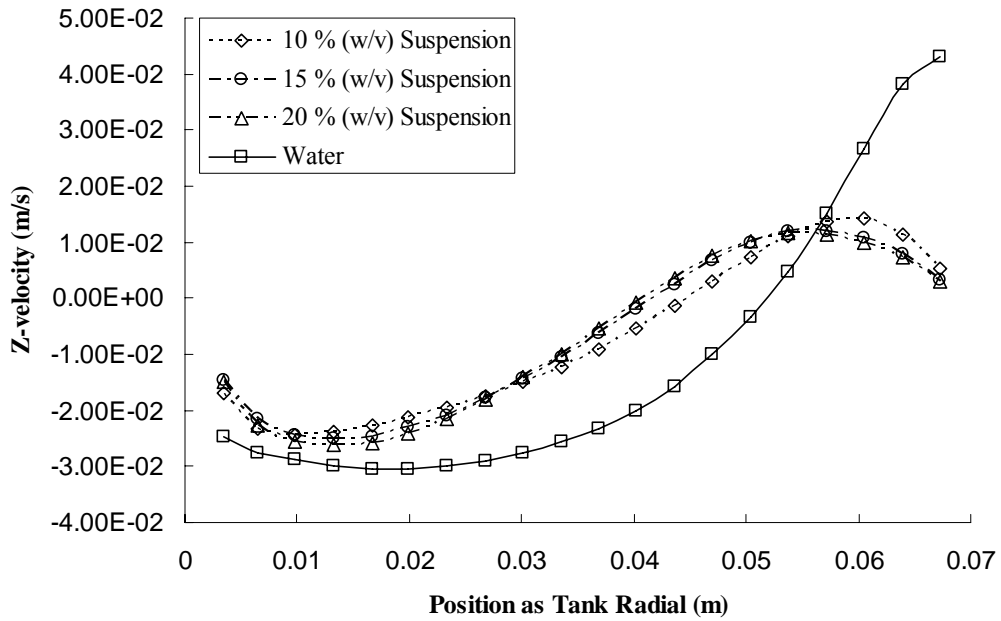


Figure V-28. Average of axial velocity of 2 L suspension as tank radial at panel 2.

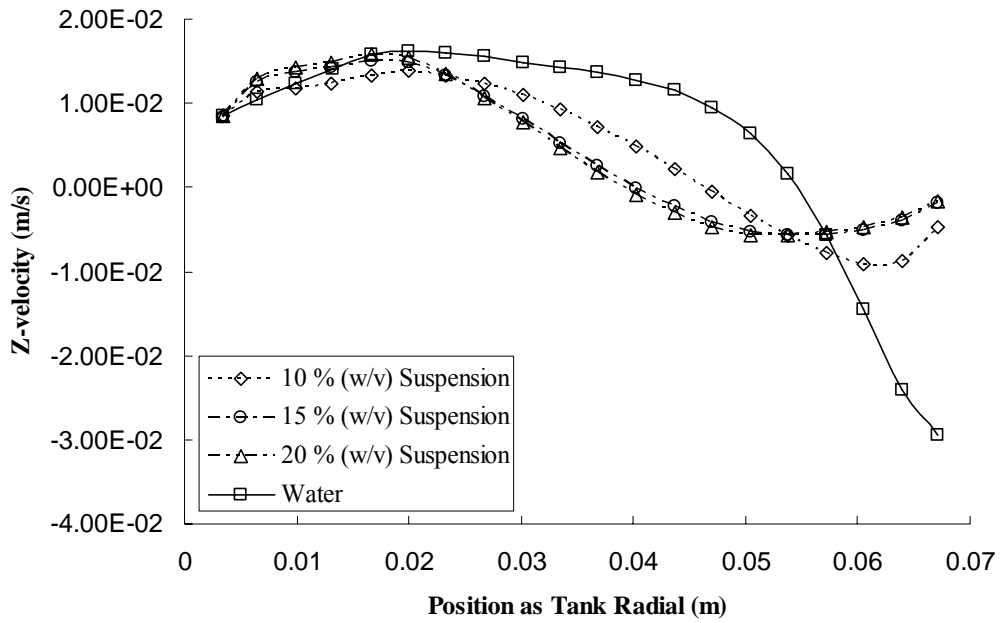


Figure V-29. Average of axial velocity of 2 L suspension as tank radial at panel 4.

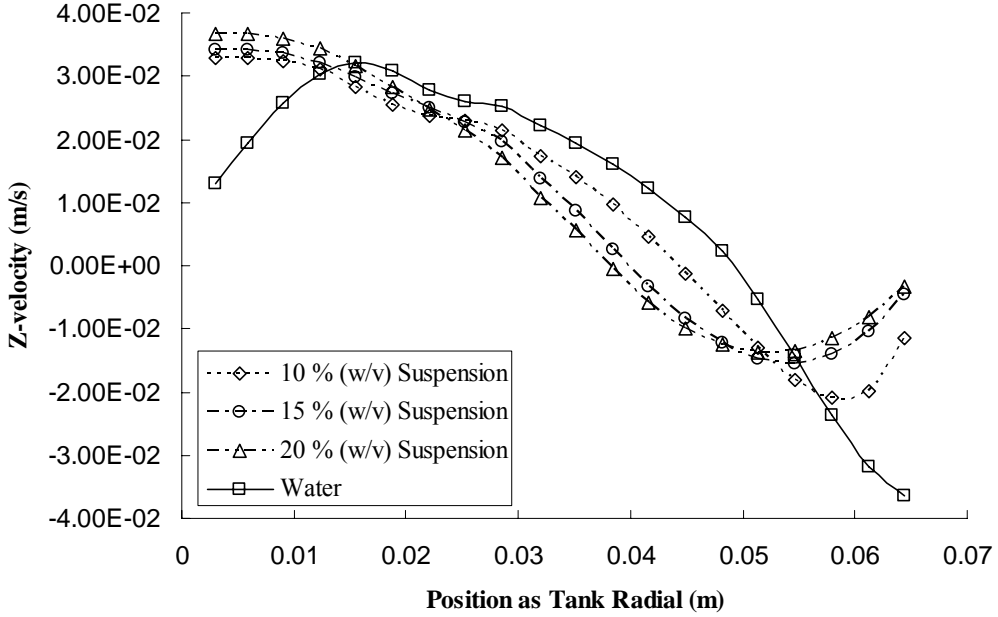


Figure V-30. Average of axial velocity of 2 L suspension as tank radial at panel 6.

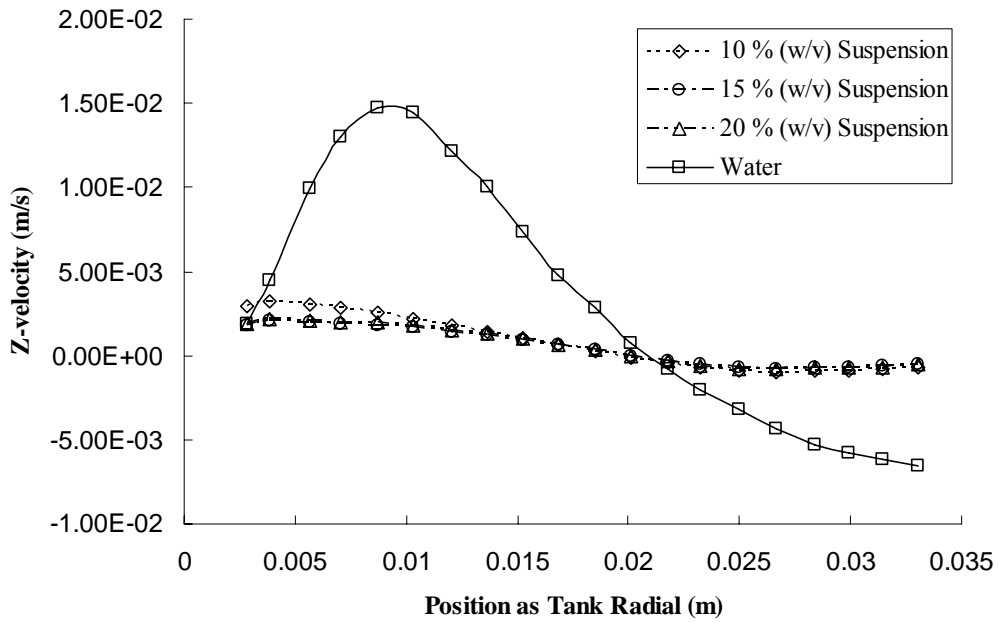


Figure V-31. Average of axial velocity of 2 L suspension as tank radial at panel 7.

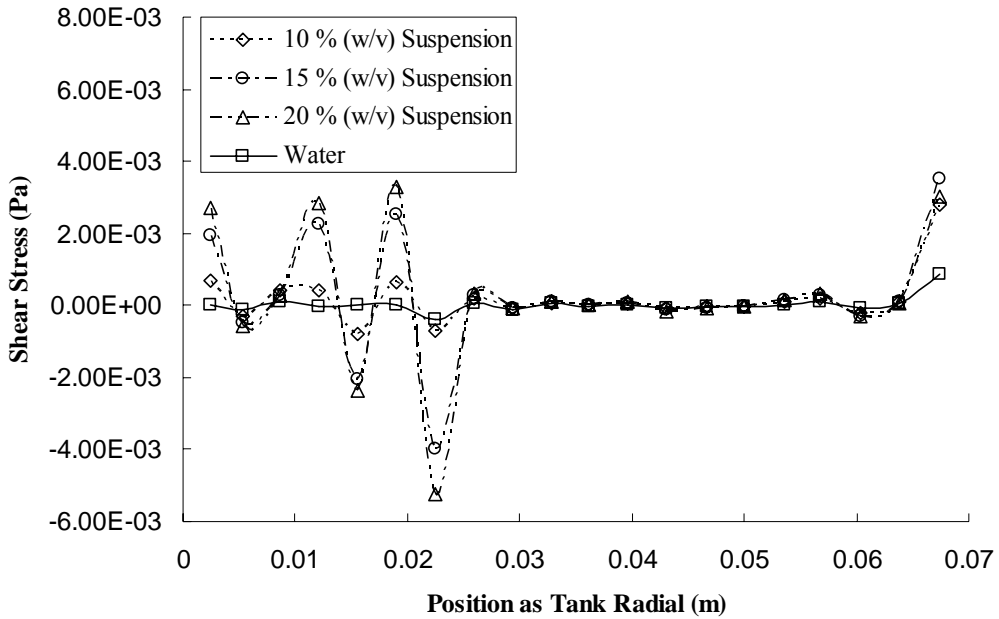


Figure V-32. Average of shear stress of 2 L suspension as tank radial at panel 1.

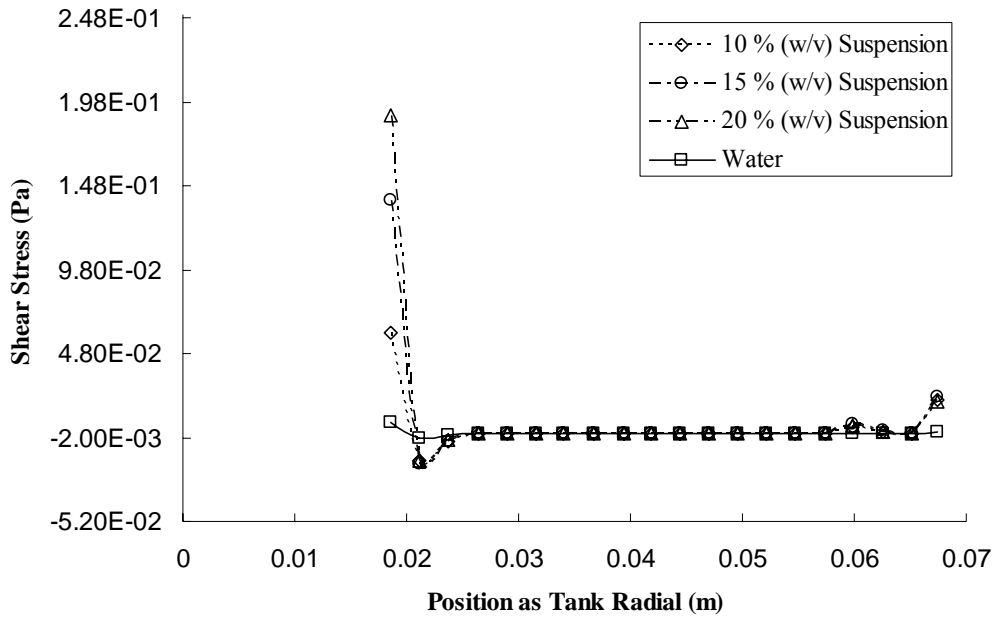


Figure V-33. Average of shear stress of 2 L suspension as tank radial at panel 3.

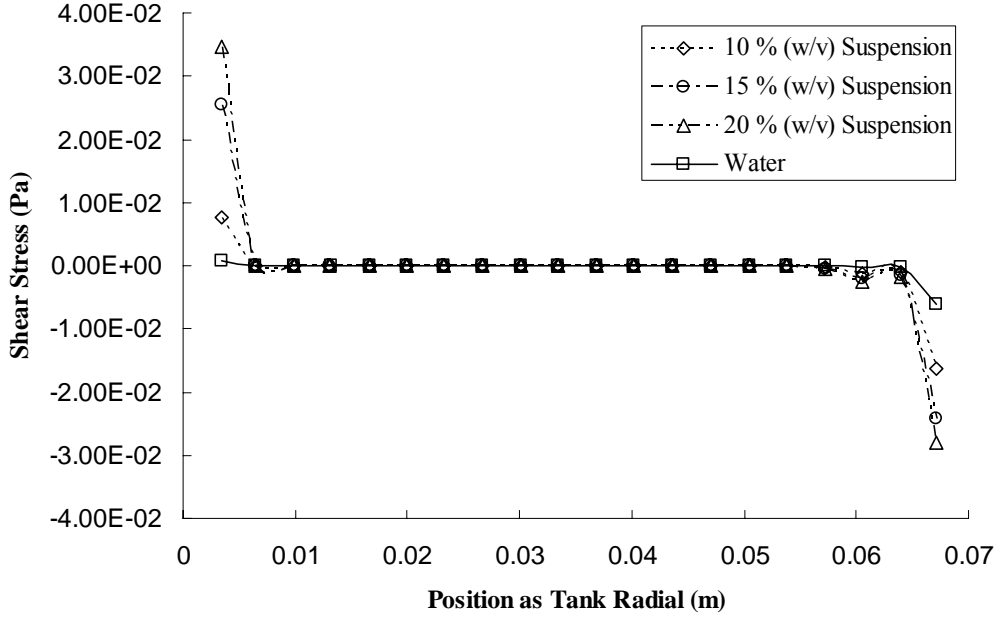


Figure V-34. Average of shear stress of 2 L suspension as tank radial at panel 4.

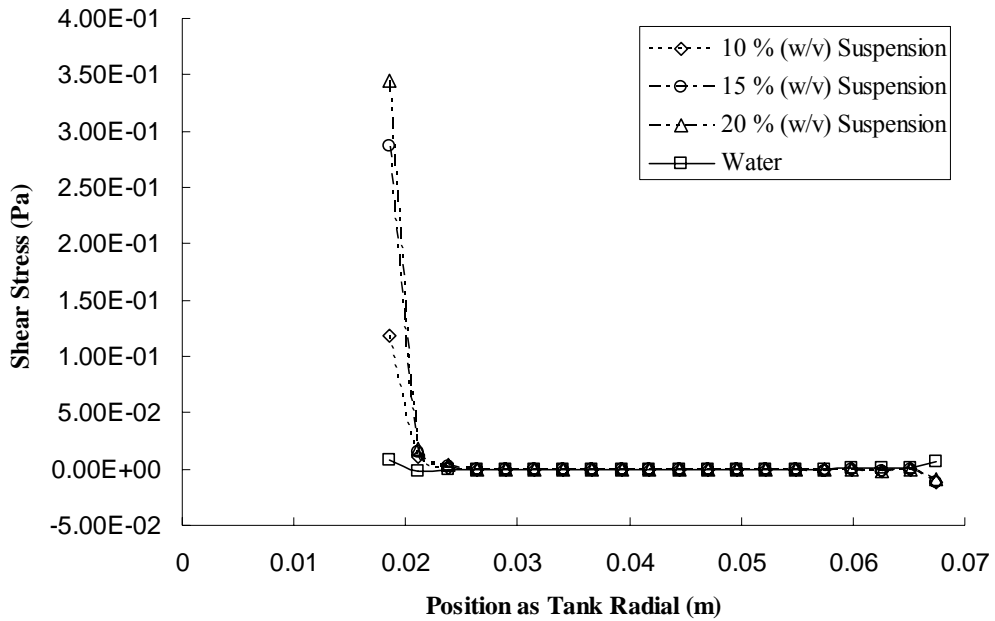


Figure V-35. Average of shear stress of 2 L suspension as tank radial at panel 5.

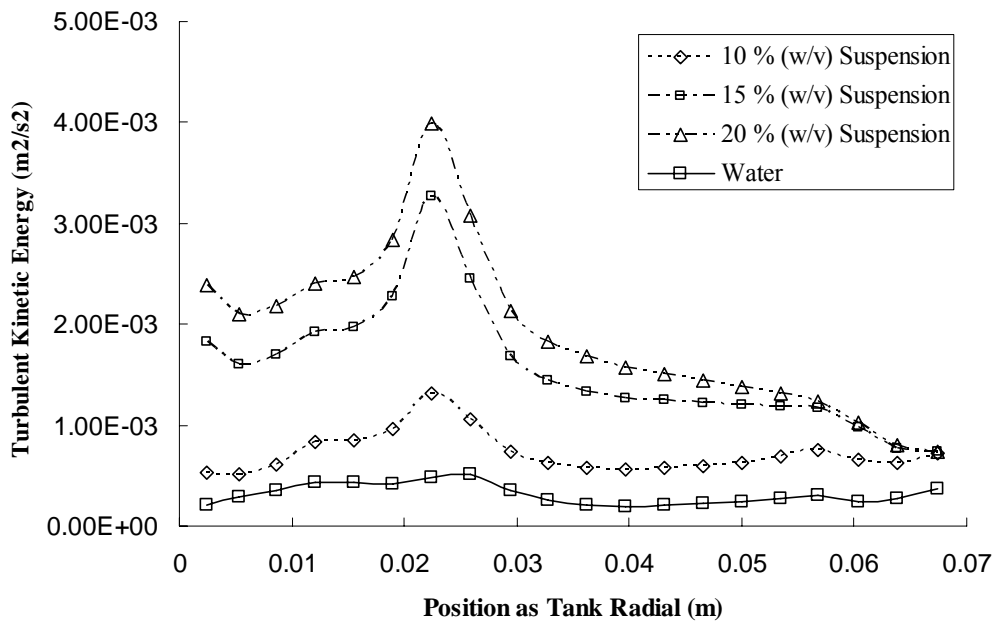


Figure V-36. Average of turbulent kinetic energy (k) of 2 L suspension as tank radial at panel 1.

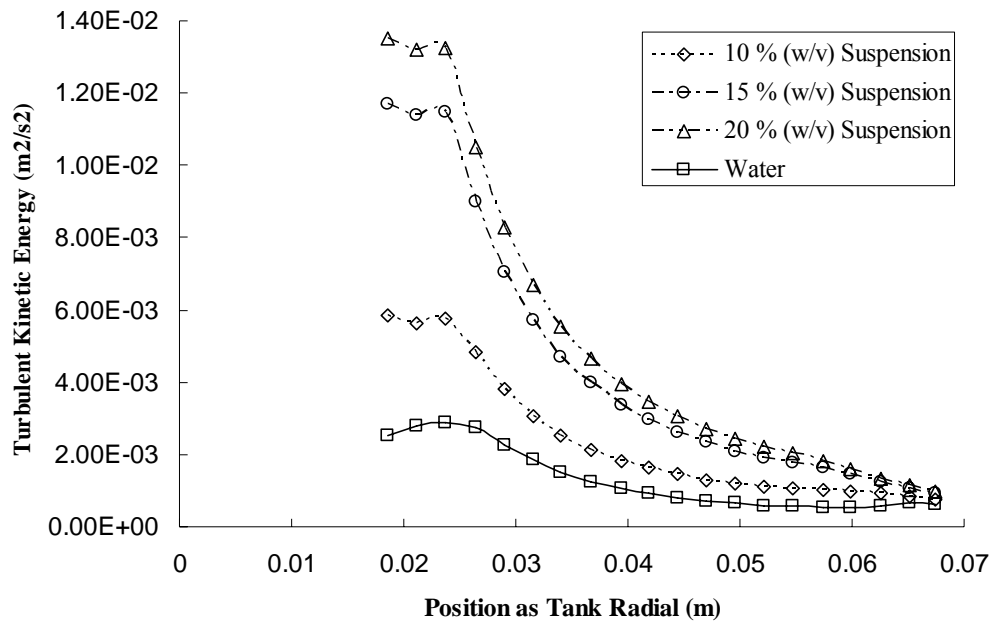


Figure V-37. Average of turbulent kinetic energy (k) of 2 L suspension as tank radial at panel 3.

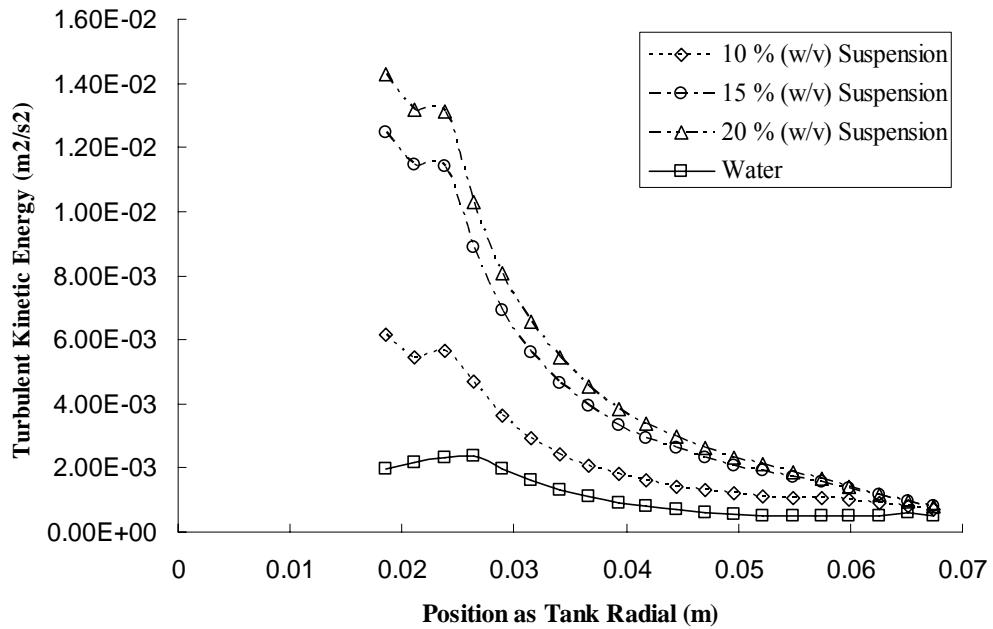


Figure V-38. Average of turbulent kinetic energy (k) of 2 L suspension as tank radial at panel 5.

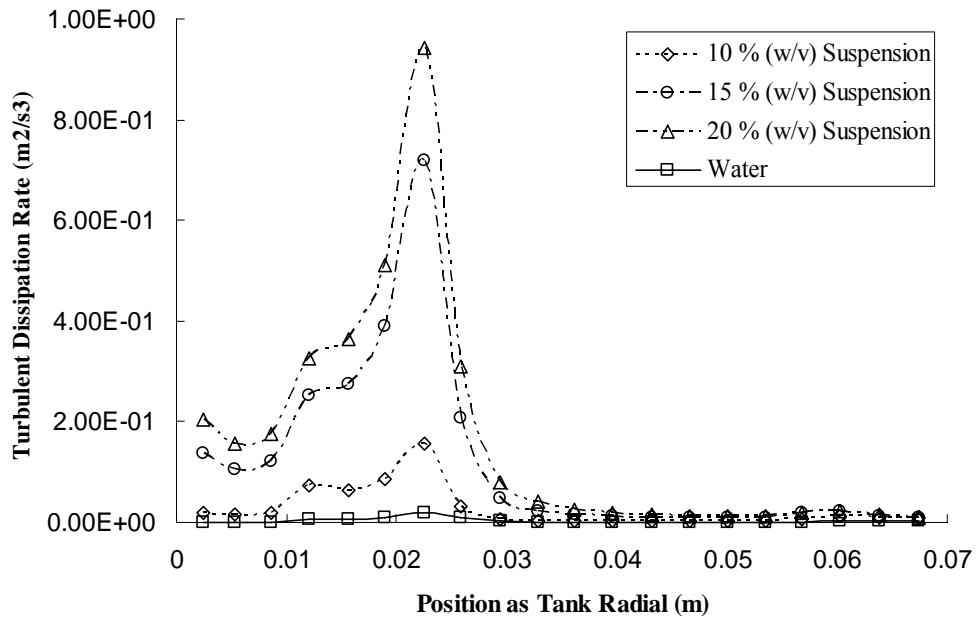


Figure V-39. Average of turbulent dissipation rate (ϵ) of 2 L suspension as tank radial at panel 1.

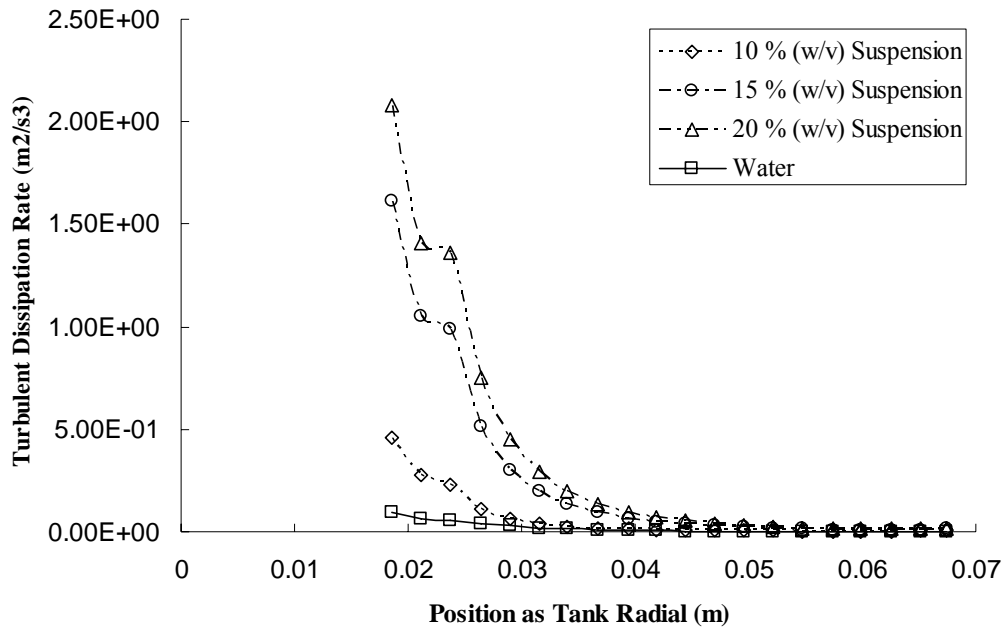


Figure V-40. Average of turbulent dissipation rate (ϵ) of 2 L suspension as tank radial at panel 3.

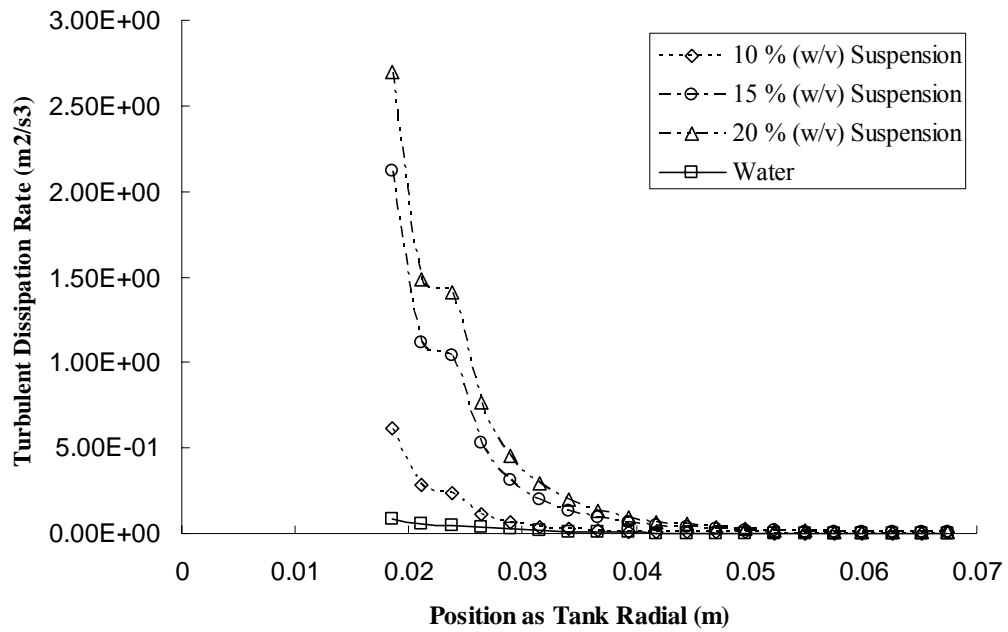


Figure V-41. Average of turbulent kinetic energy (k) of 2 L suspension as tank radial at panel 5.

CONCLUSIONS

Flow pattern calculations for potential operating conditions of multiple Rushton six blade agitators in the ellipsoidal bottom tank have been performed to assess mixing behavior. Velocity and shear stress criteria were developed to assess the ability of liquid flow to lift and suspend solids deposited on the bottom surface of the tank. The modeling results will help determine acceptable agitator speeds and tank liquid levels to ensure suspension of solid particles deposited during high solid fermentation.

A few important observations with regard to the effect of fluid viscosity on fermentation suspension in the laminar flow regime have been made in this work. The main interest was axial and mixed-flow pattern of the two impellers since they are the most important considered for viscous suspension mixing. It was found that at various Reynolds numbers, the axial flow component for these impellers was suppressed on the bottom of the tank, such that overall flow was predominantly radial. Specifically, this relatively weak distribution of axial velocities at the bottom of the tank may cause the solid particles to stay around the bottom of the tank. This condition becomes more significant with increased solid concentration.

The simulation shows that there is a potential for slow flow or stagnant fluid between the bottom of tank and the fermentor wall and also above the top impeller. In an aerobic fermentation, both of these regions could become depleted of oxygen. High shear rates and energy dissipation rates could be found near both impellers. In all of fermentations, high shear and energy dissipation regions could deactivate the microorganism.

Viscosity fields suggest a relationship between primary flow pattern and the location of high viscosity (low mass transfer) regions. These results suggest that correlations for determining the overall heat transfer coefficient in stirred tanks may need to be modified for viscous fluids.

A CFD package such as FLUENT can be used to provide valuable insight into the relationship between fermentor configuration and flow. The results of such studies should prove of interest especially to engineers who are concerned with bulk mixing, mass transfer and heat transfer in large fermentor with viscous non-Newtonian fluids.

VI. OVERALL CONCLUSIONS AND RECOMMENDATIONS

Conclusions

The following conclusions could be drawn from the experiments:

1. In baffled tanks with Rushton impellers, a better concentration distribution throughout the tank and therefore improvement in the mixing efficiency is achieved to yield high glucose conversion at high solid substrates. Applying a prehydrolysis at combined temperature (50 -30°C) in a portion loading (30 FPU/ g cellulose), the final solid concentration could be increased up to 20 per cent DM concentration. The SFF process even at relative high cellulose loading resulted in a remarkable ethanol yield (83.6, 73.4, and 21.8 per cent at 10, 15, and 20 solid per cent, respectively).
2. Three models (Herschel-Bulkley, Casson, and Bingham) were used to fit the experimental data and to determine the yield stress of the slurries. The Herschel-Bulkley model fits the data satisfactorily over the whole experimental range at 10-20 per cent solid concentration. The range of R^2 (squared multiple correlation coefficients) for Herschel-Bulkley model was 0.985 to 0.998. In addition, Bingham and Casson equations are in excellent agreement with result of enzymatic suspension and fermentation broths at 10 per cent and 20 per cent.

3. Flow pattern calculations for potential operating conditions of a Rushton six blade agitator in the ellipsoidal bottom tank (BioFlo 3000) have been performed to assess mixing behavior. Velocity and shear stress criteria were developed to assess the ability of liquid flow to lift and suspend solids deposited on the bottom surface of the tank. The modeling results will help determine acceptable agitator speeds and tank liquid levels to ensure suspension of solid particles deposited during precipitation operations.
4. Fermentation broths at three different viscosities were evaluated: 0.0192, 0.0775, 0.105 kg/m·s. at 10, 15, and 20 per cent respectively. A three-dimensional CFD approach was used with a two-equation turbulence model and multiple reference frames. Free surface motion was assumed to be negligible compared to forced convective motion for the operating conditions evaluated. The top liquid surface was assumed to be stationary at atmospheric pressure. No-slip boundary conditions were used at the blade surface and the tank walls. Rotational motion of the agitator was simulated by using a rotating reference frame with respect to the adjacent fluid media.

Recommendations

This research used process engineering methods to optimize the bioprocess for bioethanol production; however, this process offers numerous additional challenges that need to be studied in more details in order to provide better understanding of the fermentation and simulation processes.

1. In the high solids fermentation, besides the carbon sources, all other compounds such as nitrogen sources and inhibitory compounds should be clearly analyzed. Where inhibitory compounds are found, pretreatment may be required to remove these substances before use in the fermentation. In addition, the nitrogen source, which was not sufficiently present in the suspension, could be the key for determining the metabolism of lignocellulosic substrate by *Zymomonas mobilis*.
2. In long-term fermentations of mixed high carbon substrates (glucose/xylose), a portion substrate loading is necessary to maintain fungal activity and enhance ethanol fermentation. In an anaerobic reaction in which the bacterium *Z. mobilis* uses glucose to form ethanol and carbon dioxide, small amounts of acetate and glycerine are produced. If oxygen is introduced to the reaction, the production of acetate and glycerine will increase, thus decreasing the purity of the desired ethanol product. Therefore, it is important to determine the fermentation mode (aerobic or anaerobic) involved in portion loading during the fermentation. By comparing ethanol yield and its quality under the fermentation modes, the optimal feeding strategy and fermentation can be clearly determined in the pilot scale.
3. Future work will be aimed at increasing the productivity and reducing inhibition by studying continuous operation at combined temperature. Figure VI-1 shows a schematic diagram of continuous saccharification fermentation process in the pilot plant scale. Continuous operation with a series of reactors fed with partially digested biomass withdrawn from the previous tank would greatly benefit the economy of the process by minimizing the time spent on reactor startups and terminations and by overcoming of incompatible temperature

requirements during SSF process. Once validated, the CFD method will be then applied to the design of a full-scale reactor that is to be constructed without additional experiments. As fundamental equations of conservation are used, the method is readily applied to any new geometry.

4. Future simulation work will be focused on increasing the axial velocity and reducing stagnant zone around bottom of tank in high solid fermentation by modifying geometry (Figure VI-2). By simulation for the new geometry, the optimal flow pattern can be clearly determined in the pilot scale.

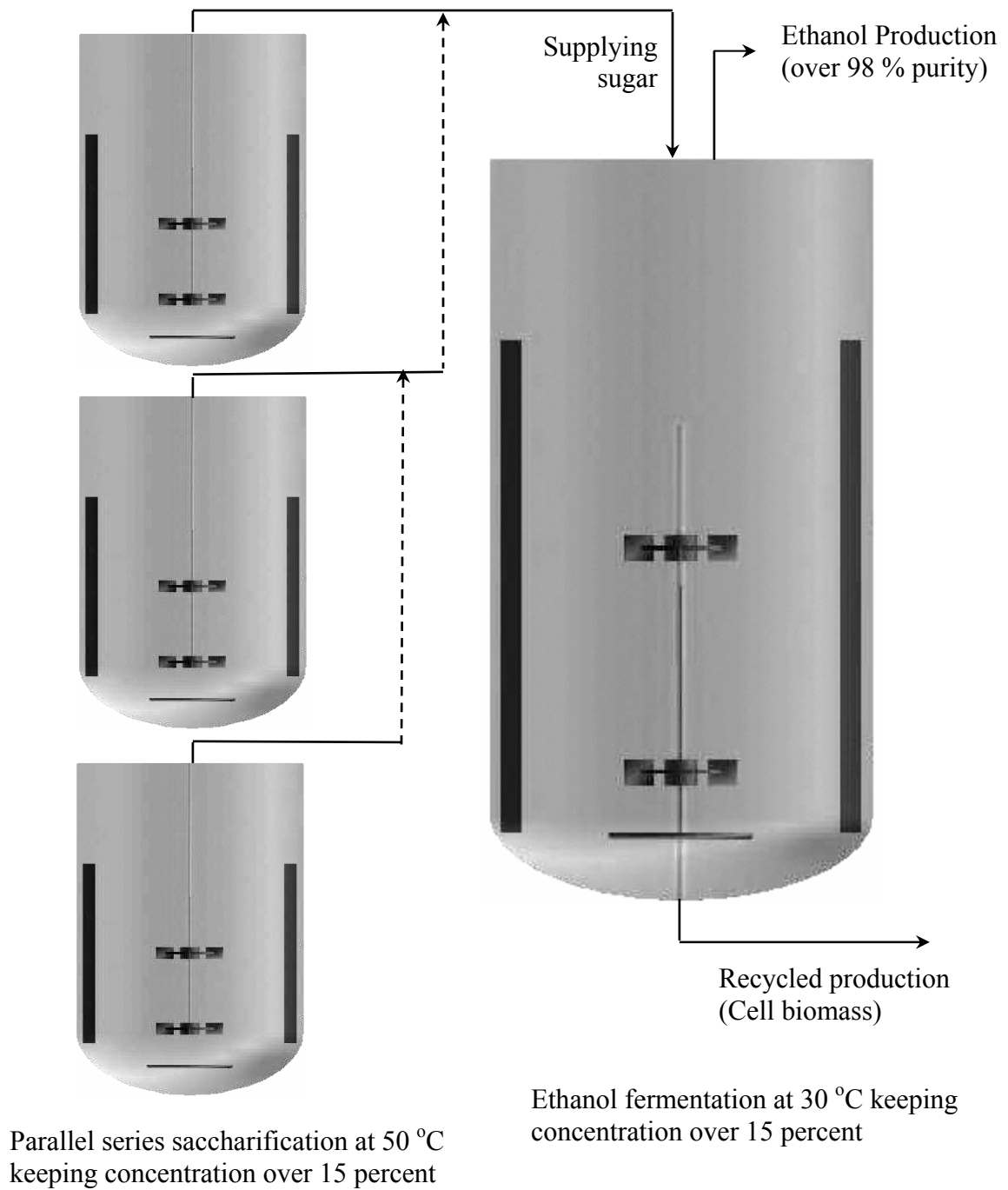


Figure VI-1. Schematic diagram of continuous saccharification and fermentation at separate temperature condition.

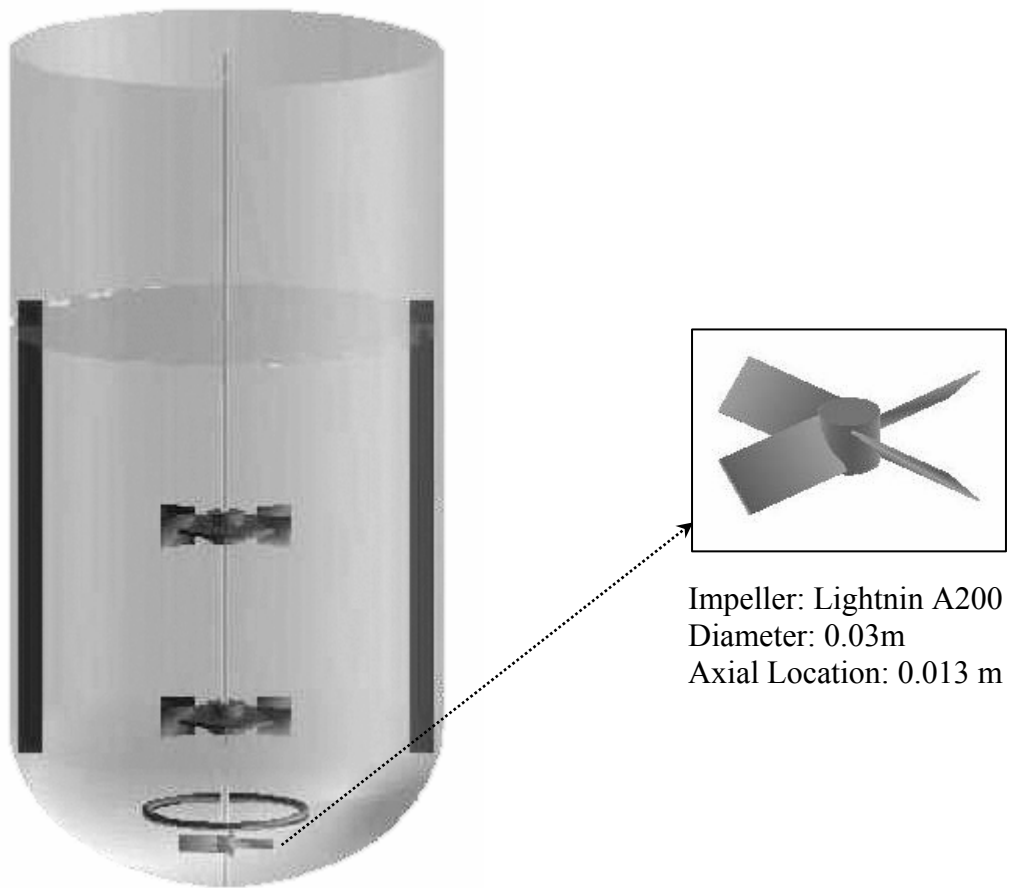


Figure VI-2. Modified existing bioreactor for improving axial velocity.
[Add bottom shaft mounted Lightnin A200]

BIBLIOGRAPHY

- Allen, D. G., and Robinson, C. W., 1990. Measurement of Rheological Properties of Filamentous Fermentation Broths, *Chem. Eng. Sci.*, 45(1), 37-48.
- Amanullah, A., Christensen, L. H., Hansen, K., Nienow, A. W., and Thomas, C. R., 2002. Dependence of morphology on agitation intensity in fed-batch cultures of *Aspergillus oryzae* and its implications for recombinant protein production, *Biotechnology and Bioengineering*, 77, 815-826.
- Andrew, S. P. S., 1982. Gas-Liquid Mass Transfer in Microbiological Reactors, *Trans IChE J.*, 60, 3-13.
- Bailey, J. E., and David, F. O., 1986. 2nd ed., *Biochemical Engineering Fundamentals*. McGraw-Hill, New York.
- Bakker, A., Fasano, J. B., and Myers, K. J., 1994. Effects of flow pattern on solid distribution in a stirred tank, *I. Chem. E. Symp. Ser.*, 136, 1-8. IChemE, Rugby.
- Bakker, A., and Gates, L. E., 1995. Properly Choose Mechanical Agitators for Viscous Liquids, *Chem. Eng. Prog.*, 25-34.
- Barrue, H., Bertrand, J., Cristol, B., and Xuereb, C., 1999. Eulerian simulation of dense solid-liquid suspension in multi-stage stirred vessel, *Proc. 3rd Int. Symp. Mixing; Ind. Process*, Osaka, 37-44 (Society of Chemical Engineers: Tokyo, Japan).
- Béguin, P., and Aubert, J. P., 1994. The biological degradation of cellulose, *FEMS Microbiol. Rev.*, 13, 25-58.
- Bird, R. B., Stewart, W. E., and Lightfoot, E. N., 2002. *Transport Phenomena*, John Wiley & Sons, Inc.
- Bisaria, V. S., 1991. Bioprocessing of Agro-residue to glucose and chemicals. In: Martin, A. M. (Ed.), *Bioconversion of waste materials to industrial products*, Elsevier Applied Science, London, New York, 210-213.
- Blotkamp, P. J., Takagi, M., and Pemberton, M. S., 1978. Enzymatic hydrolysis of cellulose and simultaneous fermentation to alcohol, *Biochemical Engineering: Renewable Source of Energy and Chemical Feedstocks*, *AICHE Symp. Series*, 74, No. 181, 85-90.

- Bongenaar, J., Kossen, N., Metz, B., and Meijboom, F., 1973. A Method for Characterizing the Rheological Properties of Viscous Fermentation Broths, *Biotechnol. Bioeng.*, 15, 201-206.
- Brito-de la Fuente, E., Leuliet, J. C., Cholpin, L. and Tanguy, P. A., 1992. On the Effect of Shear-Thinning Behavior on Mixing with a Helical Ribbon Impeller, *Process Mixing: Chemical and Biochemical Applications*, 88, 28-31.
- Capital Press Agriculture Weekly, June 05, 2005. Biomass: Our future energy source. <<http://www.capitalpress.info/>>
- Carson, Z., 2005. Alternative Fuels as a Solution: History of Alternative Fuel Development, <<http://puravida.gather.com/>>.
- Chang, M. M., Chou, C., and Tsao, G. T., 1981. Structure, Pretreatment and Hydrolysis of Cellulose. *Adv. Indus. Biochem. Eng.*, 20, 15-42.
- Charles, M., 1978. Technical Aspects of the Rheological Properties of Microbiological Cultures, *Adv. Biochem. Eng.*, 8, 1-62.
- Chum, H. L., Douglas, L. J., Feinberg, D. A., and Schroeder, H. A., 1985. In Evaluation of Pretreatments of Biomass for Enzymatic Hydrolysis of Cellulose, SERI/TP-231-2183; Solar Energy Research Institute: Golden, CO.
- Cheung, S. W., and Anderson, B. C., 1997. Laboratory Investigation of Ethanol Production from Municipal Primary Wastewater Solids, *Bioresource. Technol.*, 59, 81-96.
- Christakopoulos, P., Macris, J. B., and Kekos, D., 1990. On the mechanism of direct conversion of cellulose to ethanol by *Fusarium oxysporum*: Effect of cellulose and β -glucosidase. *Appl. Microbiol. Biotechnol.*, 33, 18-20.
- Converse, A. O., Ooshima, H., and Burns, D. S., 1990. Kinetics of Enzymatic Hydrolysis of Lignocellulosic Materials Based on Surface Area of Cellulose Accessible to Enzyme and Enzyme Adsorption on Lignin and Cellulose. *Appl. Biochem. Biotechnol.*, 24-25:67-73.
- Davis, M., Baker, J. O., Rignall, T., and Himmel, M. E., 2002. Changes in Cellulose Morphology of Pretreated Yellow Poplar during Enzymatic Hydrolysis. NREL Report No. PO-510-32125.
- Decker, S., Sommerfeld, M., 1996. Calculation of particles suspension in agitated vessels with the Euler-Lagrange approach, *ICHEME Symp. Ser.*, 140, 71-82, ICHEME, Rugby.

- Derksen, J. J., 2003. Numerical simulation of solids suspension in a stirred tank. *AIChE J.*, 49, 2700-2714.
- Dronawat, S. N., Rieth, T. C., Svihla, C. K., and Hanley, T. R., 1996. Use of a Helical Impeller to Determine Steady Shear Characteristics of Filamentous Suspensions, *Proceedings of the 5th World Congress of Chemical Engineering*, 1, 629.
- Duff, S. J. B., and Muray, W. D., 1996. Bioconversion of forest products industry waste cellulose to fuel ethanol: a review, *Bioresource Technol.*, 55, 1-33.
- Efficiency and Conservation Authority (EECA), 2005. *Renewable Energy: Improving Energy Choice* 8.
- Eriksson, T., Karlsson, J., and Tjerneld, F., 2002. A Model Explaining Declining Rate in Hydrolysis of Lignocellulosic Substrates with Cellobiohydrolase I (Cel7A) and Endoglucanase I (Cel7B) of *Trichoderma reesei*, *Appl. Biochem. Biotechnol.*, 101:41-59.
- Fan, L. T., Gharpuray, M. M., and Lee, Y. H., 1987. *Cellulose Hydrolysis*. Springer-Verlag, Berlin.
- Fan, L. T. and Lee, Y. H., 1983. Kinetic Studies of Enzymatic Hydrolysis of Insoluble Cellulose: Derivation of a Mechanistic Kinetic Model. *Biotechnol. Bioeng.*, 24, 2707-2733.
- Fein, J. E., Potts, D., Good, D., Beavan, M., O'Boyle, A., Dahlgren, D., Beck, M. J., and Griffith, R.L., 1991. Development of an Optimal Wood-to-Fuel Ethanol Process Utilizing Best Available Technology. *Energy from Biomass and Waste*, 15, 745-765.
- FLUENT INC., 1995, News Letter, 4(1).
- FLUENT INC., 2001. *FLUENT 6 User's Guide, Volume 4*, FLUENT INC., Lebanon, NH.
- FLUENT INC., 2006. *MIXSIM 2.1 User's Guide*, FLUENT INC., Lebanon, NH.
- Glazer, N. A., and Nikaido, H., 1995. Ethanol. In: *Microbial Biotechnology*. 359-391, W. H. Freeman and Company, San Francisco.
- Gould, J. M., 1984. Alkaline Peroxide Delignification of Agricultural Residues to Enhance Enzymatic Saccharification, *Biotechnol. Bioeng.*, 26, 46-52.
- Grenville, R., 1995. Blending of Miscible Liquids in the Turbulent and Transitional Regimes. Paper presented at *Mixing XV, 15th Biennial North American Mixing Conference*, Banff, AL, Canada.

- Grohmann, K., Torget, R., and Himmel, M., 1985. Optimization of Dilute Acid Pretreatment of Biomass, *Biotechnol. Bioeng. Symp.*, 15, 59-80.
- Hacking, A. J., Taylor, I. W. F., and Hanas, C. M., 1984. Selection of yeasts able to produce ethanol from glucose at 40°C, *Appl. Microbiol. Biotechnol.*, 19, 361-363.
- Hettenhaus, J. R., 1998. Ethanol Fermentation Strains. In: Present and Future Requirements for Biomass to Ethanol Commercialization, 1-25, United States Department of Energy, National Renewable Energy Laboratory.
- Hinze, J. O., 1989. Turbulence. McGraw-Hill Book Company, Inc., New York.
- Himmel, M. E., Adney, W. S., Baker, J. O., Elander, R., McMillan, J. D., Nieves, R. A., Seehan, J. J., Thomas, S. R., Vinzant, T. B. and Zhang, M., 1997. Advanced Bioethanol Production Technologies. A perspective. In: Fuels and Chemicals from Biomass. B. D. Saha, J. Woodward (eds.) ACS Symp. Ser 666, American Chemical Society, Washington, DC, Chapter 1, 1-45.
- Hogsett, D. A., Ahn, H. J., Bernardez, T. D., South, C. R., and Lynd, L. R., 1992. Direct microbial conversion: prospects, progress and obstacles, *Appl. Biochem. Biotechnol.*, 34/35, 527-541.
- Houchin, T. L., and Hanley T. R., 2004. Measurement of rheology of distiller's grain slurries using a helical impeller viscometer, *Appl. Biochem. Biotechnol.*, 113/116, 723-32.
- Hubbard, D. W., 1987. Scale-Up Strategies for Bioreactors. In: *Biotechnology Process Scale-Up and Mixing*. (Ed.), Ho, C. S. and Oldshue, J. Y., 168-184. New York: American Institute of Chemical Engineers.
- Humphrey, A., 1998. Shake Flask to Fermentor: What have we learned? *Biotechnol. Prog.*, 14, 3-7.
- Ingledeew, W. M., 1993. Yeast for production of fuel ethanol. In: the yeast, 2nd ed., vol. 5. *Yeast Technology*. (Ed.), Rose, A. H., and Harrison, J. S., New York: Academic Press.
- Johnson, E. A., Sakojo, M., Halliwell, G., Madia, A., and Demain, A. L., 1982. Saccharification of complex cellulosic substrates by the cellulase system from *Clostridium thermocellum*. *Appl. Environ. Microbiol.*, 43(5), 1123-1132.
- Ju, L. K., and Chase, G. G., 1992. Improved scale-up strategies of bioreactors, *Bioprocess Engineering*, 8, 49.

- Kaar, W. E., and Holtzapple, M. T., 1998. Benefits from Tween during Enzymatic Hydrolysis of Corn Stover, *Biotechnol. Bioeng.*, 59, 419-427.
- Karow, E. O., Bartholomew, W. H., and Sfat, M. R., 1953. Oxygen transfer and agitation in submerged fermentations, *Agricultural and Food Chemistry*, 1(4):302.
- Kadam, K. L., and McMillan, J. D., 2003. Availability of corn stover as a sustainable feedstock for bioethanol production, *Biores. Technol.*, 88, 17-25.
- Klinke, H. B., Thomsen, A. B., and Ahring, B. K., 2001. Potential inhibitors from wet oxidation of wheat straw and their effect on growth and ethanol production by *Thermoanaerobacter mathranii*, *Appl. Microbiol. Biotechnol.*, 57, 631-638.
- Kobayashi, S., Shoda, S., Donnelly, M. J., and Church, S. P., 1999. Enzymatic synthesis of cellulose, *Methods on Biotechnology*, 10. In: Bucke, C. (Ed.), *Carbohydrate Biotechnology*, Humana Press Inc., NJ, USA.
- Kuipers, J. A. M., and van Swaaij, W. P. M., 1997. Application of computational fluid dynamics to chemical reaction engineering. *Rev. Chem. Eng.*, 13, 1-118.
- Labuza, T. P., Barrera Santos, D., Roop, R. N., 1970. Engineering factors in single-cell protein production. I. Fluid properties and concentration of yeast by evaporation, *Biotechnology and Bioengineering*, 12, 123-134.
- Lauder, B. E., and Spalding, D. B., 1972. *Lectures in Mathematical Models of Turbulence*. Academic Press, London.
- Lawford, H. G., Rousseau, J. D., Mohagheghi, A., and McMillan, J. D., 1999. Fermentation Performance Characteristics of a Prehydrolyzate-Adapted Xylose-Fermenting Recombinant *Zymomonas* in Batch and Continuous Fermentations, *Appl. Biochem. Biotechnol.*, 77/79, 191-204.
- Li, Z. J., Shukla, V., Wenger, K., Fordyce, A., Pedersen, A. G. and Marten, M., 2002. Estimation of hyphal tensile strength in production-scale *Aspergillus oryzae* fungal fermentations, *Biotechnol. Bioeng.*, 77, 601-613.
- Lübbert, A., and Jørgensen, B. S., 2001. Bioreactor performance: a more scientific approach for practice, *J. Biotechnol.*, 85(2), 187-212.
- Lynd, L., Weimer, P. J., van Zyl, W. H., and Pretorius, I. S., 2002. Microbial Cellulose Utilization: Fundamentals and Biotechnology, *Microbiol. Mol. Biol. Rev.*, 6(3):506-577.

- Mancini, M., and Moresi, M., 2000. Rheological behaviour of baker's yeast suspensions, *Journal of Food Engineering*, 44,225-231.
- Mansfield, S. D., Mooney, C., Saddler, J. N., 1999. Substrate and enzyme characteristics that limit cellulose hydrolysis, *Biotechnol. Prog.*, 15:804-816.
- Mavituna, F., 1996. Strategies for Bioreactor scale-up in *Computer and Information Science Application in Bioprocess Engineering* (Moreira, A. R., and Wallace, K. K.), Kluwer Academic Publisher, Dordrecht, Netherlands.
- Maxon, W. D., and Johnson, M. J., 1953. Aeration Studies on Propagation of Baker's Yeast, *Ind. Eng. Chem.*, 45(11), 2554-2560.
- McMillan, J. D., 1994. Pretreating Lignocellulosic Biomass: A Review, in *Enzymatic Conversion of Biomass for fuel Production*, Himmel, M. E., Baker, J. O., and Overend, R. P., eds. ACS Symp. Ser. 566. Washington, DC: American Chemical Society, Chapter 15, 685-696.
- Metz, B., Kossen, N. W. F., and Van Suijdam, J. C., 1979. The Rheology of Mould Suspensions, *Adv. Biochem. Eng.*, 11, 103-155.
- Metzner, A. B., and Otto, R. E., 1957. Agitation of Non-Newtonian Fluids. *AIChE J.*, 3(1), 3-10.
- Micale, G., Scuzzarella, A., Lettieri, P., Grisafi, F., and Brueato. A., 2002. CFD simulations of solids suspension in slurred vessels with dense particle effects, *Proc. 8th Int. Conference: Multiphase Flow in Industrial Plants*, 468-484 (ANIMP: Milan. Italy).
- Mohagheghi, A., Tucker, M., Grohman, K, and Wyman, C. E., 1992. High Solid Simultaneous Saccharification and Fermentation of Pretreated Wheat Straw to Ethanol, *Appl. Biochem. Biotechnol.*, 33, 67-81.
- Montante, G., Pinelli, D., and Magelli, F., 2002. Diagnosis of solids distribution in vessels stirred with multiple PBT's and comparison of two modeling approaches, *Can. J. Chem., Eng.*, 80, 665-673.
- Montross, M. D., and Crofcheck, C. L., 2004. Effect of stover fraction and storage method on glucose production during enzymatic hydrolysis, *Bioresource Technology*, 92, 269-274.
- Murray, M. Y., Chisti, Y., and Vlach, D., 1993. Fermentation of Cellulosic Material to Mycoprotein Foods, *Biotech. Adv.*, 11, 469-479.

- Nguyen, Q. A., Tucker, M. P., Boynton, B. L., Keller, F. A., and Schell, D. J., 1998. Dilute Acid Pretreatment of Softwoods, Scientific Note, Appl. Biochem. Biotechnol., 70/72, 77-87.
- Öhgren, K., Rudolf, A., Galbe, M., and Larsson, S., 2006. Fuel ethanol production from steam pretreated corn stover using SSF at high dry matter concentration, Biomass Bioenergy, in press.
- Oldshue, J. Y., 1983. Fluid Mixing Technology, McGraw-Hill, New York.
- Ooshima, H., Burns, D. S., and Converse, A.O., 1990. Adsorption of Cellulase from *Trichoderma Reesei* on Cellulose and Lignaceous Residue in Wood Pretreated by Dilute Sulfuric Acid with Explosive Decompression, Biotechnol. Bioeng. 36, 446-452.
- Padukone, N., 1996. Advanced Process options for bioethanol production. In: Handbook on Bioethanol: Production and Utilization, Wyman, C. E. (Ed.) Taylor and Francis. Washington DC, Chapter 14, 315-327.
- Philippidis G. P., Smith T. K., and Wyman, C. E., 1993. Study of the enzymatic hydrolysis of cellulose for production of fuel ethanol by the simultaneous saccharification and fermentation process, Biotechnol. Bioeng., 41, 846-853.
- Philippidis, G. P., and Smith, T. K., 1995. Limiting factors in the simultaneous saccharification and fermentation process for conversion of cellulosic biomass to fuel ethanol, Appl. Biochem. Biotechnol., 51/52, 117-124.
- Philippidis, G. P., 1996. Cellulose bioconversion technology. In: Wyman, C. E. (Ed.), Handbook on bioethanol: production and utilization. Taylor & Francis, Washington, DC, 253-285.
- Philippidis, G. P., and Hatzis, C., 1997. Biochemical Engineering Analysis of Critical Process Factors in the Biomass-to-Ethanol Technology, Biotechnol. Prog., 13(3), 222-231.
- Pimenova, N. V., and Hanley T. R., 2003. Measurement of Rheological Properties of Corn Stover Suspensions, Appl. Biochem. Biotechnol., 105/108, 353-364.
- Ranade, V. V., 2002. Computational Fluid Modeling for Chemical Reactor Engineering, Academic Press: New York.
- Ranatunga, T. D., Jervis, J., Helm, R. F., McMillan, J. D., and Wooley, R. J., 2000. The Effect of Overliming on the Toxicity of Dilute Acid Pretreated Lignocellulosics: the Role of Inorganics, Uronic Acids and Ether-Soluble Organics, Enzyme and Microbial Technology, 27, 240-247.

- Renewable Fuels Association (RFA), 2006. Ethanol Industry Outlook: From Niche to Nation.
- Renewable Fuels Association (RFA), 2003. Ethanol Industry Outlook: Building a Secure Energy Future.
- Reese, E. T., and Ryu, D. Y., 1980. Shear inactivation of cellulase of *Trichoderma reesei*, *Enzyme and Microbial Technology*, 2(3), 239-240.
- Rodi, W., 1980. Turbulence Models and their Applications in Hydraulics. IAHR Monograph.
- Roels, J. A., Van Der Berg, J., and Voncken, R. M., 1974. The Rheology of Mycelial Broths, *Biotechnol. Bioeng.*, 16, 181-208.
- Rushton, J. H., Costich, E. W., and Everett, H. J., 1950. Power Characteristics of Mixing Impellers. *Chem. Eng. Prog.*, 9, Part I: 395-450, Part II: 467-476.
- Saxena, A., Garg, S. K., and Verma, J., 1992. Simultaneous saccharification and fermentation of waste newspaper to ethanol, *Bioresource Technol.*, 39, 13-15.
- Schell, D., Nguyen, Q., Tucker, M., and Boynton, B., 1998. Pretreatment of Softwood by Acid-Catalyzed Steam Explosion Followed by Alkali Extraction, *Appl. Biochem. Biotechnol.*, 70/72, 659-663.
- Schell, D. J., Walter, P. J., and Johnson, D. K., 1992. *Appl. Biochem. Biotechnol.*, 23/35, 659-663.
- Scott, C. D., Brian H., Scott, D. T. C., Woodward, J., Dees C., and Dena, S., 1994. An Advanced Bioprocessing Concept for the Conversion of Waste Paper to Ethanol, *Appl. Biochem. Biotechnol.*, 45/36, 641-653.
- Sha, Z., Palosaari, S., Oinas, P., and Ogawa, K., 1999. CFD simulation of solid suspension in a stirred tank, *Proceedings 3rd Int. Symp. Mixing in Industrial Processes*, Osaka, 29-36 (Society of Chemical Engineers: Tokyo, Japan).
- Shiang, M., 1985. Production, Action and Denaturation of the Cellulases of *Trichoderma Reesei Rut-C30* on Different Cellulose. Master Thesis, Colorado State University.
- Speers, R. A., Durance, T. D., Tung, M. A., and Tou, J., 1993. Colloidal properties of flocculent and nonflocculent brewing yeast suspensions, *Biotechnology Progress*, 9, 267-272.

- Spindler, D., Wyman, C. E., Mohagheghi, A., and Grohman, K., 1988. Thermotolerant Yeast for Simultaneous Saccharification and Fermentation of Cellulose to Ethanol. *Appl. Biochem. Biotechnol.*, 17, 279-293.
- Steffe, J. F., 1996. *Rheological Methods in Food Process Engineering*. Freeman Press.
- Sternberg, D., 1976. Production of cellulase by *Trichoderma*, *Biotechnol. Bioeng. Symp.*, 35-53.
- Sundaresan, S., 2000. Modeling the hydrodynamics of multiphase flow reactors: current status and challenges, *AIChE J.*, 46, 1102-1105.
- Sun, Y., and Cheng, J., 2002. Hydrolysis of lignocellulosic materials for ethanol production: a review, *Bioresource Technol.*, 83 (1), 1-11.
- Szczodrak, J., and Targonski, Z., 1989. Simultaneous saccharification and fermentation of cellulose: Effect of ethanol and cellulases on particular stages, *Acta. Biotechnol.*, 6, 555-564.
- Tamerler, C. and Keshavarz, T., 1999. Optimization of agitation for production of swainsonine from *Metarhizium anisopliae* in stirred tank and airlift reactors, *Biotechnology Letters*, 21, 501-504.
- Takagi, M., Abe, S., Suzuki, S., Emert, G. H., and Yata, N., 1978. A method for production of alcohol directly from cellulose using cellulase and yeast, In: Ghose, T. K. (Ed.), *Proceedings of bioconversion of cellulosic substances into energy, chemical and microbial protein*, I. I. T, New Delhi, India, 551-571.
- Tengborg, C., Stenberg, K., Gable, M., Zacchi, G., Larsson, S., Palmqvist, E. and Hahn-Hagerdal, B., 1998. Comparison of SO₂ and H₂SO₄ Impregnation of Softwood Prior to Steam Pretreatment on Ethanol Production, *Appl. Biochem. Biotechnol.*, 70/72, 3-15.
- Tengerdy, R. P., and Nagy, J. G., 1988. Increasing the feed value of forestry waste by ammonia freeze explosion treatment, *Biol. Wastes*, 25, 149-153.
- Teymuri, F., Laureano-Perez, L., Alizadeh, H., and Dale, B. E., 2005. Optimization of the ammonia fiber explosion (AFEX) treatment parameters for enzymatic hydrolysis of corn stover, *Biores. Techol.*, 96, 2014-2018.
- Tyson, K. S., Riley, C. J., and Humphreys, K. K., 1993. *Fuel Cycle Evaluations of Biomass Ethanol and Reformulated Gasoline*. National Renewable Energy Laboratory (NREL), Golden, CO, NREL/TP-463-4950.

- Ulbrecht, J., and Carreau, P., 1985. Mixing of Viscous Non-Newtonian Liquids. *Mixing of Liquids by Mechanical Agitation*, Ulbrecht, J., and Patterson, G. K., Eds., Gordon and Breach, New York, 93-137.
- Um, B. H., 2002. Modeling of Acid Pretreatment and Enzymatic Hydrolysis of Corn Stover, Master Thesis, Colorado State University.
- Ursula, M., Ali R. E., and John N. S., 2002. Influence of Mixing Regime on Enzymatic Saccharification of Steam-Exploded Softwood Chips, *Appl. Biochem. Biotechnol.*, 98/100, 463-472.
- USA TODAY, Jun 11, 2006. Debate brews: Has oil production peaked ?
- U. S. Department of Energy, 2001. Annual Energy Review, Energy Information Administration. U. S. Washington, D. C., DOE/EIA, 0219.
- U. S. Department of Energy, 2005. Alternative fuel.
<<http://www.eere.energy.gov/afdc/altfuel/ethanol.html>>
- Väljamäe, P., Sild, V., Pettersson, G., and Johansson, G., 1998. The initial kinetics of hydrolysis by cellobiohydrolases I and II is consistent with a cellulose surface-erosion model, *Eur. J. Biochem.*, 253(2):469-75.
- Van den Akker, H. E. A., 1997. On status and merits of computational fluid dynamics, *Proceedings 4th Int. Conf. Bioreactor and Bioprocess Fluid Dynamics*, 407-432, (MEP/BHR: London), Edinburgh.
- Varga, E., Klinke, H. B., Réczey, K., and Thomsen, A. B., 2004. High Solid Simultaneous Saccharification and Fermentation of Wet Oxidized Corn Stover to Ethanol. *Biotechnol. Bioeng.*, 88, 567-574.
- Wisconsin Biorefining Development Initiative, 2004.
<<http://www.wisbiorefine.org/feedstocks.htm>>
- Wright, J. D., 1988. Ethanol from biomass by enzymatic hydrolysis. *Chem. Eng. Pro.*, 84(8), 62-74.
- Wyman, C. E., 1994. Ethanol from Lignocellulosic Biomass: Technology, Economics, and Opportunities, *Bioresource Technology*, 50, 3-16.
- Wyman, C. E., 1996. *Handbook on Bioethanol: Production and Utilization*. Taylor and Francis, Washington, DC.
- Wyman, C.E., 2003. Potential Synergies and Challenges in Refining Cellulosic Biomass to Fuels, Chemicals, and Power, *Biotechnol. Prog.*, 19, 254-262.

- Wyman, D. K. B., Hinman, N. D., and Stevens, D. J. 1993. Ethanol and Methanol from Cellulosic Biomass, Johannson, T. E., Kelly, H., Reddy, A. K. N., and Williams, R. A. editors. Renewable Energy: Source for Fuels and Electricity, Washington, DC: Island Press. 865-923.
- Zhang, S., David, E., Wolfgang, D., and Wilson, B., 1999. Substrate Heterogeneity Causes the Nonlinear Kinetics of Insoluble Cellulose Hydrolysis, *Biotechnol. Bioeng.*, 66, 35-41.
- Zhang, Y. H. P., and Lynd, L., 2004. Toward an Aggregated Understanding of Enzymatic Hydrolysis of Cellulose: Noncomplexed Cellulase Systems, *Biotechnol Bioeng.* 88(7):797-824.
- Zheng, Y. Z., Lin, H. M., and Tsao, G. T., 1998. Pretreatment for cellulose hydrolysis by carbon dioxide explosion, *Biotechnol. Prog.*, 14, 890-896.

APPENDIX A
MEDIA FOR FERMENTATION AND BIOREACTOR PROTOCOLS

A-1. AGAR MEDIA COMPOSITIONS

Solid Agar Medium

RM Agar

Yeast Extract	10g/L
KH ₂ PO ₄	2 g/L
Bacto-agar	15 g/L
Deionized Water	900 mL
20 % Glucose Solution	100 mL

Add yeast extract, KH₂PO₄, Bacto-agar, and DI-water to an autoclavable conical flask and autoclave at 121°C for 20 minutes. After cooling, add the 20 % glucose solution (200g glucose/1000 mL DI water). Pour the plates when the temperature of the medium is about 45-50°C. Store the plates in the refrigerator.

NOTE: Filter-sterilize any sugar solutions >20% (w/v). All sugar solutions < 20 % (w/v) should be autoclaved at 121 °C for 20 minutes.

RMG Agar

RM agar + 2 % Glucose

RMX Agar

RM Agar + 2 % Xylose

RMGTc Agar

RM Agar + 2 % Glucose + 0.02 g/L Tetracycline

Liquid Culture Medium

RM Liquid (1L)

Yeast Extract	10 g/L
KH ₂ PO ₄	2 g/L
De-ionized Water	900 ml
20 % Glucose Solution	100 ml

Add yeast extract, KH_2PO_4 , and DI-water to an autoclavable conical flask and autoclave at 121°C for 20 minutes. After cooling, add the 20 % glucose solution. The liquid can be kept at room temperature or in the refrigerator.

NOTE: Filter-sterilize any sugar solutions >20% (w/v). All sugar solutions < 20 % (w/v) should be autoclaved at 121 °C for 20 minutes.

RMG Liquid

RM Liquid + 2 % Glucose

RMX Liquid

RM Liquid + 2 % Xylose

RMGTc Liquid

RM Liquid + 2 % Glucose + 0.02 g/L Tetracycline

RM Liquid (200 ml; 10 % w/v solution to be added to 3 L reactor)

Yeast Extract	2.0 g/L
KH_2PO_4	0.5 g/L
De-ionized Water	180 ml
20 % Glucose Solution	20 ml
Frozen/Liquid Cell Stocks	2.0 ml (1 % of 200 ml)

Make sure to autoclave liquid before adding glucose and bacteria. The bacterial suspensions should be grown for about 24 hours or until the OD600 reached the desired optical density. The optical densities needed for this work are 0.5 at 600nm in a 200 mL solution.

RM Liquid for growing bacterial in 10 mL solution

Yeast Extract	0.1 g/L
KH_2PO_4	0.02 g/L
De-ionized Water	9 ml
20 % Glucose Solution	1 ml
Bacteria	5~10 colonies

Make sure to autoclave liquid before adding glucose and bacteria.

A-2. REVIVAL AND GROWTH OF *Zymomonas mobilis* 39679 pZB 4L

The following procedure describes the revival and growth of *Zymomonas mobilis* 39679 pZB 4L from stabs or frozen stocks.

Step 1. Growing *Zymomonas mobilis* 39679 pZB 4L on solid agar medium.

1. Turn on incubation unit and make sure the temperature is set to 30 °C.
2. On a new Petri dish containing RMGTc agar label (cell, date, name) the back of the dish containing the agar.
3. Retrieve a frozen stock of cells from the freezer and warm by holding it in your hand.
4. Turn on light and blower in the hood.
5. Wash inside the hood with a 70 % ethanol solution.
6. Place agar media in the hood.
7. Remove inoculating loop from package and place in the hood.
8. Wearing rubber gloves, spray with the 70 % ethanol solution.
9. Remove lid from the once frozen stock of bacterial and insert the inoculating loop.
10. Streak the large section by rubbing the loop across the agar in a back and forth motion.
11. Streak each smaller section next. For these sections start streaking in the previous section first (see picture).
12. Streak each section 3 times so that cells are dilute enough to generate isolated colonies.

13. Once plates have streaked, put top on and surround the dish with parafilm laboratory film, ensuring that the top and bottom of the dish are tightly sealed to exclude air.
14. Place the dish in the incubator and leave there for three days.
15. Rewash the hood with the 70 % ethanol solution and turn the light and blower off.
16. Throw inoculating loops into red infections waste disposal can.
17. After 3days, either start next step in cultivation of bacteria or store in the refrigerator until ready to begin next step.
18. Obtain three agar plates, one RMX, one RMGTc, and one RMG agar plate, and label each plate with name, date and type of plate.
19. Using an inoculating loop, a different loop for each colony, and transfer up to twenty colonies to the three plates.
20. Pick up each colony and streak each plate in the order of RMX, RMGTc, and RMG. The streaking should be no more than a couple of streaks that the about 2 mm long.
21. Incubate each plate at 30°C for 3days.
22. After 3days, store the plates in a refrigerator no longer than two weeks.

Step 2. Growing *Zymomonas mobilis* 39679 pZB 4L in liquid medium.

23. Add K₂HPO₄, yeast extract, and DI water to an autoclavable glass tube (amounts of each ingredient for different % w/v solutions can be found in APPENDIX A-1).

24. Mix ingredients by inverting tube numerous times.
25. Place the tube in the autoclave for 20 minutes and wait 20 more minutes for autoclave to cool slightly. When removing the tube from the autoclave, watch for steam exiting the autoclave when it is opened.
26. Place the tube in the hood and allow it to cool completely.
27. Clean hood with a 70 % ethanol solution.
28. Under the hood, add glucose (20 %) to the tube using a sterilized pipet.
29. Pick one of the three plates containing the isolated 20 colonies.
30. Scrape off 5~10 colonies with an inoculating loop, under hood, and add to the liquid in the tube.
31. Cap the tube and place in the incubator for 12 hours at 30°C.
32. After 12 hours, remove the tube from the incubator and obtain a sample from the tube.
33. Measure the optical density of the sample taken from the tube.
34. Clean hood with the 70 % ethanol solution.
35. Gather 10 small corning 2 mL plastic sterilized tubes.
36. Under hood, add 0.5 mL of glycerol (60 %) to each tube.
37. Add 1 mL of the liquid culture media from the tube into each of the smaller tubes.
38. Mix by inverting the vials several times.
39. Store the vials in a -70°C freezer.

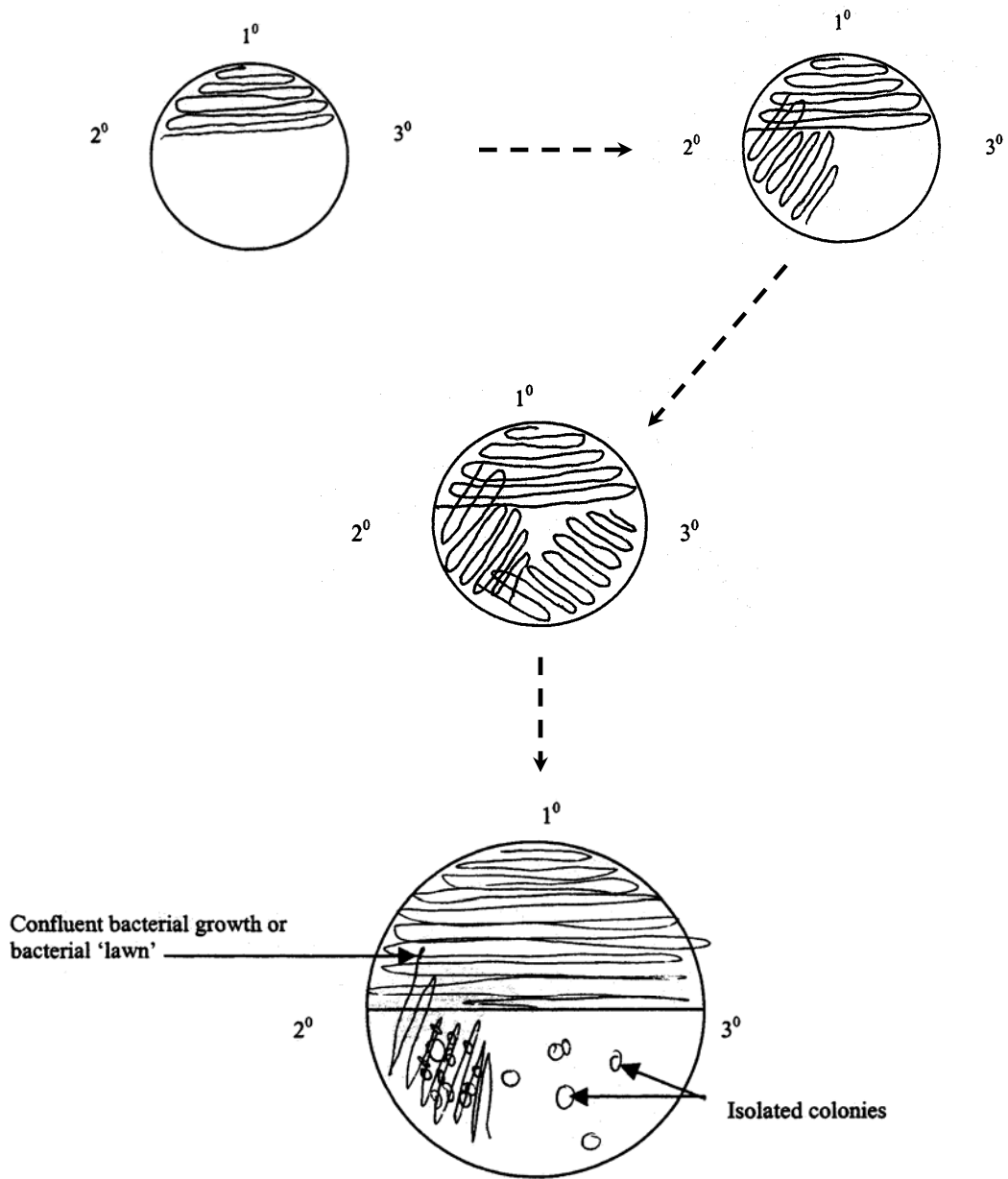


Figure A-1. Preparation and representative streak plate.

A-3. SET UP OF BioFlo 3000 (New Brunswick Scientific)

Fermentation Procedure

1. **Replace** the glass vessel onto the BioFlo stand. Set the vessel on so that the New Brunswick logo faces front.
2. **Attach** glass vessel to the heat exchange vessel using thumbscrews. Be sure that the steel ring is centered around the vessel, or it will leak. These screws should be secured as hand tight as possible, do not use any tools.
3. **Place** baffle assembly into the glass vessel such that the 2nd baffle (counting around the ring counter clockwise) is centered between the additions port directly below the New Brunswick logo and the port to its left.
4. **Pour** in media; make sure that both impellers are submerged.
5. **Place** the head plate onto the vessel and lock it to the clamping ring by tightening the thumbscrews.
6. Add 9 ml of Antifoam-A through the inoculation port.
7. **Insert** the temperature probe (RTD) with a few drops of glycerol into the thermowell and plug into the BioFlo 3000.
8. **Place** steel blank into condenser port with a few drops of glycerol and gently tighten.
9. **Place** 1/4 I.D. silicone tubing on the top of the steel blank on condenser and connect the air filter (Acro 50) such that there is tubing attached to both sides and the tube from the condenser is attached to the 'inlet' side of the filter (imprinted on filter). Bend last tube in half and secure with cable tie such that nothing can escape through the tubing. Wrap cotton and aluminum foil around the exposed tubing end.
10. **Obtain** two long (>60cm) silicone tubes.
11. **Attach** one acid/base silicone tubing (I.D. 1/32) to one of the addition ports. Bend tubing in half close to port and secure with a cable tie. Wrap cotton and aluminum foil around the exposed tubing end.
12. **Attach** the other acid/base silicone tubing (I.D. 1/32) to the other addition port. Bend tubing in half close to port and secure with a cable tie. Wrap cotton and aluminum foil around the exposed tubing end.

13. **Place** 1/4 I.D. silicone tubing on the top of the sparger tube and connect the air filter (Acro 37) such that there is tubing attached to both sides. Wrap cotton and aluminum foil around the exposed tubing end.
14. **Attach** silicone tubing to the harvest port, bend tube in half near port opening and secure with cable tie. Wrap cotton and aluminum foil around the exposed tubing end.
15. **Loosen** the inoculation port to allow ventilation.
16. **Loosen** the sampling tube, and remove the rubber bulb, make sure that there is an ample amount of glass wool in tube where the rubber bulb connects to the sampling assembly.
17. **Make** sure that the sampling valve is closed.
18. **Connect** the water out line (top) to the vessel heat exchanger (the vessel base).
19. **Connect** the water in lines (bottom) to the vessel heat exchanger.
20. **TURN ON WATER** (under the counter)
Note: The pressure gauge should read 15 psig.
21. **TURN ON AIR (Use SOP on wall above tanks)**
Note: The pressure gauge should not exceed 10 psig, 5 psig is safe.
22. **TURN ON BioFlo 3000.**

Calibration of pH Probe

23. **Check** the probe for any trapped air bubbles, tap gently at a 45 degree angle to remove bubbles.
24. **Check** electrolyte levels within the probe. They should be around 1 cm below the each of the filling ports.
25. **Remove** the rubber plugs.
26. **Attach** one end of the pH cable to the pH probe and the other end of the pH cable to BioFlo console.
27. **Go** to <Calibration> screen.

28. **Immerse** pH electrode into a pH 7 buffer solutions.
Note: Allow a few minutes for the electrode to equilibrate.
29. **Set** function column (use arrow keys to move selection on display) to **ZERO** by pressing alter and press enter.
30. **Enter** seven (**7.0**) under the zero columns and press enter.
31. **Rinse** electrode thoroughly with de-ionized water.
32. **Immerse** pH electrode into a pH 4 buffer solutions.
Note: Allow a few minutes for the electrode to equilibrate.
33. **Set** function column to **SPAN** using alter key and press enter.
34. **Enter** four (**4.0**) under the span column and press enter.
35. **Rinse** electrode with de-ionized water.
36. **Repeat** calibration.
37. **Apply** a small amount of glycerol to the probe prior to inserting into the vessel
38. **Disconnect** the cable, and replace shorting caps and rubber plugs prior to sterilization. Rubber bands, located on the pH probe, should be placed over the rubber plugs.

Installation of Dissolved Oxygen Probe

39. **Remove** protective cap (green) from the electrode end.
40. **Attach** adapter to head plate and tighten with a wrench.
41. **Carefully** insert the probe into the adapter.
42. **The** shorting plug (cap on top of probe) should be installed prior to sterilization.

Autoclaving Procedure

43. **Turn** off the power.
44. **Turn** off the water.

45. **Turn** off the air.
46. **Disconnect** water out lines to heat exchanger.
47. **Disconnect** water in lines to heat exchanger.
48. **Remove** RTD from the thermowell.
49. **Double** check all tubes and ports to ensure vessel is completely sealed up, except for inoculation port.
50. **Autoclave** entire assembly at 121°C at 15 psig for 25 minutes.

Preparation for Operation

51. **Place** the BioFlo vessel onto the console.
52. **Connect** the water out line to the vessel heat exchanger (the vessel base).
53. **Connect** the water in lines to the heat exchanger.
54. **Connect** the water out line to the condenser. (Top)
55. **Connect** the water in line to the condenser. (Bottom)
56. **Add** glycerol to thermowell and insert RTD.
57. **TURN ON NITROGEN**
Note: Approximately 5 psig, do not exceed 10 psig.
58. **TURN ON WATER** (under the counter) Make sure that the water pressure is between 15 and 20 psig.
59. **Connect** the air line (tube) from sparger to the sparger 4 gas port on the BioFlo base (near the top).
60. **Turn** on power switch.
61. **Select** Fermentation mode (#2)
62. **Go** to <Master> screen and set the temperature control mode to **PRIME** for one minute.

63. **After** a minute set the desired working temperature (**30°C**) and the control mode to **PID**.
64. **Remove** the rubber plugs and shorting cap from the pH probe and connect the pH cable.
65. **Remove** shorting cap from DO probe and connect DO cable.
66. **Place** motor onto the top of the head plate and plug into the console.

Attaching the Condenser

67. **Go** to the <Gases> screen and set the mode to **MANUAL**, DO NOT PRESS ENTER.
68. **Remove** the foil and place exhaust tubing from condenser and filter such that it collects into a beaker that is placed beside the BioFlo console.
69. **Press** enter.

Setting-up the pH Control

70. **Place** the agitation loop into **PID** control and set the set point to **120** rpm.
71. **Attach** the end of the tube from the addition port to the top of the glass tube on the ammonium hydroxide flask.
72. **Attach** the ammonium hydroxide through the peristaltic pump. Thread the tube in the following manner: from the addition port, thread the tube through the bottom of the pump and around to the top, and onto the ammonium hydroxide flask glass tube on top. The pump moves in a clockwise direction, therefore the solution will move in that direction. Verify that the ammonium hydroxide will be pumped into the vessel before proceeding to the next step.
73. **Set** the pH loop to **PID** control and set the set point to **5.0**.
74. **Set** the feed pump 1 control loop (use alter key while on pH loop to get to feed pump 1 loop) to **BASE**, and the set point to **100**.

Calibration of the Dissolved Oxygen Probe

Note: Probe cannot be calibrated until the desired working temperature has been reached.

75. **Go** to <Calibration> screen, arrow to Function column for **DO**.
76. **Unplug** DO cable from the DO probe.
77. **Set** Function column to **ZERO** and press enter.
78. **Arrow** to zero column and enter zero (**0.0**) and press enter.
79. **Reattach** cable to DO probe.
80. **Go** to <Master> screen and set Agitation to **1000** rpm.
81. **Go** to <Gases> screen and set the mode to **MANUAL**.
82. **Allow** ten to thirty minutes for the vessel to equilibrate.
83. **Go** to <Calibration> screen, arrow to Function column for **DO**.
84. **Set** Function column to **SPAN** and press enter.
85. **Arrow** to Span column and enter **100.0** and press enter.

APPENDIX B

RHEOLOGY AND RHEOLOGICAL PARAMETER DETERMINATION

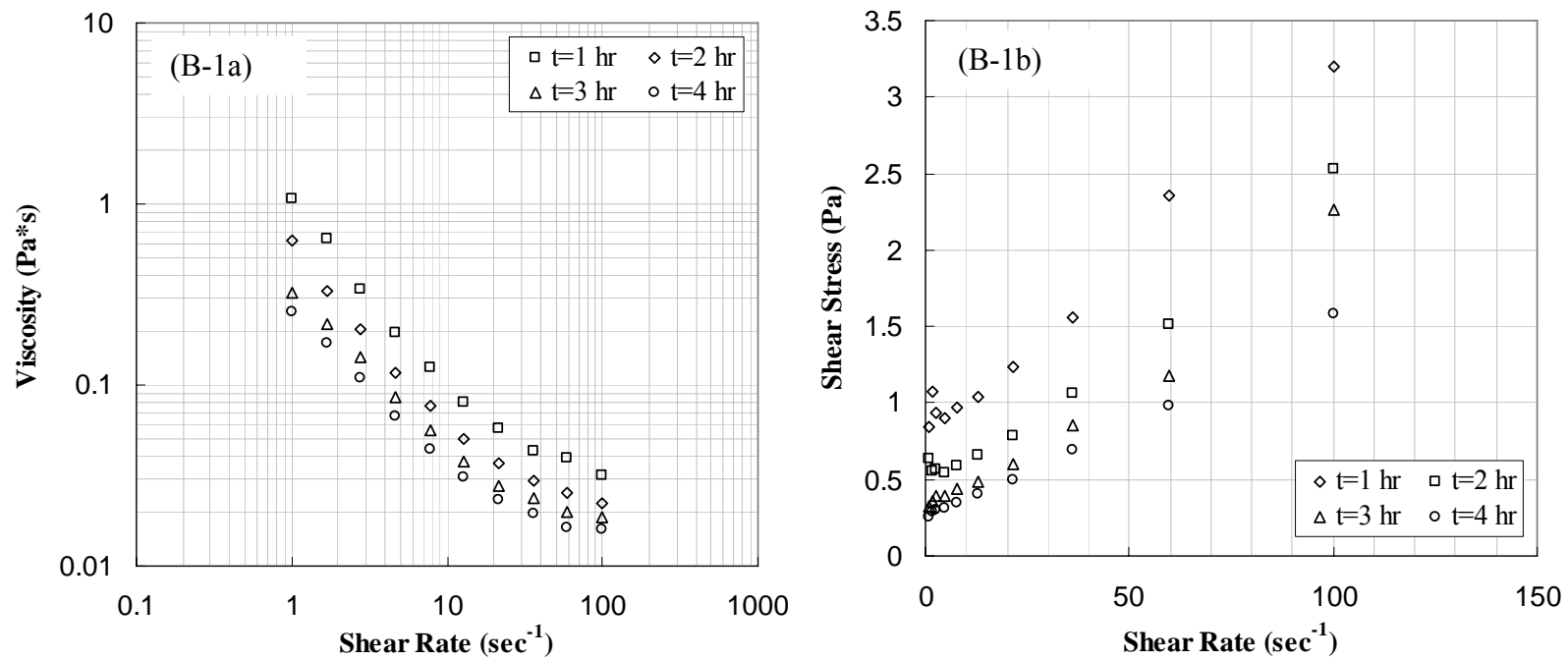


Figure B-1. Viscosity and shear stress curves as a function of shear rate for different time during initial 4-hours enzymatic hydrolysis.

Note;

1. Hydrolysis condition: 30 FPU/g of glucan, pH 4.8~5.0, 50°C, 120 rpm.
2. Substrates were added to the reactions 10 % (w/v).

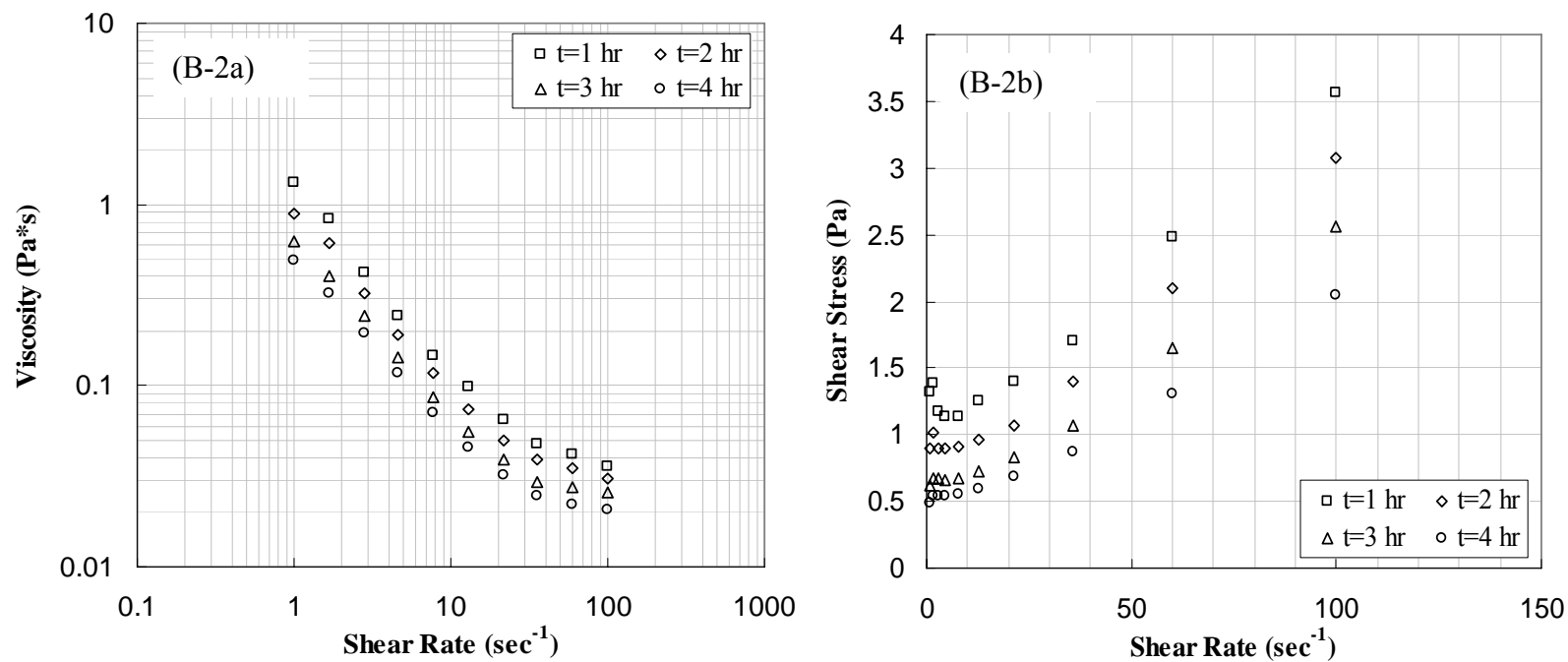


Figure B-2. Viscosity and shear stress curves as a function of shear rate for different time during initial 4-hours enzymatic hydrolysis.

Note;

1. Hydrolysis condition: 15 FPU/g of glucan, pH 4.8~5.0, 50°C, 120 rpm.
2. Substrates were added to the reactions 10 % (w/v).

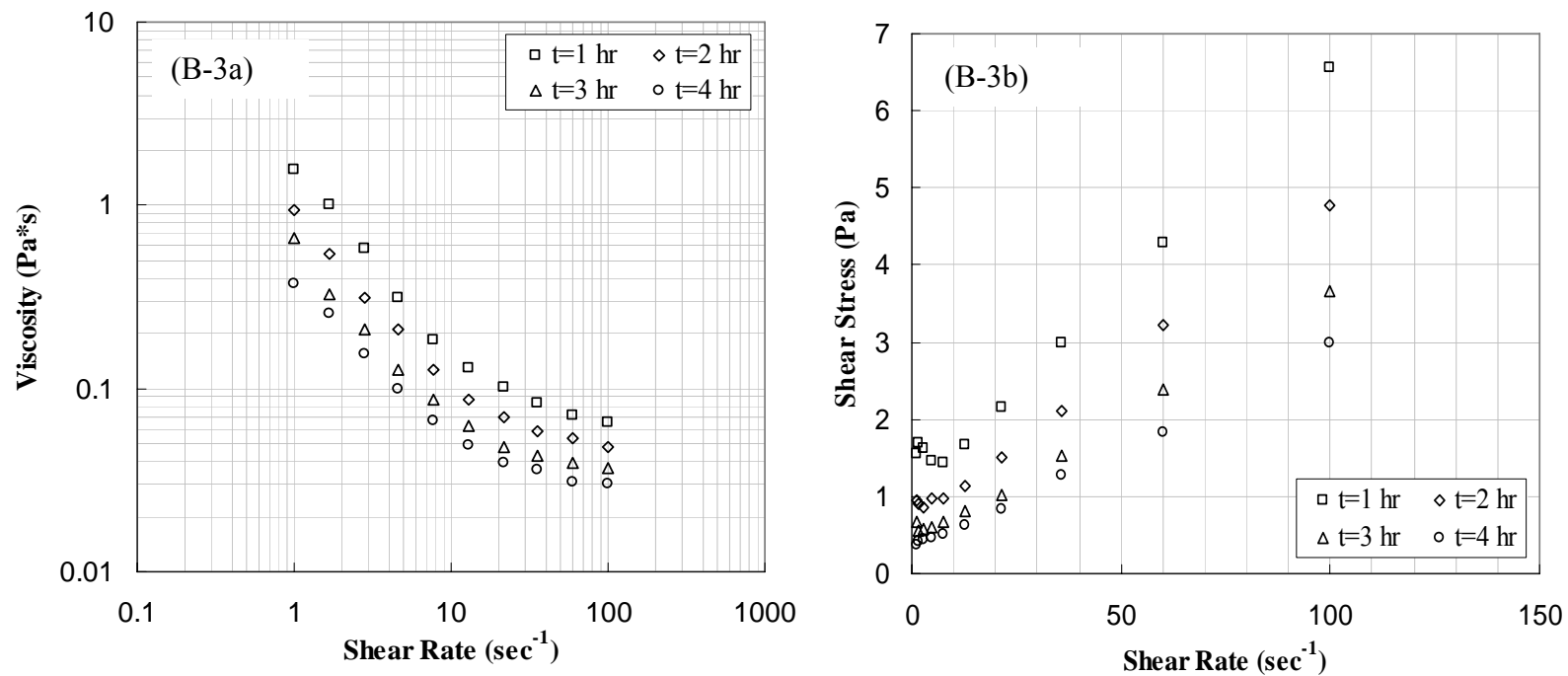


Figure B-3. Viscosity and shear stress curves as a function of shear rate for different time during initial 4-hours enzymatic hydrolysis.

Note;

1. Hydrolysis condition: 30 FPU/g of glucan, pH 4.8~5.0, 30°C, 120 rpm.
2. Substrates were added to the reactions 10 % (w/v).

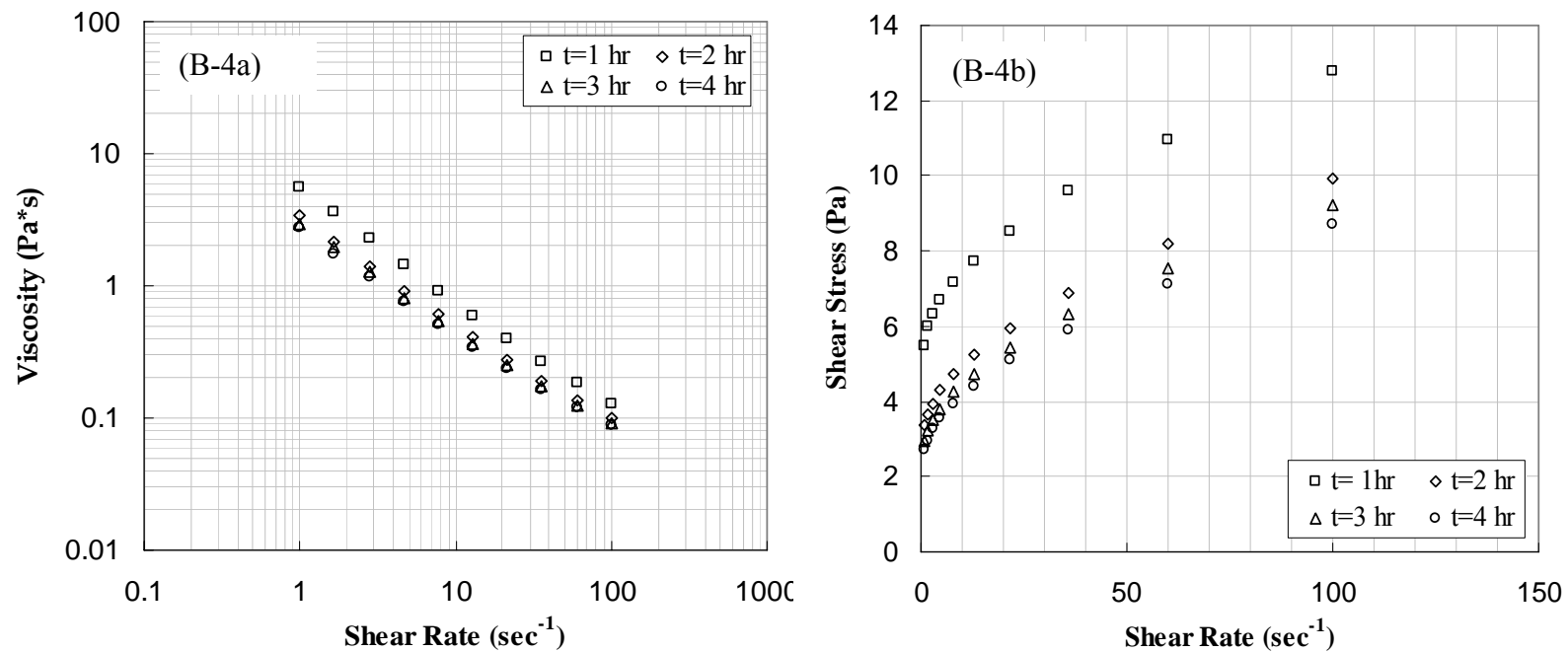


Figure B-4. Viscosity and shear stress curves as a function of shear rate for different time during initial 4-hours enzymatic hydrolysis.

Note;

1. Hydrolysis condition: 30 FPU/g of glucan, pH 4.8~5.0, 50°C, 120 rpm.
2. Substrates were added to the reactions 15 % (w/v).

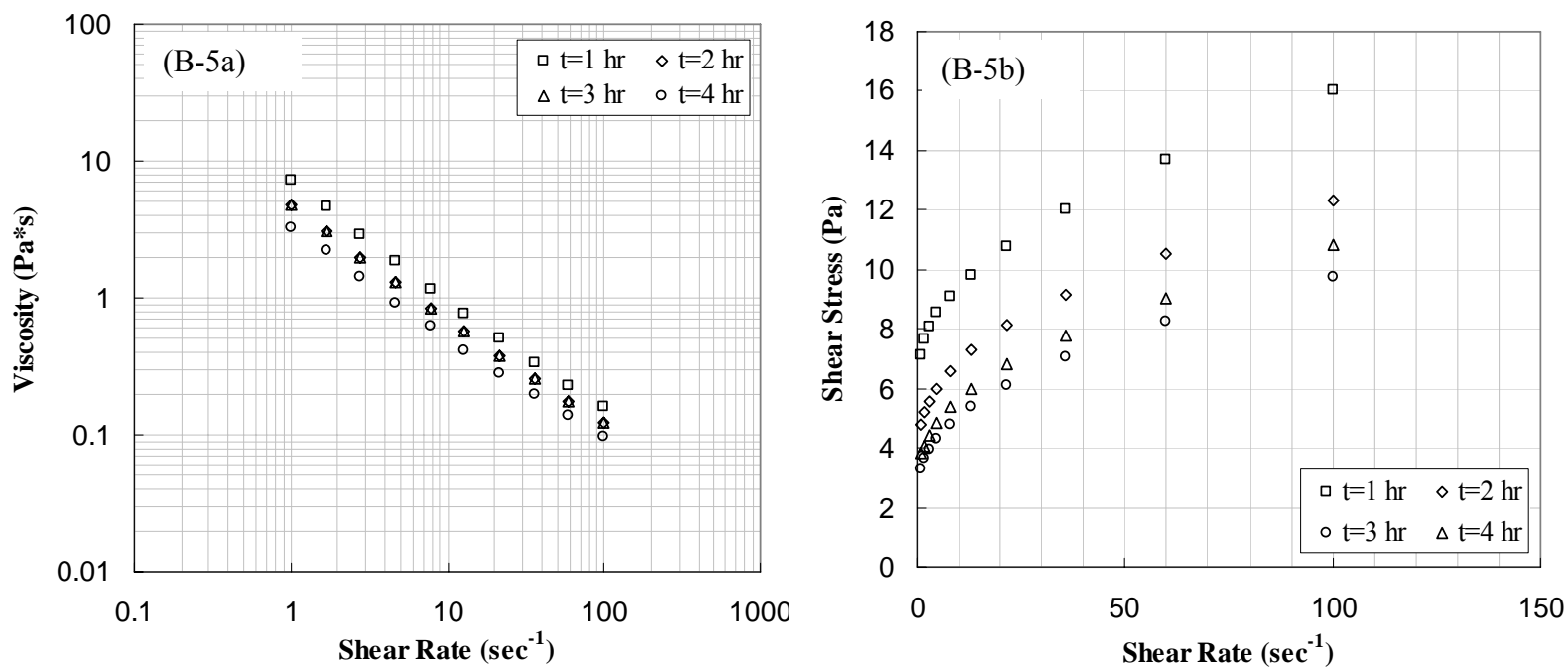


Figure B-5. Viscosity and shear stress curves as a function of shear rate for different time during initial 4-hours enzymatic hydrolysis.

Note;

1. Hydrolysis condition: 15 FPU/g of glucan, pH 4.8~5.0, 50°C, 120 rpm.
2. Substrates were added to the reactions 15 % (w/v).

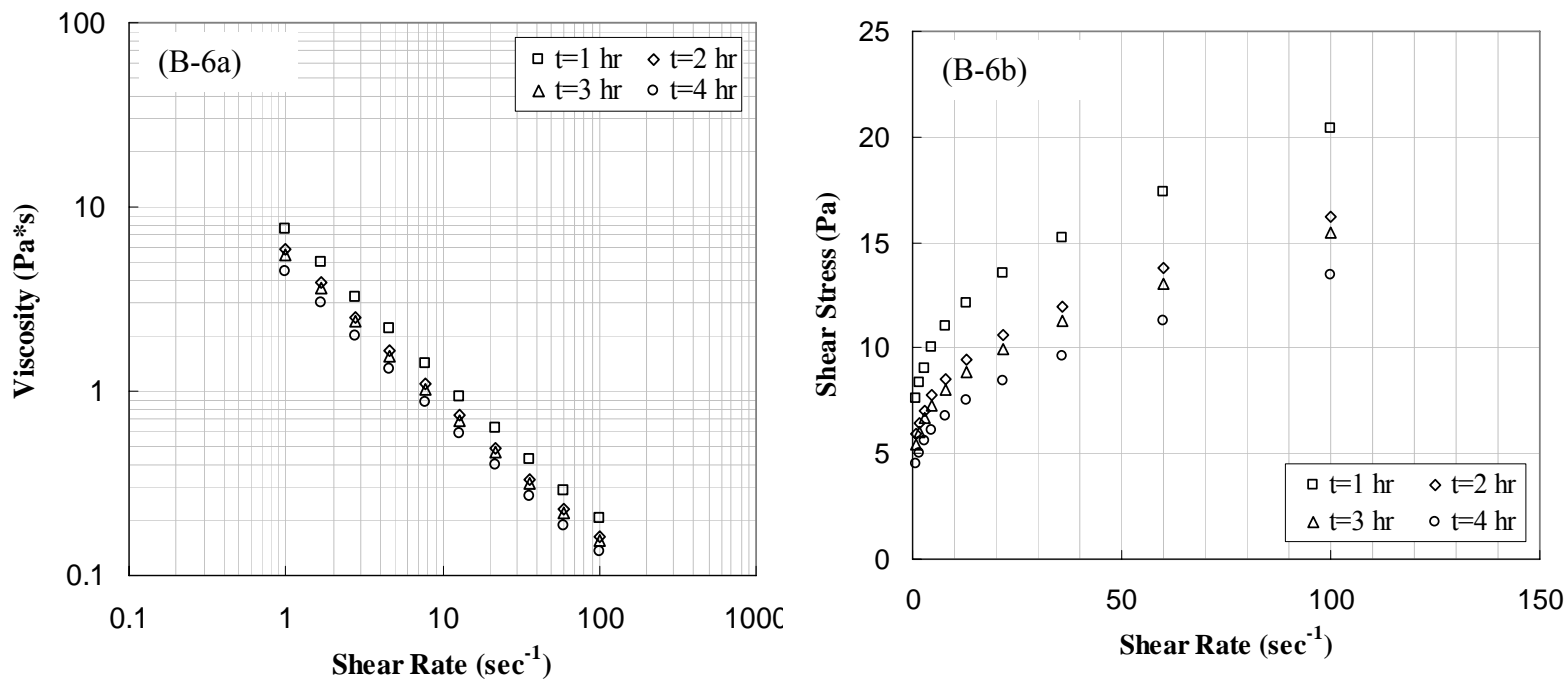


Figure B-6. Viscosity and shear stress curves as a function of shear rate for different time during initial 4-hours enzymatic hydrolysis.

Note;

1. Hydrolysis condition: 30 FPU/g of glucan, pH 4.8~5.0, 30°C, 120 rpm.
2. Substrates were added to the reactions 15 % (w/v).

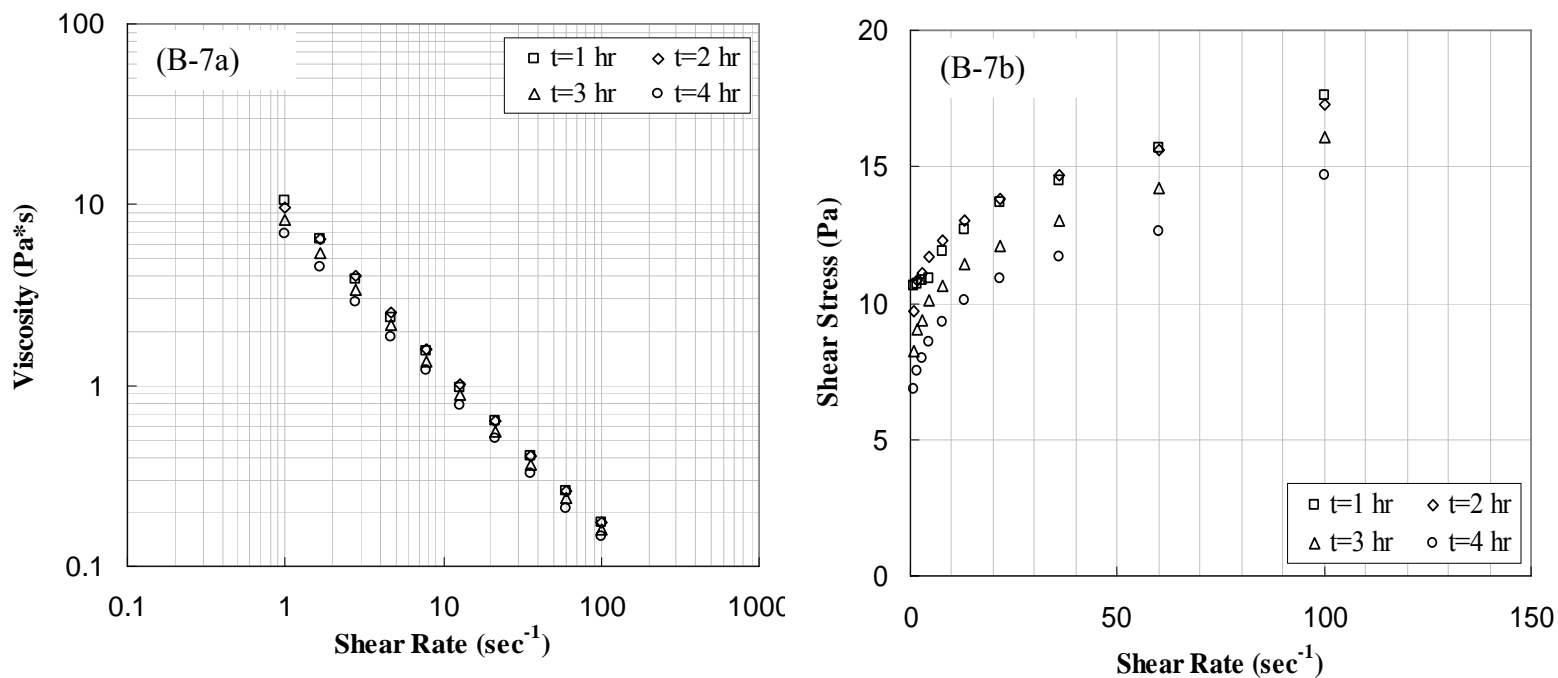


Figure B-7. Viscosity and shear stress curves as a function of shear rate for different time during initial 4-hours enzymatic hydrolysis.

Note;

1. Hydrolysis condition: 30 FPU/g of glucan, pH 4.8~5.0, 50°C, 120 rpm.
2. Substrates were added to the reactions 20 % (w/v).

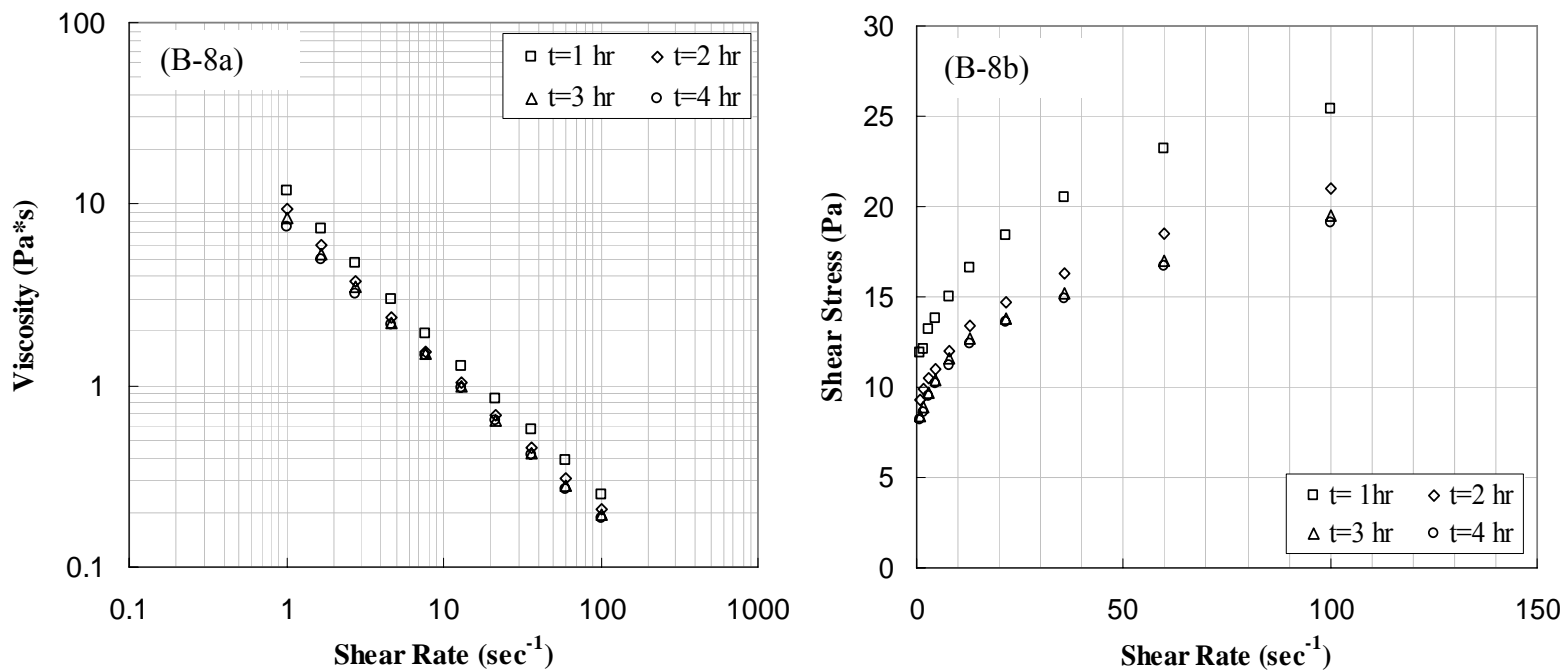


Figure B-8. Viscosity and shear stress curves as a function of shear rate for different time during initial 4-hours enzymatic hydrolysis.

Note;

1. Hydrolysis condition: 15 FPU/g of glucan, pH 4.8~5.0, 50°C, 120 rpm.
2. Substrates were added to the reactions 20 % (w/v).

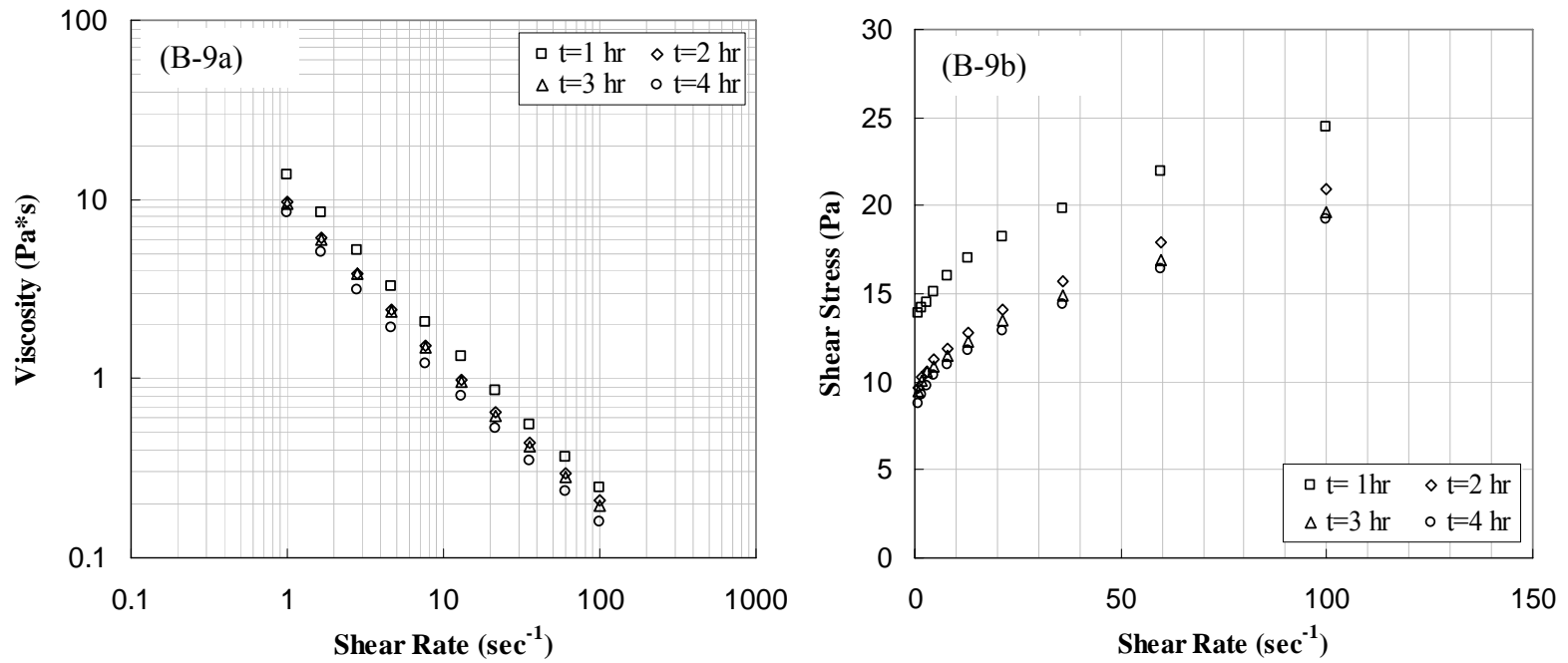


Figure B-9. Viscosity and shear stress curves as a function of shear rate for different time during initial 4-hours enzymatic hydrolysis.

Note;

1. Hydrolysis condition: 30 FPU/g of glucan, pH 4.8~5.0, 30°C, 120 rpm.
2. Substrates were added to the reactions 20 % (w/v).

Table B-1. Determination of rheological parameter as function of time during initial 4-hr enzymatic hydrolysis.

Reaction Time	Herschel-Bulkley Model $\tau = \tau_y + K \dot{\gamma}^n$				Bingham Model $\tau = \tau_y + K \dot{\gamma}$			Casson Model $\tau^{0.5} = (\tau_y)^{0.5} + n(\dot{\gamma})^{0.5}$			Power Law $\tau = K \dot{\gamma}^n$		
	τ_y (pa)	K	n	R ²	τ_y (pa)	n	R ²	τ_y (pa)	n	R ²	K	n	R ²
t= 1 hr	0.142	0.167	0.560	0.862	0.636	0.026	0.904	0.532	0.093	0.893	0.673	0.266	0.811
t= 2 hr	0.253	0.075	0.681	0.894	0.345	0.020	0.936	0.274	0.090	0.908	0.382	0.315	0.812
t= 3 hr	0.164	0.157	0.518	0.924	0.222	0.018	0.970	0.164	0.091	0.902	0.235	0.390	0.856
t= 4 hr	0.134	0.036	0.802	0.943	0.166	0.017	0.975	0.116	0.091	0.937	0.177	0.430	0.858

Note;

1. Hydrolysis condition: 30 FPU/g of glucan, pH 4.8~5.0, 50°C, 120 rpm.
2. Substrates were added to the reactions 10 % (w/v).

Nomenclatures;

τ : shear stress, Pa

τ_y : yield shear stress, Pa

n: flow behavior index

K: consistency index constant, Pasⁿ

R²: squared multiple correlation coefficient

Table B-2. Determination of rheological parameter as function of time during initial 4-hr enzymatic hydrolysis.

Reaction Time	Herschel-Bulkley Model $\tau = \tau_y + K \dot{\gamma}^n$				Bingham Model $\tau = \tau_y + K \dot{\gamma}$			Casson Model $\tau^{0.5} = (\tau_y)^{0.5} + n(\dot{\gamma})^{0.5}$			Power Law $\tau = K \dot{\gamma}^n$		
	τ_y (pa)	K	n	R ²	τ_y (pa)	n	R ²	τ_y (pa)	n	R ²	K	n	R ²
t= 1 hr	0.937	0.020	1.045	0.908	0.924	0.024	0.904	0.786	0.082	0.854	0.940	0.205	0.732
t= 2 hr	0.620	0.034	0.907	0.914	0.645	0.023	0.922	0.537	0.085	0.882	0.663	0.248	0.777
t= 3 hr	0.405	0.040	0.821	0.919	0.447	0.019	0.943	0.364	0.081	0.897	0.459	0.278	0.793
t= 4 hr	0.338	0.025	0.911	0.937	0.354	0.017	0.950	0.281	0.080	0.898	0.359	0.304	0.797

Note;

1. Hydrolysis condition: 15 FPU/g of glucan, pH 4.8~5.0, 50°C, 120 rpm.
2. Substrates were added to the reactions 10 % (w/v).

Nomenclatures;

τ : shear stress, Pa

τ_y : yield shear stress, Pa

n: flow behavior index

K: consistency index constant, Pasⁿ

R²: squared multiple correlation coefficient

Table B-3. Determination of rheological parameter as function of time during initial 4-hr enzymatic hydrolysis.

Reaction Time	Herschel-Bulkley Model $\tau = \tau_y + K \gamma^n$				Bingham Model $\tau = \tau_y + K \gamma$			Casson Model $\tau^{0.5} = (\tau_y)^{0.5} + n(\gamma)^{0.5}$			Power Law $\tau = K \gamma^n$		
	τ_y (pa)	K	n	R ²	τ_y (pa)	n	R ²	τ_y (pa)	n	R ²	K	n	R ²
t= 1 hr	1.391	0.009	1.426	0.993	1.224	0.052	0.970	0.895	0.139	0.916	1.079	0.314	0.824
t= 2 hr	0.535	0.076	0.855	0.978	0.602	0.042	0.980	0.418	0.138	0.970	0.561	0.389	0.907
t= 3 hr	0.388	0.039	0.948	0.948	0.404	0.031	0.968	0.269	0.122	0.943	0.383	0.406	0.872
t= 4 hr	0.296	0.028	0.985	0.985	0.299	0.026	0.978	0.187	0.117	0.953	0.266	0.453	0.896

Note;

1. Hydrolysis condition: 30 FPU/g of glucan, pH 4.8~5.0, 30°C, 120 rpm.
2. Substrates were added to the reactions 10 % (w/v).

Nomenclatures;

τ : shear stress, Pa

τ_y : yield shear stress, Pa

n: flow behavior index

K: consistency index constant, Pasⁿ

R²: squared multiple correlation coefficient

Table B-4. Determination of rheological parameter as function of time during initial 4-hr enzymatic hydrolysis.

Reaction Time	Herschel-Bulkley Model $\tau = \tau_y + K \gamma^n$				Bingham Model $\tau = \tau_y + K \gamma$			Casson Model $\tau^{0.5} = (\tau_y)^{0.5} + n(\gamma)^{0.5}$			Power Law $\tau = K \gamma^n$		
	τ_y (pa)	K	n	R ²	τ_y (pa)	n	R ²	τ_y (pa)	n	R ²	K	n	R ²
t= 1 hr	4.308	0.868	0.454	0.991	5.624	0.069	0.957	4.774	0.124	0.988	4.841	0.169	0.977
t= 2 hr	2.352	0.666	0.503	0.991	3.339	0.070	0.968	2.630	0.147	0.997	2.752	0.240	0.987
t= 3 hr	1.343	0.264	0.533	0.991	1.743	0.032	0.969	1.407	0.095	0.992	1.460	0.219	0.975
t= 4 hr	1.429	0.149	0.614	0.979	1.664	0.027	0.967	1.378	0.082	0.980	1.422	0.195	0.954

Note;

1. Hydrolysis condition: 30 FPU/g of glucan, pH 4.8~5.0, 50°C, 120 rpm.
2. Substrates were added to the reactions 15 % (w/v).

Nomenclatures;

τ : shear stress, Pa

τ_y : yield shear stress, Pa

n: flow behavior index

K: consistency index constant, Pasⁿ

R²: squared multiple correlation coefficient

Table B-5. Determination of rheological parameter as function of time during initial 4-hr enzymatic hydrolysis.

Reaction Time	Herschel-Bulkley Model $\tau = \tau_y + K \dot{\gamma}^n$				Bingham Model $\tau = \tau_y + K \dot{\gamma}$			Casson Model $\tau^{0.5} = (\tau_y)^{0.5} + n(\dot{\gamma})^{0.5}$			Power Law $\tau = K \dot{\gamma}^n$		
	τ_y (pa)	K	n	R ²	τ_y (pa)	n	R ²	τ_y (pa)	n	R ²	K	n	R ²
t= 1 hr	4.683	0.952	0.463	0.997	6.138	0.078	0.962	5.167	0.135	0.994	5.248	0.175	0.982
t= 2 hr	2.749	0.686	0.507	0.999	3.779	0.073	0.969	3.013	0.146	0.997	3.133	0.228	0.986
t= 3 hr	2.352	0.666	0.503	0.999	3.339	0.070	0.968	2.630	0.146	0.997	2.752	0.240	0.987
t= 4 hr	2.111	0.651	0.499	0.999	3.066	0.067	0.968	2.399	0.146	0.997	2.520	0.247	0.988

Note;

1. Hydrolysis condition: 15 FPU/g of glucan, pH 4.8~5.0, 50°C, 120 rpm.
2. Substrates were added to the reactions 15 % (w/v).

Nomenclatures;

τ : shear stress, Pa

τ_y : yield shear stress, Pa

n: flow behavior index

K: consistency index constant, Pasⁿ

R²: squared multiple correlation coefficient

Table B-6. Determination of rheological parameter as function of time during initial 4-hr enzymatic hydrolysis.

Reaction Time	Herschel-Bulkley Model $\tau = \tau_y + K \gamma^n$				Bingham Model $\tau = \tau_y + K \gamma$			Casson Model $\tau^{0.5} = (\tau_y)^{0.5} + n(\gamma)^{0.5}$			Power Law $\tau = K \gamma^n$		
	τ_y (pa)	K	n	R ²	τ_y (pa)	n	R ²	τ_y (pa)	n	R ²	K	n	R ²
t= 1 hr	3.952	3.604	0.324	0.992	8.717	0.143	0.933	7.134	0.199	0.980	7.320	0.210	0.989
t= 2 hr	3.184	2.157	0.376	0.997	6.792	0.115	0.946	5.519	0.180	0.988	5.671	0.214	0.991
t= 3 hr	3.341	2.194	0.366	0.996	6.329	0.111	0.944	5.126	0.178	0.987	5.279	0.219	0.992
t= 4 hr	2.714	1.855	0.376	0.997	5.238	0.101	0.947	4.193	0.173	0.988	4.347	0.230	0.992

Note;

1. Hydrolysis condition: 30 FPU/g of glucan, pH 4.8~5.0, 30°C, 120 rpm.
2. Substrates were added to the reactions 15 % (w/v).

Nomenclatures;

τ : shear stress, Pa

τ_y : yield shear stress, Pa

n: flow behavior index

K: consistency index constant, Pasⁿ

R²: squared multiple correlation coefficient

Table B-7. Determination of rheological parameter as function of time during initial 4-hr enzymatic hydrolysis.

Reaction Time	Herschel-Bulkley Model				Bingham Model			Casson Model			Power Law		
	$\tau = \tau_y + K \dot{\gamma}^n$				$\tau = \tau_y + K \dot{\gamma}$			$\tau^{0.5} = (\tau_y)^{0.5} + n(\dot{\gamma})^{0.5}$			$\tau = K \dot{\gamma}^n$		
	τ_y (pa)	K	n	R ²	τ_y (pa)	n	R ²	τ_y (pa)	n	R ²	K	n	R ²
t= 1 hr	9.576	0.849	0.488	0.995	10.986	0.076	0.960	9.835	0.109	0.993	9.861	0.111	0.966
t= 2 hr	5.614	4.393	0.206	0.996	11.063	0.074	0.916	9.918	0.108	0.975	9.851	0.115	0.993
t= 3 hr	5.727	2.712	0.283	0.997	9.335	0.080	0.934	8.198	0.121	0.983	8.185	0.135	0.992
t= 4 hr	3.217	3.721	0.236	0.997	7.883	0.081	0.920	6.795	0.131	0.977	6.800	0.157	0.996

Note;

1. Hydrolysis condition: 30 FPU/g of glucan, pH 4.8~5.0, 50°C, 120 rpm.
2. Substrates were added to the reactions 20 % (w/v).

Nomenclatures;

- τ : shear stress, Pa
- τ_y : yield shear stress, Pa
- n: flow behavior index
- K: consistency index constant, Pasⁿ
- R²: squared multiple correlation coefficient

Table B-8. Determination of rheological parameter as function of time during initial 4-hr enzymatic hydrolysis.

Reaction Time	Herschel-Bulkley Model				Bingham Model			Casson Model			Power Law		
	$\tau = \tau_y + K \dot{\gamma}^n$				$\tau = \tau_y + K \dot{\gamma}$			$\tau^{0.5} = (\tau_y)^{0.5} + n(\dot{\gamma})^{0.5}$			$\tau = K \dot{\gamma}^n$		
	τ_y (pa)	K	n	R ²	τ_y (pa)	n	R ²	τ_y (pa)	n	R ²	K	n	R ²
t= 1 hr	9.685	2.096	0.459	0.999	12.877	0.169	0.961	10.788	0.201	0.995	10.966	0.179	0.984
t= 2 hr	7.175	2.155	0.404	0.999	10.324	0.129	0.949	8.686	0.175	0.993	8.793	0.176	0.989
t= 3 hr	4.869	3.501	0.307	0.999	9.524	0.122	0.932	7.999	0.172	0.985	8.077	0.181	0.996
t= 4 hr	4.540	3.590	0.301	0.999	9.278	0.123	0.931	7.783	0.172	0.984	7.861	0.183	0.996

Note;

1. Hydrolysis condition: 15 FPU/g of glucan, pH 4.8~5.0, 50°C, 120 rpm.
2. Substrates were added to the reactions 20 % (w/v).

Nomenclatures;

τ : shear stress, Pa

τ_y : yield shear stress, Pa

n: flow behavior index

K: consistency index constant, Pasⁿ

R²: squared multiple correlation coefficient

Table B-9. Determination of rheological parameter as function of time during initial 4-hr enzymatic hydrolysis.

Reaction Time	Herschel-Bulkley Model $\tau = \tau_y + K \dot{\gamma}^n$				Bingham Model $\tau = \tau_y + K \dot{\gamma}$			Casson Model $\tau^{0.5} = (\tau_y)^{0.5} + n(\dot{\gamma})^{0.5}$			Power Law $\tau = K \dot{\gamma}^n$		
	τ_y (pa)	K	n	R ²	τ_y (pa)	n	R ²	τ_y (pa)	n	R ²	K	n	R ²
t= 1 hr	12.385	0.8041	0.5729	0.996	13.777	0.112	0.976	12.193	0.137	0.996	12.275	0.1227	0.962
t= 2 hr	9.260	1.8764	0.4096	0.997	12.076	0.115	0.955	10.497	0.149	0.993	10.544	0.1431	0.985
t= 3 hr	7.755	2.0681	0.3910	0.997	10.768	0.116	0.953	9.244	0.156	0.992	9.309	0.1567	0.988
t= 4 hr	8.058	1.4869	0.4520	0.999	10.344	0.115	0.962	8.842	0.157	0.997	8.929	0.1591	0.984

Note;

1. Hydrolysis condition: 30 FPU/g of glucan, pH 4.8~5.0, 30°C, 120 rpm.
2. Substrates were added to the reactions 20 % in one time.

Nomenclatures;

τ : shear stress, Pa

τ_y : yield shear stress, Pa

n: flow behavior index

K: consistency index constant, Pasⁿ

R²: squared multiple correlation coefficient

APPENDIX C
SIMULATION METHODS, PROCEDURES, AND APPRATUS

C-1. START MIXSIM AND FLUENT

The simulations were performed using software package:

1. MixSim V 2.1.10
2. FLUENT V 6.2.20

1. Starting Mixsim

When IBM system is used, MixSim can be started by typing Mixsim from the command line of an xterm window (Hummingbird). The Mixsim console window will appear on the computer screens. The TUI, GUI will show up when new simulation new model starts. GUI showing a tank with some of the default dimensions will open.

2. Starting the Session

Model

From the model, analysis type and tank type were selected - Geometry (Multiple Reference Frame), or geometry (sliding mesh). In most simulations 3D cylindrical with the velocity data model was chosen.

Continuum and Fluid

Viscous model and fluid properties category from the continuum was selected to enter the appropriate flow regime and physical properties of the fluid, including the fluid density and viscosity.

Cylindrical Tank

The Tank Geometry definition includes: Bottom Shape with choices of ASME Dish, spherical, conical, curved, Tank Diameter, Tank Height, and Liquid Height. In all

simulation an Ellipsoidal was chosen to be the tank bottom shape and a top-surface is a wall choice was deactivated to impose a slip boundary condition on the upper surface of the liquid. After all dimensions were entered, by clicking Apply button, the tank outline in the graphics window was drawn accordingly.

3. Add Object

Drive Shaft

In defining a top shaft, a distance off bottom, shaft diameter, rotational direction (clockwise or counter-clockwise), and rotational speed need to be determined. The distance off bottom of the shaft set the length of the shaft. The shaft had to go as far as the lowest impeller in the tank. If this condition was not chosen, an error message will appear.

Impellers (Rushton Turbine)

An impeller is added to the tank by clicking the add button. The data from the library can be edited in the edit menu that includes impeller characteristics. General impeller characteristics include diameter, axial location, the name of the blade (which can be edited), number of blades of the impeller. In the parametric characteristics, either the library data for the impeller detail dimensions or edited data can be used. When using the impeller, the velocity data is provided in the MixSim Library. The location where the velocity data is applicable could be below, above, or at the outer radius of the impeller. Data for impellers could also be imported from an external file in the Geometric Impeller Characteristics category. The correlations category includes flow number and power number for the impeller. The most updated tank outline equipped

with impellers and draft tube was shown in the graphic window after clicking on the Apply button.

Baffles

In all simulations, baffles were used. Four baffles were used in the Bioreactor tank simulations. When determining the size of the baffle, the length of the baffles was designed so that the baffles would not extend below the tank bottom and the radial width would be 10 percent of the tank diameter.

4. Generate Grid and Grid Check

To create the geometry and generate the grid, MixSim uses GAMBIT in the background. When the geometry is created, MixSim saves the GAMBIT files. You can use these files to generate the mesh on your own or add custom objects using GAMBIT.

The grid is generated in GAMBIT and then exported as a .msh file. The mesh file is read into MixSim automatically and the grid is checked during the process. As the grid is checked, MixSim reports on the grid properties and the grid quality by displaying the cell distribution based on skewness level in the console.

5. Reporting the Model Information

In the Report pull-down menu, the Model Info category was selected to examine the model information in report format. The complete report can be sent either to console or to file.

6. Writing the MixSim File

The MixSim file had to be written to save the completely specified problem. This file will contain all of the information that has been entered in the session and can be read into MixSim at a later time to execute the simulation or to make modification to the problem definition.

In the File pull-down menu, Write MixSim category was selected to write the MixSim file. A name for the file was chosen and the file was written by clicking on the OK button.

7. Performing the Calculation

The completely specified problem was ready to solve. In the Solve pull-down menu, Calculate category was chosen to start the calculation. Once the number of iterations was entered, the iteration began starting with grid generation by preBFC. The iteration was performed by FLUENT 6.2.10.

When the session file in the MixSim session was not completed, entering zero iteration as the number of iterations did enabling the writing of the case file of the problem. This step allowed the generation of the grid so that the case file could be written. Once the case file has been written, the calculation began by selecting the Iteration category under the Solve pull-down menu and entering a number of iterations.

8. Examination the Results (MixSim 2.1.10 or FLUENT 6.2.20)

The solution of the iterations was examined using some of the graphics features provided by FLUENT or MixSim under the Display pull-down menu. These features include

plotting vectors and contours of the flow field. Slices of the geometry in the x-direction (radial-direction) and z-direction (angular direction) were created to better show the flow pattern of the area of concern. In most cases velocity magnitude vectors, radial velocity vectors, axial velocity vectors and tangential velocity vectors were examined. Energy dissipation rate throughout the tank was presented in the contour plot.

9. Saving the Graphics Feature from FLUENT

The graphics presentations were improved using the View command in the Display pull-down menu. The graphics features presented in a graphics window were rotated for better viewing. These features were then saved as hardcopy files in postscript type of file to enable them to be printed using a personal computer. Adobe Acrobat 7.0 Professional program was used to view and print this graphics feature.

10. Writing FLUENT Files

When the session file was not completed in MixSim, a new name had to be entered as a data file to enable the file to be written. To write a data file the write data category was selected in the file pull-down menu and name of the file was entered.

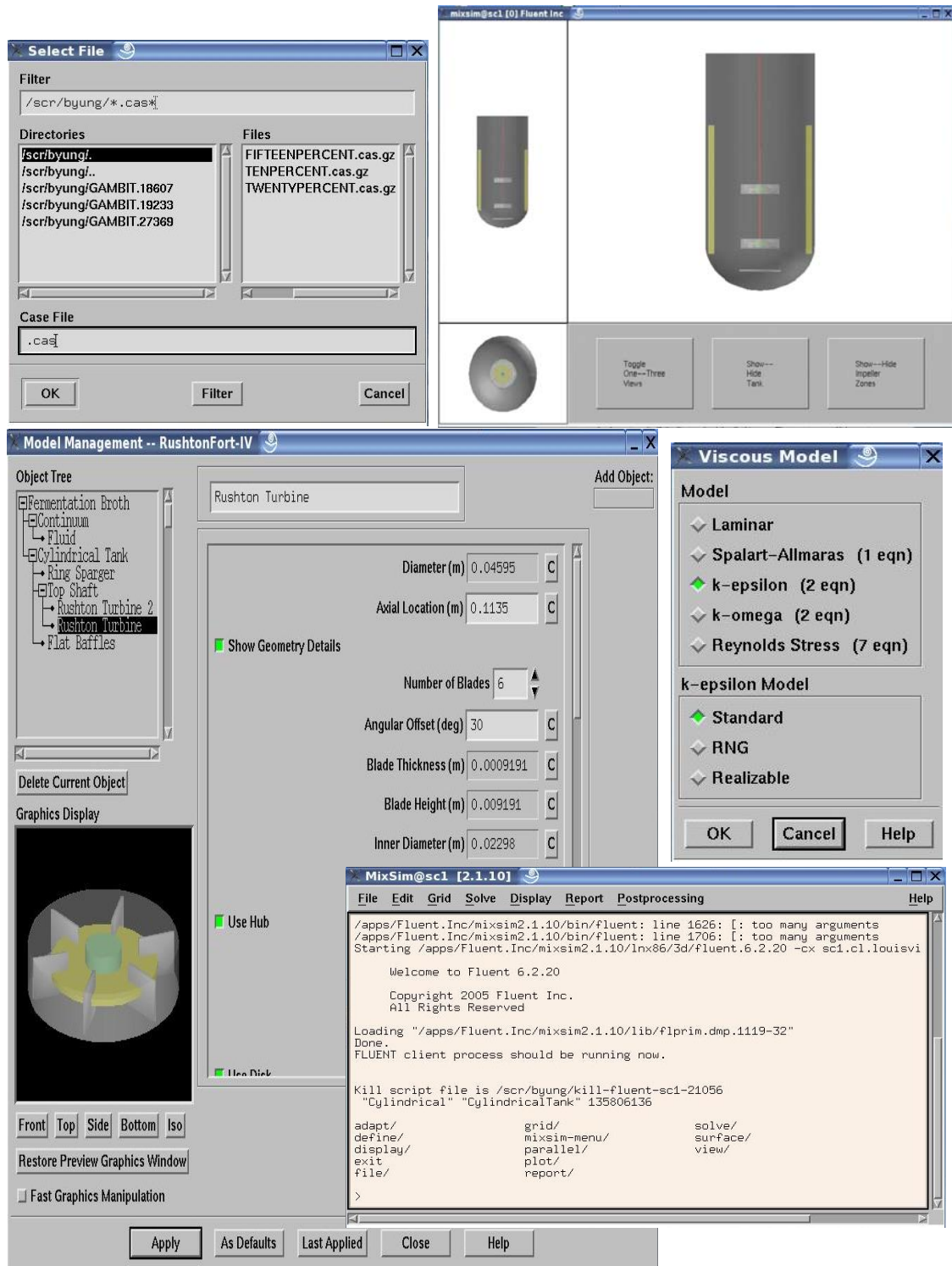


Figure C-1. The graphical user interface (GUI) components (MixSim 2.1.10).

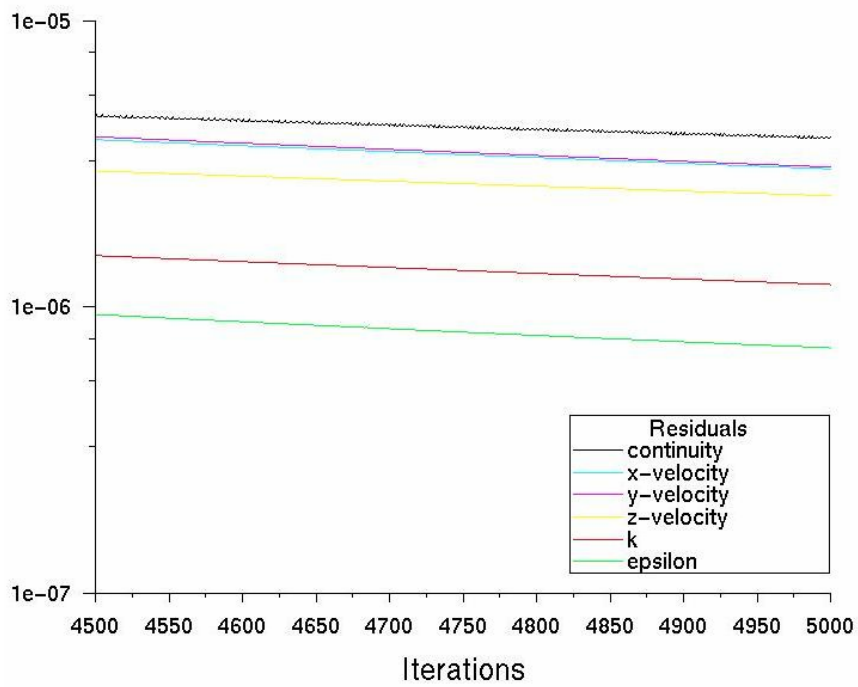


Figure C-2. Scaled residuals.

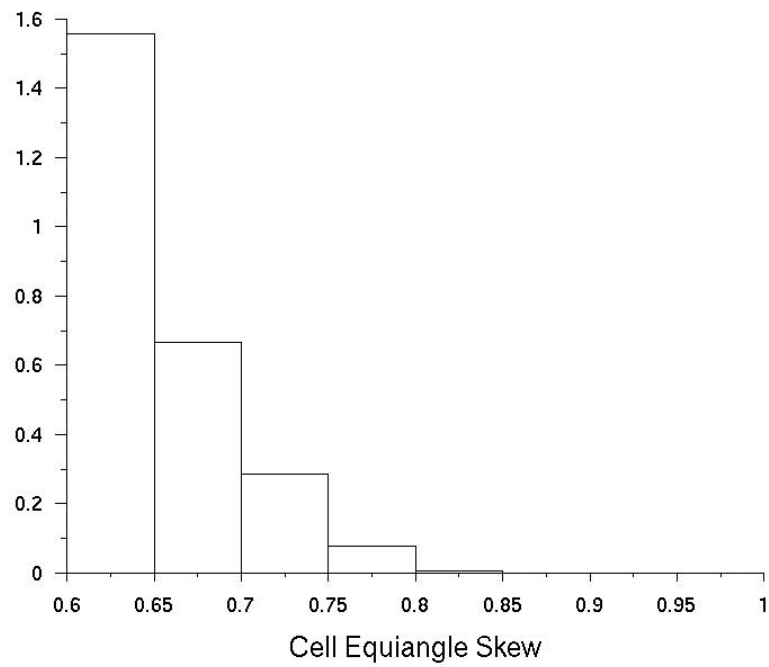


Figure C-3. Histogram of tank cell equiangular skew.

Table C-1. Geometry of 3 L mixing tank.

BioFlo 3000 (3L Mixing Tank, NBS)	
Cylindrical Tank	
Diameter (m)	0.138
Tank Height (m)	0.265
Liquid Level (m)	0.177
Top Style	Flat
Bottom Style	Ellipsoidal
Flat Baffles	
Bottom Elevation (m)	0.042
Top Elevation (m)	0.185
Width (m)	0.008
Top Shaft	
Shaft Diameter (m)	0.0025
Speed (rpm)	120
Shaft Tip Elevation (m)	0.0503
Impeller (Rushton I)	
Diameter (m)	0.046
Axial Location (m)	0.114
Number of Blade	6
Impeller (Rushton II)	
Diameter (m)	0.046
Axial Location (m)	0.053
Number of Blade	6
Ring Sparger	
Ring Diameter (m)	0.050
Tube Diameter (m)	0.003
Axial Location (m)	0.023

Table C-2. Blend time and flow rate (RPM=120).

Blend Time for a Single Impeller			
$t_{99} = \frac{4.605}{aN \left(\frac{D}{T}\right)^b \left(\frac{T}{Z}\right)^c}$			
N(rps)	2	a	1.06
D(m)	0.046	b	2.17
T(m)	0.138	c	0.5
Z(m)	0.177	T ₉₉ (s)	26.7446
N _b	6		
$t_{99} = \frac{4.605}{\sum a_i N_i \left(\frac{D}{T}\right)^{b_i} \left(\frac{T}{Z}\right)^{c_i}}$			
Blend Time for All Impellers In the Vessel			
T _{99, eff} (s)		13.3723	

Radial Disk Impellers (for flow rate calculations)			
$N_Q = a \left(\frac{N_b}{6}\right)^b \frac{W_b}{D} \left(\frac{D}{T}\right)^c$			
a	6	c	0.3
b	0.7		
Flow Rate			
$Q = N_Q ND^3$			
N (rps)	2	N _q	0.8628
D (m)	0.046	Q(m ³ /s)	0.0002

Table C-3. Power draw and correlation for water simulation ($\mu=0.0010$, RPM=120).

Impeller Type (for power draw calculations)			
$N_p = a \left(\frac{W_b}{0.2D} \right) \left(\frac{N_b}{6} \right)^b$			
W_b (m)	0.0092	a	5
N_b	6	b	0.8
D(m)	0.046		
Power Draw			
$P = N_p \rho N^3 D^5$			
ρ (kg/m ³)	998.2	N_p	5
N (rps)	2	P(W)	0.0082
D(m)	0.046	μ (Kg/m·s)	0.0010

Report Torque (Top Shaft)	
Upper Impeller	
Shaft Torque (n-m)	0.00064612
Shaft Power (W)	0.00811943
Impeller Torque (n-m)	0.00033790
Impeller Power (W)	0.00424617
Lower Impeller	
Shaft Torque (n-m)	0.00064612
Shaft Power (W)	0.00811943
Impeller Torque (n-m)	0.00030822
Impeller Power (W)	0.00387326

Correlations	
Single or Multiple Impellers	
Number of Impellers	2
Blend Time (s)	13.3723
Single Impeller	
Impeller Type	Radial
Reynolds Number	4203.33
Froude Number	0.0187
Power Draw (w)	0.0082
Flow Rate (m ³ /s)	0.0002

Table C-4. Power draw and correlation for 10 % Solka Floc fermentation broth ($\mu=0.0192$, RPM=120).

Impeller Type (for power draw calculations)			
$N_p = a \left(\frac{W_b}{0.2D} \right) \left(\frac{N_b}{6} \right)^b$			
W_b (m)	0.0092	a	5
N_b	6	b	0.8
D (m)	0.046		
Power Draw			
$P = N_p \rho N^3 D^5$			
ρ (kg/m ³)	1130	N_p	5
N (rps)	2	P (W)	0.0093
D (m)	0.046	μ (Kg/m·s)	0.0192

Report Torque (Top Shaft)	
Upper Impeller	
Shaft Torque (n-m)	0.00075451
Shaft Power (W)	0.00948143
Impeller Torque (n-m)	0.00038094
Impeller Power (W)	0.00478698
Lower Impeller	
Shaft Torque (n-m)	0.00075451
Shaft Power (W)	0.00948143
Impeller Torque (n-m)	0.00037357
Impeller Power (W)	0.00469445
Working Volume =0.002 m ³	

Correlations	
Single or Multiple Impellers	
Number of Impellers	2
Blend Time (s)	13.3723
Single Impeller	
Impeller Type	Radial
Reynolds Number	248.573
Froude Number	0.0187
Power Draw (w)	0.0093
Flow Rate (m3/s)	0.0002

Table C-5. Power draw and correlation for 15 % Solka Floc fermentation broth
($\mu=0.0775$, RPM=120).

Impeller Type (for power draw calculations)			
$N_p = a \left(\frac{W_b}{0.2D} \right) \left(\frac{N_b}{6} \right)^b$			
W_b (m)	0.0092	a	5
N_b	6	b	0.8
D(m)	0.046		
Power Draw			
$P = N_p \rho N^3 D^5$			
ρ (kg/m ³)	1183.6	N_p	5
N (rps)	2	P(W)	0.0097
D(m)	0.046	μ (Kg/m·s)	0.0775

Report Torque (Top Shaft)	
Upper Impeller	
Shaft Torque (n-m)	0.00102215
Shaft Power (W)	0.01284475
Impeller Torque (n-m)	0.00051455
Impeller Power (W)	0.00646603
Lower Impeller	
Shaft Torque (n-m)	0.00102215
Shaft Power (W)	0.01284475
Impeller Torque (n-m)	0.00050760
Impeller Power (W)	0.00637872
Working Volume =0.002 m ³	

Correlations	
Single or Multiple Impellers	
Number of Impellers	2
Blend Time (s)	13.3723
Single Impeller	
Impeller Type	Radial
Reynolds Number	64.503
Froude Number	0.0187
Power Draw (w)	0.0097
Flow Rate (m3/s)	0.0002

Table C-6. Power draw and correlation for 20 % Solka Floc Fermentation Broth
($\mu=0.1050$, RPM=120).

Impeller Type (for power draw calculations)			
$N_p = a \left(\frac{W_b}{0.2D} \right) \left(\frac{N_b}{6} \right)^b$			
W_b (m)	0.0092	a	5
N_b	6	b	0.8
D(m)	0.046		
Power Draw			
$P = N_p \rho N^3 D^5$			
ρ (kg/m ³)	1250.6	N_p	5
N (rps)	2	P(W)	0.0103
D(m)	0.046	μ (Kg/m·s)	0.1050

Report Torque (Top Shaft)	
Upper Impeller	
Shaft Torque (n-m)	0.00117487
Shaft Power (W)	0.01476383
Impeller Torque (n-m)	0.00059345
Impeller Power (W)	0.00745749
Lower Impeller	
Shaft Torque (n-m)	0.00117487
Shaft Power (W)	0.01476383
Impeller Torque (n-m)	0.00058142
Impeller Power (W)	0.00730634
Working Volume =0.002 m ³	

Correlations	
Single or Multiple Impellers	
Number of Impellers	2
Blend Time (s)	13.3723
Single Impeller	
Impeller Type	Radial
Reynolds Number	50.3044
Froude Number	0.0187
Power Draw (w)	0.0103
Flow Rate (m3/s)	0.0002